New oxide-based electrodes for advanced redox supercapacitors

Tuyen Nguyen

To cite this version:

Tuyen Nguyen. New oxide-based electrodes for advanced redox supercapacitors. Materials. Université Grenoble Alpes; Instituto superior técnico (Lisbonne), 2015. English. NNT : 2015GREAI095 . tel-01278418

HAL Id: tel-01278418
https://theses.hal.science/tel-01278418v1

Submitted on 24 Feb 2016

THÈSE

Pour obtenir le grade de

DOCTEUR DE L'UNIVERSITÉ GRENOBLE ALPES

préparée dans le cadre d'une cotutelle entre l'*Université Grenoble Alpes* et *Universidade de Lisboa*

Spécialité : **Matériaux, Mécanique, Génie Civil, Electrochimie**

Arrêté ministériel : le 6 janvier 2005 - 7 août 2006

Présentée par

Tuyen NGUYEN

Thèse dirigée par **Michel BOUDARD** et **Fátima MONTEMOR**

préparée au sein des **Laboratoire des Matériaux et du Génie Physique, UMR 5628 CNRS/Grenoble INP**
dans **L'Ecole Doctorale IMEP-2**
et du **Centro de Química Estrutural**
dans **Instituto Superior Técnico**

Electrodes innovantes à base d'oxyde pour les supercondensateurs redox

Thèse soutenue publiquement le **22nd October 2015**,
devant le jury composé de:

M. João BORDADO
Professor, IST Lisbon, Portugal (Président)
M. Christopher BRETT
Professor, Universidade de Coimbra, Portugal (Rapporteur)
Mme. Amélia ALMEIDA
Assistant Professor, CeFEMA, IST Lisbon, Portugal (Rapporteur)
M. Mário FERREIRA
Professor, Universidade de Aveiro, Portugal (Examinateur)
Mme. Liliane GUERLOU-DEMOURGUES
Professor, ICMCB-CNRS, Bordeaux, France (Examinateur)
Mme. Teresa MOURA e SILVA
Assistant Professor, ISEL Lisbon, Portugal (Examinateur)
Mme. Fátima MONTEMOR
Assistant Professor, CQE, IST Lisbon, Portugal (Directeur de Thèse)
M. Michel BOUDARD
Chargé de Recherche, LMGP-CNRS, Grenoble, France (Directeur de Thèse)

Titre: Electrodes innovantes à base d'oxyde pour les supercondensateurs redox

Résumé

Les oxydes simple ou double de métaux de transition (OMTs) sont des matériaux prometteurs pour les applications en tant qu'électrode dans des pseudo supercondensateurs ou des supercondensateur redox car ils peuvent présenter un gain de densité d'énergie résultant des réactions redox.

Ce mémoire de thèse a pour but l'étude et l'optimisation du comportement électrochimique d'électrodes d' oxydes simple de manganèse ainsi que le développement de nouvelles électrodes à base d'oxydes doubles (OMTs) conçues pour le stockage d'énergie dans les supercondensateurs redox , grâce au dépôt de ces matériaux actifs sur un collecteur de courant en acier inoxydable par électrodéposition ce qui représente une technique flexible et peu couteuse.

Afin d'étudier ces électrodes, leurs propriétés physico-chemique ont été caractérisées par microscopie électronique (SEM/TEM), spectroscopie X à dispersion d'énergie (EDX), par diffraction X (XRD), par spectroscopies Raman & Infrarrougee (FTIR), par microsopie à force atomique (AFM) et par magnétométrie SQUID (superconducting quantum interference device). Leurs propriétés electrochimique ont été caractérisées par voltamperométrie cyclique et chronopotentiométrie.

Les résultats détaillent la croissance et les caractérisations physico-chimique et électrochimique de plusieurs oxydes TMOS (TM=Mn, Mn-Co, Ni-Mn) ainsi que d'hydroxydes de Ni-Co préparés par électrodéposition. Le contrôle de la morphologie et de l'architecture des électrodes, en vue de créer des surfaces ayant des grandes surfaces actives, est le paramètre clé pour augmenter la performance du pseudo-condensateur. Dans le détail, le travail de recherche a contribué au développement de nouveau matériaux pour des électrodes à base d'oxyde (et hydroxydes) pour les supercondensateurs redox par: (i) la mise en œuvre de nouvelles électrodes avec des bonnes performances pseudocapacitive pour des supercondesateurs (Mn oxydes, Ni-Mn oxydes, Ni-Co hydroxydes), (ii) la pleine compréhension de l'effet du recuit sur la transformation de l'hydroxyde préparés par électrodéposition en oxyde et de la corrélation résultante avec les propriétés électrochimiques pour des électrodes à base d'oxyde Mn-Co, (iii) la description détaillée du mécanisme de croissance de films d' oxyde de Mn préparés par électrodéposition à partir d'électrolytes à base de nitrates, (iv) la mise en évidence d'une méthode prometteuse de mise en forme et contrôle de la morphologie de surface d'oxydes mixtes préparés par électrodéposition et ce à travers le contrôle de la croissance d'oxyde simples , (v) la compréhension du mécanisme de nucléation des hydroxydes préparés par électrodéposition (Ni-Co hydroxydes).

Les résultats de ce mémoire de thèse vont au delà de l'état de l'art et apportent des faits marquants pour l'avancée du développement de nouveaux matériaux pour électrodes dans des supercondensateurs redox.

Title: New oxide-based electrodes for advanced redox supercapacitors

Abstract

Transition metal oxides (TMOs) and double TMOs are promising materials for application as electrodes in pseudo supercapacitors or redox supercapacitors because they can exhibit increased energy density resulted from redox reactions.

This PhD dissertation aims at studying and improving the electrochemical behavior of single TMOs - manganese oxides and at developing new double TMOs electrodes tailored for energy storage in redox supercapacitors, by depositing the active materials directly on stainless steel current collector *via* a flexible and costless electrodeposition route.

To study these electrodes for supercapacitors, their physico-chemical properties were characterized by scanning/transmission electron microscopy (SEM/TEM), energy-dispersive X-ray spectroscopy (EDX), X-ray diffraction (XRD), Raman & Infrared spectroscopy (FTIR), atomic force microscopy (AFM) and superconducting quantum interference device (SQUID). Their electrochemical properties were characterized by cyclic voltammetry and chronopotentiometry.

The results have detailed the growing, physico-chemical and electrochemical characterizations of Mn oxides, Mn-Co oxides, Ni-Mn oxides and Ni-Co hydroxides prepared by electrodeposition. Tailoring the morphology and architecture these electrodes and creating surfaces exhibiting high surface area are key parameters for enhanced pseudocapacitive performance. In detail, the research work contributed to the development of novel oxide (and hydroxides) materials for redox supercapacitors by: (i) providing novel electrodes with good pseudocapacitive performance for supercapacitors (Mn oxides, Ni-Mn oxides, Ni-Co hydroxides), (ii) fully understanding the effect of annealing on the transformation from electrodeposited mixed hydroxides to mixed oxide and their correlation with electrochemical properties for the Mn-Co oxide – based electrodes, (iii) detailing the growing mechanisms of Mn oxide films electrodeposited from nitrate based electrolyte, (iv) revealing a promising way of tailoring surface morphology of electrodeposited mixed oxides by controlling the growth of single oxides, (v) understanding the nucleation mechanism of hydroxides prepared by electrodeposition (Ni-Co hydroxides).

Thus, the results of this PhD dissertation go beyond the state-of-the-art and provided valuable highlights to advance the development of novel electrode materials for redox supercapacitors.

Keywords: electrodeposition, electrodes, nanostructure, supercapacitors, transition metal oxides

Extended abstract

Transition metal oxides (TMOs) are promising materials for application as electrodes in pseudo supercapacitors or redox supercapacitors because they can exhibit increased energy density compared to electrochemical double layer supercapacitors based on carbon nanomaterials. The high energy density of electrodes based on TMOs is due to the redox reactions of the metal oxide/hydroxide with ions in the electrolyte. This redox contribution results in increased specific capacitance and thus high energy density. For this purpose, different single metallic oxides (or hydroxides), characterized by multiple valence states have been investigated and lead to promising results.

In this context, double (mixed) TMOs are expected to present higher energy density compared to their corresponding single TMOs, because more redox reactions can take place, thanks to the presence of various valences of two different metals. Several double TMOs have been proposed as redox-responsive materials for electrodes used in electrochemical energy storage systems. Surface morphology, oxide conductivity, and micro/nano architectures (including surface area and porosity) of TMO electrodes are amongst the most important factors determining the charge storage capability of the electrodes.

This PhD dissertation aims at studying and improving the electrochemical behavior of single oxides - manganese oxides and at developing new double TMOs electrodes tailored for energy storage in redox supercapacitors, by depositing the active materials directly on stainless steel current collector *via* a flexible and costless electrodeposition route. On the one hand, this route avoids the need of binders and additives that introduce additional resistances into the active material and ensures long-term adhesion as well as increased corrosion resistance. On the other hand, by controlling the deposition parameters it is possible to tailor the surface morphology and chemical composition of the electrodes, maximizing their charge storage capacity. For this purpose the work addresses the development of double (mixed) oxide electrodes based on the combination around Mn, Co and Ni

oxides by electrodeposition for application in redox supercapacitors. To study these electrodes for supercapacitors, their physico-chemical properties were characterized by scanning/transmission electron microscopy (SEM/TEM), energy-dispersive X-ray spectroscopy (EDX), X-ray diffraction (XRD), Raman & Infrared spectroscopy (FTIR), atomic force microscopy (AFM) and superconducting quantum interference device (SQUID). Their electrochemical properties were characterized by cyclic voltammetry and chronopotentiometry.

Chapter 1 of the dissertation presents a brief introduction about supercapacitors and current state-of-the-art in double TMOs electrode studies for supercapacitors. Chapter 2 presents an overview of the electrodeposition method and its application to the fabrication of nanostructured metal oxides, and the electrochemical methods used to characterize the capacitive response. Chapter 3 presents the results and its discussion and is organized into 7 sub-chapters in format of papers, which are either published or accepted, or already in a final form to be submitted. Brief summaries, status of the papers and my specific contribution will be given below. Chapters 4 and 5 present the general discussion of the results and conclusions and outlook, respectively.

Mn based mixed oxides were firstly developed. Thus, the first step consisted on the electrodeposition of manganese oxides and the study of their electrochemical response and physico-chemical properties (Sub-Chapter 3.1). Concomitantly, because Ni oxides and Co oxides, which display pseudocapacitive response in alkaline electrolyte, are used to fabricate the double TMOs, the electrochemical response of electrodeposited manganese oxide electrodes in alkaline electrolyte was investigated too. Sub-Chapter 3.1 was accepted for publication in the International Journal of Hydrogen Energy. My contribution was to: fabricate the electrodes, perform SEM and electrochemical measurements, interpret the results, and write the article.

Based on the previous results a new route was proposed to design manganese oxide electrodes with improved electrochemical response. The fabrication approach was based on the hydrogen bubbling-assisted electrodeposition, leading to the formation of the hierarchical micro-nano Mn oxide electrodes (Sub-Chapter 3.2). The results showed that the novel micro-nano structured MnO_2 films displayed good pseudocapacitive performance, making this approach a promising way to fabricate high performance metal oxide electrodes for redox supercapacitors. This Sub-Chapter 3.2 is planned to be submitted. My contribution was to: fabricate the electrodes, perform SEM, AFM and electrochemical measurements, interpret the results, and write the article.

Sub-Chapters 3.3 – 3.5 are focused on the fabrication and study of double TMOs. Theoretical calculations demonstrate that $MnCo_2O_4$ are expected to deliver very high specific capacitances amongst various possible double TMOs. Thereby, I decided to prepare a set of $MnCo_2O_4$ electrodes. The deposition process was based on the formation of electrodeposited TM hydroxides that are transformed to the spinel phase by thermal annealing. The evolution from the electrodeposited TM hydroxide phases into the spinel phase by thermal annealing and its correlation with electrochemical response is unclear up to now and therefore it was addressed in Section 3.3. Thus, this chapter studied in detail the chemical composition, structural, morphological evolution and electrochemical properties at each stage of the thermal annealing. $MnCo_2O_4$ electrodes revealed poor cycling stability, nevertheless the results provided interesting findings related to the effect of the annealing temperature. Sub-Chapter 3.3 is published in RSC Advances 2015, 5, 27844-27852. My contribution was to: fabricate the electrodes, perform SEM, AFM, FTIR, XRD and electrochemical measurements, interpret the results, and write the article.

Following the previous results a novel double TMO based on Ni and Mn oxides was electrodeposited (Sub-Chapter 3.4). The previous achievements allowed at selecting an annealing temperature of 250°C. Additionally, the Ni to Mn ratio was changed to study the corresponding changes in morphological, structural and electrochemical properties. The results revealed that these are very sensitive to the Ni:Mn ratio, with the optimum value being 1:3. The electrochemical results demonstrated a synergistic effect of redox reactions in the double Ni-Mn oxides. Furthermore, the electrodes based on Ni-Mn oxide deposited at Ni:Mn ratio of 1:3 exhibited a remarkable cycling stability, making it a very promising pseudocapacitive material. Sub-Chapter 3.4 is published in Journal Materials Chemistry A, 2015, 3, 10875-10882. My contribution was to: fabricate electrodes, perform SEM and electrochemical measurements, interpret the results, and write the article.

With the aim of increasing the charge storage capacity of the Ni-Mn oxide based electrodes, resulting from its very promising redox performance, this oxide was electrodeposited on 3D metallic foams prepared by hydrogen bubbling assisted electrodeposition (Sub-Chapter 3.5). The novel electrodes, composed of Ni-Mn oxide nanosheets on metallic foams, exhibited an enhanced pseudocapacitive performance compared to the corresponding oxides deposited directly on the stainless steel. Sub-Chapter 3.5 is published in Nanoscale 2015, 7, 12452-12459. My contribution was to: fabricate the oxide layers, perform SEM and electrochemical measurements, interpret the results, and write the article.

Since the mixed oxides based on Ni oxide displayed a good pseudocapacitive performance and since Ni-Co oxides/hydroxides have been proposed as redox-active materials for charge storage due to the synergistic contribution from the Ni and Co oxides/hydroxides, they were also electrodeposited over stainless steel current collectors (Sub-Chapter 3.6). The electrode was engineered in a way that it was possible to deposit two consecutive layers of $Ni(OH)_2$ and $Co(OH)_2$. This strategy is expected to sum up the contribution of the individual hydroxides to the total redox response. In fact, these electrodes presented specific capacitance values 30% above those resulting from the synergistic redox contribution in mixed Ni-Co hydroxides. Sub-Chapter 3.6 is planned to be submitted. My contribution was to: fabricate electrodes, perform SEM and electrochemical measurements, interpret the results, and write the article.

In this work, electrodeposition was used to prepare the electrodes because there is no need of using binders or foreign additives to prepare the active films. Given the relevance of this approach, the last part of this dissertation (Sub-Chapter 3.7) concerns to the fundamental understanding of the growing processes, which are still scarcely discussed. Therefore, the mechanisms of film formation were studied by fitting the current transients with different 3D growing models. The study was complemented by in-situ electrochemical AFM. The instantaneous nucleation based growing mechanism has been retrieved from these studies. Sub-Chapter 3.7 is planned to be submitted. My contribution was to: perform the current transients, *ex-situ* SEM and AFM, and *in-situ* electrochemical AFM measurements, perform the fittings, interpret the results, and write the article.

Overall, the results have detailed the growing, physico-chemical and electrochemical characterizations of Mn oxides, Mn-Co oxides, Ni-Mn oxides and Ni-Co hydroxides prepared by electrodeposition. Tailoring the morphology and architecture these electrodes and creating surfaces exhibiting high surface area are key parameters for enhanced pseudocapacitive performance. In detail, the research work contributed to the development of novel oxide (and hydroxides) materials for redox supercapacitors by:

- Providing novel electrodes with good pseudocapacitive performance for supercapacitors (Mn oxides, Ni-Mn oxides, Ni-Co hydroxides).

- Fully understanding the effect of annealing on the transformation from electrodeposited mixed hydroxides to mixed oxide and their correlation with electrochemical properties for the Mn-Co oxide – based electrodes.

- Detailing the growing mechanisms of Mn oxide films electrodeposited from nitrate based electrolyte.

- Revealing a promising way of tailoring surface morphology of electrodeposited mixed oxides by controlling the growth of single oxides.

- Understanding the nucleation mechanism of hydroxides prepared by electrodeposition (Ni-Co hydroxides).

Thus, the results of this PhD dissertation go beyond the state-of-the-art and provided valuable highlights to advance the development of novel electrode materials for redox supercapacitors.

Acknowledgements

I would like to express my special thank to Prof. Fátima Montemor not only for her scientific guidance during my whole thesis period but also for her encouragements and trust in my research activities.

I deeply appreciate Michel Boudard for his supervision during my thesis period in LMGP, Grenoble INP, especially for his guidance in the structural study and for the fruitful discussion in diverse scientific topics and surrounding issues.

I would like to thank the International Doctoral School in Functional Materials Science (IDS-FunMat) team, who has been organizing nice joint European doctoral school and annual training school.

Thanks to Maria João Carmezim, Sónia Eugénio and Rui Pedro Silva for their help since the starting of my experimental work and for their continuous support during my period in Instituto Superior Técnico.

Thanks to Laetitia Rapenne, Odett Chaix, Béatrice Doisneau, Carmen Jimenez and Hervé Roussel for their support and helpful discussion in microscopic, spectroscopic and diffraction measurements.

Thanks to João Jeremias, Pedro Nolasco, Bruno Nunes and Patricia Carvalho for their support with the Atomic Force Microscope measurements.

Thanks to Eric Eyraud (Institut Néel) for his support with SQUID measurements.

Thanks to Isabel Nogueira for Electron Microscope measurements.

Thanks to Francois Weiss for making the connection of the joint PhD project between IST Lisboa and Grenoble INP.

Thanks to the past and current directors of LMGP: Bernard Chenevier, Franz Bruckert and Carmen Jimenez for their welcome into the lab.

Thanks to Michèle San Martin, Arnaud Robin and Virginie Charrière for their help in administrative works.

Thanks to Valerie Stambouli and Marianne Weidenhaupt for their welcome in the office.

Thanks to the current and alumni members of the Corrosion Science and Surface Engineering Group in IST Lisboa and LMGP, Grenoble INP: Alberto Adám Mas, Alejandra Gomez-Garcia, Ana Lúcia Morais, Andreia Marques, Darya Snihirova, Kevin Mason, Kush Upadhyay, Laura Córdoba, Maryna Taryba, Miguel Ferreira, Mirela Lourenço, Ricardo Pinto, Sofia Panão, Yegor Morozov, Daniel Langley, Shanting Zhang, Hai Le, Ionela Iliescu…

Thanks to Vietnamese mates in the IDS-FunMat School: Lo Nhat Truong, Le Quang Tri and Dao Ngoc Tuyen.

Without their support, my thesis may not be done!

Table of contents

Abbreviations

AFM	Atomic Force Microscope
CD	Charge-Discharge
CV	Cyclic Voltammetry
DFTEM	Dark Field Transmission Electron Microscope
EDX	Energy Dispersed X-ray Spectroscopy
FC	Field Cooled
FEG-SEM	Field Emission Gun – Scanning Electron Microscope
FFT	Fast Fourier Transforms
FTIR	Fourier Transformed Infrared Spectroscopy
FWHM	Full Width at Half Maximum
HRTEM	High Resolution Transmission Electron Microscope
NMO	Nickel manganese oxide
SAED	Selected Area Electron Diffraction
SQUID	Superconducting Quantum Interference Device
STEM	Scanning Transmission Electron Microscope
TEM	Transmission Electron Microscope
TM	Transition metals
TMO	Transition metal oxide
XRD	X-ray Diffraction
ZFC	Zero Field Cooled

Chapter 1. Introduction

1.1. Supercapacitors

1.1.1. Current state-of-the-art in materials for energy conversion and storage

The fossil depletion, due to the overuse of fossil resources by the traditional electrical generation systems based on combustion engines with low energy conversion efficiency governed by Carnot cycle, and the finite natural resources available, result in increased energy price and boost the need of developing new high efficiency energy production technologies. The traditional electrical generation systems are not only limited by their low efficiency but also contribute for climate change as a result of hazard gases (CO, CO_2, NO_2…) produced during the energy production process, affecting directly environment and human-health. Thus, the development of new and green energy generations systems that overcome the limitation of Carnot cycle, and reduce the air pollution, are currently receiving considerable attention in the research community.

In this progress, natural energy available resources, based on renewable energies such as wind, ocean, bio and solar are current being investigated for electrical generation towards large scale or grid applications.

Other electrical generation systems such as fuel cells, metal-air batteries are being studied for both large/small scale and for mobile applications. Hydrogen fuel cells are promising devices because they display high energy conversion efficiency, with water as the only by-product. However, efficient ways to generate hydrogen and safe ways to store hydrogen still require developments. Along these lines, the development of catalysts and storage materials are receiving a lot of attention. For examples, semiconductor oxide photocatalysts for water photolysis hydrogen generation, transition metal (TM) or TM oxide electrocatalysts for water electrolysis hydrogen generation based on light metal (complex) hydrides systems for the reversible solid state hydrogen storage are currently under study. Small organic molecules based liquid fuels such as methanol, ethanol, and formic acid can also be used in fuel cells, reducing concerns about fuel storage. Nevertheless, regardless the fuels used, the development of efficient electrocatalysts is necessary, especially oxygen electrocatalysts, which is a main drawback to commercialize fuel cells, due to the high overpotential of oxygen reduction reaction. Methods for converting CO_2 into small organic molecules such as alcohols and formic acid to be used as fuels are also being developed.

Thermoelectric devices based on thermoelectric materials, with ability of converting heat energy into electrical energy are also of great interest to utilize waste heat generated by other systems/devices such as fuel cells. Current researches focus on the development of thermoelectric materials with enhanced phonon boundary scatterings and thermopower to improve its efficiency.

Metal-air (Li/Zn/Al/Si/Mg/Fe-air) batteries with high specific energy, as a result of redox reactions of metal with oxygen from air, are promising energy generation devices. Metals are considered the fuel (requiring regular replacement) in these devices, so these are also named as metal-air fuel cells. Similar to other fuel cells, anode/cathode/electrolyte engineering/studying is still necessary to improve the efficiency of this device, namely the anode lifetime.

Presently renewable energy sources that include wind/water flow/solar energies are strategic, but these are environmentally dependent intermittent energies. The energy supply/demand varies significantly during the day, and the grid requires strategies to smooth the peak off/ peak on variations. Energy storage systems are envisaged as one of the most suitable routes to harmonize the supply/demand cycles. For this purpose the (electrical/charge) energy storage devices displaying high energy density and high power density are of utmost relevance. In this context, Li/Na ion batteries are extremely promising, but still far from applications and these are being under development and despite its increased energy densities drawbacks still exist, namely in what concerns safety issues. These drawbacks are presently subject of intensive research. On the other hand, redox flow batteries are another option but these still lack energy density as well as demanding installation / maintenance requirements. Presently, supercapacitors are already used as “peak-shavers” in the peak on/peak off cycles and on smoothing the grid and are emerging candidates for larger scale energy storage too.

Batteries offer high energy density, due to the bulk insertion/conversion/alloying reaction (or combining of these reactions) mechanisms or electrolyte redox reactions, but are limited in lifetime. Supercapacitors offer high power density due to the charge accumulation or fast surface redox reaction and long lifetime, but are limited in energy density.

The energy density and power density comparison of batteries and supercapacitors are depicted in Figure 1.1. Traditionally, supercapacitors are used in combination with batteries to provide additional power for applications requiring high power density. Their low energy density is an obstacle, and thus supercapacitors are normally not used as a single energy storage device. However, considering the advantages of supercapacitors in terms of power density and lifetime, and the fact that their energy density can be enhanced, it can result in a very promising energy storage device.

The key for increased energy density of supercapacitors resides on the electrode material. Currently, the development of new electrodes for enhanced energy density supercapacitors are receiving considerable attention, with some promising results being available. Thus, this PhD dissertation aims at contribution for this crucial objective by delivering novel electrode materials characterized by increased energy storage performance.

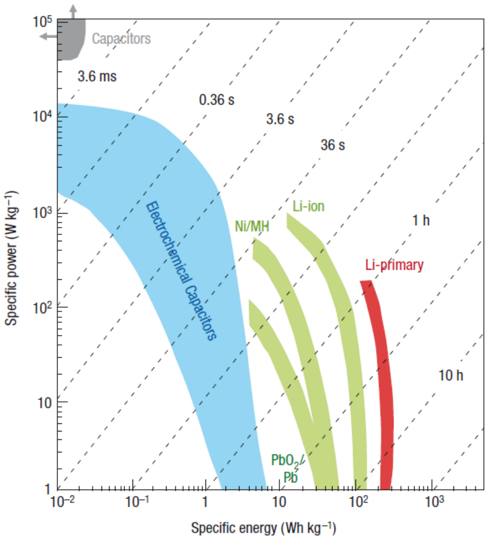

Figure 1.1. Power density vs. energy density of several electrical energy storage devices: capacitors, supercapacitors, and batteries [1].

The discussion above highlights the importance of materials science/engineering and electrochemistry for the development of energy conversion and storage devices. A few milestone review papers, highlighting the most recent trends can be found in literature [1-6]. New emerging journals of high impact are paying attention to this critical issue, and well-recognized journals of high level are releasing new separated sections concerning materials for energy conversion and storage. Examples are journals from different publishers and scientific societies such as Energy & Environmental Science (RSC), Advanced Energy Materials (Wiley), Journal of Materials Chemistry A: Materials for energy and sustainability (RSC), Nano Energy (Elsevier), ChemSusChem (Wiley) and Nature Energy (launching in 2016, NPG) are key indicators of the relevance of materials research in the energy field. Indeed, we are in the energy research era and there is still a plenty of chances for researchers to study and to overcome the current state of the art in developing a new generation devices for electrical production and storage. The future application of these devices may not just rely on single component but can be in hybrid devices, taking synergistic advantages of each single device.

1.1.2. Supercapacitors configuration, storage mechanism and classification

First supercapacitors, with charge storage mechanism based on the adsorption of ions in electrolyte onto the surface of electrode materials, forming a Helmholtz double layer, were reported in 1957 [7]. Even though the charge storage mechanism was not understood at that time, the relation between the specific surface area of the electrode material and the charge storage capacity was identified. Carbon materials of high specific surface have been the prime choice for this class of supercapacitors, and have been continuously applied and studied.

Generally, supercapacitors configurations are similar to other electrochemical energy conversion/storage devices. It is composed of an anode and a cathode electrode separated by a solid separator within an electrolyte (Figure 1.2).

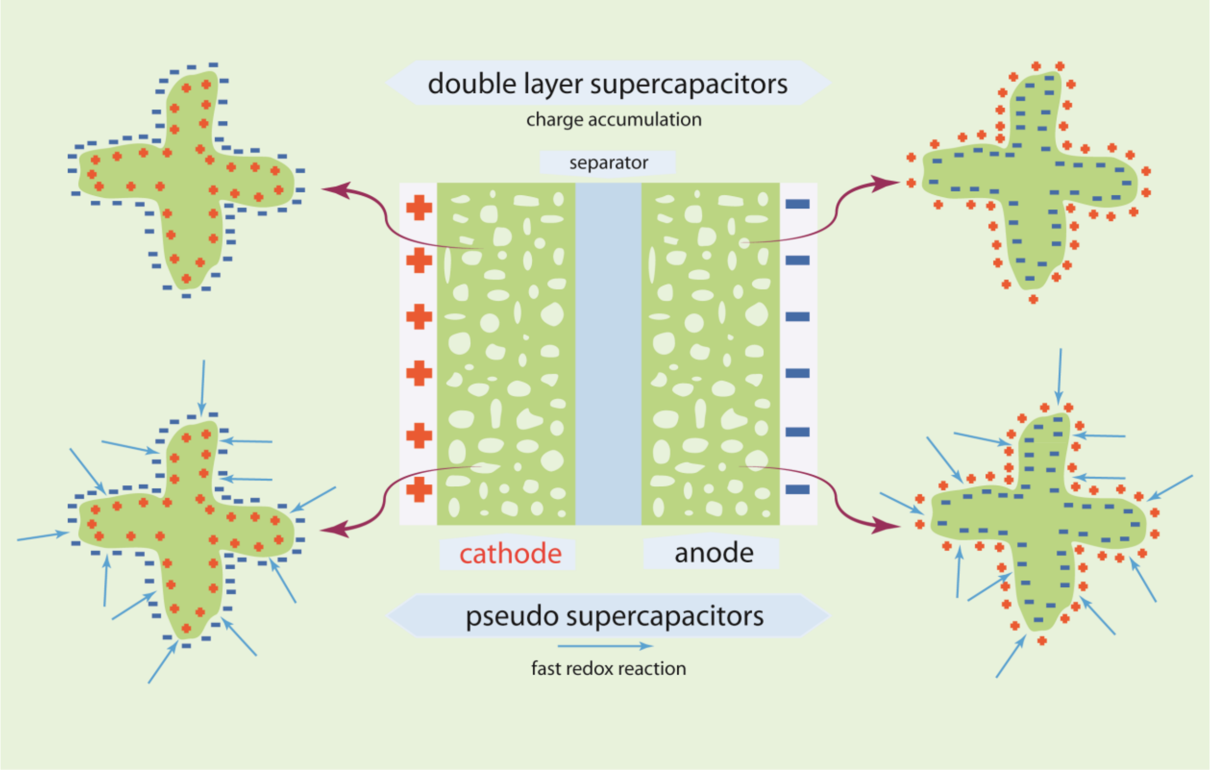

Figure 1.2. Supercapacitor configuration and their classification based on charge storage mechanism: double layer supercapacitors and pseudo supercapacitors.

Depending on the charge storage mechanism, supercapacitors are classified in two classes (Figure 1.2) which included: (1) double layer supercapacitors which are based on non-Faradaic processes and that involve solely the formation of electrochemical double layers at the surface of the electrode and (2) pseudo-supercapacitors, which are based on Faradaic reactions between the electrode material and the electrolyte. Supercapacitors can also be composed of two electrodes that store charge differently, one like that of double layer supercapacitors and the other one like that of pseudo supercapacitor, and so-called hybrid supercapacitors.

1.1.3. Double layer supercapacitors

Double layer supercapacitors are based on the fast non-Faradaic process due to the formation of an electrochemical double layer on the electrode surface, which are characterized by rectangular shape cyclic voltammograms and linear charge-discharge curves (Figure 1.3a and b). The fast non-Faradaic process leads to the high power density of the device, however, the charge storage is rather limited, being totally governed by the specific surface area of electrodes, and therefore the energy density is quite low (5-10 Wh kg^{-1}) [8, 9].

Porous carbons with high surface area and good conductivity including activated carbons, carbon aerogels, and carbon nanotubes are commonly studied for double layer supercapacitors [10-16].

Studies involve developing new preparation/activation methods to obtain high surface area carbons, tailoring carbons surface by doping, or assembling in 3D hierarchical structure to improve supercapacitive response [10-13, 17-19]. Fundamental studies relating to the correlation of electrode properties such as pore size and distribution and electrolyte properties such as ionic radius, neutral, acidic and alkaline environments to the specific capacitance have also been reported [14, 15]. The use and the study of ionic liquids in order to overcome the potential limitation of aqueous electrolyte due to water electrolysis have been also frequently reported [16].

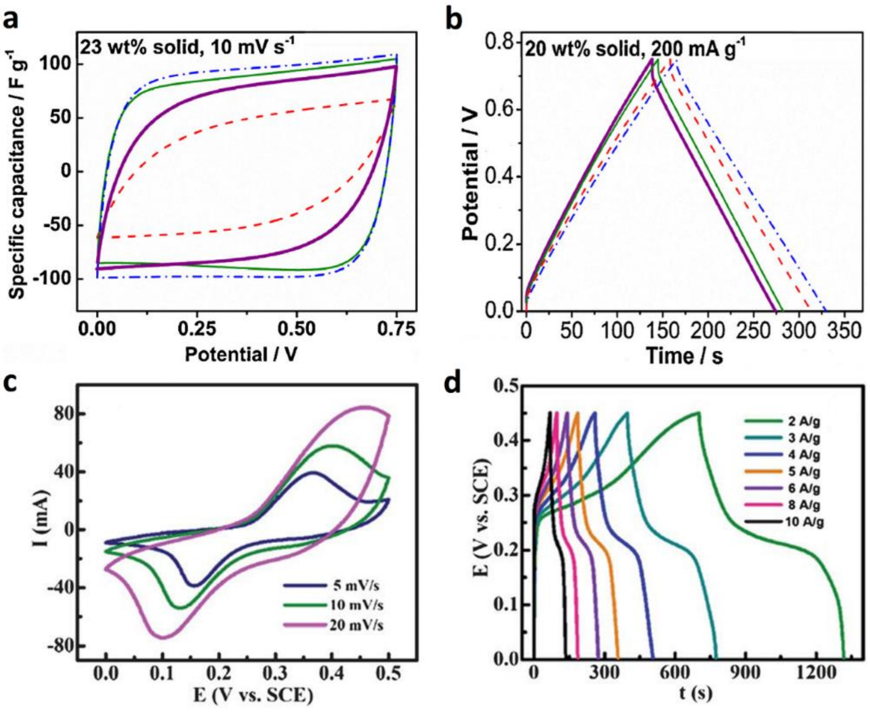

Figure 1.3. Typical cyclic voltammetry and charge discharge curves of (a, b) double layer supercapacitors [20] and (c, d) pseudo supercapacitors [21].

Recent attention has been paid to newly discovered graphene and their derivatives as new advanced materials for supercapacitors electrodes with huge number of publications due to its high electrical conductivity and high theoretical specific surface area of 2630 m^2 g^{-1} [22-24]. The supercapacitive response of graphene - based electrodes, however, do not really show a significant advantage compared to other carbon materials. It is very interesting in term of discovering new properties and designing new architectures of the new material [25]. However, in terms of materials to be used as supercapacitor electrodes, other carbon materials (structuring and designing in a rational way) can also have comparable or even better supercapacitive response than that of graphene and its derivatives [12, 26-32].

1.1.4. Pseudo supercapacitors

The pseudocapative behavior was first discovered on RuO_2 electrode by S. Trasatti [33] and was extensively studied by B. Conway [34, 35] on RuO_x and CoO_x for pseudo supercapacitors. Different from double layer supercapacitors, which have been quite known before these studies, pseudo supercapacitors involve Faradaic redox reactions of the electrode material with ions in the electrolyte. High specific surface area is also a requirement for the oxide-based electrodes to achieve an enhanced pseudocapacitive performance. RuO_2 based pseudocapacitive electrodes display rectangular shape cyclic voltamograms, similar to that of double layer supercapacitors, resulting from consecutive redox reactions over the broad range of the potential window. This pseudocapacitive response is due to the multivalent states of Ru. For other transition metal oxides, the redox reactions take place in a narrower potential window, resulting in the presence of well-defined redox peaks in the cyclic voltammograms (Figure 1.3c). The charge-discharge curves also display a non-linear response, consequence of the redox reactions observed in the non-rectangular cyclic voltammograms (Figure 1.3d).

Several Faradaic processes may contribute to the total pseudocapacitance of the electrodes [36], which are (i) underpotential deposition, (ii) redox pseudocapacitance and (iii) intercalation/insertion pseudocapacitance.

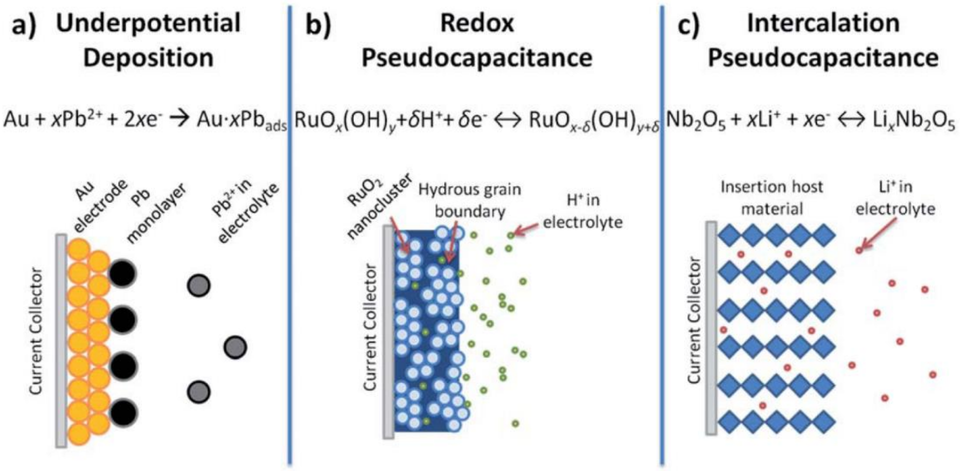

Figure 1.4. Processes contributing to pseudocapacitance: (a) underpotential deposition, (b) redox pseudocapacitance and (c) intercalation/insertion pseudocapacitance [37].

(i) Underpotential deposition relates to the monolayer absorption of metal ions on another metal surface at a potential lower than that of the equilibrium redox potential. However, since pseudocapacitive materials normally work in aqueous electrolyte, this phenomenon is not important.

(ii) Redox pseudocapacitance is based on surface redox reactions of electrode materials with ions from the electrolyte. The reactions depend upon the interface between the electrode and electrolyte. Therefore, the porosity and surface area of the electrode materials are of relevance to obtain high specific capacitance values. Pseudo supercapacitors used this type of pseudocapacitive materials are further classified into redox supercapacitors.

(iii) Intercalation/insertion pseudocapacitance is based on the intercalation and redox reaction of electrolyte ions in the interlayer of pseudocapacitive materials with/without involving of phase changes. The electrode materials must have a crystal structure, with high interlayer distance among lattice planes, to allow the diffusion of ions into interlayers. The requirement of high porosity is less important as compared to redox pseudocapacitance relied on the surface absorption and charge transfer of electrolyte ions and electrodes. Pseudo supercapacitors used this type of pseudocapacitive materials are further classified into intercalation supercapacitors.

1.1.5. Electrochemical response underlying pseudosupercapacitors

The pseudocapacitive response and the underlying electrochemical process relating to the charge storage mechanism can be characterized by cyclic voltammetry and charge-discharge cycling (details about these techniques will be presented in the experimental method of the thesis). The electrochemical process depends on the scan rate in cyclic voltammetry and on the applied current density in charge-discharge cycling.

As a result, the current response in cyclic voltamograms depends on a scan rate. This dependence can be described as [38]:

$$i(V) = k_1 v^{1/2} + k_2 v \qquad (1.1)$$

where i (A cm^{-2}) is the current response, v (mV s^{-1}) is the scan rate, k_1 and k_2 are constant numbers.

The first term is a contribution of redox/intercalation reactions, the reactions have been known as diffusion controlled process, varying with $v^{1/2}$. The second term is a contribution of surface adsorption reaction or charge accumulation, which is a fast process, therefore the current response varies with v.

The contribution of redox capacitance and surface adsorption can be separated by determining k_1 and k_2 at each potentials, giving a quantitative contribution of those processes to the total charge storage.

The total pseudocapacitive response can also be described as [39]

$$Q = Q_{v=\infty} + k v^{-1/2} \qquad (1.2)$$

where Q is the total charge, $Q_{v=\infty}$ is the capacity governs by the surface process and it is independent of the scan rate. The diffusion-controlled capacity is depended on $v^{-1/2}$.

Thereby, by applying these approaches, it is possible to separate the current response from the two contributions, and to calculate the contribution of the double layer capacitance and the contribution of the diffusion-controlled redox capacitance to the total capacitance.

Charge-discharge measurements with different current densities also show time variation; hence this test contains kinetic information inside. However, in many reports [40, 41] charge-discharge curves tend to better evidence the double layer effect compared to cyclic voltamograms. Consequently, the slope of the charge-discharge curves tends to be more linear even though well-defined redox peaks can be observed in the cyclic voltamograms. Thus, kinetic information extracted from charge-discharge curves often show very high contribution from the double layer capacitance or surface adsorption even if the cyclic voltamograms display well-defined redox peaks, giving inaccurate information when applying the most common description of current plateau in the charge-discharge curves [42]. The development of more appropriate models is thus necessary to extract kinetic information from the charge-discharge curve.

1.1.6. Supercapacitors metrics of electrode materials

- Capacitance (C) quantifies the amount of charge stored in a specific potential window for a known weight (or area or volume) of pseudocapacitive material. High specific capacitance is the key requirement for high charge storage or high energy density electrode.

- Rate capability is the charge storage/energy density capacity at high applied current density compared to the value at low applied current density. High rate capability value is an important requirement for high-rate applications and for fast charge of supercapacitors.

- Energy density (E) is the amount of energy that can be stored per mass (Wh/kg) or per volume (Wh/l), which is directly related to the specific capacitance by the following relationship $E = \frac{1}{2}CV^2 = \frac{QV}{2}$.

- Power density (P) is charge/discharge rate, which describes how fast the same amount of energy can be absorb or deliver for a given time, P=E/t, which is directly related to rate capability.

- Cycling stability is charge capacity degradation for a given number of fully charge-discharge cycles. High cycling stability is the important requirement for the practical application of pseudocapacitive electrodes in supercapacitors.

These metrics are totally determined by properties of electrode/electrolyte interface. For electrode materials, the following properties are of significant important to performance of supercapacitors: surface morphology, architecture, porosity, conductivity, ionic diffusion and redox activity.

1.1.7. Materials for redox supercapacitors

Ruthenium oxides RuO_x have been widely studied in pseudocapacitor research [43-45]. Experimentally, RuO_x exhibit very good pseudocapacitive performance, characterized by square shape cyclic voltammograms and high specific capacitance, as described previously, making it the ideal pseudocapacitive materials. However, the high cost of RuO_x prohibits their ability to be integrated in supercapacitive devices for practical uses. Therefore, cheaper oxides have been searched and studied over the last 20 years, for example, manganese oxides, nickel oxides, and cobalt oxides. They offer, not only low cost due to their natural abundance, but also a good pseudocapacitive response, thereby making them promising pseudocapacitive materials for supercapacitors. The next section will describe some promising metallic oxides and hydroxides for pseudocapacitor electrodes.

1.1.7.1. Manganese oxides

The charge storage mechanism of manganese oxides (the most commonly studied phase is MnO_2) is based on surface redox reactions with cations in neutral or acidic electrolytes as below [46-48]:

$$MnO_2/Mn_3O_4 + C^+ + e- \leftrightarrow MnOOC/Mn_3O_4\text{-}C \qquad C^+=H^+/Na^+/K^+/Li^+ \qquad (1.3)$$

where C^+ is cations in electrolyte such as H^+, Na^+, K^+ or Li^+.

Few studies have also been proposed about the pseudocapacitive response in alkaline electrolyte based on redox reaction with hydroxyl ions [49, 50].

Similar to RuO_x, due to the multi valence states of manganese in manganese oxides, their cyclic voltamograms display a rectangular shape, indicating a very good pseudocapacitive behavior.

1.1.7.2. Nickel oxides

Nickel oxides in alkaline electrolytes undergo the following reversible redox reactions [51, 52]:

$$NiO + OH^- \leftrightarrow NiOOH^- + e^- \qquad (1.4)$$

The redox reaction of NiO with OH^- results in phase change, thus displaying well-defined redox peaks in cyclic voltamograms, leading to very high theoretical specific capacitance.

1.1.7.3. Cobalt oxides

Cobalt oxides display alkaline electrolytes can display a capacitive response due to the following reversible redox reactions [53, 54]:

$$Co_3O_4 + H_2O + OH^- \leftrightarrow 3CoOOH + e^- \qquad (1.5)$$

$$3CoOOH + 3OH^- \leftrightarrow 3CoO_2 + 3H_2O + e^- \qquad (1.6)$$

The first reaction is similar to the case of nickel oxide, and then it is followed by the second redox reactions, contributing for an increased capacitive response compared to nickel oxides. Nevertheless, it is also characterized by cyclic voltammograms with well-defined redox peaks.

1.1.8. Materials for intercalation/insertion supercapacitors

This class of materials includes several metal oxides/hydroxides [55-57] with high interlayer lattice such as MnO_2, MoO_3, Nb_2O_5, V_2O_5, TiO_2, $Ni(OH)_2$ and $Co(OH)_2$.

The charge storage is based on the intercalation/insertion reaction within the host lattice. For example [55, 56, 58, 59]

$$[V_2O_5]_{bulk} + xLi^+ + xe^- \leftrightarrow [Li_xV_2O_5]_{bulk} \quad (1.7)$$

$$[Ni(OH)_2]_{bulk} + OH^- \leftrightarrow [NiOOH]_{bulk} + H_2O + e^- \quad (1.8)$$

The surface area is less important to the total charge storage, however high surface area electrodes are still needed for better pseudocapacitive performance.

1.1.9. Theoretical and experimental specific capacitance value

The theoretical specific capacitance (C/F g^{-1}) can be calculated based on number of electrons that are stored/released in the redox reactions and is given by the following equation

$$C = \left(\frac{nF}{m}\right)\frac{X}{E} \quad (1.9)$$

where n is number of electron stored/released in the redox reactions, F is Faraday constant (96485 C mol^{-1}), m is molar mass of metal oxides and E is the working potential window.

X is the surface fraction (or electrode/electrolyte interface) of the pseudocapacitive materials. It shows that high experimental specific capacitance values can only be archived if the pseudocapacitive electrodes possess high specific surface area to maximize the number of active sites for the redox reactions. Therefore, it highlights the importance of the specific surface area to the total specific capacitance of the electrode. Nanosizing and nanostructuring are thus crucial routes to prepare electrode materials with enhanced energy storage capacitive [60-69].

Table 1.1. Theoretical specific capacitance (F g^{-1}) of MnO_2, NiO and Co_3O_4 in potential windows ranging from 0.3 to 1 V.

Potential window/ V	0.3	0.4	0.5	0.6	0.7	0.8	0.9	1
MnO_2	3700	2775	2220	1850	1585	1387	1233	1110
NiO	4305	3229	2583	2152	1845	1614	1435	1291
Co_3O_4	2670	2002	1602	1335	1144	1001	890	801

By applying equation (1.9) and based on the redox reactions presented above, the theoretical specific capacitance values (X=1) of MnO_2, Co_3O_4 and NiO have been calculated with varying potential window and shown in Table 1.1, taking into account the molar mass of MnO_2, Co_3O_4 and NiO are 86.93 g mol^{-1}, 240.80 g mol^{-1}, 74.69 g mol^{-1}, respectively.

1.2. Current state of the art in studying double transition metal oxides for supercapacitors.

In the past few years, studies on mixed oxides, mainly double transition metal oxides, have been gained a lot of attention as electrodes for charge storage, namely for high energy density supercapacitors due to their extraordinary electrochemical energy storage ability compared to the corresponding single transition metal oxides. Several mixed oxides have been prepared and reported for supercapacitor electrodes such as Ni-Co, Mn-Co and Ni-Mn oxides.

In this part of the thesis, a brief review of recent development of mixed oxide electrodes for supercapacitors will be presented.

1.2.1. M-Co (M=Ni/Mn) Oxides

The M-Co oxides reported as materials for supercapacitors are normally in the form of spinel oxide - AB_2O_4, with M at the A sites and Co at the B sites of the spinel oxides.

The Faradaic processs of MCo_2O_4 oxides in alkaline electrolytes are based on the following redox reactions proposed in literature [70]:

$$MCo_2O_4 + OH^- \leftrightarrow MOOH + 2CoOOH + e^- \quad (1.10)$$

$$2(CoOOH + OH^- \leftrightarrow CoO_2 + H_2O + e^-) \quad (1.11)$$

The first reaction related to the phase change, provides an electrochemical response that is typical of a battery behavior. In the second reaction, the phase changes back to the oxide state, hence extending the potential window of the redox reaction, thereby presenting pseudocapacitive behaviour. Taking into account the total redox reaction, the pseudocapacitive mechanism of MCo_2O_4 spinel oxide relates to three electrons transfer process.

The pseudocapacitive mechanisms, with the contribution of the redox reactions involving both metals in the mixed oxide originates an extra contribution for the high specific capacitance values typical of mixed oxides.

1.2.1.1. Ni-Co oxides

Although the theoretical specific capacitance values of each single metal oxides (mainly Co_3O_4 and NiO) are widely published and discussed (normally the published values correspond to a potential window of 0.5 V for these single metal oxides), the theoretical specific capacitance of $NiCo_2O_4$ is scarcely discussed in literature. Based on the pseudocapacitive mechanism, involving three electrons in the storage/release process, taking into account the molar mass of $NiCo_2O_4$ is 240.5574 g mol^{-1} and by applying the equation (1.9), the theoretical specific capacitance values of $NiCo_2O_4$ were calculated. The resulting values are presented in Table 1.2 as a function of the working potential window. $NiCo_2O_4$ spinel oxides are normally active in the potential window ranging from 0.3 to 0.6 V, hence the theoretical specific capacitance is of 4010 – 2005 F g^{-1}, respectively. The values are higher than those of Co_3O_4 and MnO_2 and comparable to NiO.

Table 1.2. Theoretical specific capacitance (TSC, F g^{-1}) values of $NiCo_2O_4$ in the potential window (V) ranging from 0.3 – 1 V.

Potential window/V	0.3	0.4	0.5	0.6	0.7	0.8	0.9	1
TSC	4010	3007	2406	2005	1718	1503	1336	1203

Concerning the crystal structure, MCo_2O_4 have spinel structure with the general formula AB_2O_4 as previously mentioned. It is arranged in a cubic closed-packed lattice as depicted in Figure 1.5. Generally, the A^{2+} cations occupy octahedral sites and the B^{3+} cations occupy tetrahedral sites. The mixed valences of A^{2+}, A^{3+}, B^{2+}, and B^{3+} cations at both the octahedral and tetrahedral sites are also commonly reported in literature [71].

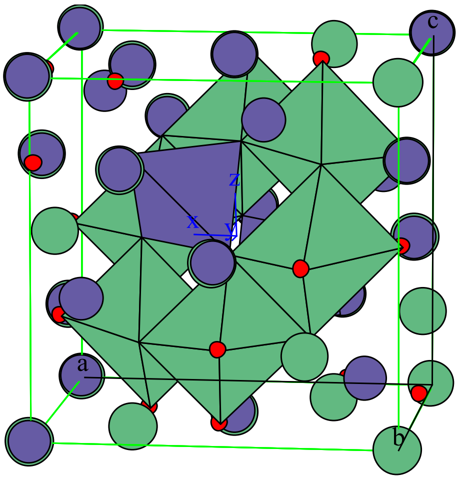

Figure 1.5. Crystal structure of spinel oxide AB_2O_4.

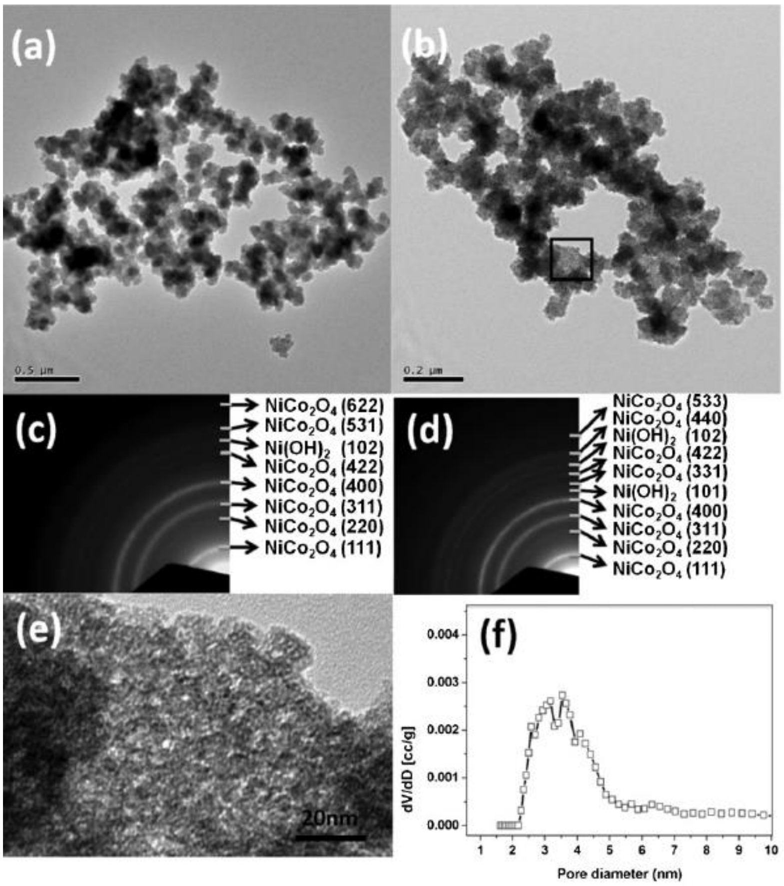

Figure 1.6. (a, b) TEM images, (c, d) SAED patterns, (e) HRTEM image and (d) pore size distribution of $NiCo_2O_4$ nanopowders prepared by the sol-gel technique [72].

Studies on $NiCo_2O_4$ as pseudocapacitive material for supercapacitor electrodes were initiated after the work by Hu et al. [72], reporting a $NiCo_2O_4$ aerogel prepared *via* epoxide-driven sol–gel process.

$NiCo_2O_4$ aerogel was characterized by a mesoporous structure composed of nanocrystals, with size of approximately 6 nm, displaying a surface area of 122 m^2 g^{-1} (Figure 1.6). Moreover, the material presented a narrow pore-size distribution (2-5 nm, Figure 1.6e and f), two orders of magnitude higher in electric conductivity, and enriched redox reaction possibilities due to the contribution both from Ni and Co cations, when compared to the corresponding single metal oxides. These properties resulted in an enhanced electrochemical capacitive response, characterized by specific capacitance values up to 1400 F g^{-1} at 25 mV s^{-1} in 1 M NaOH electrolyte and in a potential window from 0.04 to 0.52 V after 650 cycles of activation. Furthermore, the electrochemical tests revealed a capacitance decay of 9% compared to the maximum specific capacitance after 2000 cycles, indicating a very good cycling stability of the $NiCo_2O_4$ material.

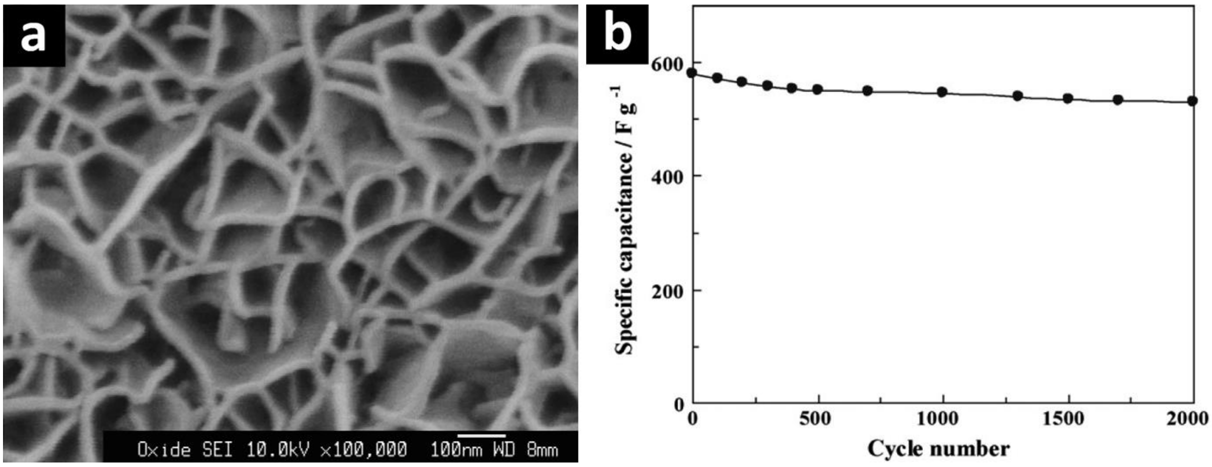

Figure 1.7. (a) FEG-SEM image and (b) stability of the $NiCo_2O_4$ on stainless steel prepared by electrodeposition [73].

Almost at the same time, Gupta et al. [73] studied $NiCo_2O_4$ films prepared by electrodeposition for pseudo supercapacitors. The deposition process is based on the formation of a Ni-Co hydroxide precursor, and then it was transformed into the spinel $NiCo_2O_4$ phase by thermal annealing at 200 ^oC. The films displayed a porous morphology constituted of nanosheets, with thickness of approximately 10 nm and long range interconnectivity (Figure 1.7a). The electrochemical response was assigned to the Ni^{II}/Ni^{III} and Co^{II}/Co^{III} redox reactions in 1M KOH electrolyte. The advanced properties resulted in electrodes displaying high pseudocapacitive performance, with specific capacitance values of 580 F g^{-1} at 0.5 A g^{-1} and 570 F g^{-1} at 50 A g^{-1} in the potential window from 0.1 V to 0.45 V. The specific capacitance retention was 95% after 1000 charge-discharge cycles and 94% after 2000 charge-discharge cycles (Figure 1.7b). Even though this work received much less attention and citations than the previously mentioned one, it is actually one of the adopted approaches in the recent development of $NiCo_2O_4$ electrodes for supercapacitors.

Two main strategies were envisaged by these pioneer researches: (i) the preparation of nanostructured $NiCo_2O_4$ in the form of power and assembly on current collectors by mixing with binder materials, and (ii) direct deposition of nanostructured $NiCo_2O_4$ on current collectors. Currently, most of the published works have been involved into these two approaches.

In the first approach, the preparation of various nanostructured $NiCo_2O_4$ powders for supercapacitors have been published. These $NiCo_2O_4$ nanostructures include one dimension nanowires/nanotubes [74-76], two dimension nanosheets [77], and three dimension nanoparticles [78, 79]. For example, $NiCo_2O_4$ nanowires [74] have been prepared by polyethylene glycol-assisted method and post thermal annealing at 250 ^{o}C. The nanowires displayed polycrystalline nature and have mesoporous structure composed of nanoparticles with size of approximately 3-6 nm (Figure 1.8a). It showed very high specific surface area of 202.2 m^2 g^{-1}, pore size of 2.4 nm and pore volume of approximately 1.14 cm^3 g^{-1}. Electrochemical studies in 1 M KOH electrolyte showed a high specific capacitance value of 743 F g^{-1} at 1 A g^{-1} and high rate capability with capacitive retention of 78.6% at 40 A g^{-1}, and 93.8% capacitance retention after cycling for 3000 cycles, resulting from their structural and morphological advantages. $NiCo_2O_4$ nanotubes have been prepared by electrospinning technique [75]. The nanotubes have diameter of 100 nm and wall thickness of 33 nm (Figure 1.8b). The nanotube wall displayed porous structure composed of nanocrystals with size of approximately 10 nm and pores with size ranging from 3 nm to 10 nm. They possessed Brunauer–Emmett–Teller (BET) surface are of 36.9 m^2 g^{-1} and pore volume of 0.22 cm^2 g^{-1}. As a result of this unique nanotube architecture, which facilitates ions and electron transports, the material displayed a high specific capacitance value of 1647 F g^{-1} at 1 A g^{-1} in 2 M KOH in the potential window from 0 V to 0.41 V (*vs.* AgCl/Ag), high rate capability of 77.3% at 25 A g^{-1}, and high stability with capacitance retention of 93.6% after 3000 cycles.

$NiCo_2O_4$ square nanosheets [77] were synthesized using a solvothermal route (Figure 1.8c). The uniform square nanosheets, with length of few μm and thickness of 50-100 nm, consisted of nanoparticles with size of approximately 5 nm constituting porous structure. The BET surface area was 100 cm^2 g^{-1}, pore distribution was narrow, ordered and pore size was of about 5 nm and pore volume was of about 0.227 cm^3 g^{-1}. These interesting properties resulted in specific capacitance values of 980 and 384 F g^{-1} at current densities of 0.5 and 10 A g^{-1}, and good cycling stability with 91% capacitance retention after 1000 cycles.

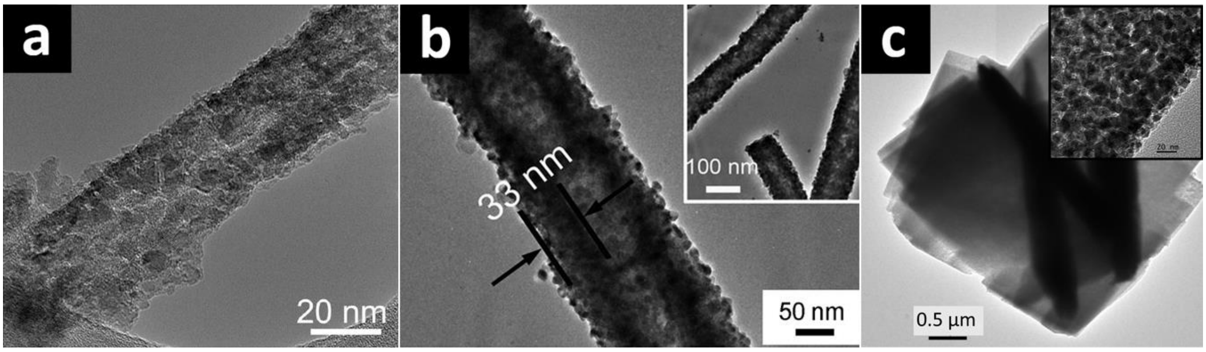

Figure 1.8. TEM images of (a) porous $NiCo_2O_4$ nanowire [74], (b) electrospun porous $NiCo_2O_4$ nanotube [75], (c) hexagonal $NiCo_2O_4$ nanosheets composed of aggregated nanoparticles [77].

By this way, the electrode materials are connected together by binders; therefore the adhesion between active materials and current collectors can be easily controlled and improved. However, the disadvantage of using binders is the reduction of the active sites for the redox reactions, hence reducing the pseudocapacitive response. Moreover most of the binders create additional resistances, thus decreasing the conductivity of the materials and increasing its equivalent series resistance (ESR).

Recent research work on $NiCo_2O_4$ electrodes for supercapacitors are based on the second approach, which allows the preparation of the pseudocapacitive materials directly on current collectors such as titanium plate, stainless steel plate, thereby avoiding the use of binders, leading to an enhanced active sites for redox reactions. Both one dimension nanowires [80], two dimension nanosheets [81] have been deposited, by different methods, directly on current collectors. For example, $NiCo_2O_4$ nanosheets films [81] were prepared by galvanostatic electrodeposition in the anodic regime at 70 ^oC and post-thermal annealing at 200 ^oC. The nanosheets films have specific capacitance of 453 F g^{-1} at a scan rate of 5 mV s^{-1} and 506 F g^{-1} at a current density of 1 A g^{-1}, which was improved 50% when compared to single cobalt oxide, and capacitance retention of about 94% after 2000 cycles. The good pseudocapacitive response of the films was a result of their porous surface morphologies, which were composed of long range interconnected nanosheets. And each nanosheets also displayed porous structure with high BET surface area of 227.3 m^2 g^{-1} and average pore diameter of about 9.77 nm.

It should be noted that the high specific capacitance of pseudocapacitive electrodes (close to the theoretical value) can only be achieved by preparing very thin layers (few nm) of active materials directly on a flat substrate. This approach is useful in terms of fundamental studies because the redox active electrodes are less limited by the bulk diffusion, thereby very high specific capacitance values can be obtained. However, due to the very low mass loading, it is not suitable for practical applications. Thereby, regarding to this point, 3D porous current collectors offer great advantages. Its macro-porous structure allows the better dispersion of the active materials and the better diffusion of electrolyte ions into the electrode, hence reducing the diffusion length of electrolyte, increasing the electrochemical response. Carbon fiber papers [82], carbon cloths [83] and nickel foams [80] are amongst the most used 3D porous current collectors have been reported up to now.

$NiCo_2O_4$ layers have been deposited on carbon fiber papers by a solvothermal method and post thermal annealing at 350 ^oC [82]. The deposited $NiCo_2O_4$ displayed interconnected nanosheets morphology and conformably covered carbon fibers inside the carbon paper (Figure 1.9a). Each nanosheets consisted of nano-sized pores of approximately 2-5 nm. BET results revealed the mesoporous structure, with surface area of approximately 206.7 m^2 g^{-1} and pore size distributed from 2 nm to 5 nm. As a result, a high specific capacitance value of 1422 F g^{-1} and 999 F g^{-1} at current densities of 1 A g^{-1} and 20 A g^{-1} have been reported. The capacitance loss was about 15.6% after 3000 cycles. $NiCo_2O_4$ films were also prepared surfactant-assisted hydrothermal method on carbon textiles [83]. The films uniformly covered fibers of the textiles, displaying porous morphology composed of nanowires (Figure 1.9b). The nanowires diameter was about 150 nm and their length was about several μm. The nanowires were also composed of nanoparticles of 10-20 nm in size, making porous structure with pore size of about 6 nm. They exhibited high specific capacitance of 1283 F g^{-1} and 1010 F g^{-1} at current densities of 1 A g^{-1} and 20 A g^{-1} and very good charge-discharge stability with no-significant decay. At the end, the use of carbon textiles makes it a possible candidate for application as flexible electrodes.

$NiCo_2O_4$ films prepared by electrodeposition on nickel foams have also been reported [80]. Films composed of ultra-thin $NiCo_2O_4$ nanosheets with thickness of 2-4 nm were obtained (Figure 1.9c), displaying very high specific capacitance of 2010 and 1450 F g^{-1} at current densities of 2 A g^{-1} and 20 A g^{-1} and 94% of specific capacitance is retained after charge-discharge cycling at different current densities for 2000 cycles. Those high pseudocapacitive values not only resulted from the ultrathin property of the nanosheets but also from inter-particle mesopores in the nanosheets with size ranged from 2 to 5 nm.

It should be noted that the first published work [84], to the author's knowledge, reporting the use of a porous substrate to deposit $Ni(OH)_2$ on nickel foam, displayed quite poor capacitance retention after cycling (only about 52% of initial capacitance retained after 300 cycles). Even though the obtained specific capacitance was very high as 3152 F g^{-1} at 4 A g^{-1}. Latter work reporting the use of NiO on nickel foam [85], after thermal annealing at 350 ^{o}C for 2 hours, evidenced specific capacitance values of 674.2 F g^{-1} at a current density of 1 A g^{-1}, and capacitance retention of 93.5% after 5000 cycles. The good stability observed for NiO deposited over nickel foam might not be related only to the phase, but perhaps more related to the increased adhesion of the film to the current collector as a result of the thermal annealing. The lowered specific capacitance values can be due to the reduced surface area and the reduced bulk diffusion (due to the transformation from hydroxide to oxide phase) after thermal annealing.

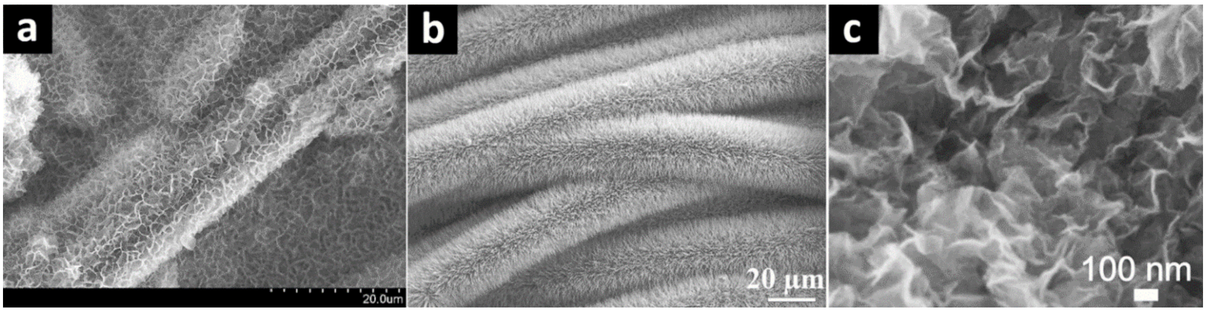

Figure 1.9. FEG-SEM images of (a) $NiCo_2O_4$ nanosheets on carbon fiber paper [82], (b) $NiCo_2O_4$ nanowire array on carbon textiles [83], (c) ultrathin $NiCo_2O_4$ nanosheets on Ni foam [71].

Thus, these results point out the advantages of using porous current collectors for supercapacitors electrodes. Nevertheless, for practical applications as supercapacitors electrodes, the mass and volume of the porous current collectors should be taken into account.

Another approach that must be mentioned in $NiCo_2O_4$ studies for supercapacitors is the development of hybrid structures of $NiCo_2O_4$ with either double layer capacitive materials or pseudocapacitive materials in powder form or directly deposited over current collectors. This is an attractive approach, because the combination of two materials with different properties may result in an enhanced effect, combining the advantage of each single material, leading to an enhanced supercapacitive response. $NiCo_2O_4$-carbon nanotube [86], $NiCo_2O_4$-graphene [87]. NiCo hydroxide/$NiCo_2O_4$ nanowire [88], MnO_2/$NiCo_2O_4$ nanoflakes/nanowires [89], $NiCo_2O_4$/$NiCo_2O_4$ nanoflakes/nanoflakes [90] were amongst hybrid materials have been reported.

Concerning hybrid double layer capacitive materials-pseudocapacitive materials, hybrid $NiCo_2O_4$-single wall carbon nanotube (SWCNT) [86] were prepared by hydrolysis method in ethanol-water solvent, hybrid $NiCo_2O_4$-reduced graphene oxide (RGO) [87] were prepared by the self-assembly of positively and negatively charged nanosheets. Due to the high conductivity of the carbon nanomaterials, the better dispersion of $NiCo_2O_4$ on high surface area carbon nanomaterials, an enhanced supercapacitive performance of the hybrid materials compared to the non-hybrid $NiCo_2O_4$ was obtained. Hybrid $NiCo_2O_4$-SWCNT [86], with 6-10 nm $NiCo_2O_4$ nanocrystals grown around SWCNT bundles, displayed specific capacitance values of 1642 F g^{-1} at 0.5 A g^{-1} and of 879 F g^{-1} at 20 A g^{-1} in the potential window of 0.45 V and capacitance retention of 94.1% after 2000 charge-discharge cycles. Hybrid $NiCo_2O_4$-RGO [87], with homogeneously $NiCo_2O_4$ anchored reduced graphene oxide, displayed high specific capacitance values of 835 F g^{-1} at 1 A g^{-1} and 615 F g^{-1} at 20 A g^{-1} in the potential window of about 0.5 V, the specific capacitance value increased to 908 F g^{-1} after 4000 charge-discharge cycles.

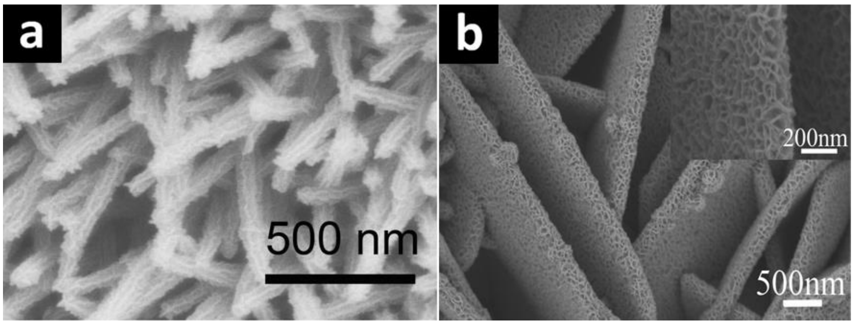

Figure 1.10. FEG-SEM images of (a) hierarchical $MnO_2/NiCo_2O_4$ nanosheets/nanowires [89] and (b) $NiCo_2O_4@NiCo_2O_4$ core/shell nanoflakes array on nickel foam [90].

Concerning hybrid pseudocapacitive materials, hybrid active/active $MnO_2/NiCo_2O_4$ nanosheets/nanowires electrodes [89] were prepared by two-step hydrothermal process (Figure 1.10a) and $NiCo_2O_4/NiCo_2O_4$ nanoflakes/nanoflakes electrodes [90] were prepared two step hydrothermal and chemical bath deposition (Figure 1.10b). The studies showed improved pseudocapacitive response due to the combined redox reactions of the two pseudocapacitive materials and the rationally designed core-shell structure resulted in an increased specific surface area, and therefore high number of active sites. $MnO_2/NiCo_2O_4$ [89] electrodes were composed of almost vertically aligned slim $NiCo_2O_4$ mesoporous nanowires (pore sizes are about 3-5 nm) with sharp tips which were uniformly covered by 10 nm MnO_2 nanoflakes layer. They displayed specific capacitance values of 3.31 F cm^{-2} and 1.66 F cm^{-2} at 2 mA cm^{-2} and 20 mA cm^{-2} and 88% capacitance retention after 2000 cycles. $NiCo_2O_4/NiCo_2O_4$ electrodes [90] were composed of mesoporous nanoflakes cores which were consisted of 10-20 nm nanocrystals and of continuous nanoflakes shell with thickness of about 60 nm. They displayed capacitance values of 1.55 F cm^{-2} and 1.16 F cm^{-2} at 2 mA cm^{-2} and 40 mA cm^{-2}; it increases to 2.17 F cm^{-2} after 4000 cycles. Thus, those reports revealed the remarkable pseudocapacitive performance of the hybrid active electrodes.

1.2.1.2. Mn-Co oxides

Several attempts have been conducted to search for new mixed oxides materials based on the substitution of nickel sites with other transition metals. Of the proposed materials, $MnCo_2O_4$ has some interesting properties as electrode for pseudocapacitors, because of various valence states and multiple redox reaction of manganese oxide. Few studies about $MnCo_2O_4$ for supercapacitors have been reported.

In alkaline electrolytes, the pseudocapacitive mechanisms are quite similar to the mechanism described previously for MCo_2O_4. The difference is that manganese oxyhydroxide (MnOOH) may undergo a second redox reaction like in the case of cobalt oxyhydroxide CoOOH. It is worth to note that this reaction is not possible for NiOOH. The reaction involving MnOOH is given be eq. 1.12:

$$MnOOH + OH^- \leftrightarrow MnO_2 + H_2O + e^- \qquad (1.12)$$

Considering these redox reactions, the pseudocapacitive mechanism of $MnCo_2O_4$ involves the storage/release of four-electrons.

The theoretical specific capacitance of $MnCo_2O_4$ can also be calculated using equation (1.9), taking into account the molar mass of $MnCo_2O_4$ of 236.80 g mol^{-1}.

Table 1.3. Theoretical specific capacitance values (F g^{-1}) of $MnCo_2O_4$ in the potential window (V) ranging from 0.3 – 1 V.

Potential window/V	0.3	0.4	0.5	0.6	0.7	0.8	0.9	1
TSC	5430	4072	3258	2715	2327	2036	1810	1629

The charge storage mechanism, based on four electron transfer process, results in a very high theoretical specific capacitance of $MnCo_2O_4$ as shown in Table 1.3, making it a very promising material to prepare pseudocapacitive charge storage electrodes.

Published work, reporting the preparation and pseudocapacitive performance of $MnCo_2O_4$ as supercapacitor electrodes is hereby briefly reviewed.

A mesoporous flake-like manganese-cobalt oxide ($MnCo_2O_4$) was synthesized by the hydrothermal method [91]. The nanoflakes were composed of numerous mesopores, and revealed a surface area of 18.06 m^2 g^{-1} (determined by BET) and pore size of 13 nm. The flake-like $MnCo_2O_4$ displayed a specific capacitance value of 1487 F g^{-1} at 1 A g^{-1} in 1 M KOH, and capacitance retention of 93% after 2000 charge-discharge cycles. The surface area of the $MnCo_2O_4$ electrodes was rather lower than those of $NiCo_2O_4$ electrodes previously discussed. However, the specific capacitance value of 1487 F g^{-1} was quite high and comparable to the values reported for $NiCo_2O_4$ electrodes, thus revealing the high active of $MnCo_2O_4$ electrode for the redox reactions identified above.

$MnCo_2O_4$ films on carbon woven substrate have been prepared by electroless deposition of MnCo and its electro-oxidation in 0.7 M sodium hydroxide-ethanol solution [92]. The films displayed porous surface morphology, which was composed of textured platelets (Figure 1.11a), displaying specific capacitance value of 833 F g^{-1} at 20 mV s^{-1} and 354 F g^{-1} at 250 mV s^{-1} in 0.5 M Na_2SO_4 and 80 %

capacitance retention after 1000 cycles. Moreover, the cyclic voltamograms displayed rectangular shape up to scan rates of 100 mV s^{-1}, which indicated very good pseudocapacitive behavior of the electrode. The author proposed the pseudocapacitive mechanism was based on the redox reaction with OH^-, however Na_2SO_4 was used in the electrochemical tests, and therefore the proposed pseudocapacitive mechanism in this work should be further discussed.

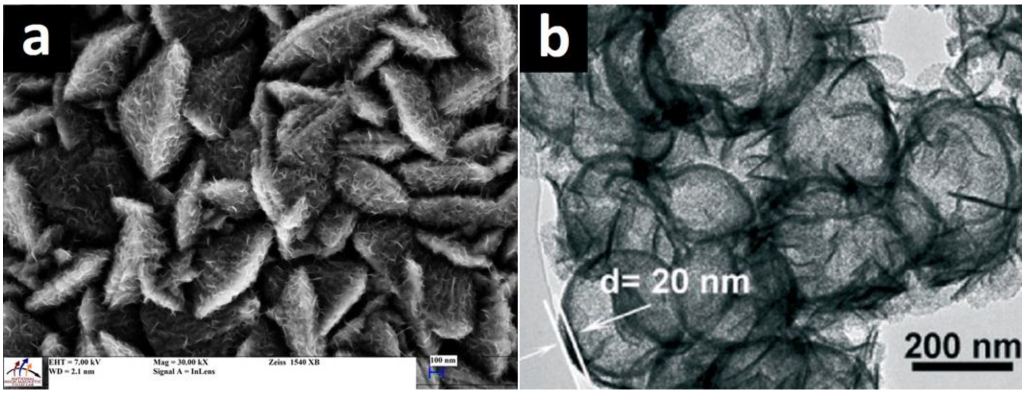

Figure 1.11. (a) FEG-SEM image of electroless deposited $MnCo_2O_4$ [92] and (b) TEM image of hollow C@$MnCo_2O_4$ [93].

$MnCo_2O_{4.5}$ powders were synthesized by the hydrothermal method. The obtained materials displayed porous urchin-like structures with diameter of approximately 4–6 μm (Figure 1.11b), composed of 10-50 nm granular nanoneedles. The material presented modest specific capacitance value in 1 M KOH of 151.2 F g^{-1} at 5 mV s^{-1} in potential window of 0-0.5 V and 129.2 F g^{-1} and 108 F g^{-1} at current densities of 0.1 and 5 A g^{-1}, but the capacitance retention was 100% after 2400 charge-discharge cycles [94].

$MnCo_2O_4$ nanowires were prepared by solvothermal thermal techniques and thermal decomposition of organometallic compounds precursors. The nanowires displayed a mesoporous structure, which consisted of polycrystalline nanoparticles with surface area of 106.6 m^2 g^{-1} and pore size of 3-5.5 nm, showing specific capacitance values of 1342 F g^{-1} at 1 A g^{-1} and 988 F g^{-1} at 20 A g^{-1} in 2 M KOH. The specific capacitance increased to 2108 F g^{-1} after 4000 charge-discharge cycles, as result of further cycling activation [95].

$MnCo_2O_4$ nanowires have also been deposited on nickel foam substrates by the hydrothermal method [96]. The nanowires were single crystals with nano-size pores. The average length and the average diameter of nanowires were approximately 1 μm and 100 nm, respectively. Due to the higher number of active sites and a reduced contact resistance by depositing on 3D nickel foam, the nanowires films displayed a specific capacitance value in 1 M $LiClO_4$ in propylene carbonate (PC) organic electrolyte of 783.1 F g^{-1} and 346.9 F g^{-1} at scan rates of 1 mV s^{-1} and 5 mV s^{-1} and capacitance retention of 96.8% after 3000 cycles.

$MnCo_2O_4$-carbon hybrid materials have also been reported as electrodes for supercapacitors. For example, $MnCo_2O_4$/reduced graphene oxide (RGO) has been prepared by hydrothermal method [97]. A well-dispersed $MnCo_2O_4$ on RGO nanosheets were obtained, displaying a specific capacitance value of 334 F g^{-1} at 1 A g^{-1}, and capacitance retention of 98% after 2000 charge-discharge cycles [97]. $MnCo_2O_4$ nanosheets covered on a hollow carbon shell $MnCo_2O_4$/C were prepared by hydrothermal method and post-thermal treatment [93], Figure 1.11b. The spherical hybrid structure with diameter of 400-500 nm composed of conductive carbon and flower-like $MnCo_2O_4$ nanopetals presented an improved electron conductivity and ionic diffusion. Furthermore, it showed BET surface area of 347 m^2 g^{-1} and small and narrow pore distribution, with pore size of about 3.5 nm. This materials displayed specific capacitance values in 6 M KOH of 728.4 F g^{-1} and 519 F g^{-1} at 1 A g^{-1} and 10 A g^{-1} in the potential window of 0-0.5 V and capacitance retention of 95.9% after 1000 cycles [93].

Generally, the specific capacitances of $MnCo_2O_4$ in the above-discussed review are lower than $NiCo_2O_4$, taking into account the structure and the current collector used. The theoretical specific capacitance value of $MnCo_2O_4$, as calculated above, is higher than the corresponding value of $NiCo_2O_4$. Other changes in the property of the materials may lead to the low specific capacitance values, for example, decreased electrical conductivity as the result of Mn incorporation in the Co based spinel oxides.

1.2.2. M-Mn (M=Ni/Co) oxides

Mixed oxides based on manganese oxides are also of interest for supercapacitors electrodes because of the good pseudocapacitive behavior of manganese oxides.

Few works regarding M-Mn oxides have been reported as pseudocapacitive materials for supercapacitors. Among the published works, Ni was the most used metal that has been combined with manganese for preparing electrodes based on double transition metal oxides. Differently from M-Co oxides, in which single phases (commonly spinel phase) are normally formed, several Ni-Mn oxide phases (including co-existing of several phases in electrodes) have been reported for supercapacitor electrodes. For example, spinel $NiMn_2O_4$, ilmenite $NiMnO_3$ and co-existing phases of NiO and MnO_2 have been reported as pseudocapacitive electrodes.

The pseudocapacitive mechanism of electrodes based on $NiMn_2O_4$ oxides has been proposed as below

$NiMn_2O_4 + Na^+ + e^- \leftrightarrow NaNiMn_2O_4$ in neutral electrolyte (1.13)

$NiMn_2O_4 + OH^- + H_2O \rightarrow NiOOH + 2MnOOH + e^-$ in alkaline electrolyte (1.14)

$2(MnOOH + OH^- \leftrightarrow MnO_2 + H_2O + e^-)$ (1.15)

The pseudocapacitive mechanism in neutral electrolyte is based on one electron transfer. In alkaline electrolyte, it is based on three-electron transfer. Thus, without any calculation, it pin points the higher specific capacitance value of $NiMn_2O_4$ in the alkaline electrolyte. The theoretical specific capacitance can also be calculated, taking into account the molar mass of $NiMn_2O_4$ of 232.56 g mol^{-1} and is presented in Table 1.4 as function of the potential window.

Concerning the mixed nickel manganese oxides with co-existing phases, the pseudocapacitive mechanism includes the contribution of different phases, hence making difficult to calculate a theoretical specific capacitance from those materials.

Table 1.4. Theoretical specific capacitance (TSC) values (F g^{-1}) of $NiMn_2O_4$ in the potential window (V) ranging from 0.3 – 1 V.

Potential window/V	0.3	0.4	0.5	0.6	0.7	0.8	0.9	1
TSC in Na_2SO_4	1383	1037	830	691	592	518	461	415
TSC in KOH	4146	3110	2488	2073	1777	1555	1382	1244

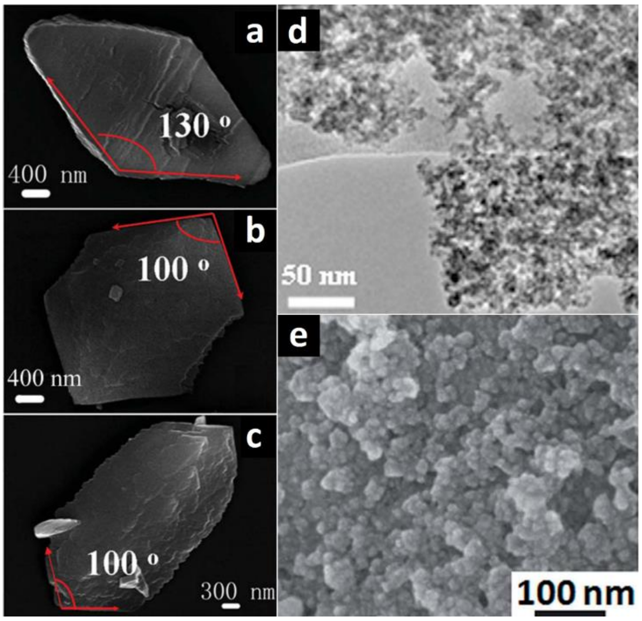

Figure 1.12. TEM images of nickel manganese oxides with (a) bipyramid, (b) fusiform, (c) plate form [98] and (d) porous structure prepared by solgel method [99]. (e) FEG-SEM image of granular $Ni_yMn_{1-y}O_x$ [100].

$NiMn_2O_4$ powders have been prepared by the thermal decomposition of oxalate precursors $NiMn_2(C_2O_4)_3 \cdot nH_2O$ in air. The materials with different morphologies, including porous bipyramid, fusiform and plate were obtained (Figure 1.12a-c). They displayed BET specific surface area of 127.0, 118.3 and 115.1 m^2 g^{-1} for bipyramid, fusiform and plate forms, respectively, and pore size of 5-10 nm. Electrochemical studies revealed that $NiMn_2O_4$ porous plate structure showed specific capacitance values of 180 F g^{-1} at 250 mA g^{-1} in potential window of 0-0.8 V and high charge-discharge stability of 92.8% after 1000 cycles [98].

Later on, spinel $NiMn_2O_4$ has also been prepared from an epoxide-driven sol−gel process [99], in the way that was quite similar to the work of Hu et al. [72], and this step was followed by thermal treatment at 300 °C for 5 hours. Porous structures were formed (Figure 1.12d and e), displaying high specific surface area of 201 m^2 g^{-1} and pore size of about 8–10 nm [99]. This spinel oxide presented specific capacitance values of about 243 F g^{-1} and 169 F g^{-1} in 1M Na_2SO_4 at scan rates of 5 mV s^{-1} and 20 mV s^{-1} in potential window from -0.2 V to 0.8 V. It also showed good cycling stability with specific capacitance retention of 96% after 5000 cycles.

Ilmenite $NiMnO_3$ dispersed on nitrogen (N) doped graphene composite has been synthesized by the hydrothermal method [101]. Silk-like $NiMnO_3$ structure on N-doped graphene was obtained. Due to the good dispersion and enhanced interaction of the ilmenite and N-doped graphene, as compared to graphene, the hybrid material exhibited a specific capacitance value of 750.2 F g^{-1} in 1 M Na_2SO_4 in a potential window from 0 V to 0.8 V at a scan rate of 1 mV s^{-1} and capacitance retention of 88.5% after 1000 charge-discharge cycles [101].

Mixed MnO_2-NiO oxides films were electrodeposited by galvanostatic mode in the anodic region on a stainless steel substrate and post-thermal annealing at 300 °C [102]. The films presented porous surface morphology composed of interconnected nanoflakes. The optimal films displayed specific capacitance values of 681 F g^{-1} and 435 F g^{-1} at a scan rate of 1 mVs^{-1} and about 250 F g^{-1} and 200 F g^{-1} at 20 mV s^{-1} in 0.5 M KOH and 0.5 M Na_2SO_4 in potential windows of 0-1 V and -1-0.5 V, respectively. The specific capacitance increased with the number of charge-discharge cycles in Na_2SO_4. On the contrary, the capacitance retention was only 50% after 900 cycles in KOH. The poor stability in 1 M KOH electrolyte was assigned to a partial dissolution of the film in the electrolyte.

Recently, mixed nickel manganese oxides ($Ni_yMn_{1-y}O_x$; $0 \le y \le 0.4$) have been synthesized by in-situ inclusion of nickel during the growth of manganese oxide [100]. They present granular morphology composed of particles agglomeration with diameter of approximately 10 nm, forming porous channels. BET surface area of 118 $m^2 g^{-1}$ increased as compared to manganese oxide - 80.5 $m^2 g^{-1}$. The optimized mixed oxide displayed a specific capacitance value of about 380 F g^{-1}, which was significant higher than the value of manganese oxide (180 F g^{-1}) prepared by the same method. The mixed oxide revealed good cycling stability and capacitance retention of 92% after 3000 cycles.

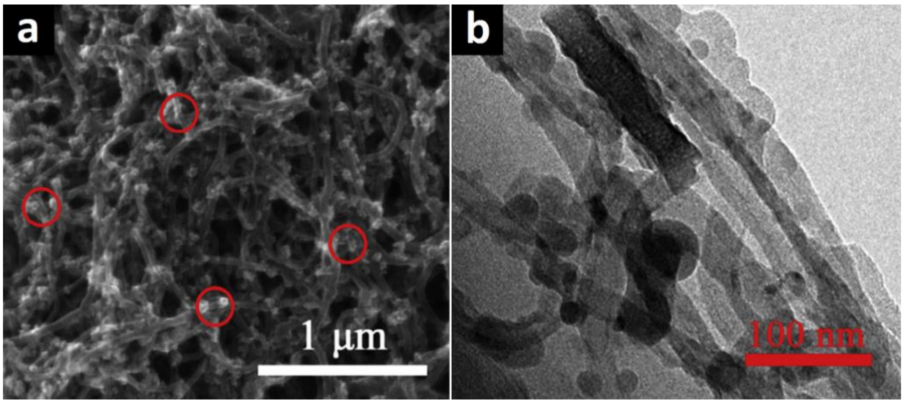

Figure 1.13. (a) FEG-SEM and (b) TEM images of nickel manganese oxide deposited on carbon nanotube/carbon fiber paper [103].

The Ni-Mn oxides have also been deposited on porous current collectors [103]. For examples, randomly distributed multiwall carbon nanotubes have been growth on carbon fiber papers by chemical vapor deposition to prepare porous current collectors (Figure 1.13) [103]. Ni-Mn oxides were then electrodeposited on these current collectors by electrodeposition, resulting in the formation of well-dispersed nanoparticles, with size of about 20 nm on carbon nanotubes. The porous hierarchical structure obtained resulted in the electrode with specific capacitance of 961.5 F g^{-1} at a scan rate of 10 mV s^{-1} and a good cycling stability with 89.32% capacitance retention after 1000 cycles.

Other materials of the type MMn_2O_4 have also been studied. For example $CoMn_2O_4$ nanowires were grown by thermal decomposition of organometallic compounds [95], exhibiting very high specific capacitance of 2108 F g^{-1} at 1 A g^{-1} and 1191 F g^{-1} at 20 A g^{-1}.

1.3. Aims of the thesis

Based on the current state of the art of the oxide and mixed oxide- based pseudocapacitive materials overviewed in the previous sections, the aim of this PhD dissertation is: electrodeposition, electrochemical and physico-chemical characterization of novel double TMOs and TMOs based on Ni, Mn and Co as pseudocapacitive materials for application in charge storage electrodes for redox supercapacitors. Thus, this dissertation includes seven chapters, describing the various materials proposed and its characterization and testing. Further details will be presented in the introduction of each chapter.

1. First, the cathodic electrodeposition of manganese oxides from nitrate-based electrolytes was optimized and its electrochemical response in alkaline electrolyte was studied and correlated to the deposition condition and to the surface morphology. This was the first step to further study mixed oxides with manganese.

2. A new route, based on the hydrogen bubbling-assisted electrodeposition, was proposed to design the hierarchical micro-nano Mn oxide electrodes. The morphological, structural features and pseudocapacitive performance of the novel micro-nano structured MnO_2 films were studied.

3. Considering the high theoretical specific capacitance of $MnCo_2O_4$ spinel oxides among other double TMOs as identified above, the Mn-Co oxides were chosen as the first double TMOs to be studied in this dissertation. Effect of thermal conditioning on the morphological, structural and electrochemical properties were be studied and correlated in order to optimize the electrochemical response.

4. Ni-Mn oxide was chosen as the second double TMOs for the electrodeposition as the cycling stability of the electrodeposited $MnCo_2O_4$ is rather poor. The effect of the Ni to Mn ratio to the morphological, structural, and electrochemical properties was studied and correlated.

5. To further improve the pseudocapacitive performance of the Ni-Mn oxide based electrode, 3D open porous metallic foams were used as current collectors for the electrodeposition. Morphological, structural and electrochemical properties of the film deposited on two different foams were studied.

6. Ni and Co hydroxides were also redesigned by performing electrodeposition in various steps, to fabricate a two layers film with single Ni and Co hydroxides in each layer in order to compare its pseudocapacitive response with that of Ni-Co hydroxides.

7. Finally, nucleation studies were conducted on Ni-Co hydroxide as a representative system in the thesis by current transient analysis and *in-situ* electrochemical AFM. The aim was to better understand the electrochemical mechanism governing the growth of these materials.

References

[1] P. Simon, Y. Gogotsi, Materials for electrochemical capacitors, Nat Mater, 7 (2008) 845-854.

[2] A.S. Aricò, P. Bruce, B. Scrosati, J.-M. Tarascon, W. Van Schalkwijk, Nanostructured materials for advanced energy conversion and storage devices, Nat Mater, 4 (2005) 366-377.

[3] L. Schlapbach, A. Züttel, Hydrogen-storage materials for mobile applications, Nature, 414 (2001) 353-358.

[4] B.C. Steele, A. Heinzel, Materials for fuel-cell technologies, Nature, 414 (2001) 345-352.

[5] G.J. Snyder, E.S. Toberer, Complex thermoelectric materials, Nat Mater, 7 (2008) 105-114.

[6] M. Winter, R.J. Brodd, What are batteries, fuel cells, and supercapacitors?, Chemical reviews, 104 (2004) 4245-4270.

[7] H.I. Becker, Low voltage electrolytic capacitor, Google Patents, 1957.

[8] A. Ghosh, Y.H. Lee, Carbon-Based Electrochemical Capacitors, ChemSusChem, 5 (2012) 480-499.

[9] F. Yao, D.T. Pham, Y.H. Lee, Carbon-Based Materials for Lithium-Ion Batteries, Electrochemical Capacitors, and Their Hybrid Devices, ChemSusChem, 8 (2015) 2284–2311.

[10] L.L. Zhang, X.S. Zhao, Carbon-based materials as supercapacitor electrodes, Chem. Soc. Rev., 38 (2009) 2520-2531.

[11] C. Zhang, W. Lv, Y. Tao, Q.-H. Yang, Towards superior volumetric performance: design and preparation of novel carbon materials for energy storage, Energy & Environmental Science, 8 (2015) 1390-1403.

[12] M. Sevilla, R. Mokaya, Energy storage applications of activated carbons: supercapacitors and hydrogen storage, Energy & Environmental Science, 7 (2014) 1250-1280.

[13] J.P. Paraknowitsch, A. Thomas, Doping carbons beyond nitrogen: an overview of advanced heteroatom doped carbons with boron, sulphur and phosphorus for energy applications, Energy & Environmental Science, 6 (2013) 2839-2855.

[14] K. Fic, G. Lota, M. Meller, E. Frackowiak, Novel insight into neutral medium as electrolyte for high-voltage supercapacitors, Energy & Environmental Science, 5 (2012) 5842-5850.

[15] C. Largeot, C. Portet, J. Chmiola, P.-L. Taberna, Y. Gogotsi, P. Simon, Relation between the ion size and pore size for an electric double-layer capacitor, J. Am. Chem. Soc., 130 (2008) 2730-2731.

[16] M. Armand, F. Endres, D.R. MacFarlane, H. Ohno, B. Scrosati, Ionic-liquid materials for the electrochemical challenges of the future, Nat Mater, 8 (2009) 621-629.

[17] Z.-Y. Yu, L.-F. Chen, L.-T. Song, Y.-W. Zhu, H.-X. Ji, S.-H. Yu, Free-standing boron and oxygen co-doped carbon nanofiber films for large volumetric capacitance and high rate capability supercapacitors, Nano Energy, 15 (2015) 235-243.

[18] Z.-S. Wu, G. Zhou, L.-C. Yin, W. Ren, F. Li, H.-M. Cheng, Graphene/metal oxide composite electrode materials for energy storage, Nano Energy, 1 (2012) 107-131.

[19] Y. Li, C. Lu, S. Zhang, F.-Y. Su, W. Shen, P. Zhou, C. Ma, Nitrogen- and oxygen-enriched 3D hierarchical porous carbon fibers: synthesis and superior supercapacity, Journal of Materials Chemistry A, 3 (2015) 14817-14825.

[20] J.W. Campos, M. Beidaghi, K.B. Hatzell, C.R. Dennison, B. Musci, V. Presser, E.C. Kumbur, Y. Gogotsi, Investigation of carbon materials for use as a flowable electrode in electrochemical flow capacitors, Electrochimica Acta, 98 (2013) 123-130.

[21] C. Yuan, L. Yang, L. Hou, L. Shen, X. Zhang, X.W. Lou, Growth of ultrathin mesoporous Co_3O_4 nanosheet arrays on Ni foam for high-performance electrochemical capacitors, Energy & Environmental Science, 5 (2012) 7883-7887.

[22] A.C. Ferrari, F. Bonaccorso, V. Fal'ko, K.S. Novoselov, S. Roche, P. Boggild, S. Borini, F.H.L. Koppens, V. Palermo, N. Pugno, J.A. Garrido, R. Sordan, A. Bianco, L. Ballerini, M. Prato, E. Lidorikis, J. Kivioja, C. Marinelli, T. Ryhanen, A. Morpurgo, J.N. Coleman, V. Nicolosi, L. Colombo, A. Fert, M. Garcia-Hernandez, A. Bachtold, G.F. Schneider, F. Guinea, C. Dekker, M. Barbone, Z. Sun, C. Galiotis, A.N. Grigorenko, G. Konstantatos, A. Kis, M. Katsnelson, L. Vandersypen, A. Loiseau, V. Morandi, D. Neumaier, E. Treossi, V. Pellegrini, M. Polini, A. Tredicucci, G.M. Williams, B. Hee Hong, J.-H. Ahn, J. Min Kim, H. Zirath, B.J. van Wees, H. van der Zant, L. Occhipinti, A. Di Matteo, I.A. Kinloch, T. Seyller, E. Quesnel, X. Feng, K. Teo, N. Rupesinghe, P. Hakonen, S.R.T. Neil, Q. Tannock, T. Lofwander, J. Kinaret, Science and technology roadmap for graphene, related two-dimensional crystals, and hybrid systems, Nanoscale, 7 (2015) 4598-4810.

[23] Y. Huang, J. Liang, Y. Chen, An Overview of the Applications of Graphene-Based Materials in Supercapacitors, Small, 8 (2012) 1805-1834.

[24] H.-J. Choi, S.-M. Jung, J.-M. Seo, D.W. Chang, L. Dai, J.-B. Baek, Graphene for energy conversion and storage in fuel cells and supercapacitors, Nano Energy, 1 (2012) 534-551.

[25] K. Chen, S. Song, D. Xue, Beyond graphene: materials chemistry toward high performance inorganic functional materials, Journal of Materials Chemistry A, 3 (2015) 2441-2453.

[26] S. Dutta, A. Bhaumik, K.C.W. Wu, Hierarchically porous carbon derived from polymers and biomass: effect of interconnected pores on energy applications, Energy & Environmental Science, 7 (2014) 3574-3592.

[27] S. Pan, H. Lin, J. Deng, P. Chen, X. Chen, Z. Yang, H. Peng, Novel Wearable Energy Devices Based on Aligned Carbon Nanotube Fiber Textiles, Advanced Energy Materials, 5 (2014) 1401438.

[28] P. Xu, T. Gu, Z. Cao, B. Wei, J. Yu, F. Li, J.-H. Byun, W. Lu, Q. Li, T.-W. Chou, Carbon Nanotube Fiber Based Stretchable Wire-Shaped Supercapacitors, Advanced Energy Materials, 4 (2014) 1300759.

[29] Z. Li, L. Zhang, B.S. Amirkhiz, X. Tan, Z. Xu, H. Wang, B.C. Olsen, C.M.B. Holt, D. Mitlin, Carbonized Chicken Eggshell Membranes with 3D Architectures as High-Performance Electrode Materials for Supercapacitors, Advanced Energy Materials, 2 (2012) 431-437.

[30] W. Zhang, H. Lin, Z. Lin, J. Yin, H. Lu, D. Liu, M. Zhao, 3 D Hierarchical Porous Carbon for Supercapacitors Prepared from Lignin through a Facile Template-Free Method, ChemSusChem, 8 (2015) 2114-2122.

[31] X. Wu, L. Jiang, C. Long, Z. Fan, From flour to honeycomb-like carbon foam: Carbon makes room for high energy density supercapacitors, Nano Energy, 13 (2015) 527-536.

[32] D.S. Su , R. Schlögl, Nanostructured Carbon and Carbon Nanocomposites for Electrochemical Energy Storage Applications, ChemSusChem, 3 (2010) 136-168.

[33] S. Trasatti, G. Buzzanca, Ruthenium dioxide: a new interesting electrode material. Solid state structure and electrochemical behaviour, Journal of Electroanalytical Chemistry and Interfacial Electrochemistry, 29 (1971) A1-A5.

[34] B.E. Conway, Transition from “supercapacitor” to “battery” behavior in electrochemical energy storage, Journal of the Electrochemical Society, 138 (1991) 1539-1548.

[35] T.-C. Liu, W. Pell, B. Conway, Stages in the development of thick cobalt oxide films exhibiting reversible redox behavior and pseudocapacitance, Electrochimica Acta, 44 (1999) 2829-2842.

[36] B. Conway, Electrochemical supercapacitor, Scientific Fundamentals and Technological Applications, Kluwer Academic/Plenum Publishers New York1999.

[37] V. Augustyn, P. Simon, B. Dunn, Pseudocapacitive oxide materials for high-rate electrochemical energy storage, Energy & Environmental Science, 7 (2014) 1597-1614.

[38] S. Ardizzone, G. Fregonara, S. Trasatti, “Inner” and “outer” active surface of RuO_2 electrodes, Electrochimica Acta, 35 (1990) 263-267.

[39] T. Brezesinski, J. Wang, J. Polleux, B. Dunn, S.H. Tolbert, Templated Nanocrystal-Based Porous TiO_2 Films for Next-Generation Electrochemical Capacitors, J. Am. Chem. Soc., 131 (2009) 1802-1809.

[40] X. Li, S. Xiong, J. Li, J. Bai, Y. Qian, Mesoporous NiO ultrathin nanowire networks topotactically transformed from α-$Ni(OH)_2$ hierarchical microspheres and their superior electrochemical capacitance properties and excellent capability for water treatment, Journal of Materials Chemistry, 22 (2012) 14276-14283.

[41] L. Li, Y. Dou, L. Wang, M. Luo, J. Liang, One-step synthesis of high-quality N-doped graphene/Fe_3O_4 hybrid nanocomposite and its improved supercapacitor performances, RSC Adv., 4 (2014) 25658-25665.

[42] J.J. Lingane, Analytical aspects of chronopotentiometry, Analyst, 91 (1966) 1-9.

[43] B.E. Conway, V. Birss, J. Wojtowicz, The role and utilization of pseudocapacitance for energy storage by supercapacitors, Journal of Power Sources, 66 (1997) 1-14.

[44] C.-C. Hu, K.-H. Chang, M.-C. Lin, Y.-T. Wu, Design and Tailoring of the Nanotubular Arrayed Architecture of Hydrous RuO_2 for Next Generation Supercapacitors, Nano Lett., 6 (2006) 2690-2695.

[45] C.-C. Hu, W.-C. Chen, K.-H. Chang, How to Achieve Maximum Utilization of Hydrous Ruthenium Oxide for Supercapacitors, Journal of The Electrochemical Society, 151 (2004) A281-A290.

[46] W. Wei, X. Cui, W. Chen, D.G. Ivey, Manganese Oxide-based Materials as Electrochemical Supercapacitor Electrodes, Chem. Soc. Rev., 40 (2011) 1697-1721.

[47] C. Xu, F. Kang, B. Li, H. Du, Recent progress on manganese dioxide based supercapacitors, Journal of Materials Research, 25 (2010) 1421-1432.

[48] X. Lang, A. Hirata, T. Fujita, M. Chen, Nanoporous metal/oxide hybrid electrodes for electrochemical supercapacitors, Nat Nano, 6 (2011) 232-236.

[49] B. Messaoudi, S. Joiret, M. Keddam, H. Takenouti, Anodic Behaviour of Manganese in Alkaline Medium, Electrochimica Acta, 46 (2001) 2487-2498.

[50] T. Zhou, S. Mo, S. Zhou, W. Zou, Y. Liu, D. Yuan, Mn_3O_4/Worm-like Mesoporous Carbon Synthesized via A Microwave Method for Supercapacitors, J Mater Sci, 46 (2011) 3337-3342.

[51] C.D. Lokhande, D.P. Dubal, O.-S. Joo, Metal oxide thin film based supercapacitors, Current Applied Physics, 11 (2011) 255-270.

[52] F.-b. Zhang, Y.-k. Zhou, H.-l. Li, Nanocrystalline NiO as an electrode material for electrochemical capacitor, Materials Chemistry and Physics, 83 (2004) 260-264.

[53] S.-K. Chang, Z. Zainal, K.-B. Tan, N.A. Yusof, W.M.D. Wan Yusoff, S.R.S. Prabaharan, Recent development in spinel cobaltites for supercapacitor application, Ceramics International, 41 (2015) 1-14.

[54] R.B. Rakhi, W. Chen, D. Cha, H.N. Alshareef, Substrate Dependent Self-Organization of Mesoporous Cobalt Oxide Nanowires with Remarkable Pseudocapacitance, Nano Lett., 12 (2012) 2559-2567.

[55] F. Wang, S. Xiao, Y. Hou, C. Hu, L. Liu, Y. Wu, Electrode materials for aqueous asymmetric supercapacitors, RSC Adv., 3 (2013) 13059-13084.

[56] V. Aravindan, J. Gnanaraj, Y.-S. Lee, S. Madhavi, Insertion-Type Electrodes for Nonaqueous Li-Ion Capacitors, Chemical Reviews, 114 (2014) 11619-11635.

[57] J.P. Cheng, J. Zhang, F. Liu, Recent development of metal hydroxides as electrode material of electrochemical capacitors, RSC Adv., 4 (2014) 38893-38917.

[58] S. Yang, X. Wu, C. Chen, H. Dong, W. Hu, X. Wang, Spherical α-$Ni(OH)_2$ nanoarchitecture grown on graphene as advanced electrochemical pseudocapacitor materials, Chemical Communications, 48 (2012) 2773-2775.

[59] M.P. Yeager, W. Du, B. Bishop, M. Sullivan, W. Xu, D. Su, S.D. Senanayake, J. Hanson, X. Teng, Storage of Potassium Ions in Layered Vanadium Pentoxide Nanofiber Electrodes for Aqueous Pseudocapacitors, ChemSusChem, 6 (2013) 2231-2235.

[60] J. Jiang, Y. Li, J. Liu, X. Huang, C. Yuan, X.W.D. Lou, Recent advances in metal oxide-based electrode architecture design for electrochemical energy storage, Advanced Materials, 24 (2012) 5166-5180.

[61] C. Yuan, H.B. Wu, Y. Xie, X.W.D. Lou, Mixed Transition-Metal Oxides: Design, Synthesis, and Energy-Related Applications, Angewandte Chemie International Edition, 53 (2014) 1488-1504.

[62] T.T. Liu, G.J. Shao, M.T. Ji, Z.P. Ma, Research Progress in Nano-Structured MnO_2 as Electrode Materials for Supercapacitors, Asian J. Chem., 25 (2013) 7065-7070.

[63] M.M. Najafpour, M. Hołyńska, S. Salimi, Applications of the “nano to bulk” Mn oxides: Mn oxide as a Swiss army knife, Coordination Chemistry Reviews, 285 (2015) 65-75.

[64] Y. Yue, H. Liang, Hierarchical micro-architectures of electrodes for energy storage, Journal of Power Sources, 284 (2015) 435-445.

[65] L. Yu, Z.Y. Qian, N.N. Shi, Q. Liu, J. Wang, X.Y. Jing, Interface chemistry engineering in electrode systems for electrochemical energy storage, RSC Adv., 4 (2014) 37491-37502.

[66] U. Patil, S.C. Lee, S. Kulkarni, J.S. Sohn, M.S. Nam, S. Han, S.C. Jun, Nanostructured pseudocapacitive materials decorated 3D graphene foam electrodes for next generation supercapacitors, Nanoscale, 7 (2015) 6999-7021.

[67] M. Yu, W. Qiu, F. Wang, T. Zhai, P. Fang, X. Lu, Y. Tong, Three dimensional architectures: design, assembly and application in electrochemical capacitors, Journal of Materials Chemistry A, 3 (2015) 15792-15823.

[68] Q. Xu, Y. Lv, C. Dong, T.S. Sreeprased, A. Tian, H. Zhang, Y. Tang, Z. Yu, N. Li, Three-dimensional micro/nanoscale architectures: fabrication and applications, Nanoscale, 7 (2015) 10883-10895.

[69] M.F. Montemor, S. Eugénio, N. Tuyen, R.P. Silva, T.M. Silva, M.J. Carmezim, Nanostructured Transition Metal Oxides Produced by Electrodeposition for Application as Redox Electrodes for Supercapacitors, in: M. Aliofkhazraei, A.S.H. Makhlouf (Eds.) Handbook of Nanoelectrochemistry, Springer International Publishing2015, pp. 1-27.

[70] Z. Wu, Y. Zhu, X. Ji, $NiCo_2O_4$-based materials for electrochemical supercapacitors, Journal of Materials Chemistry A, 2 (2014) 14759-14772.

[71] C. Yuan, J. Li, L. Hou, X. Zhang, L. Shen, X.W. Lou, Ultrathin Mesoporous $NiCo_2O_4$ Nanosheets Supported on Ni Foam as Advanced Electrodes for Supercapacitors, Advanced Functional Materials, 22 (2012) 4592-4597.

[72] T.-Y. Wei, C.-H. Chen, H.-C. Chien, S.-Y. Lu, C.-C. Hu, A Cost-Effective Supercapacitor Material of Ultrahigh Specific Capacitances: Spinel Nickel Cobaltite Aerogels from an Epoxide-Driven Sol–Gel Process, Advanced Materials, 22 (2010) 347-351.

[73] V. Gupta, S. Gupta, N. Miura, Electrochemically synthesized nanocrystalline spinel thin film for high performance supercapacitor, Journal of Power Sources, 195 (2010) 3757-3760.

[74] H. Jiang, J. Ma, C. Li, Hierarchical porous $NiCo_2O_4$ nanowires for high-rate supercapacitors, Chemical Communications, 48 (2012) 4465-4467.

[75] L. Li, S. Peng, Y. Cheah, P. Teh, J. Wang, G. Wee, Y. Ko, C. Wong, M. Srinivasan, Electrospun porous $NiCo_2O_4$ nanotubes as advanced electrodes for electrochemical capacitors, Chemistry-A European Journal, 19 (2013) 5892-5898.

[76] C. An, Y. Wang, Y. Huang, Y. Xu, L. Jiao, H. Yuan, Porous $NiCo_2O_4$ nanostructures for high performance supercapacitors via a microemulsion technique, Nano Energy, 10 (2014) 125-134.

[77] N. Garg, M. Basu, A.K. Ganguli, Nickel Cobaltite Nanostructures with Enhanced Supercapacitance Activity, J. Phys. Chem. C, 118 (2014) 17332-17341.

[78] C. Wang, X. Zhang, D. Zhang, C. Yao, Y. Ma, Facile and low-cost fabrication of nanostructured $NiCo_2O_4$ spinel with high specific capacitance and excellent cycle stability, Electrochimica Acta, 63 (2012) 220-227.

[79] Y.Q. Wu, X.Y. Chen, P.T. Ji, Q.Q. Zhou, Sol–gel approach for controllable synthesis and electrochemical properties of $NiCo_2O_4$ crystals as electrode materials for application in supercapacitors, Electrochimica Acta, 56 (2011) 7517-7522.

[80] G.Q. Zhang, H.B. Wu, H.E. Hoster, M.B. Chan-Park, X.W. Lou, Single-crystalline $NiCo_2O_4$ nanoneedle arrays grown on conductive substrates as binder-free electrodes for high-performance supercapacitors, Energy & Environmental Science, 5 (2012) 9453-9456.

[81] X. Lu, X. Huang, S. Xie, T. Zhai, C. Wang, P. Zhang, M. Yu, W. Li, C. Liang, Y. Tong, Controllable Synthesis of Porous Nickel–Cobalt Oxide Nanosheets for Supercapacitors, Journal of Materials Chemistry, 22 (2012) 13357-13364.

[82] F. Deng, L. Yu, G. Cheng, T. Lin, M. Sun, F. Ye, Y. Li, Synthesis of ultrathin mesoporous $NiCo_2O_4$ nanosheets on carbon fiber paper as integrated high-performance electrodes for supercapacitors, Journal of Power Sources, 251 (2014) 202-207.

[83] L. Shen, Q. Che, H. Li, X. Zhang, Mesoporous $NiCo_2O_4$ Nanowire Arrays Grown on Carbon Textiles as Binder-Free Flexible Electrodes for Energy Storage, Advanced Functional Materials, 24 (2014) 2630-2637.

[84] G.-W. Yang, C.-L. Xu, H.-L. Li, Electrodeposited nickel hydroxide on nickel foam with ultrahigh capacitance, Chemical Communications, (2008) 6537-6539.

[85] M. Huang, F. Li, J.Y. Ji, Y.X. Zhang, X.L. Zhao, X. Gao, Facile synthesis of single-crystalline NiO nanosheet arrays on Ni foam for high-performance supercapacitors, CrystEngComm, 16 (2014) 2878-2884.

[86] X. Wang, X. Han, M. Lim, N. Singh, C.L. Gan, M. Jan, P.S. Lee, Nickel cobalt oxide-single wall carbon nanotube composite material for superior cycling stability and high-performance supercapacitor application, J. Phys. Chem. C, 116 (2012) 12448-12454.

[87] H.-W. Wang, Z.-A. Hu, Y.-Q. Chang, Y.-L. Chen, H.-Y. Wu, Z.-Y. Zhang, Y.-Y. Yang, Design and synthesis of $NiCo_2O_4$–reduced graphene oxide composites for high performance supercapacitors, Journal of Materials Chemistry, 21 (2011) 10504-10511.

[88] L. Huang, D. Chen, Y. Ding, S. Feng, Z.L. Wang, M. Liu, Nickel–Cobalt Hydroxide Nanosheets Coated on $NiCo_2O_4$ Nanowires Grown on Carbon Fiber Paper for High-Performance Pseudocapacitors, Nano Lett., 13 (2013) 3135-3139.

[89] L. Yu, G. Zhang, C. Yuan, X.W.D. Lou, Hierarchical $NiCo_2O_4$@MnO_2 core–shell heterostructured nanowire arrays on Ni foam as high-performance supercapacitor electrodes, Chemical Communications, 49 (2013) 137-139.

[90] X. Liu, S. Shi, Q. Xiong, L. Li, Y. Zhang, H. Tang, C. Gu, X. Wang, J. Tu, Hierarchical $NiCo_2O_4$@$NiCo_2O_4$ Core/Shell Nanoflake Arrays as High-Performance Supercapacitor Materials, ACS Appl. Mater. Interfaces, 5 (2013) 8790-8795.

[91] A.K. Mondal, D. Su, S. Chen, A. Ung, H.-S. Kim, G. Wang, Mesoporous $MnCo_2O_4$ with a Flake-Like Structure as Advanced Electrode Materials for Lithium-ion batteries and Supercapacitors, Chemistry – A European Journal, 21 (2015) 1526–1532.

[92] J. Gomez, E.E. Kalu, High-performance binder-free Co–Mn composite oxide supercapacitor electrode, Journal of Power Sources, 230 (2013) 218-224.

[93] L. Li, F. He, S. Gai, S. Zhang, P. Gao, M. Zhang, Y. Chen, P. Yang, Hollow structured and flower-like C@$MnCo_2O_4$ composite for high electrochemical performance in a supercapacitor, CrystEngComm, 16 (2014) 9873-9881.

[94] W. Li, K. Xu, G. Song, X. Zhou, R. Zou, J. Yang, Z. Chen, J. Hu, Facile synthesis of porous $MnCo_2O_{4.5}$ hierarchical architectures for high-rate supercapacitors, CrystEngComm, 16 (2014) 2335-2339.

[95] Y. Xu, X. Wang, C. An, Y. Wang, L. Jiao, H. Yuan, Facile synthesis route of porous $MnCo_2O_4$ and $CoMn_2O_4$ nanowires and their excellent electrochemical properties in supercapacitors, Journal of Materials Chemistry A, 2 (2014) 16480-16488.

[96] S.G. Mohamed, T.-F. Hung, C.-J. Chen, C.K. Chen, S.-F. Hu, R.-S. Liu, Efficient energy storage capabilities promoted by hierarchical $MnCo_2O_4$ nanowire-based architectures, RSC Adv., 4 (2014) 17230-17235.

[97] Y. Yuan, H. Bi, G. He, J. Zhu, H. Chen, A Facile Hydrothermal Synthesis of a $MnCo_2O_4$@Reduced Graphene Oxide Nanocomposite for Application in Supercapacitors, Chemistry Letters, 43 (2014) 83-85.

[98] H. Pang, J. Deng, S. Wang, S. Li, J. Du, J. Chen, J. Zhang, Facile synthesis of porous nickel manganite materials and their morphology effect on electrochemical properties, RSC Adv., 2 (2012) 5930-5934.

[99] M. Zhang, S. Guo, L. Zheng, G. Zhang, Z. Hao, L. Kang, Z.-H. Liu, Preparation of $NiMn_2O_4$ with large specific surface area from an epoxide-driven sol–gel process and its capacitance, Electrochimica Acta, 87 (2013) 546-553.

[100] P. Ahuja, S.K. Ujjain, R.K. Sharma, G. Singh, Enhanced supercapacitor performance by incorporating nickel in manganese oxide, RSC Adv., 4 (2014) 57192-57199.

[101] S. Giri, D. Ghosh, C.K. Das, One pot synthesis of ilmenite-type $NiMnO_3$–"nitrogen-doped" graphene nanocomposite as next generation supercapacitors, Dalton Trans., 42 (2013) 14361-14364.

[102] Rusi, S.R. Majid, High performance super-capacitive behaviour of deposited manganese oxide/nickel oxide binary electrode system, Electrochimica Acta, 138 (2014) 1-8.

[103] Y.-H. Li, Q.-Y. Li, H.-Q. Wang, Y.-G. Huang, X.-H. Zhang, Q. Wu, H.-Q. Gao, J.-H. Yang, Synthesis and electrochemical properties of nickel–manganese oxide on MWCNTs/CFP substrate as a supercapacitor electrode, Applied Energy, 153 (2015) 78–86.

Chapter 2. Experimental methods

The principles of metal oxides electrodeposition and the electrochemical experimental methods to characterize them concerning its application as redox-supercapacitor electrodes will be briefly presented in this part of the thesis. The first part is an introduction focused on the experimental setup and details about cathodic and anodic electrodeposition of (nanostructured) metal oxide. The second part concerns the use of electrochemical techniques (cyclic voltammetry and chronopotentiometry) as central methods to study the redox supercapacitive behavior of electrodes. This chapter is dedicated to the electrodeposition and electrochemical techniques. Techniques for physico-chemical characterization of the materials (such as FEG-SEM, XRD, AFM, Raman and TEM) are not described in this chapter. Its fundamentals and main characteristics can be found elsewhere [1]. Specific experimental details for the various physico-chemical characterization techniques used are presented in each separated chapter (from Chapter 3.1 to Chapter 3.7).

2.1. Electrodeposition of metal oxides and nanostructured metal oxides

Electrodeposition has been widely known as a very flexible route for metals and alloys plating. However, the deposition of metals/alloys is out of scope of the thesis and will not be discussed. Further detail about this can be found in references such as [2] and [3] and this part of the thesis overviews the principle of metal oxide electrodeposition.

The electrodeposition experiments are normally performed in the three-electrode electrochemical configuration in an electrolytic cell to control and monitor the deposition experiments (two electrode cells are also commonly used, but with less ability to precisely control the potential at the working electrode and to monitor the experiment). The electrolytic cell is composed of electrolyte, a cathode and an anode. It is assumed that the electrode/electrolyte interface is inert in this cell, and redox reaction in the cell is driven by external voltage/current, which is controlled by a potentiostat.

The three-electrode configuration includes the working electrode, the counter electrode and the reference electrode, in which:

- Working electrode: in the electrodeposition process, it acts as the substrate for the film deposition, and normally the form of electrode can be varied depending on specific needs. It is important that the working electrode should not react with the electrolyte used for electrodeposition. Also, the distribution of current and potential should be homogeneous over the surface of the electrode.

- Counter electrode: is used to supply the current necessary for redox reactions of interest to occur at the working electrode. It is required that the measured current/potential response of the cell should not be limited by processes on the counter electrode.

- Reference electrode: is the electrode with stable and known potential and is used to fix the potential to be independent of the current density (or redox reactions) during the experimental process.

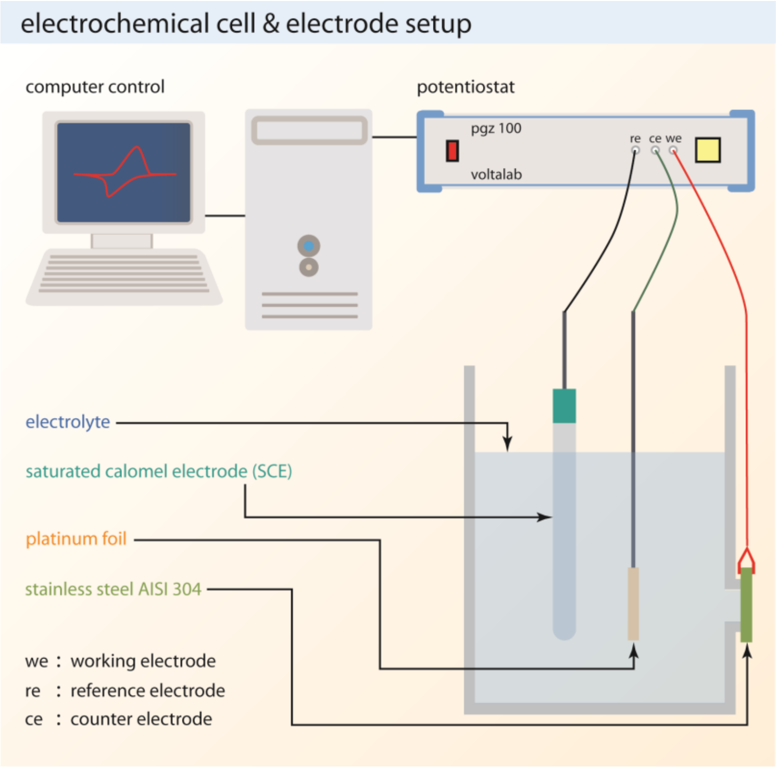

Figure 2.1. The scheme of the three-electrode cell under potentiostat control.

The current/potential response from the cell is normally controlled by a potentiostat (or a power source) to record or apply the potential difference between the working electrode and the reference electrode or the current between the working electrode and the counter electrode. The schematic illustration of a three-electrode cell controlled by a potentiostat is presented in Figure 2.1.

The film formation by electrodeposition happens through two-steps involving nucleation and crystal growth [4]. Generally, these steps depend upon mass transport (diffusion, migration, and convection) and electron transport, which can be controlled by electrolyte, electrode, temperature, applied potential, applied charge and deposition mode [4].

Galvanostatic and potentiostatic electrodeposition, which are the electrodeposition in the constant current mode and constant potential mode, are normally used for electrodepositing metal oxides. The current and potential mode can also be tuned, for changing relevant parameters such as pulse current/potential and current/potential values.

In potentiostatic electrodeposition, the applied potential is controlled, hence the produced films (phases) can also be controlled, knowing its standard potential. In galvanostatic electrodeposition, the potential can vary during the deposition process, which can result in the formation of multiple products/phases. The applied current/potential depends on the nature of electrolytes and temperature.

2.1.1. Cathodic electrodeposition

In principle, to deposit metal oxides in the cathodic region, electrochemical reduction reactions of metal ions in high valence states in the electrolyte to low valence states metal ions in the deposited film are required. A list of possible reactions is presented in Table 2.1. The ions in electrolytes are electro-reduced according to those reactions to form metal oxide films deposited on a substrate.

Porous manganese dioxide with typical pore size of about 100–200 nm has been prepared by this approach for supercapacitor electrodes [5]. However, this approach is rather limited to few transition metals with high valence states such as Mn, Fe and Mo [5-8]. To the author knowledge, it is only possible with the reactions listed in the Table 2.1, so it is not commonly used to electrodeposit metal oxides.

Table 2.1. The reduction reaction of transition metals with high valence state [9].

Reduction reactions	**Standard reduction potential V *vs.* SHE**
$MnO_4^- + 2H_2O + 3e^- \rightarrow MnO_2(s) + 4OH^-$ $2FeO_4^{2-} + 5H_2O + 6e^- \rightarrow Fe_2O_3(s) + 10OH^-$ $H_2MoO_4 + 2H^+ + 2e^- \rightarrow MoO_2(s) + 2H_2O$	0.59 0.81 0.65

Table 2.2. OH^- generation reactions and their corresponding standard reduction potential [10, 11].

Anion reduction reactions	**Standard reduction potential V *vs.* SHE**
$NO_3^- + H_2O + 2e^- \rightarrow NO_2^- + 2OH^-$ $NO_3^- + 7H_2O + 8e^- \rightarrow NH4^+ + 10OH^-$ $ClO_4^- + H_2O + 2e^- \rightarrow ClO_3^- + 2OH^-$ $ClO_4^- + 4H_2O + 8e^- \rightarrow Cl^- + 8OH^-$	0.01 0.36 0.51
Water electrolysis	
$2H_2O + 2e^- \rightarrow H_2 + 2OH^-$	-0.83
Oxygen reduction reaction	
$O_2 + 2H_2O + 2e^- \rightarrow H_2O_2 + 2OH^-$ (acidic media) $O_2 + 2H_2O + 4e^- \rightarrow 4OH^-$	0.70 +0.40
Hydrogen peroxide reduction reaction	
$H_2O_2 + 2e- \rightarrow 2OH^-$	

Generally, when the potential difference between the working electrode and reference electrode is more negative than the standard reduction potential of metal ions in the electrolyte, the reduction reaction of metal ions into metal takes place at the electrode/electrolyte interface, forming the electrodeposited metal film. However, under certain circumstances, which are depended on electrolytes, other reactions can also happen, being competitive with the metal deposition. And in case of thermodynamic favorable, the metal deposition can be prevented, the other reactions dominate at the electrode/electrolyte interface. This assumption is commonly applied to electrodeposit metal oxides reported in literature.

An oxygen source is needed in order to deposit metal oxides. Hydroxyl ions have been used as the oxygen source for the formation of metal oxides. Generally, hydroxyl ions can be generated in the cathodic regime by water electrolysis, anions reduction reaction, oxygen reduction reaction or hydrogen peroxide reduction reaction. The generation of hydroxyl anion results in an increase of local pH at the electrode/electrolyte interface. And if it is thermodynamically favorable than metal deposition, then the reaction of metal ions with OH^- near the interface will happen, forming metal hydroxide films deposited on the electrode. Depending on the air stability of the hydroxide, it can be transformed directly into oxide phases, or the transformation can be done by thermal annealing process. A list of OH^- generation reaction is given in Table 2.2.

In term of thermodynamics, the reactions occurring at more positive equilibrium potentials will dominate. The reduction reaction and the corresponding standard reduction potential of several transition metals studied for supercapacitors are listed in Table 2.3. In comparison with standard reduction reaction of OH^- generation reaction, most of the metal reduction reactions have more negative reduction potentials, hence the metal deposition will be prevented, and the hydroxide deposition will be taken place.

The water electrolysis reaction happens at more positive potential than manganese and vanadium depositions, thereby it can be used to deposit manganese oxide and vanadium oxide.

Table 2.3. Standard reduction potential of several transition metal ions [12].

Reduction reaction	**Standard reduction potential V *vs.* SHE**
$Ni^{2+} + 2e^- \rightarrow Ni$	-0.25
$Co^{2+} + 2e^- \rightarrow Co$	-0.28
$Fe^{2+} + 2e^- \rightarrow Fe$	-0.44
$Zn^{2+} + 2e^- \rightarrow Zn$	-0.76
$Mn^{2+} + 2e^- \rightarrow Mn$	-1.18
$V^{2+} + 2e^- \rightarrow V$	-1.13
$Sn^{2+} + 2e^- \rightarrow Sn$	-0.13

Several hydroxides are not stable in air, therefore they are transformed directly into oxide phases after exposing in air, for example $Zn(OH)_2$ or $Sn(OH)_2$. The oxidation reactions are presented below:

$$Sn^{4+} + 4OH^- \rightarrow SnO_2\ (s) + H_2O \qquad (2.1)$$

$$Zn^{2+} + 2OH^- \rightarrow ZnO\ (s) + H_2O \qquad (2.2)$$

$$Zn^{2+} + 2OH^- \rightarrow Zn(OH)_2\ \ (s) \qquad (2.3)$$

$$Zn(OH)_2 \rightarrow ZnO\ (s) + H_2O \qquad (2.4)$$

Concerning the oxygen reduction reaction, if a four-electron transfer process is involved, the metal hydroxide will be formed after electrodeposition. However, the four-electron transfer process is hard to take place, and normally requires electrocatalysts to promote the reaction. In the case of two electrons transfer process, the hydroxide phase formed can be oxidized by hydrogen peroxide to the oxide phases [13].

Table 2.4. Metal oxides electrodeposited based on OH^- generation: OH^- source used, hydroxide/oxide transformation and surface morphology.

Films	**OH^- source**	**Hydroxide/ oxide transformation**	**Morphology**	**Ref.**
ZnO	Oxygen reduction	No need	Not reported/Nanowires	[14, 15]
ZnO	Hydrogen peroxide reduction	No need	Dense film	[11]
SnO_2	Nitrate reduction	No need	Porous films composed of large particles	[16]
NiO	Nitrate reduction	Annealing	Porous films composed of agglomerated nano-particles	[17]
$Ni(OH)_2$	Perchlorate reduction	Not performed	Not reported	[18]
$Co(OH)_2$	Perchlorate reduction	Not performed	Not reported	[18]
MnO_2	Water electrolysis			
MnO_2	Nitrate reduction	Annealing	Nanorods	[19]
Mn_2O_3	Nitrate reduction	No need	Not reported	[18]
Co_3O_4	Nitrate reduction	Annealing	Nanosheets	[20]
$NiCo_2O_4$	Nitrate reduction	Annealing	Nanosheets	[21]

Interestingly, metal hydroxides have layered structures (trigonal symmetry) and commonly grow into 1D or 2D nanostructures depending on the reaction conditions. Using this advantage, high porosity nanostructured oxide films can be obtained. Therefore, electrodeposition of metal oxides is a flexible and easy route to prepare transition metal oxides based electrodes for supercapacitors or for other energy storage purposes. Examples of metal oxides deposition based on OH^- generation can be found in table 2.4.

It should be noted that by optimizing composition and pH of electrolytes, it could be also possible to deposit metal oxides in the cathodic regime according to the potential-pH dependence diagram (Pourbaix diagram) [22].

2.1.2. Anodic electrodeposition

Electrodeposition in anodic regime concerns the oxidation of metal ions to the higher valence state (reaction 2.5), hence directly forming metal oxides.

$$M^{2+} \rightarrow M^{(2+x)} + xe^- \qquad (2.5)$$

Based on this approach, the anodic electrodeposition of manganese oxide - MnO_2 with porous and tunable morphology has been widely reported in literature [23-26], following by the below reaction.

$$Mn^{2+} \rightarrow Mn^{4+} + 2e^- \qquad (2.6)$$

However, except the case of manganese oxides, the anodic electrodeposition of other transition metal oxides is rather limited and difficult. It is probably due to the higher oxidation states of other transition metal (for examples Fe^{3+}, Ni^{3+} and Co^{3+}) are tend to dissolve in the electrolyte rather than to deposit on the electrode.

Nevertheless, the anodic electrodeposition of other transition metal oxides have been reported, being based on the colloid formation of higher valence state ions and anodic oxidation. The colloids form either by optimizing pH of solutions, OH^- generation on the cathode as presented in the previous part or through the hydrolysis of anions to generate OH^-.

For example, when using acetates precursors for the deposition, the following hydrolysis reaction occurs, accompanied by OH^- release:

$$CH_3COO^- + H_2O \rightarrow CH_3COOH + OH^- \qquad (2.7)$$

The colloid hydroxide formed will be oxidized and deposited on the electrodes [27, 28].

$$M^{2+} \rightarrow M^{3+} + e^- \quad (2.8)$$

$$M^{3+} + 3OH^- \rightarrow M(OH)_3 \quad (2.9)$$

$$M(OH)_3 \rightarrow MOOH + H_2O \quad (2.10)$$

or

$$M^{3+} + 3OH^- \rightarrow MOOH + H_2O \quad (2.11)$$

$$MOOH + H^+ + e^- \rightarrow M(OH)_2 \quad (2.12)$$

Due to the fact that deposition and dissolution take place simultaneously, porous films can be easily obtained. Table 2.5 shows few examples of films deposited by anodic electrodeposition and their surface morphology.

Table 2.5. Anodic electrodeposition of several transition metal oxides: deposition mechanism and surface morphology.

Film	Deposition mechanism	Post oxidation	Morphology	Ref.
MnO_2	Anodic oxidation	No	Nano-needles/rods, & nanoflakes	[25]
Fe_2O_3	Colloid formation and anodic oxidation	Annealing	Nanorods/nanosheets	[29]
NiO	Colloid formation and anodic oxidation	Annealing	Nanoflakes	[28, 30]
CoO	Colloid formation and anodic oxidation	Annealing	Not reported	[31]
Ni-Co oxide	Colloid formation and anodic oxidation	Annealing	Not reported	[32]

The deposition of the mixed oxides can be achieved by simply using electrolytes composed of different metal precursors.

2.2. Electrochemical methods to characterize electrodes for supercapacitors

In this thesis, to characterize the electrochemical or pseudocapacitive response of the electrodeposited films, a half-cell configuration within the three-electrode electrochemical cell, as described above, is used with the electrodeposited films as working electrode.

2.2.1. Cyclic voltammetry

Cyclic voltammetry has been known as a powerful technique to study electrode/electrolyte interface reaction mechanisms and respective potentials by varying potential and recording the current response. In this section, a brief introduction of cyclic voltammetry method used to study the electrochemical and pseudocapacitive response of supercapacitive electrodes involving general reversible redox reactions as below will be presented.

$$Ox + xe^{-} \leftrightarrow Red \qquad (2.13)$$

Ox: is an oxidizing agent, and Red is a reducing agent.

When varying the potential of the working electrode, there are two different types of current flow into the electrode, which account for the non-Faradaic reaction due to the formation of double layers and the Faradaic reaction due to the redox reactions. The current of non-Faradaic reactions increases linearly with the scan rate due to the fast reactions, while the peak current response from the redox reactions normally increase with the scan rate to the power of x ($x < 1$), which results in a decreased contribution of the redox response at increasing scan rates.

The non-Faradaic reaction results from the formation of a double layer capacitor, whose charge accumulation (Q) is proportional to capacitance (C) and potential (E):

$$Q = CE \qquad (2.14)$$

Whereas the capacitance can be described by the Helmholtz model using a following equation:

$$\frac{C}{A} = \frac{\varepsilon\varepsilon_0}{l} \tag{2.15}$$

where C is capacitance, A is the area of electrodes, l is the separation distance between electrodes, ε_0 is the free space permittivity and ε is separating material permittivity.

Assuming that the double layer capacitance is constant, its current response can be determined by the derivative of equation (2.14) with time (t), which results in

$$\frac{dQ}{dt} = C\frac{dE}{dt} \tag{2.16}$$

where current $i = \frac{dQ}{dt}$ and scan rate $v = \frac{dE}{dt}$, so

$$i = Cv \tag{2.17}$$

Concerning the Faradaic redox reaction, electron transfer kinetic and diffusion rates of redox species govern the Faradaic current response. Assuming that electron transfer kinetics are fast enough, the concentration of the redox species can be described by Nernst equation:

$$E_{red} = E_{red}^0 + \frac{RT}{zF} ln \frac{C_{Ox}}{C_{Red}} \tag{2.18}$$

where E_{red} is the reduction potential, E_{red}^0 is the equilibrium reduction potential, R is the gas constant, T is absolute temperature, C_{Ox} is the concentration of oxidizing agent and C_{Red} is the concentration of reducing agent at the electrode surface.

Assuming the reversible (diffusion controlled) redox reactions take place, current peaks in the CV voltamograms can be described by Sevcik equation (at room temperature):

$$i_p = (2.69 \times 10^5) n^{3/2} A D^{1/2} v^{1/2} C_b \tag{2.19}$$

where i_p is the peak current (A), n is number of electron transfer, D is the diffusion coefficient ($cm^2\ s^{-1}$) and C_b is the bulk concentration.

The current response of the non-Faradic process and of the diffusion controlled Faradaic processes thus vary with v and $v^{1/2}$ as stated before in the introduction part (equations 1.1 and 1.2).

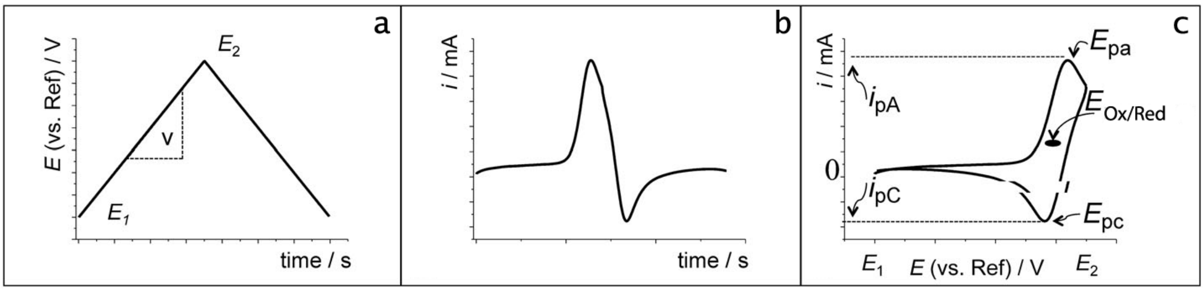

Figure 2.2. Cyclic voltammetry measuring scheme (a, b) and curves (c) [33]. i_{pA}/i_{pC} is anodic/cathodic peak current density and E_{pa}/E_{pc} is a peak potential (potential displaying peak current). E_1 and E_2 are the two end limits of the working potential (potential window). $E_{Ox/Red}$ is the standard potential of Ox/Red reactions.

The cyclic voltammetry measuring scheme is depicted in Figure 2.2. In this procedure, a linearly increasing/decreasing potential with scan rate v between two potential limits E_1 and E_2 is applied to the working electrode, Figure 2.2a. The current response with time is recorded, as shown in Figure 2.2b. Both potential and current are time-dependent; thereby it can be correlated and described as a cyclic voltammogram (current *vs.* potential) in Figure 2.2c. The background in the CV curve is due to the contribution of non-Faradaic double layers. The current raising and peaks are related to the Faradaic redox reactions.

The CV curves can also be recorded at increasing scan rates, allowing studying redox reactions at different rates. Therefore, it can be used to extract information about the nature of redox reactions and ability of electrodes to work at high rate.

2.2.2. Chronopotentiometry

The time dependent reversible reaction potential can be described as (at room temperature)

$$E = \mu - \frac{0.05915}{n} log \frac{t^{1/2}}{\tau^{1/2} - t^{1/2}} \tag{2.20}$$

where μ is the standard chemical potential of the redox reaction, τ is the transition time (second).

The transition time, in a plane electrode, can be described by the Sand equation

$$\tau^{1/2} = \frac{\pi^{1/2} nFAD^{1/2}C}{2i} \qquad (2.21)$$

where i is the constant current density (A), F is Faraday constant (96493 C).

Chronopotentiometry curves can be obtained in several applied current modes (Figure 2.3), which are constant current (Figure 2.3a), linearly varying current (Figure 2.3b), reversed constant current (Figure 2.3c) and cyclic reverse constant current (Figure 2.3d).

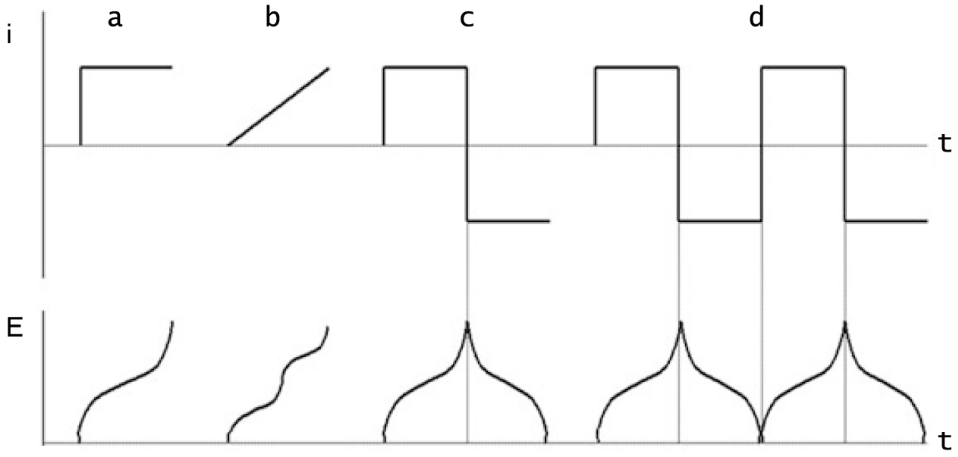

Figure 2.3. Chronopotentiometry measurement scheme. (a) constant current, (b) linearly increasing current, (c) reverse constant current, (d) cyclic reverse constant current [34].

In constant current and linearly varying current modes, the applied constant or varying anodic/cathodic current between two potential limits results in redox reactions at a constant/varying rate. Thereby, they can be used for studying the rate dependent redox reactions. The curve's shape is determined by the nature/reversibility of the redox reactions.

In the reverse constant current, or charge-discharge for studying supercapacitors or batteries, a constant current and reverse constant current are applied in a potential window. Species formed during the anodic/cathodic process will be reduced/oxidized in the reverse current. Thereby, it allows studying the reversible of the redox reactions.

In supercapacitor research, the charge-discharge at a constant current allows to calculate a specific capacitance value of active materials via an equation:

$$C = \frac{It}{\Delta V} \tag{2.22}$$

where C (F g^{-1}) is the specific capacitance of the materials, I (A g^{-1}) is the charge/discharge current density, t (s) is the discharge time, ΔV is the charge/discharge potential windows (V).

The charge-discharge measurements can be repeated in the cyclic reverse constant current mode (Figure 2.3d), which allow studying the charge-discharge cycling stability of the materials, which reveal information about capacitance retention or life time of electrodes.

Rate capability was stated as one of the most important metrics for supercapacitor electrode materials in the previous section of the thesis. By performing charge-discharge measurements at increasing current densities, information about the rate capability can be extracted.

References

[1] A. Yu, V. Chabot, J. Zhang, Electrochemical supercapacitors for energy storage and delivery: fundamentals and applications, CRC Press2013.
[2] M. Paunovic, M. Schlesinger, Fundamentals of electrochemical deposition, John Wiley & Sons2006.
[3] M. Schlesinger, M. Paunovic, Modern electroplating, John Wiley & Sons2011.
[4] A. Bard, L. Faulkner, Electrochemical Methods: Fundamentals and Applications, John Wiley & Sons, Inc2001.
[5] I. Zhitomirsky, M. Cheong, J. Wei, The cathodic electrodeposition of manganese oxide films for electrochemical supercapacitors, JOM, 59 (2007) 66-69.
[6] S. Licht, C. De Alwis, Conductive-Matrix-Mediated Alkaline Fe(III/VI) Charge Transfer: Three-Electron Storage, Reversible Super-Iron Thin Film Cathodes, J. Phys. Chem. B, 110 (2006) 12394-12403.
[7] L. Zhao, B.-S. Chen, J.-L. Zhang, D.-L. Wang, EQCM studies of composition and electrochemical performance of film prepared by electrochemical reduction of sodium ferrate, J Solid State Electrochem, 16 (2012) 2079-2084.

[8] D.D. Yao, J.Z. Ou, K. Latham, S. Zhuiykov, A.P. O'Mullane, K. Kalantar-zadeh, Electrodeposited α- and β-Phase MoO_3 Films and Investigation of Their Gasochromic Properties, Crystal Growth & Design, 12 (2012) 1865-1870.

[9] P. Atkins, Physical Chemistry. 6th, Oxford University Press, 1998.

[10] G.H.A. Therese, P.V. Kamath, Electrochemical synthesis of metal oxides and hydroxides, Chemistry of materials, 12 (2000) 1195-1204.

[11] T. Pauporté, D. Lincot, Hydrogen peroxide oxygen precursor for zinc oxide electrodeposition I. Deposition in perchlorate medium, Journal of the Electrochemical Society, 148 (2001) C310-C314.

[12] W.M. Haynes, CRC handbook of chemistry and physics, CRC press2013.

[13] L. Dai, Y. Xue, L. Qu, H.-J. Choi, J.-B. Baek, Metal-Free Catalysts for Oxygen Reduction Reaction, Chemical Reviews, 115 (2015) 4823-4892.

[14] A. Goux, T. Pauporté, D. Lincot, Oxygen reduction reaction on electrodeposited zinc oxide electrodes in KCl solution at 70 °C, Electrochimica Acta, 51 (2006) 3168-3172.

[15] J. Elias, R. Tena-Zaera, C. Lévy-Clément, Effect of the Chemical Nature of the Anions on the Electrodeposition of ZnO Nanowire Arrays, J. Phys. Chem. C, 112 (2008) 5736-5741.

[16] X. Chen, J. Liang, Z. Zhou, H. Duan, B. Li, Q. Yang, The preparation of SnO_2 film by electrodeposition, Materials Research Bulletin, 45 (2010) 2006-2011.

[17] K.-W. Nam, K.-B. Kim, A study of the preparation of NiO_x electrode via electrochemical route for supercapacitor applications and their charge storage mechanism, Journal of the Electrochemical Society, 149 (2002) A346-A354.

[18] L. Indira, P.V. Kamath, Electrogeneration of base by cathodic reduction of anions: novel one-step route to unary and layered double hydroxides (LDHs), Journal of Materials Chemistry, 4 (1994) 1487-1490.

[19] T. Yousefi, A.N. Golikand, M. Hossein Mashhadizadeh, M. Aghazadeh, Facile synthesis of α-MnO_2 one-dimensional (1D) nanostructure and energy storage ability studies, Journal of Solid State Chemistry, 190 (2012) 202-207.

[20] X.W.D. Lou, Growth of ultrathin mesoporous Co_3O_4 nanosheet arrays on Ni foam for high-performance electrochemical capacitors, Energy & Environmental Science, 5 (2012) 7883-7887.

[21] C. Yuan, J. Li, L. Hou, X. Zhang, L. Shen, X.W. Lou, Ultrathin Mesoporous $NiCo_2O_4$ Nanosheets Supported on Ni Foam as Advanced Electrodes for Supercapacitors, Advanced Functional Materials, 22 (2012) 4592-4597.

[22] M. Pourbaix, Atlas of electrochemical equilibria in aqueous solutions, 2nd English ed. ed., National Association of Corrosion Engineers 1974.

[23] W. Wei, X. Cui, W. Chen, D.G. Ivey, Manganese Oxide-based Materials as Electrochemical Supercapacitor Electrodes, Chem. Soc. Rev., 40 (2011) 1697-1721.

[24] B. Babakhani, D.G. Ivey, Anodic deposition of manganese oxide electrodes with rod-like structures for application as electrochemical capacitors, Journal of Power Sources, 195 (2010) 2110-2117.

[25] S. Chou, F. Cheng, J. Chen, Electrodeposition synthesis and electrochemical properties of nanostructured γ-MnO_2 films, Journal of Power Sources, 162 (2006) 727-734.

[26] C.-C. Hu, T.-W. Tsou, Ideal capacitive behavior of hydrous manganese oxide prepared by anodic deposition, Electrochemistry Communications, 4 (2002) 105-109.

[27] M.-S. Wu, R.-H. Lee, Electrochemical growth of iron Oxide thin films with nanorods and nanosheets for capacitors, Journal of The Electrochemical Society, 156 (2009) A737-A743.

[28] M.-S. Wu, C.-H. Yang, M.-J. Wang, Morphological and structural studies of nanoporous nickel oxide films fabricated by anodic electrochemical deposition techniques, Electrochimica Acta, 54 (2008) 155-161.

[29] M.-S. Wu, R.-H. Lee, J.-J. Jow, W.-D. Yang, C.-Y. Hsieh, B.-J. Weng, Nanostructured iron oxide films prepared by electrochemical method for electrochemical capacitors, Electrochem. Solid-State Lett., 12 (2009) A1-A4.

[30] M.-S. Wu, Y.-A. Huang, C.-H. Yang, J.-J. Jow, Electrodeposition of nanoporous nickel oxide film for electrochemical capacitors, International Journal of Hydrogen Energy, 32 (2007) 4153-4159.

[31] T. Yoshino, N. Baba, Characterization and properties of electrochromic cobalt oxide thin film prepared by electrodeposition, Solar Energy Materials and Solar Cells, 39 (1995) 391-397.

[32] G. Wu, N. Li, D.-R. Zhou, K. Mitsuo, B.-Q. Xu, Anodically electrodeposited Co+Ni mixed oxide electrode: preparation and electrocatalytic activity for oxygen evolution in alkaline media, Journal of Solid State Chemistry, 177 (2004) 3682-3692.

[33] S.-I. Pyun, H.-C. Shin, J.-W. Lee, J.-Y. Go, Electrochemistry of Insertion Materials for Hydrogen and Lithium, Springer Science & Business Media2012.

[34] F. Harnisch, S. Freguia, A basic tutorial on cyclic voltammetry for the investigation of electroactive microbial biofilms, Chemistry–An Asian Journal, 7 (2012) 466-475.

Chapter 3. Results and discussion

3.1. Cathodic electrodeposition and electrochemical response of manganese oxide pseudocapacitor electrodes✧

Tuyen Nguyen[a,b], M. João Carmezim[a,c], Michel Boudard[b], M. Fátima Montemor[a]

[a] CQE - Centro de Química Estrutural, Insituto Superior Técnico, Universidade de Lisboa, Lisbon 1049-001, Portugal.

[b] LMGP, Univ. Grenoble Alpes, CNRS, F-38000 Grenoble, France.

[c] ESTSetúbal, Instituto Politécnico de Setúbal, 1959-007 Setúbal, Portugal.

In this work, we reported the cathodic electrodeposition of manganese oxide films from nitrate based electrolytes for pseudocapacitors working in alkaline media. The correlation of the post-thermal treatment, the deposition potential, the electrolyte concentration and the applied charge on surface morphology and electrochemical response of the electrodeposited films were studied. Morphological characteristics and electrochemical response varied depending on the deposition parameter. *Via* the optimized deposition process, the hierarchical nanoparticles/nanoflakes Mn_3O_4 films were obtained, exhibiting a high specific capacitance value of 416 F g^{-1} at current density of 1 A g^{-1} in 1 M NaOH electrolyte. It exhibited specific capacitance retention of 64% when increasing current density from 1 A g^{-1} to 10 A g^{-1}. The films showed the specific capacitance value 196 F g^{-1} after continuous charge-discharge at 1 A g^{-1} for 1000 cycles, thus pointing out the possibility of using cathodically deposited manganese oxide electrodes for pseudocapacitors.

Keywords: cathodic electrodeposition, manganese oxides, supercapacitors, alkaline media

---

✧ **Adapted from International Journal of Hydrogen Energy, DOI: 10.1016/j.ijhydene.2015.10.041**

3.1.1. Introduction

During the last decade, manganese oxides have been emerged as promising materials for pseudocapacitor electrodes due to its low cost and environmental friendliness, compared to other transition metal oxides that have been studied for pseudocapacitors, and a high theoretical specific capacitance value of 1320 F g^{-1} [1-5]. The good electrochemical response and high theoretical capacitance value of manganese oxides are the result of multi oxidation states ranging from divalent to quadrivalent [6]. Besides, manganese oxides are also the important materials in other research branches such as catalysts [7, 8], batteries [9-11], and magnetic [12] applications. Therefore, the development of new routes to prepare functional and optimized manganese oxides are being received a lot of attention.

Chemical solution routes have been widely used to prepare manganese oxide based electrodes [6, 13]. Depending on the preparation parameters, manganese oxides with different morphologies can be obtained such as nanoflowers [14, 15], nanowires/nanorods [10, 16, 17], and nanotubes [18, 19]. Electrodes based on these materials exhibited different pseudocapacitive performance due to their different surface morphologies. The electrode preparation processes generally involves the use of binders to connect the active materials and current collectors together, leading to a reduction of the active part of materials, to a reduction of both the penetration of the electrolyte and the active mass of the pseudocapacitive electrodes and severe film/collector de-adhesion problems.

As compared to chemical solution methods, electrodeposition provides a single step, and binder free route to fabricate manganese oxide electrodes with good adhesion to the current collector [20]. Therefore, it is of great interest not only due to a facile process but also because of the scale up suitability for large-scale production. Concerning manganese oxides electrodes prepared by electrodeposition, many studies have been focused on anodic electrodeposition, in which Mn^{2+} ions in electrolytes are oxidized to Mn^{4+} forming deposited films onto substrates. For example, B. Babakhani et al. [21] have prepared rod-liked manganese oxide nanocrystals electrodes with a specific capacitance value of 185 F g^{-1}. S. Chou et al. [22] reported carambola-like γ-MnO_2 nanoflakes electrodes with a specific capacitance value of 240 F g^{-1}. Amorphous hydrous manganese oxides deposited on a graphite substrate showed a specific capacitance value of 260-320 F g^{-1} [23]. MnO_2 nanofiber electrodes displayed a specific capacitance value of 392 F g^{-1} [24].

Manganese oxides can also be prepared by electrodeposition in the cathodic regime. The process, when Mn^{2+} ions are used as precursors in the electrolyte, generally involves an increase of the pH value at the electrode/electrolyte interface through the formation of hydroxyl ions, either through water electrolysis, oxygen reduction reaction or nitrate reduction [25] and the reaction of Mn^{2+} cations with the generated hydroxyls. This route was applied to electrodeposit MnO_2 and to fabricate MnO_2/carbon aerogel composites that showed a specific capacitance value of 515.5 F g^{-1} [26]. When MnO_4^- is used as precursor, it involves a reduction of Mn^{7+} to Mn^{4+} [27]. For example, MnO_2 films electrodeposited from $KMnO_4$ electrolyte composed of nanosheets with different compactness showed specific capacitance values of 196 F g^{-1} and 128 F g^{-1} [28].

Surface area and porosity of the active materials are crucial factors for the enhanced performance of pseudocapacitors. Therefore, in several electrodeposition experiments, hard templates such as anodic aluminum membranes were used in order to create well-ordered porous structures [29, 30]. Micro/nano porous substrates such as nickel foams [31], nanoporous de-alloyed gold [32], carbon nanofibers/nanotubes [33, 34] and TiO_2 nanotubes [35] with open porous channels were also used for the electrodeposition of manganese oxides to enhance the diffusion of the electrolyte to the active material. In the case of using flat substrates such as stainless steels, the surface morphology of the resulting film must be controlled by the deposition parameters.

Despite the valuable work already published, the influence of the deposition conditions when manganese oxides are cathodically electrodeposited from the nitrate electrolytes on their surface morphology and pseudocapacitive response have not been reported, to the best of authors' knowledge. Thus, in this work we aim at studying and optimizing the electrodeposition of manganese oxide films from nitrate based electrolytes for the fabrication of electrodes for pseudocapacitor applications. The deposition parameters such as potential, electrolyte concentration, applied charge and post-thermal treatment were optimized to obtain electrodes with good pseudocapacitive performance, operating in alkaline electrolyte. This optimization results in the formation of hierarchical Mn_3O_4 nanoparticles/nanoflakes films, which display good pseudocapacitive electrochemical response.

3.1.2. Experimental

Materials: Manganese nitrate $Mn(NO_3)_2$ and sodium hydroxide NaOH, from Sigma-Aldrich, were used for electrodeposition and for the electrochemical evaluation experiments, respectively. The chemicals were used as received without further purification process. A stainless steel (AISI 304) was used as substrate for electrodeposition. This substrate was previously polished with SiC sandpapers from 500, 800 to 1000 grits, rinsed with deionized water, ethanol and dried by a jet of compressed air at room temperature.

Electrodeposition: The electrodeposition experiments were performed in a conventional three-electrode electrochemical system under ambient atmosphere at room temperature using Voltalab PGZ 100 Potentiostat from Radiometer with a stainless steel as working electrode, saturated calomel electrode (SCE) as reference electrode and platinum foil as counter electrode. The electrodeposition was performed in a constant potential mode. The electrolyte concentration, applied charge and deposition potential were varied to induce changes in the surface morphology and to optimize the electrochemical activity. The post-thermal treatment was performed in air and the respective temperatures were optimized too.

Characterization: Field emission gun scanning electron microscope (FEG-SEM, JEOL 7001F microscope) was used for studying surface morphology of the films. Raman spectroscopy (Horiba/Jobin Yvon LabRam spectrometer) and Fourier transform infrared spectroscopy (FTIR, Digilab Excalibur Series spectrometer) were used for studying structural characteristics. For Raman measurements, the 632.8 nm He-Ne laser was used for excitation on a spot of 1 μm^2 and the counting time was 400 seconds. The structural details were studied by transmission electron microscope (TEM, JEOL JEM-2010 microscope) at acceleration voltage of 200 kV. Magnetic measurements were performed by SQUID magnetometer (Quantum Design). To evaluate electrochemical response, cyclic voltammetry (CV) at a scan rate of 20 mV s^{-1} and charge-discharge (CD) at current density of 1 A g^{-1}, were carried out in a conventional three-electrode system as described above with the films were used as working electrode and 1 M NaOH was used as electrolyte. All potentials referred in this work are potentials versus SCE. The specific capacitance values of the films were calculated from the CD curves using the below formula:

$$C = \frac{It}{\Delta V} \qquad (3.1.1)$$

where C, I, t and ΔV are the specific capacitance of the films (F g^{-1}), the CD current density (A g^{-1}), the discharge time (s) and the charge-discharge potential windows (V), respectively.

3.1.3. Results and Discussion

In the present work, manganese oxides were electrodeposited onto the stainless steel substrates from the nitrate based precursor - $Mn(NO_3)_2$. Films electrodeposited from nitrate baths in the cathodic regime involve generation either through nitrate reduction or water electrolysis, of hydroxyl OH^- anions near the substrate, which raise pH value at the substrate/electrolyte interface. Manganese ions Mn^{2+} in the electrolyte then react with generated OH^- anions at the substrate/electrolyte interface, forming $Mn(OH)_2$ that precipitates at the substrate. At the end, $Mn(OH)_2$ is oxidized in air to form the manganese oxides. The reactions are described below as [25]:

$$2H_2O + 2e^- \rightarrow H_2 + 2OH^- \qquad (3.1.2)$$

$$NO_3^- + 7H_2O + 8e^- \rightarrow NH_4^+ + 10OH^- \qquad (3.1.3)$$

$$Mn^{2+} + 2OH^- \rightarrow Mn(OH)_2 \qquad (3.1.4)$$

$$Mn(OH)_2 + \frac{x-1}{2}O_2 \rightarrow MnO_x + H_2O \qquad (3.1.5)$$

The electrodeposited films can also be treated by post thermal annealing to facilitate the oxidation process and to enhance the pseudocapacitive performance of the electrodes. The influences of relevant parameters, during and after electrodeposition, are studied and discussed envisaging manganese oxide based pseudocapacitive electrodes.

3.1.3.1. Effect of post-thermal treatment

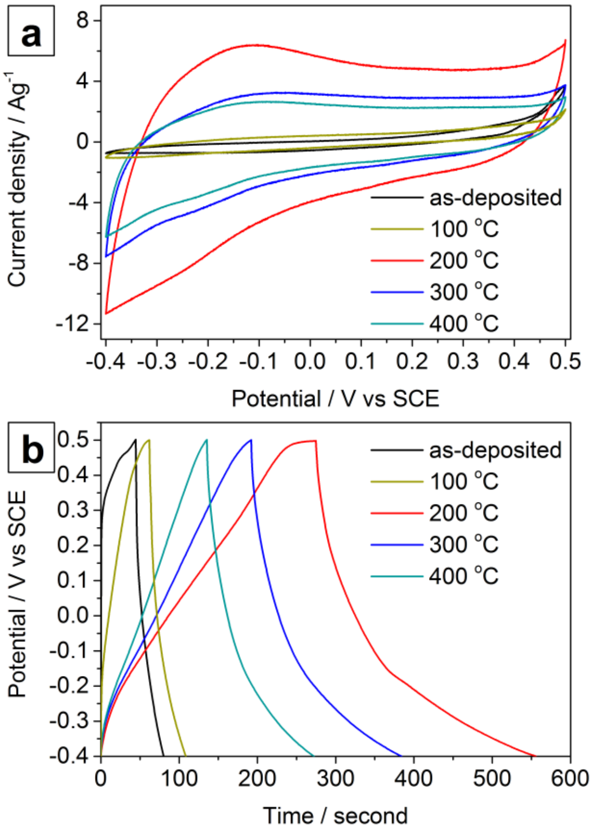

Figure 3.1.1. (a) Cyclic voltammetry at scan rate of 20 mV s^{-1} and (b) charge-discharge curves at current density of 1 A g^{-1} of films deposited at -1.5 V and after thermally treated at 100 °C, 200 °C, 300 °C and 400 °C for 1 hour.

The films were fabricated from a $Mn(NO_3)_2$ electrolyte of concentration of 0.1 M, using a deposition potential of -1.5 V and a total applied charge of -0.6 C cm^{-2}. The as-deposited films were subjected to thermal annealing at temperatures of 100 °C, 200 °C, 300 °C and 400 °C in air for one hour in order to optimize the thermal annealing process to an enhanced electrochemical response. Figure 3.1.1 showed CV and CD curves of the as-deposited films and of the thermally annealed films at different temperatures. As shown in Figure 3.1.1a, the current response of the films significantly increased after thermal annealing at 200 °C. Redox peaks at anodic/cathodic potential of -0.15/-0.25 V could be observed in CV curve, which gave rise to the pseudocapacitive response. In alkaline electrolyte, probably the redox response involved the reaction of manganese with OH^- as proposed elsewhere [36, 37]:

$$Mn^{x+} + \delta OH^- \leftrightarrow Mn^{(x-\delta)}(OH)_\delta \quad (3.1.6)$$

The enhanced redox response after thermal annealing could be due to increased electron conductivity and an increased interconnectivity of the active materials. The current response decreased when further increasing annealing temperature to 300 °C and 400 °C, probably due to an increase of crystal size, which led to decreased porosity of the electrodes and therefore poorest pseudocapacitive response [37]. CD curves at a current density of 1 A g^{-1} in Figure 3.1.1b confirmed the trend obtained from CV results. The specific capacitance values calculated from the CD curves using equation (1) were 41 F g^{-1}, 47 F g^{-1}, 310 F g^{-1}, 213 F g^{-1}, and 151 F g^{-1} for the as-deposited film and for the films annealed at 100 °C, 200 °C, 300 °C, and 400 °C, respectively. The obtained data revealed that thermal annealing at 200 °C resulted in films with the highest pseudocapacitive response among the ones tested. Thus, the annealing temperature of 200 °C was selected for the thermal treatment of the films produced.

3.1.3.2. Effect of deposition potential

The deposition potential was varied in a window from -1.0 V to -1.5 V, with steps of 0.1 V, while keeping a total applied charge of -0.6 C cm^{-2}, electrolyte concentration of 0.1 M and post-thermal annealing at 200 °C to study the effect of the deposition potential on the surface morphology and on the electrochemical response. Chronoamperometry curves in Figure 3.1.2a showed long deposition times of about 3000 seconds at the applied potential of -1.0 V. The deposition time decreased quickly when increasing the applied potential above (more negative) -1.0 V. The long deposition time at -1.0 V was probably due to a slow growing process at a less negative potential. At more negative potentials, the electromotive force of the cathodic reduction reactions increases, leading to fast growing processes.

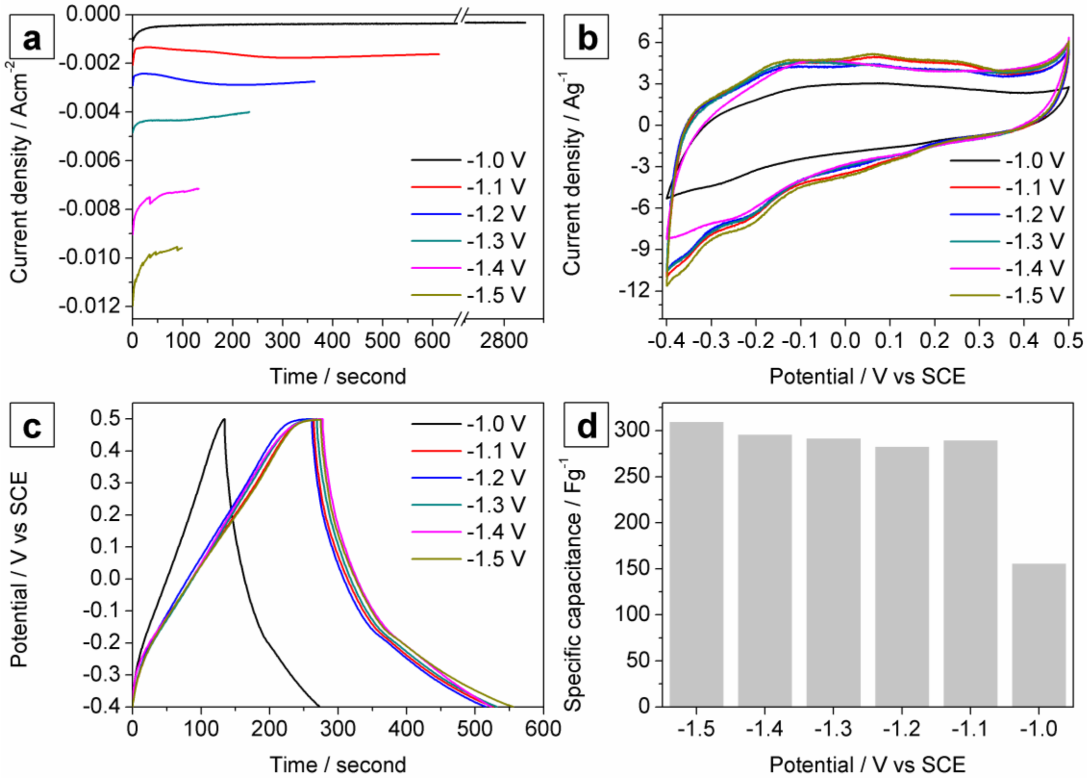

Figure 3.1.2. (a) Chronoamperometry curves at different potentials with total applied charge of -0.6 C cm^{-2}, (b) cyclic voltammetry at a scan rate of 20 mV s^{-1}, (c) charge-discharge at current density of 1 A g^{-1} and (d) specific capacitance values of the films deposited at different applied potentials.

FEG-SEM images of the films deposited at -1.0 V, Figure 3.1.3a, revealed the presence of connected islands, which do not fully cover the substrate, confirming the slow growing process [38] as stated above. At potentials of -1.1 V, -1.3 V and -1.5 V, FEG-SEM images (Figure 3.1.3b-d) showed the presence of interconnected worm-like nanostructures, horizontally accumulated nanoflakes and vertically interconnected roughed nanoflakes, respectively. The average length of nanoworms, horizontally grown nanoflakes and vertically grown nanoflakes were 280 nm, 190 nm and 410 nm, respectively. The different morphologies observed can be justified, assuming that films grown at different potentials are governed by different growing modes, leading to changes in the surface morphology. It should be noted that thermal annealing at 200 ^{o}C for one hour did not change the surface morphology of the films, as shown in Figure 3.1.3d and e, which compare the surface morphology of the as-deposited film at -1.5 V (Figure 3.1.3e) and the film deposited at -1.5 V followed by annealing at 200 ^{o}C (Figure 3.1.3d). Further increase of the deposition potentials (less negative) resulted in unstable films, which were easily detached from the substrate when dried at atmosphere. This could be due to the fast growing rate leading to an unstable connection in the films. Furthermore, at high deposition potential, hydrogen evolution was more intense and could contribute to film de-adhesion. To avoid the instability of the film, N. Nagarajan et al. [39] added a polyethylenimine (PEI) during co-cathodic electrodeposition with manganese oxides to obtain films with good adhesion.

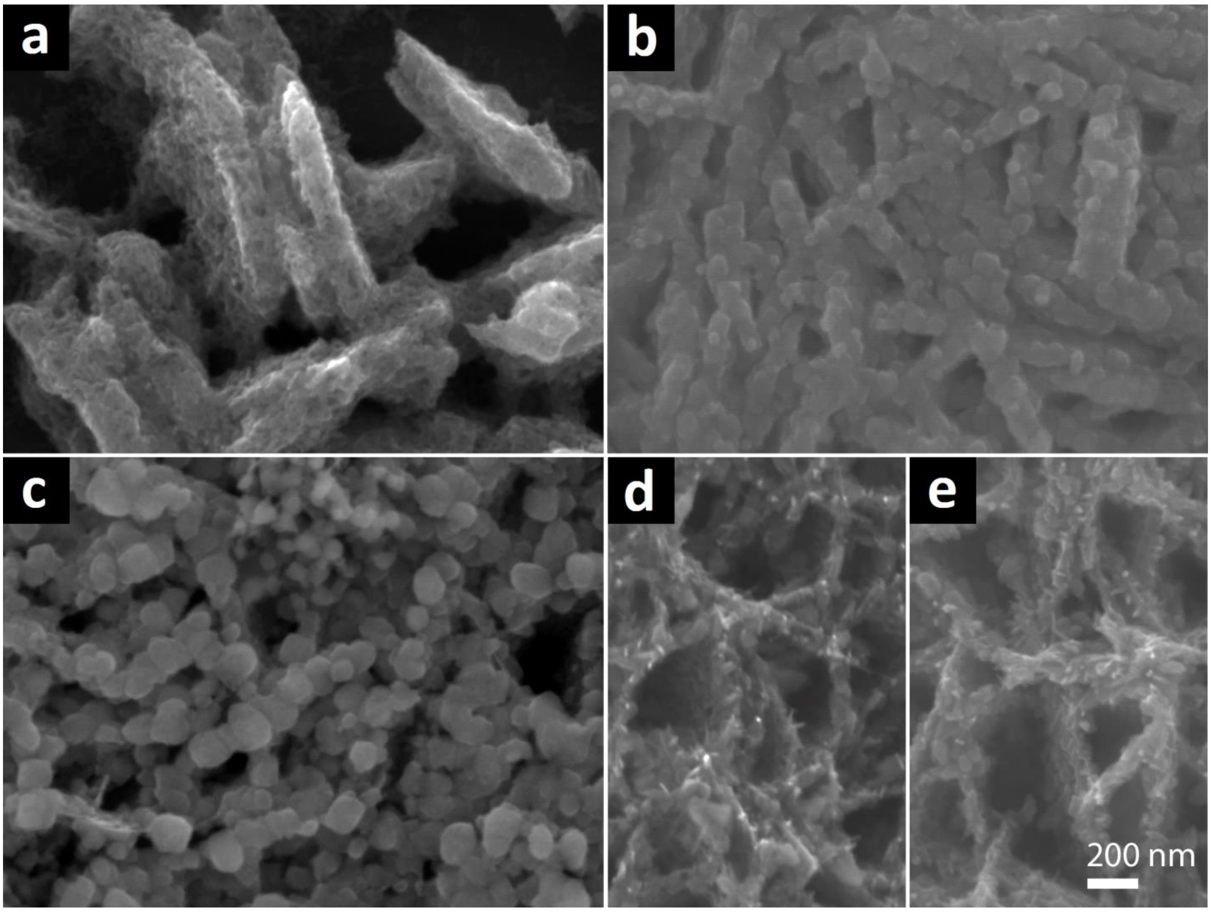

Figure 3.1.3. FEG-SEM images of the films deposited at (a) -1.0 V, (b) -1.1 V, (c) -1.3 V and (d) -1.5 V and annealed at 200 ^{o}C and (e) an image of the as-deposited film at -1.5 V. Scale bar at the bottom right is applied for all images in the figure.

The CV curves in Figure 3.1.2b displayed well-defined redox peaks and showed an increased current response for the films deposited at potentials between -1.1 V and -1.5 V compared to the films deposited at -1.0 V. The current response of the films deposited at potentials between -1.1 V and -1.5 V was rather similar to each other. The CD curves, Figure 3.1.2c, showed non-linear slopes, which resulted from the presence of redox processes as observed in the CV results. The specific capacitances of the films deposited at different potentials were calculated from the CD curves and represented in Figure 3.1.2d. The specific capacitance value of 150 F g^{-1} at potential of -1.0 V was the lowest one amongst the values obtained for the films deposited at different potentials. The specific capacitance values obtained at potentials of -1.1 V to -1.5 V were approximately 300 F g^{-1}. The variation of the specific capacitance values can be explained considering the morphological features revealed by FEG-SEM. At -1.0 V, the slow growing film resulted in the formation of more dense islands, probably of decreased surface area/porosity, leading to lower specific capacitance values. At higher applied potentials, the films were composed of nanostructures that display increased porosity, resulting in the high specific capacitance values compared to the film deposited at -1.0 V. The similar specific capacitance values of the films deposited in the potential ranging from -1.1 V to -1.5 V was probably due to the identical surface area/porosity of the different nano-architectures.

3.1.3.3. Effect of precursor concentration

The $Mn(NO_3)_2$ concentration was changed to 0.25 M and 0.5 M to study the effect of the precursor concentration on the electrochemical response of the manganese oxide films. The potential of -1.3 V was selected, the total applied charge was kept at -0.6 C cm^{-2} and the post-thermal annealing was performed at 200 ^{o}C for one hour in air. The surface morphology of the films was sensitive to the precursor concentration in the electrolyte as revealed by the FEG-SEM images in Figure 3.1.4a and b. The films deposited with an electrolyte concentration of 0.25 M were composed of interconnected nanoflakes with the presence of nanoparticles attached on their surface. The average size of the nanoparticles was approximately 50 nm. The average thickness of the nanoflakes was approximately

14 nm. When the $Mn(NO_3)_2$ concentration was further increased to 0.5 M, the nanoparticles attached on the surface of the nanoflakes became less evident (Figure 3.1.4b). The average thickness of the nanoflakes was approximately 14 nm, which was similar to the value of the film deposited at 0.25 M.

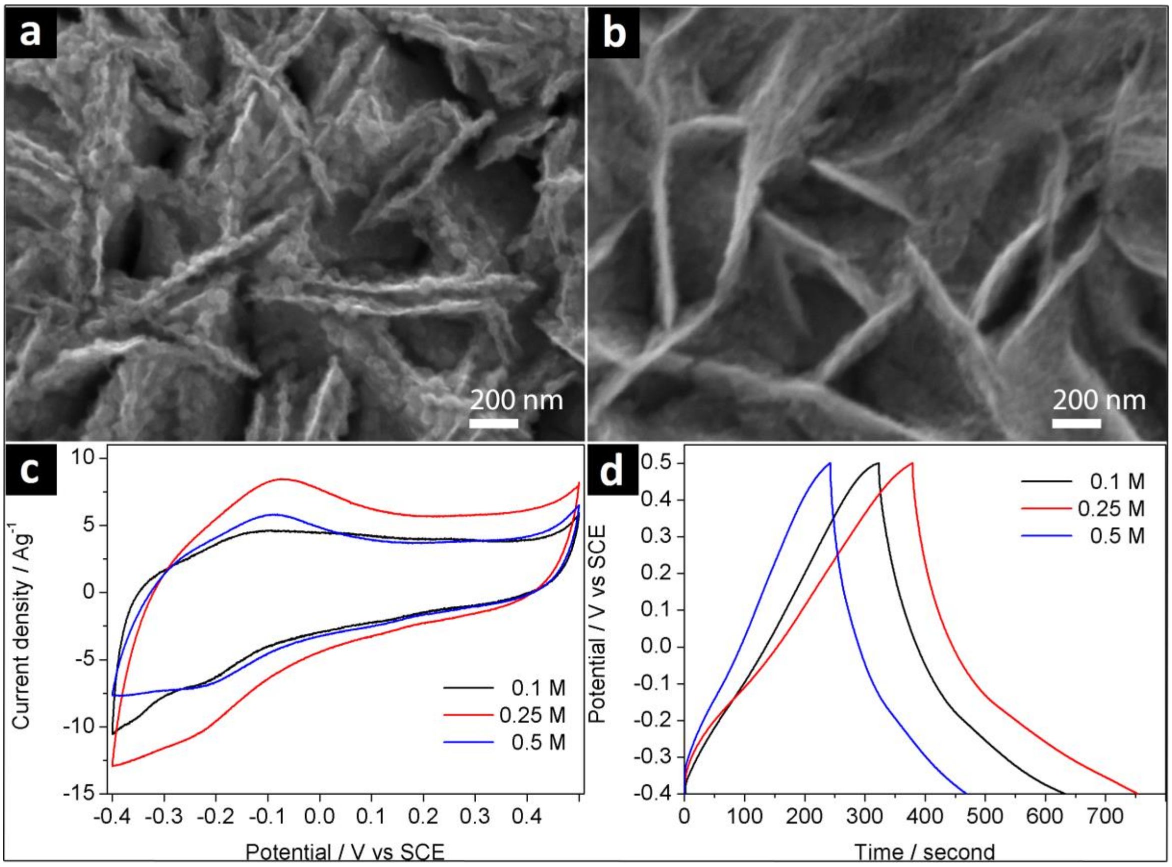

Figure 3.1.4. FEG-SEM images of the films deposited with $Mn(NO_3)_2$ concentration of (a) 0.25 M and (b) 0.5 M at potential of -1.3 V and applied charge of -0.6 C cm^{-2}. (c) Cyclic voltammetry curves at a scan rate of 20 mV s^{-1} and (d) charge-discharge curves at current density of 1 A g^{-1} of the films deposited with different $Mn(NO_3)_2$ concentration.

The electrochemical response of the films is depicted in CV and CD curves in Figure 3.1.4c and d. The CV curves showed that the film deposited at a concentration of 0.25 M exhibited the best electrochemical response. The specific capacitance calculated from the CD curves revealed that the film deposited at 0.25 M of $Mn(NO_3)_2$ displayed the highest specific capacitance value of 416 F g^{-1}, in good agreement with the CV results. The specific capacitance value of the film deposited at 0.5 M was 252 F g^{-1}. The high specific capacitance of the film deposited at 0.25 M was probably due an optimized surface area/porosity resulting from the formation of the hierarchical nanoparticles/nanoflakes structure.

3.1.3.4. Effect of applied charge

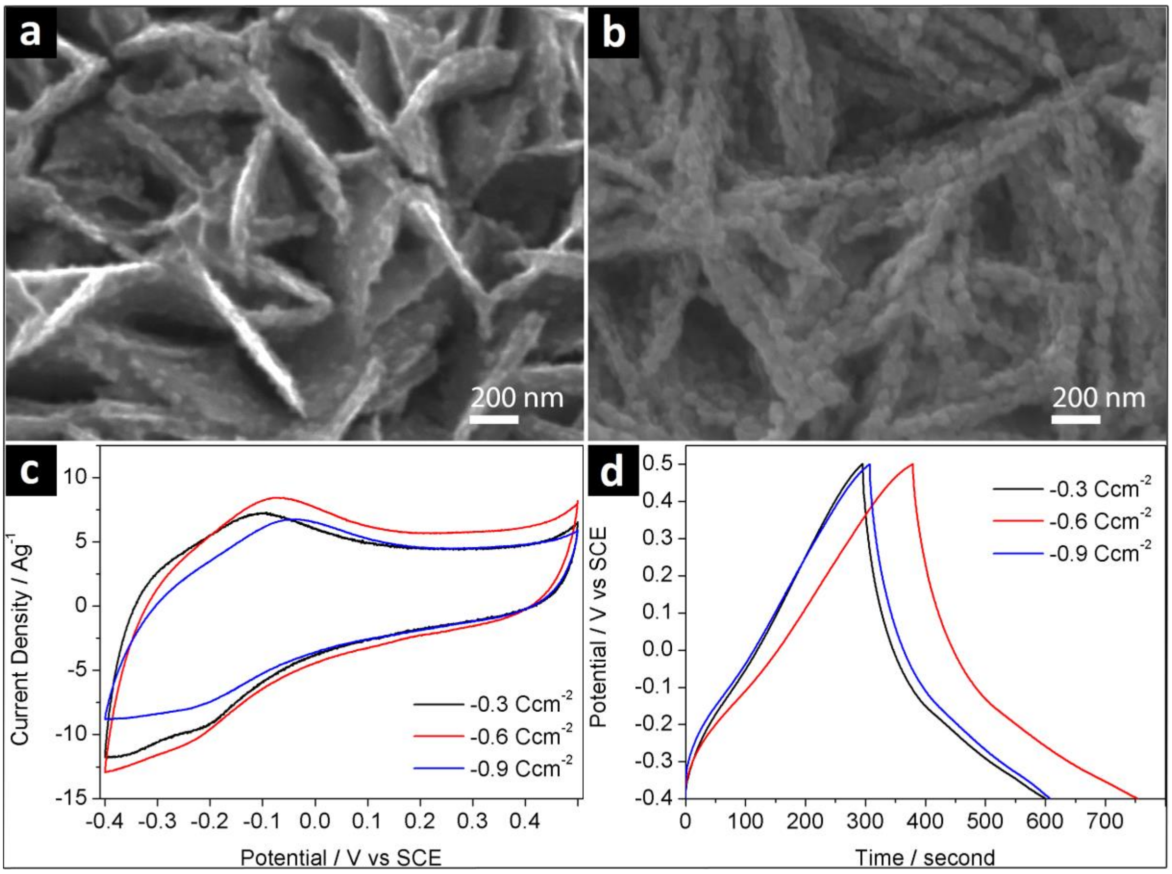

Figure 3.1.5. FEG-SEM images of the films deposited with total applied charge of (a) -0.3 C cm^{-2} and (b) -0.9 C cm^{-2}. (c) Cyclic voltammetry curves at a scan rate of 20 mV s^{-1} and (d) charge-discharge curves at current density of 1 A g^{-1} of the films deposited with different total applied charge.

The total applied charge was also optimized. Thus the charge was varied, while keeping the deposition potential at -1.3 V, $Mn(NO_3)_2$ electrolyte concentration of 0.25 M and post-thermal annealing at 200 °C for one hour to correlate the total applied charge with the resulting electrochemical response. Furthermore, by varying the total applied charge it is possible to better understand the film growth process leading to the formation of the nanoparticles/nanoflakes morphology at the precursor concentration of 0.25 M, which in this work exhibited the highest specific capacitance values. As shown in FEG-SEM image, Figure 3.1.5a, with the total applied charge of -0.3 C cm^{-2}, vertically interconnected nanoflakes with few nanoparticles attached on them were observed. The number and size of the nanoparticles increased when increasing the total applied charge to -0.6 C cm^{-2} as previously shown in Figure 3.1.4a. Under a total applied charge of -0.9 C cm^{-2}, the nanoflakes were fully covered with nanoparticles. Thus, the FEG-SEM results revealed that, at the concentration of 0.25 M, the films grown through the formation of nanoflakes at the beginning of electrodeposition followed by the deposition of nanoparticles on their surface.

The CV and CD curves of the films deposited under different applied charge are presented in Figure 3.1.5c and d. The curves showed no changes in shape in comparison to the previously discussed ones, indicating a similar pseudocapacitive mechanism. The film deposited under the total applied charge of -0.6 C cm^{-2} still displayed the highest current response in the CV curves, Figure 3.1.5c. The specific capacitance values calculated from the CD curves were 338 F g^{-1} and 334 F g^{-1} for the films deposited at total applied charge of -0.3 C cm^{-2} and -0.9 C cm^{-2}, respectively. These values were lower than that the ones determined for the films deposited with -0.6 C cm^{-2}. The formation of less nanoparticles attached nanoflakes and nanoparticles completely covered nanoflakes, resulted in decreased surface area/porosity, leading to lower specific capacitance values. In comparison with the recently reported two steps electrodeposition process for fabricating hierarchical structures of nanoflakes/nanoflakes [40], the results obtained in this work, using a simple one step electrodeposition route, suggested that hierarchical structures based on nanoflakes can also be obtained through optimization of the electrodeposition parameters. It should be mentioned that, via anodic electrodeposition, multilayer nanoflakes were formed when varying the total applied charge rather than forming the hierarchical nanoflakes/nanoflakes structure as demonstrated in the present work [41].

3.1.3.5. Structural studies

The structural studies were carried out on the optimized representative films: electrodeposited at -1.3 V with a total applied charge of -0.6 C cm^{-2}, from the 0.25 M electrolyte and post-thermal annealing at 200 °C. These films were the ones exhibiting the highest specific capacitance values amongst the films deposited in this work. Raman, FTIR and SQUID were used for the structural studies.

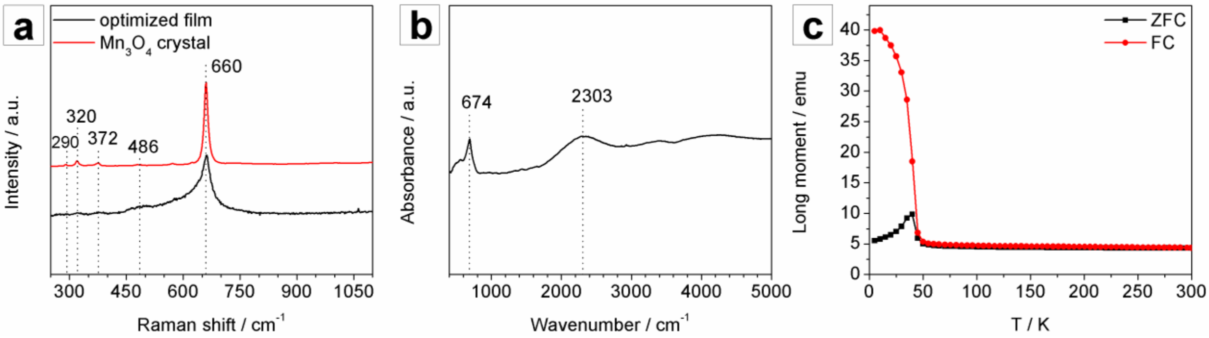

Figure 3.1.6. Raman spectrum (a), FTIR spectrum (b) and zero field cool and field cool curves (c) of the optimized film.

Figure 3.1.6 showed the Raman spectrum, FTIR spectrum and zero field cool (ZFC) and field cool (FC) curves of the optimized film. For comparison, the Raman spectrum of the Mn_3O_4 crystal is also added in the Raman spectra plot as reference. The Mn_3O_4 single crystal reference displayed five Raman bands at 290 cm^{-1}, 320 cm^{-1}, 372 cm^{-1} and 486 cm^{-1}, and 660 cm^{-1}, which can be assigned to T_{2g} symmetry, E_g symmetry, T_{2g} symmetry, and A_{1g} symmetry “breathing” modes [42]. The Raman spectrum of the optimized sample showed an intense and broad band at 660 cm^{-1}, which matched very well with the intense band of the reference spectrum. Other small shoulder in the Raman spectrum of the films could also be observed at positions similar to that of the reference spectrum. Even though, it is not completely matched in intensity, the recorded Raman spectra can be assigned to the Mn_3O_4 Raman spectra. The difference can be due to the nanocrystalline nature of the film, leading to the broadening and reducing intensity of the Raman bands as reported elsewhere in literature [43, 44].

The FTIR spectrum showed two bands at positions of 674 cm^{-1} and 2303 cm^{-1}. The band at 2303 cm^{-1} was due to to the C=O vibration of absorbed CO_2 from air [45]. The band at 674 cm^{-1} was assigned to

Mn-O vibration mode at the MnO_6 octahedral sites of Mn_3O_4 [46]. Therefore, this result is in good agreement with the Raman ones.

ZFC and FC curves were performed in magnetic field of 500 Oe. The ZFC was measured by decreasing temperature from 300 K to 5 K in zero field, then the signal was recorded when temperature increased from 5 K to 300 K in the magnetic field of 500 Oe. While, the FC curve was measured in magnetic field of 500 Oe when decreasing temperature from 300 K to 5 K. ZFC-FC curves revealed the Curie temperature of 42 K, corresponding the transition temperature of Mn_3O_4 [47].

Thus, the above structural studies are all in good agreement, revealing the formation of the FCT Mn_3O_4 phase.

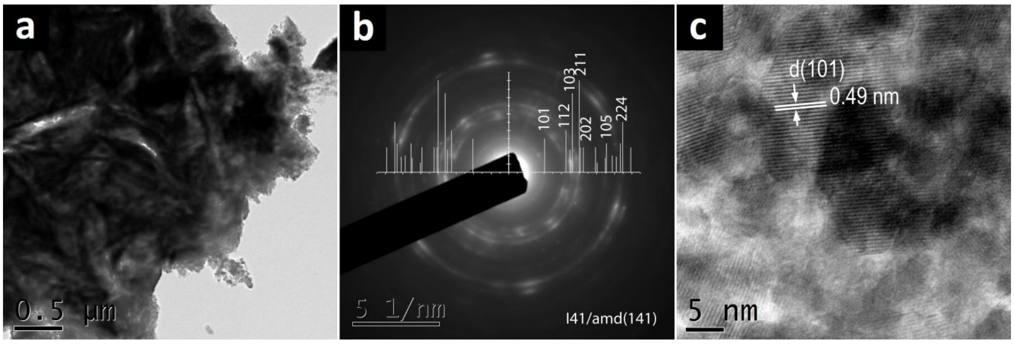

Figure 3.1.7. (a) TEM image, (b) SAED pattern and (c) HR-TEM image of the optimized sample.

The structural details were studied by TEM and the results are presented in Figure 3.1.7. The low magnification TEM image, Figure 3.1.7a, revealed the presence of nanoflaked particles, in agreement with the FEG-SEM results. Selected area electron diffraction (SAED) pattern, Figure 3.1.7b, was composed of diffraction rings, indicating the polycrystalline nature of the film. The diffraction rings can be well indexed with the diffraction from (101), (112), (103), (211), (202), (105) and (224) lattice planes of FCT Mn_3O_4 (ICDD-00-024-0734). The high resolution TEM (HRTEM) image, Figure 3.1.7b, showed randomly distributed nanocrystals evidencing lattice spacing of 0.49 nm, which corresponds to (101) planes of FCT Mn_3O_4. The crystal size was approximately 20 nm. The TEM results are in good agreement with the previous characterization results, confirming the formation of the nanostructured Mn_3O_4 film.

3.1.3.6. Pseudocapacitive performance

To further evaluate pseudocapacitive performance of the optimized film, CV at scan rates varying from 10 mV s^{-1} to 100 mV s^{-1} and CD with current density up to 10 A g^{-1} were performed. The results are presented in Figure 3.1.8a and b. CV curves showed that the main redox peaks shifted and that the current density increased with the scan rate, indicating the quasi-reversibility of the redox reactions and thus the good pseudocapacitive behavior [48]. The potential difference, between the anodic peak and the cathodic peak, increased due to polarization of the electrode at increased scan rates. The potential differences between the anodic peaks or cathodic peaks at scan rates of 10 mV s^{-1} and 100 mV s^{-1} was approximately 100 mV, indicating the low polarization of the electrode. The shape of the cyclic voltamograms was almost preserved up to the highest scan rate of 100 mV s^{-1}, indicating the easy diffusion of ions in the electrolyte into the film.

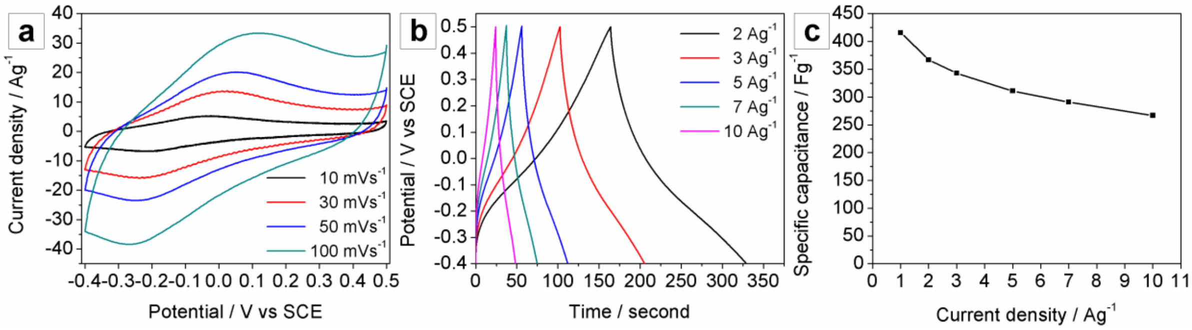

Figure 3.1.8. Pseudocapacitive performance of the optimized film. (a) Cyclic voltammetry curves at different scan rate, (b) charge-discharge curves at different current density and (c) dependence of specific capacitance with current density.

CD results at different current density, which represent the rate capability of the film, showed that the potential drop was more marked and the discharge time decreased when the current density increased, thereby reducing the specific capacitance. The specific capacitance depended upon the applied current density, Figure 3.1.8c, and showed a specific capacitance of 64% when the current increased from 1 A g^{-1} to 10 A g^{-1}, highlighting the good rate capability of the film. The specific capacitance reduction was probably consequence of inaccessible active sites at high-applied current densities.

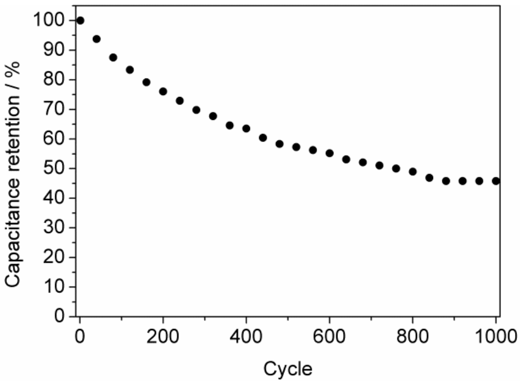

Figure 3.1.9. Cycling stability with continuous charge-discharge at current density of 1 A g^{-1} of the optimized film.

To evaluate the possibility of using the electrodeposited manganese oxide film for pseudocapacitor electrodes working in alkaline media, the continuous CD cycling was carried out on the optimized film for 1000 cycles. The results are presented in Figure 3.1.9 that showed a capacitance retention of 46% after 1000 cycles, corresponding to a specific capacitance value of 196 F g^{-1}. The capacitance retention was rather poor, probably due to occurrence of irreversible redox reactions. Nevertheless, the specific capacitance value determined after 1000 cycles was still comparable with values reported in other work, before charge-discharge cycling, for manganese oxide based electrodes working in neutral electrolyte such as Na_2SO_4 and Li_2SO_4 [6]. Thus, the results pin point the applicability of the electrodeposited manganese oxides as pseudocapacitor electrodes working in alkaline electrolytes.

3.1.4. Conclusions

In summary, the cathodic electrodeposition of manganese oxides using nitrate-based electrolyte was studied, optimized and characterized, aiming to use these oxides as pseudocapacitive electrodes working in alkaline media. Morphological changes were observed when varying the electrodeposition parameters and the post thermal annealing temperature; the correlation between the surface morphology and electrochemical response was investigated and discussed. *Via* the optimized one-step electrodeposition process, directly on the current collector, the formation of hierarchical Mn_3O_4 nanoparticles/nanoflakes morphology was obtained, exhibiting high specific capacitance of 416 F g^{-1} at 1 A g^{-1} in 1 M NaOH. The capacitance retention was 64 % when increasing the current density from 1 A g^{-1} to 10 A g^{-1}. The specific capacitance value obtained after 1000 continuous CD cycles was 196 F g^{-1}. The results demonstrated the applicability of manganese oxide as pseudocapacitive electrodes for redox supercapacitors operating in alkaline media.

Acknowledgements

The authors would like to thank Fundação para a Ciência e Tecnologia (FCT) for the funding under the contract PTDC/CTM-MET/119411/2010 and UID/QUI/00100/2013, IDS-FunMat Erasmus Mundus PhD School, and the European COST Action MP1004. We also thank E. Eyraud (Institut Néel), C. Jimenez, O. Chaix and L. Rapenne (LMGP) for their supports for SQUID, FTIR, Raman and TEM experiments.

References

[1] P. Simon, Y. Gogotsi, Materials for Electrochemical Capacitors, Nat Mater, 7 (2008) 845-854.

[2] A. Manthiram, Y. Fu, Y.-S. Su, In Charge of the World: Electrochemical Energy Storage, The Journal of Physical Chemistry Letters, 4 (2013) 1295-1297.

[3] J.R. Miller, P. Simon, Electrochemical Capacitors for Energy Management, Science, 321 (2008) 651-652.

[4] T. Nguyen, S. Eugenio, M. Boudard, L. Rapenne, M.J. Carmezim, T. Moura Silva, M.F. Montemor, Hybrid nickel manganese oxide nanosheets-3D metallic dendrites percolation network electrodes for high-rate electrochemical energy storage, Nanoscale, (2015).

[5] W. Wei, X. Cui, W. Chen, D.G. Ivey, Manganese Oxide-based Materials as Electrochemical Supercapacitor Electrodes, Chem. Soc. Rev., 40 (2011) 1697-1721.

[6] S.L. Brock, N. Duan, Z.R. Tian, O. Giraldo, H. Zhou, S.L. Suib, A review of porous manganese oxide materials, Chemistry of Materials, 10 (1998) 2619-2628.

[7] M.M. Thackeray, C.S. Johnson, J.T. Vaughey, N. Li, S.A. Hackney, Advances in manganese-oxide ‘composite’electrodes for lithium-ion batteries, Journal of Materials Chemistry, 15 (2005) 2257-2267.

[8] W.S. Seo, H.H. Jo, K. Lee, B. Kim, S.J. Oh, J.T. Park, Size‐dependent magnetic properties of colloidal Mn_3O_4 and MnO nanoparticles, Angewandte Chemie International Edition, 43 (2004) 1115-1117.

[9] J. Ni, W. Lu, L. Zhang, B. Yue, X. Shang, Y. Lv, Low-temperature synthesis of monodisperse 3D manganese oxide nanoflowers and their pseudocapacitance properties, J. Phys. Chem. C, 113 (2008) 54-60.

[10] P. Yu, X. Zhang, D. Wang, L. Wang, Y. Ma, Shape-controlled synthesis of 3D hierarchical MnO_2 nanostructures for electrochemical supercapacitors, Crystal Growth and Design, 9 (2008) 528-533.

[11] W. Li, Q. Liu, Y. Sun, J. Sun, R. Zou, G. Li, X. Hu, G. Song, G. Ma, J. Yang, MnO_2 ultralong nanowires with better electrical conductivity and enhanced supercapacitor performances, J. Mater. Chem., 22 (2012) 14864-14867.

[12] H. Jiang, T. Zhao, J. Ma, C. Yan, C. Li, Ultrafine manganese dioxide nanowire network for high-performance supercapacitors, Chem. Commun., 47 (2011) 1264-1266.

[13] D. Zheng, S. Sun, W. Fan, H. Yu, C. Fan, G. Cao, Z. Yin, X. Song, One-step preparation of single-crystalline β-MnO_2 nanotubes, J. Phys. Chem. B, 109 (2005) 16439-16443.

[14] W. Xiao, H. Xia, J.Y. Fuh, L. Lu, Growth of single-crystal α-MnO_2 nanotubes prepared by a hydrothermal route and their electrochemical properties, Journal of Power Sources, 193 (2009) 935-938.

[15] B. Babakhani, D.G. Ivey, Anodic deposition of manganese oxide electrodes with rod-like structures for application as electrochemical capacitors, Journal of Power Sources, 195 (2010) 2110-2117.

[16] S. Chou, F. Cheng, J. Chen, Electrodeposition synthesis and electrochemical properties of nanostructured γ-MnO_2 films, Journal of Power Sources, 162 (2006) 727-734.

[17] C.-C. Hu, T.-W. Tsou, Ideal capacitive behavior of hydrous manganese oxide prepared by anodic deposition, Electrochemistry Communications, 4 (2002) 105-109.

[18] G.H.A. Therese, P.V. Kamath, Electrochemical Synthesis of Metal Oxides and Hydroxides, Chemistry of Materials, 12 (2000) 1195-1204.

[19] J. Wei, N. Nagarajan, I. Zhitomirsky, Manganese oxide films for electrochemical supercapacitors, Journal of materials processing technology, 186 (2007) 356-361.

[20] J. Duay, S.A. Sherrill, Z. Gui, E. Gillette, S.B. Lee, Self-Limiting Electrodeposition of Hierarchical MnO_2 and $M(OH)_2/MnO_2$ Nanofibril/Nanowires: Mechanism and Supercapacitor Properties, ACS Nano, (2013).

[21] H. Xia, J. Feng, H. Wang, M.O. Lai, L. Lu, MnO_2 nanotube and nanowire arrays by electrochemical deposition for supercapacitors, Journal of Power Sources, 195 (2010) 4410-4413.

[22] M.-J. Deng, J.-K. Chang, C.-C. Wang, K.-W. Chen, C.-M. Lin, M.-T. Tang, J.-M. Chen, K.-T. Lu, High-performance electrochemical pseudo-capacitor based on MnO_2 nanowires/Ni foam as electrode with a novel Li-ion quasi-ionic liquid as electrolyte, Energy & Environmental Science, 4 (2011) 3942-3946.

[23] X. Lang, A. Hirata, T. Fujita, M. Chen, Nanoporous metal/oxide hybrid electrodes for electrochemical supercapacitors, Nature Nanotechnology, 6 (2011) 232-236.

[24] H. Zhang, G. Cao, Z. Wang, Y. Yang, Z. Shi, Z. Gu, Growth of manganese oxide nanoflowers on vertically-aligned carbon nanotube arrays for high-rate electrochemical capacitive energy storage, Nano Lett., 8 (2008) 2664-2668.

[25] J. Liu, J. Essner, J. Li, Hybrid supercapacitor based on coaxially coated manganese oxide on vertically aligned carbon nanofiber arrays, Chemistry of Materials, 22 (2010) 5022-5030.

[26] B. Messaoudi, S. Joiret, M. Keddam, H. Takenouti, Anodic Behaviour of Manganese in Alkaline Medium, Electrochimica Acta, 46 (2001) 2487-2498.

[27] T. Nguyen, M. Boudard, L. Rapenne, O. Chaix-Pluchery, M.J. Carmezim, M.F. Montemor, Structural evolution, magnetic properties and electrochemical response of $MnCo_2O_4$ nanosheet films, RSC Adv., 5 (2015) 27844-27852.

[28] L. Xu, Y.-S. Ding, C.-H. Chen, L. Zhao, C. Rimkus, R. Joesten, S.L. Suib, 3D Flowerlike α-Nickel Hydroxide with Enhanced Electrochemical Activity Synthesized by Microwave-assisted Hydrothermal Method, Chemistry of Materials, 20 (2007) 308-316.

[29] N. Nagarajan, H. Humadi, I. Zhitomirsky, Cathodic electrodeposition of MnO_x films for electrochemical supercapacitors, Electrochimica Acta, 51 (2006) 3039-3045.

[30] X. Liu, S. Shi, Q. Xiong, L. Li, Y. Zhang, H. Tang, C. Gu, X. Wang, J. Tu, Hierarchical $NiCo_2O_4$@ $NiCo_2O_4$ Core/shell Nanoflake Arrays as High-Performance Supercapacitor Materials, ACS Appl. Mater. Interfaces, 5 (2013) 8790-8795.

[31] Z.-P. Feng, G.-R. Li, J.-H. Zhong, Z.-L. Wang, Y.-N. Ou, Y.-X. Tong, MnO_2 multilayer nanosheet clusters evolved from monolayer nanosheets and their predominant electrochemical properties, Electrochemistry Communications, 11 (2009) 706-710.

[32] M. Kim, X. Chen, X. Wang, C. Nelson, R. Budakian, P. Abbamonte, S. Cooper, Pressure and field tuning the magnetostructural phases of Mn_3O_4: Raman scattering and x-ray diffraction studies, Phys. Rev. B, 84 (2011) 174424.

[33] J. Zuo, C. Xu, Y. Liu, Y. Qian, Crystallite size effects on the Raman spectra of Mn_3O_4, Nanostructured Materials, 10 (1998) 1331-1335.

[34] T. Nguyen, M. Boudard, L. Rapenne, M.J. Carmezim, M.F. Montemor, Morphological changes and electrochemical response of mixed nickel manganese oxides as charge storage electrodes, Journal of Materials Chemistry A, 3 (2015).

[35] H.B. Li, M.H. Yu, F.X. Wang, P. Liu, Y. Liang, J. Xiao, C.X. Wang, Y.X. Tong, G.W. Yang, Amorphous Nickel Hydroxide Nanospheres with Ultrahigh Capacitance and Energy Density as Electrochemical Pseudocapacitor Materials, Nat Commun, 4 (2013).

[36] S. Gnanam, V. Rajendran, Synthesis of CeO_2 or α–Mn_2O_3 nanoparticles via sol–gel process and their optical properties, Journal of sol-gel science and technology, 58 (2011) 62-69.

[37] N. Wang, L. Guo, L. He, X. Cao, C. Chen, R. Wang, S. Yang, Facile Synthesis of Monodisperse Mn_3O_4 Tetragonal Nanoparticles and Their Large ‐ Scale Assembly into Highly Regular Walls by a Simple Solution Route, Small, 3 (2007) 606-610.

[38] T.P. Gujar, V.R. Shinde, C.D. Lokhande, W.-Y. Kim, K.-D. Jung, O.-S. Joo, Spray deposited amorphous RuO_2 for an effective use in electrochemical supercapacitor, Electrochemistry Communications, 9 (2007) 504-510.

3.2. Hydrogen bubbling-induced micro/nano porous MnO_2 electrodes for electrochemical energy storage

Tuyen Nguyen[a,b], Michel Boudard[b], M. João Carmezim[a,c], M. Fátima Montemor[a]

[a] CQE - Centro de Química Estrutural, Instituto Superior Técnico, Universidade de Lisboa, 1049-001 Lisboa, Portugal.

[b] LMGP, Univ. Grenoble Alpes, CNRS, F-38000 Grenoble, France.

[c] ESTSetúbal, Instituto Politécnico de Setúbal, 1959-007 Setúbal, Portugal.

Micro/nano porous manganese oxide MnO_2 films for electrochemical energy storage electrodes were deposited by cathodic electrodeposition over stainless steel using hydrogen bubbling as a dynamic template. The morphology of the resulting film consisted of nanoporous MnO_2 crumpled nanosheets and homogeneously distributed micro-holes. The electrochemical studies revealed that the micro/nano porous MnO_2 electrodes displayed good pseudocapacitive response. The specific capacitance of the electrode was 305 F g^{-1} at 1 A g^{-1} in a potential window of 1 V, and the rate capability was 61% when the current density increased from 1 A g^{-1} to 10 A g^{-1}.

Keywords: manganese oxides, nanosheets, pseudocapacitors, hydrogen bubbles, micro/nano porous electrodes

3.2.1. Introduction

Manganese oxides are being considered as prospective materials for fabricating electrodes for energy storage because they show good pseudocapacitive performance (which results in increased energy density in aqueous electrolytes), low cost, natural abundance and environmental friendliness [1]. The electrochemical response of the manganese oxide-based electrodes is characterized by nearly rectangular cyclic voltammograms in a potential window of approximately 1 V, in aqueous electrolytes as a consequence of their multi-valence states [2]. The formation of nanostructured morphologies with high porosity has been considered as one of the most important parameters for enhanced pseudocapacitive performance [3]. Therefore, a rational design of porous nanostructured manganese oxide electrodes is still necessary for optimizing their pseudocapacitive performance [4, 5]. Moreover, due to its extensive applications in other areas such as batteries, catalysts and magnetism, the preparation methods of manganese oxides have received considerable attention in the research community [6-8].

Electrodeposition have been widely used to prepare porous manganese oxide films for electrochemical energy storage electrodes in supercapacitors [2]. In the anodic regime, the films can be formed by oxidation of Mn^{2+} to Mn^{4+} [9, 10]. In the cathodic regime, they can be formed either by reaction of Mn^{2+} with generated OH^- and post oxidation or by the reduction of Mn^{7+} to Mn^{4+} [11, 12]. Nanostructured manganese oxides films composed of nanosheets [13], nanorods [14], nanoflowers [15] and nanowires arrays/networks [16] have been reported as materials displaying good pseudocapacitive performance. Hard templates, such as anodic aluminum membranes, were also used to electrodeposit porous manganese oxide nanowires arrays [17].

Cathodic electrodeposition, involving hydrogen evolution, has been used to create metallic foams of Ni, Cu, Pd, Ag, Pt, and Au [18, 19]. The hydrogen bubbles that continuously evolve from the substrate prevent the deposition of the metal on these sites, therefore acting as a dynamic negative template that leads to the formation of porous metallic foams with controlled micro-scale pores [20]. Although metallic foams with micro pore size induced by hydrogen bubbling have been widely published for application mainly in electrocatalysis, the possibility of applying this approach to deposit metal oxides for application in supercapacitors is still an open discussion. Generally, it is expected that hierarchical structures of metal oxides in general, and of manganese oxides in particular, characterized by well-defined porosity, will provide superior pseudocapacitive performance [18, 19].

Thus, this work aims at using the hydrogen bubbling as dynamic templates to electrodeposit micro/nano porous manganese oxide films to be used as electrochemical energy storage electrodes. Results on the formation and characterization of the multi-scale porous oxide films, and on the electrochemical response will be presented.

3.2.2. Experimental

The potentiostatic electrodeposition was performed in a conventional three-electrode electrochemical cell, at room temperature, using Radiometer Voltalab PGZ 100 Potentiostat with stainless steel (AISI 304, Goodfellow) as a substrate (working electrode), platinum foil as counter electrode and the saturated calomel electrode (SCE) as reference electrode. The electrolytes were 0.1 M $MnSO_4$ + 0.1 M Na_2SO_4. Deposition potentials and applied charges were varied to control the surface morphology of the electrodeposited films. All the potentials referred in this work are *vs.* SCE. After the electrodeposition process, the films were stabilized by potential cycling in Na_2SO_4 0.1 M for 10 cycles. The mass of the deposited films was estimated by carefully weighting substrates before and after electrodeposition using Sartorius micro-balance with precision of 0.01 mg.

Field emission gun scanning electron microscopy (FEG-SEM, JEOL 7001F microscope) was used for studying the surface morphology of the deposited films. Topographic images were obtained with an atomic force microscope (AFM, Nanosurf Easyscan microscope) working in tapping mode. Raman spectroscopy (Horiba/Jobin Yvon LabRam spectrometer) was carried out for studying the structural characteristics of the formed films, using 632.8 nm He-Ne laser exciting over an area of 1 μm^2. The structural details of the films were studied by transmission electron microscopy (TEM, JEOL JEM-2010 microscope) working at an acceleration voltage of 200 KeV.

The electrochemical performance of the electrodes was determined by cyclic voltammetry (CV) and charge-discharge (CD) in 1 M Na_2SO_4 electrolytes. Electrochemical impedance spectroscopy (EIS, Solartron Potentiostat) was performed with applied voltage amplitude of 10 mV and frequency scanning from 5 mHz to 10 kHz at an open circuit potential. All the electrochemical tests were carried out in the conventional three-electrode cell as described above using the films deposited on steel as working electrodes.

The specific capacitance (F g^{-1}) of the films was calculated from the CD curves using the formula:

$$C = \frac{It}{\Delta V} \tag{3.2.1}$$

where I, t, ΔV are the CD current density (A g^{-1}), the discharge time (s) and the working potential range (V), respectively.

3.2.3. Results and Discussion

Figure 3.2.1 shows FEG-SEM images of the manganese oxide films deposited at different potentials and total applied charges (TACs). The film deposited at -1.1 V with a TAC of -1.1 C cm^{-2} (Figure 3.2.1a) presents a smooth and continuous surface morphology, at the magnification used to obtain the image, thus revealing a homogeneous electrodeposited film. At -1.3 V (TAC of -1.1 C cm^{-2}, Figure 3.2.1b) the formation of micro-holes with diameters in the range of 3-20 µm can be observed. The micro-holes, induced by the hydrogen evolution present an averaged diameter around 9 µm and are uniformly distributed over the surface. At -1.5 V (TAC of -1.1 C cm^{-2}, Figure 3.2.1c) the micro-holes increase in size and its diameters are in the range of 12-60 µm; the average hole diameter is approximately 30 µm. When the applied potential is more negative than -1.5 V, there is formation of non-adherent films, probably due to the extensive hydrogen evolution at higher applied potential.

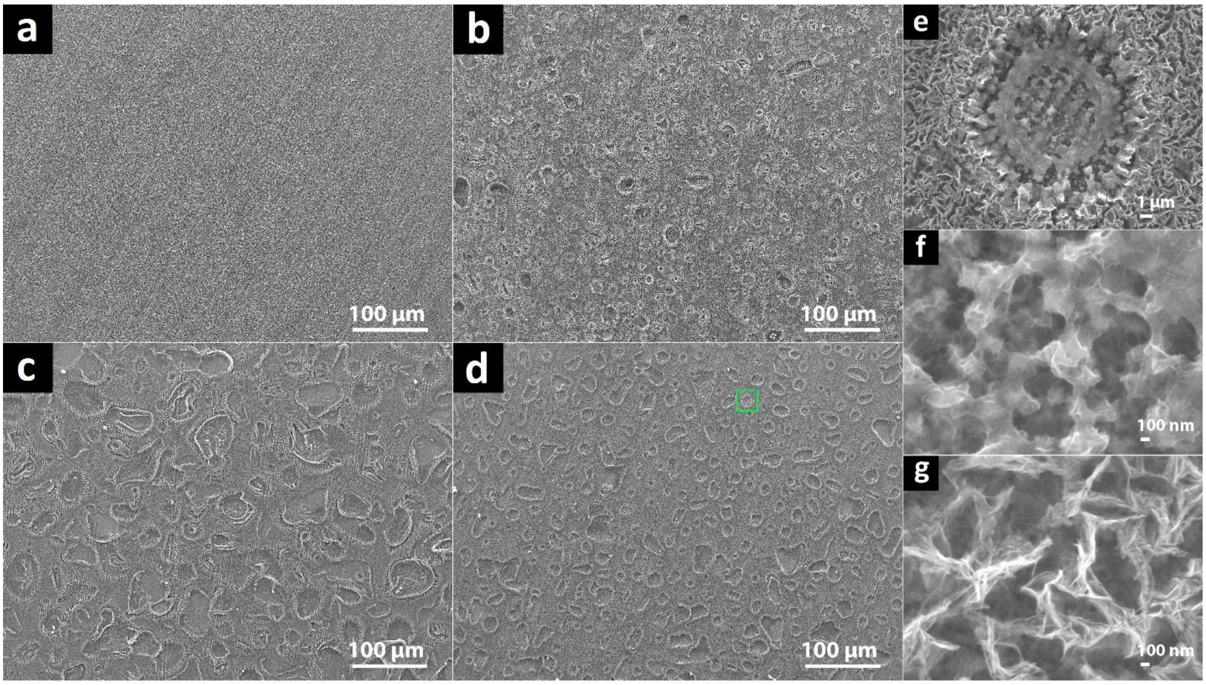

Figure 3.2.1. FEG-SEM images of the films deposited at different potentials of (a) -1.1 V, (b) -1.3 V, (c) -1.5 V under a total applied charge of -1.1 C cm^{-2}, and (d) deposited at potential of -1.5 V under a total applied charge of -0.55 C cm^{-2}. (e) FEG-SEM image of a micro-hole marked by a green rectangular, and high magnified images (f) inside and (g) outside the micro-hole.

The TAC was decreased to -0.55 C cm^{-2}, at the applied potential of -1.5 V (Figure 3.2.1d). The resulting film reveals well-defined micro-holes in the range of 10-50 μm with an average diameter of 18 μm. The FEG-SEM images of a representative micro-hole are shown in Figure 3.2.1e-g. The micro-holes are characterized by the presence of nanoparticles (Figure 3.2.1f) in its inner part whereas the surrounding region outside it is composed of crumpled nanosheets (Figure 3.2.1g) forming a nanoporous structure. The nanoparticles inside the micro-holes cannot grow into nanosheets probably due to the hydrogen evolution.

Considering the electrodeposition conditions, the film electrodeposition is based on the generation of hydroxyl ions (OH$^-$) via water electrolysis in cathodic regime:

$$2H_2O + 2e^- \leftrightarrow H_2\,(gas) + 2OH^- \qquad (3.2.2)$$

Then, it is followed by the reaction of Mn^{2+} ions with generated OH^- to form $Mn(OH)_2$ deposited on the substrates, according to:

$Mn^{2+} + 2OH^- \leftrightarrow Mn(OH)_2$ (solid) (3.2.3)

The deposited $Mn(OH)_2$ is expected to oxidize when exposed to air to form manganese oxide. However, in this work, this process was performed by carrying out ten voltammetry cycles after the electrodeposition step. This procedure also contributed to the stabilization of the electrodeposited electrode.

It should be noted that by applying cathodic potential, the reduction reaction of Mn^{2+} to Mn can also be taken place:

$Mn^{2+} + 2e^- \leftrightarrow Mn$ (solid) (3.2.4)

However, the standard electrode potential (SEP) of water electrolysis is −0.827 V *vs.* standard hydrogen electrode (SHE) and that of Mn^{2+} reduction reaction is −1.185 V *vs.* SHE [21]. In terms of thermodynamics, the cathodic reactions with less negative potentials are favored to take place [11]. Thus, the Mn^{2+} reduction reaction was inhibited, and the reaction (2) and (3) occurred in the electrodeposition process. This principle has been applied for electrodeposition of $Ni(OH)_2$, $Co(OH)_2$ and mixed hydroxides for supercapacitor electrodes, in these cases nitrate reduction reactions (SEP of 0.01 V *vs.* SHE [11], whereas those of Ni^{2+} and Co^{2+} reduction reactions to Ni and Co are −0.25 and −0.28 V *vs.* SHE [21], respectively) are concerned to generate OH^- sources [22, 23].

While the micro-holes are formed due to the hydrogen evolution, the formation of nanosheets can be due to the preferential growth of layered hydroxides as proposed previously in literature [23, 24].

Thus, by optimizing the electrodeposition process, using hydrogen bubbling as dynamic template, it is possible to fabricate a multi-scale micro/nano (hierarchical) porous manganese oxide films. Recent work have highlighted that the formation of hierarchical structured electrode composed of micro and nano pore sizes is crucial for the enhanced diffusion of ions, and thereby for an optimized pseudocapacitive response [25, 26]. Thus, the obtained manganese oxide film with hierarchical structure is expected to display good pseudocapacitive response.

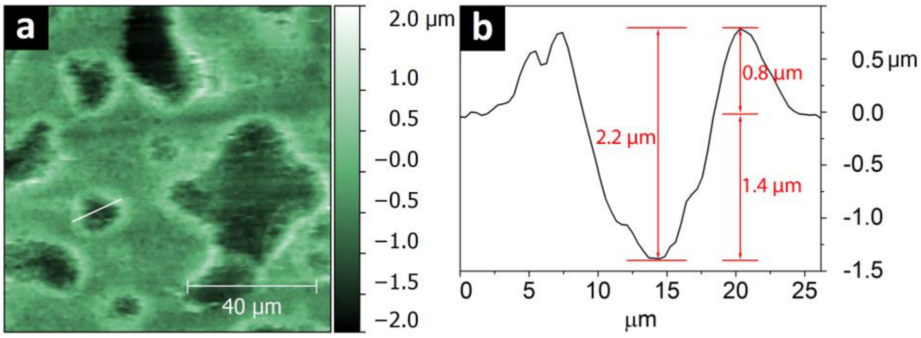

Figure 3.2.2. (a) Tapping mode AFM topography image of the representative film obtained in 100 x 100 μm^2 region. Color scale on the right part indicates the out of plane scale. (b) Height profile of a corresponding white line in the image.

The AFM topography image of a representative film (deposited at -1.5 V, TAC of -0.55 C cm^{-2}) measured in a 100 x 100 μm^2 area is shown in Figure 3.2.2a. The image confirms the presence of the micro-holes previously identified by the FEG-SEM analysis. The height profile of the corresponding white line in the image depicted in Figure 3.2.2b reveals that the micro-holes depth is about 2.2 μm. The surface surrounding the micro-holes is higher than other areas of the surface; the difference is about 0.8 μm. This difference shows that the borders of the hole are thicker probably due to displacement of the deposited material during hydrogen evolution. Thus, the result further confirmed the formation of micro-architecture in the manganese oxide electrode.

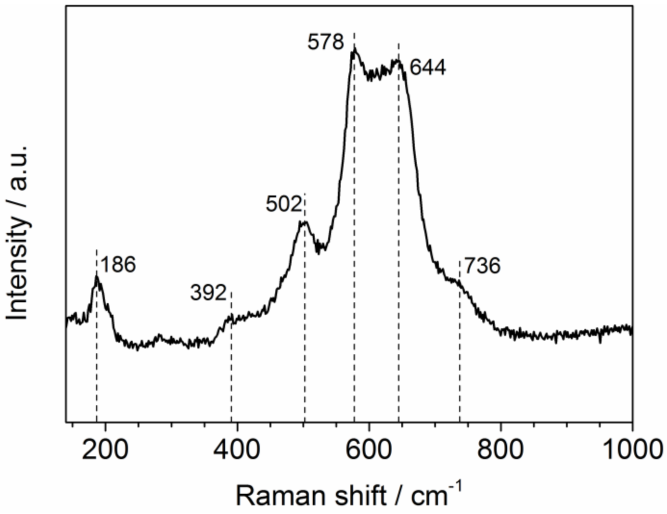

Figure 3.2.3. Typical Raman spectrum of the manganese oxide film. Important Raman bands are highlighted. Vertical lines are only for visual guide.

The Raman spectrum of the film (Figure 3.2.3) reveals the formation of the MnO_2 phase [27-29]. The broadening of the bands accounts for the nanocrystalline nature of the MnO_2 film. Two intense bands, at 578 cm^{-1} and 644 cm^{-1}, can be assigned to A_g symmetry mode from Mn-O breathing vibrations in MnO_6 octahedra [29]. The weak bands at 186, 392, 502 and 736 cm^{-1} can be related to an external vibration due to the translational motion of the MnO_6 octahedra, the Mn−O bending vibrations, the stretching vibrations of MnO_6 octahedra, and the antisymmetric Mn−O stretching vibrations, respectively [29, 30].

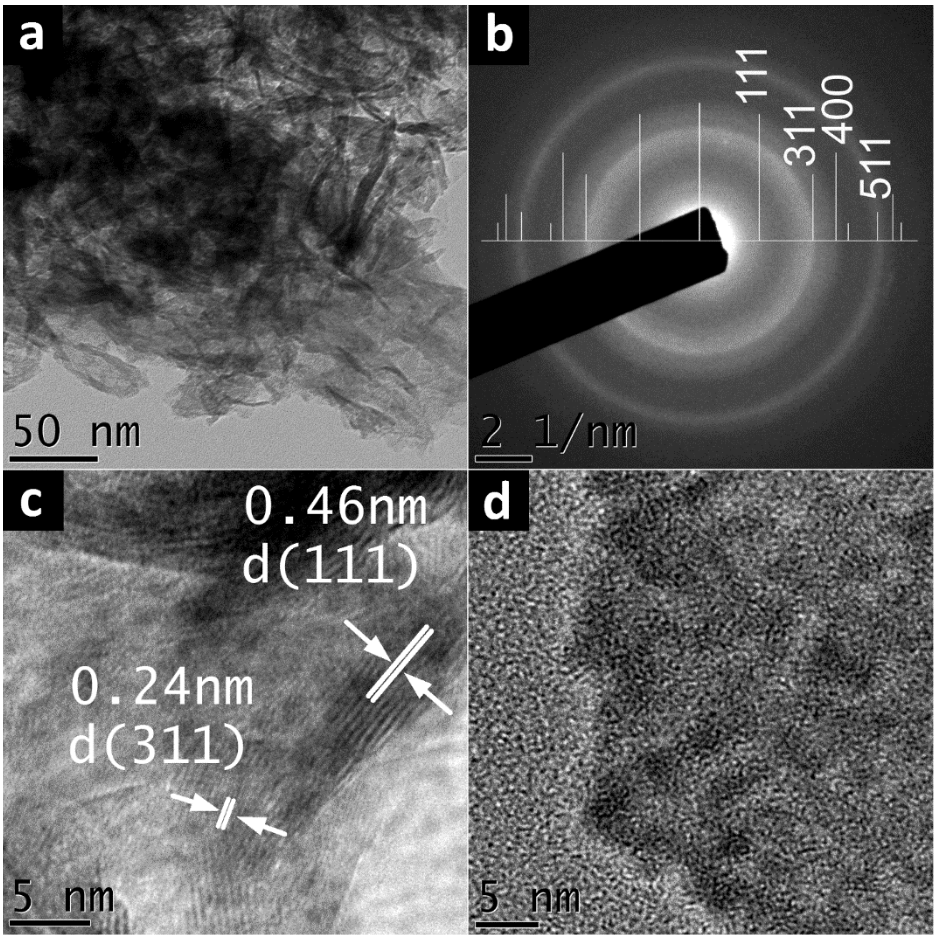

Figure 3.2.4. (a) Low magnification TEM image, (b) SAED pattern and (c,d) HRTEM images measuring at different spots of a representative nanosheet.

The representative nanosheets were studied by transmission electron microscopy (TEM) and the results are shown in Figure 3.2.4. The low magnified TEM image (Figure 3.2.4a) evidences the presence of very thin nanosheets that are in a crumpled form, in good agreement with FEG-SEM observations. The selected area electron diffraction (SAED) pattern (Figure 3.2.4b) presents broad diffraction rings, indicating low crystallinity and/or the partial amorphous nature of the nanosheets. The intense rings in the pattern can be assigned to the (111), (311), (400) and (511) diffraction lines of MnO_2 phase (ICDD no. 00-042-1169) The lattice fringes, with spacing of about 0.46 nm and 0.24 nm, are visible in the high resolution TEM (HRTEM) image (Figure 3.2.4c) corresponding to (111) and (311) lattice planes of the MnO_2 structure. The HRTEM image extracted from a different area of the film in Figure 3.2.4d reveals a disordered structure without any evident lattice fringes, which probably correlates to the diffuse SAED rings. Thus, TEM results are in agreement with Raman analysis, indicating the formation of low crystallinity and partial amorphous nanosheets.

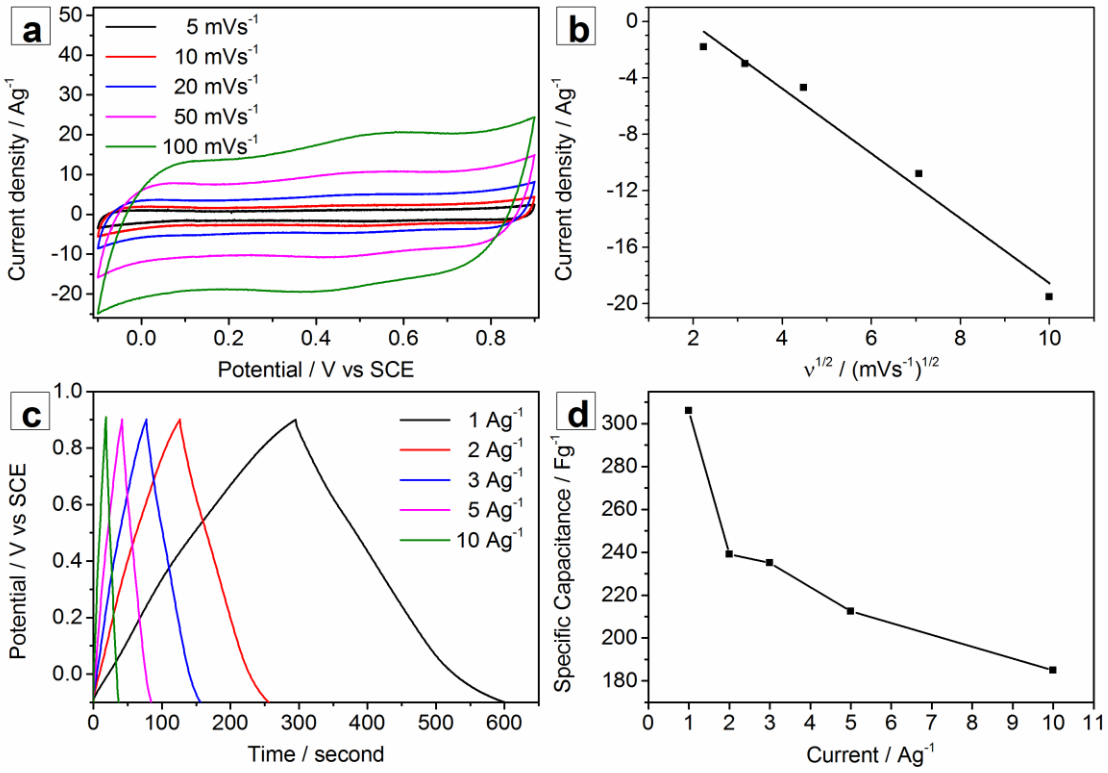

Figure 3.2.5. (a) CV with different scan rates and (b) the relation of cathodic peak current density *vs.* the square root of scan rate. (c) Charge-discharge at different current densities and (d) rate capability of the film deposited at -1.5 V (TAC of -0.55 C cm^{-2}).

To evaluate the electrochemical response of the micro/nano porous manganese oxide film (deposited at -1.5 V, TAC of -0.55 C cm^{-2}), CV and CD tests were carried out, respectively at different scan rates ranging from 5 mV s^{-1} to 100 mV s^{-1} and at different constant currents ranging from 1 A g^{-1} to 10 A g^{-1} in the potential window between -0.1 and 0.9 V.

CV results in Figure 3.2.5a show that the electrode response is characterized by a nearly rectangular shape, stating the very good pseudocapacitive behaviour. The nearly rectangular shape of the CV curve results from the Faradic surface adsorption reaction (5) in the Na_2SO_4 neutral electrolyte as proposed elsewhere [2]:

$$(MnO_2)_{surface} + Na^+ + e^- \leftrightarrow (MnOONa)_{surface} \quad (3.2.5)$$

The broad redox peaks observed in CV curves can be due to the intercalation reaction (6) [31]:

$$MnO_2 + Na^+ + e^- \leftrightarrow MnOONa \quad (3.2.6)$$

The CD results are presented in Figure 3.2.5c. The nearly linear CD curves obtained are a consequence of the nearly rectangular cyclic voltammograms. The calculated specific capacitance value at 1 A g^{-1} is 305 F g^{-1}. The high specific capacitance values obtained in the micro/nano porous MnO_2 films confirm the advantage of the multi-scale porous architecture, facilitating the diffusion of electrolyte into the electrode. For comparison, the hierarchical MnO_2 nanofibril/nanowire array prepared using anodized aluminum oxide as a hard template [17] displayed specific capacitance values of 298 F g^{-1} at 1 A g^{-1} and hierarchical MnO_2/carbon nanotubes [32] displayed specific capacitance values of 223 F g^{-1} at 1 A g^{-1}. Thus, the present results indicate that the new MnO_2 micro/nano porous architecture induced by hydrogen bubbling is a promising route to fabricate MnO_2 based supercapacitor electrodes.

The CV results obtained at different scan rates, Figure 3.2.5a, show that the shapes of the cyclic voltamograms are almost preserved up to the highest scan rate of 100 mV s^{-1}, indicating the good diffusion of electrolyte ions into the film. The main redox peaks shift and the current density increases with the scan rate, indicating the good reversibility of the intercalation reactions and thus the good pseudocapacitive behavior [33]. The potential difference, between the anodic peak and the cathodic peak, increases with the scan rate due to polarization of the electrode. The cathodic current density peak *vs.* the square root of the scan rate in Figure 3.2.5b evidences a linear relation, indicating diffusion-controlled processes, thus confirming the involvement of the intercalation reactions in the redox peaks (2) [34].

Rate capability, which is an important parameter for evaluating the suitability of a material to work as an electrode for supercapacitors and electrochemical energy storage, was assessed from CD measurements with increasing applied currents up to 10 A g^{-1}, Figure 3.2.5c. The results show that the potential drop is more obvious and that the discharge time decreases when the current density increases, thereby reducing the specific capacitance. The specific capacitance depends upon the applied current density and Figure 3.2.5d shows that the specific capacitance retention is about 61% when the current increases from 1 A g^{-1} to 10 A g^{-1}. This result points out the good rate capability of the film. The decreased capacitance is probably due to increased Ohmic contributions and less accessible surface-active regions which become progressively excluded as the reaction rate is enhanced by the increasing current density.

The total specific capacitance includes the contribution of the Faradic surface adsorption and of the bulk Faradic intercalation reaction. To better understand the mechanisms of charge storage and the contribution of both processes for the total capacity, the cyclic voltamograms with different scan rates were fitted with a kinetic model proposed elsewhere [35, 36].

In this model the relationship between charge ($Q/Coulomb$) and the scan rate in cyclic voltamograms is described by the equations (4) and (5) as reported elsewhere [35]

$$Q = Q_{v=\infty} + constant\left(v^{-1/2}\right) \tag{3.2.4}$$

$$Q^{-1} = Q_{v=0}^{-1} + constant(v^{1/2}) \tag{3.2.5}$$

with $Q_{v=\infty}$ is the surface adsorption charge, which is the value at $v = \infty$. $Q_{v=0}$ is the total charge, which is the value at $v = 0$. Therefore, by plotting Q *vs.* $v^{-1/2}$, and Q^{-1} *vs.* $v^{1/2}$, the surface adsorption capacitance and the total capacitance can be retrieved from the y-axis intercepts, Figure 3.2.6a and b.

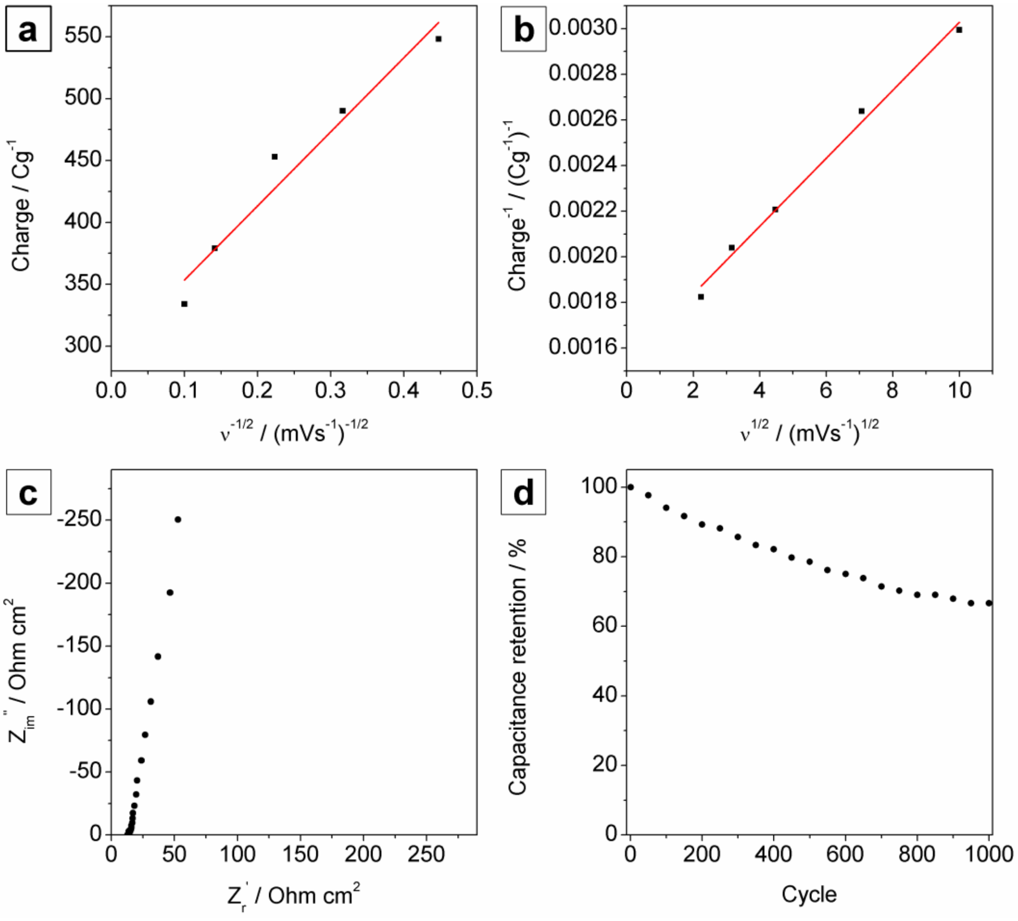

Figure 3.2.6. Kinetic analysis of the representative film: (a) The relation of charge (Q) vs. $v^{-1/2}$ and (b) of Q^{-1} vs. $v^{1/2}$. (c) Electrochemical impedance spectroscopy at open circuit potential and (d) charge-discharge cycling stability of the representative film at constant current of 5 A g^{-1} for 1000 cycles.

The calculation reveals that the contribution from the Faradic surface adsorption is about 45%, and the contribution from the intercalation reaction is about 55%. Thus, it indicates the almost equal contribution from both the reactions to the total charge storage, leading to the nearly rectangular cyclic voltamograms.

EIS measurements of the film are depicted in a Nyquist plot (Figure 3.2.6c) in a frequency domain, ranging from 5 mHz to 10 kHz. The intersect at the high frequency region of the plot with the real axis is the bulk resistance of the electrochemical system (including the electrolyte resistance since the measurement was performed using a 3 electrodes setup). It revealed a low value of 13 Ohm cm^2. The low bulk resistance values are probably due to the formation of multi-scale micro/nano porous structure.

The cycling stability of the micro/nano porous film was tested by continuous charge-discharge cycling for 1000 cycles at an applied current density of 5 A g^{-1}. Figure 3.2.6d shows that the specific capacitance retention after 1000 cycles is about 67%. In comparison with several published works [15, 37], this value is rather low, probably relating to the decreased adhesion of the electrode due to hydrogen evolution. Nevertheless, this stability is comparable with hierarchical structured Ni/Co oxide/hydroxides electrodes working in a narrower potential window of 0.5 V [38, 39]. Finally, considering the novel designed manganese oxide electrodes reported in this work, it could be a promising approach for further studying toward applications in pseudocapacitors and other-related fields.

3.2.4. Conclusions

In this work hydrogen bubbling was used as dynamic template to electrodeposit micro/nano porous manganese oxides electrodes with enhanced pseudocapacitive behavior. The micro/nano porous electrodes were composed of MnO_2 nanosheets and well-distributed micro-holes which porosity depends upon the applied potentials. The multi-scale porous MnO_2 electrode displayed very good pseudocapacitive response characterized by nearly rectangular cyclic voltammograms and nearly capacitive impedance response. The specific capacitance of the electrode attained 305 F g^{-1} under an applied current density of 1 A g^{-1}, and the rate capability was 61% when current density increased from 1 A g^{-1} to 10 A g^{-1}. Both the Faradic adsorption reactions and intercalation reactions contributed almost equally to the total pseudocapacitive response. The high specific capacitance obtained is due to the formation of multi-scale porous structure leading to the low diffusion resistance and bulk resistance.

Acknowledgements

We would like to thank Fundação para a Ciência e Tecnologia (FCT) for the funding under the contract PTDC/CTM-MET/119411/2010 & UID/QUI/00100/2013, IDS-FunMat Erasmus Mundus PhD School and the European COST Action MP1004. L. Rapenne (LMGP, Univ. Grenoble Alpes) is acknowledged for TEM measurements.

References

[1] G. Wang, L. Zhang, J. Zhang, A Review of Electrode Materials for Electrochemical Supercapacitors, Chem. Soc. Rev., 41 (2012) 797-828.

[2] W. Wei, X. Cui, W. Chen, D.G. Ivey, Manganese oxide-based materials as electrochemical supercapacitor electrodes, Chem. Soc. Rev., 40 (2011) 1697-1721.

[3] Q. Lu, J.G. Chen, J.Q. Xiao, Nanostructured Electrodes for High-Performance Pseudocapacitors, Angewandte Chemie International Edition, 52 (2013) 1882-1889.

[4] Y. Wang, Y. Xia, Recent Progress in Supercapacitors: From Materials Design to System Construction, Advanced Materials, 25 (2013) 5336-5342.

[5] B.L. Ellis, P. Knauth, T. Djenizian, Three-Dimensional Self-Supported Metal Oxides for Advanced Energy Storage, Advanced Materials, 26 (2014) 3368-3397.

[6] C. Zhu, G. Saito, T. Akiyama, A new $CaCO_3$-template method to synthesize nanoporous manganese oxide hollow structures and their transformation to high-performance $LiMn_2O_4$ cathodes for lithium-ion batteries, Journal of Materials Chemistry A, 1 (2013) 7077-7082.

[7] C. Fang, D. Zhang, S. Cai, L. Zhang, L. Huang, H. Li, P. Maitarad, L. Shi, R. Gao, J. Zhang, Low-temperature selective catalytic reduction of NO with NH_3 over nanoflaky MnO_x on carbon nanotubes in situ prepared via a chemical bath deposition route, Nanoscale, 5 (2013) 9199-9207.

[8] W.S. Seo, H.H. Jo, K. Lee, B. Kim, S.J. Oh, J.T. Park, Size ‐ dependent magnetic properties of colloidal Mn_3O_4 and MnO nanoparticles, Angewandte Chemie International Edition, 43 (2004) 1115-1117.

[9] B. Babakhani, D.G. Ivey, Anodic deposition of manganese oxide electrodes with rod-like structures for application as electrochemical capacitors, Journal of Power Sources, 195 (2010) 2110-2117.

[10] Y. Qiu, P. Xu, B. Guo, Z. Cheng, H. Fan, M. Yang, X. Yang, J. Li, Electrodeposition of manganese dioxide film on activated carbon paper and its application in supercapacitors with high rate capability, RSC Adv., 4 (2014) 64187-64192.

[11] G.H.A. Therese, P.V. Kamath, Electrochemical Synthesis of Metal Oxides and Hydroxides, Chemistry of Materials, 12 (2000) 1195-1204.

[12] J. Wei, N. Nagarajan, I. Zhitomirsky, Manganese oxide films for electrochemical supercapacitors, Journal of materials processing technology, 186 (2007) 356-361.

[13] J. Yang, L. Lian, H. Ruan, F. Xie, M. Wei, Nanostructured porous MnO_2 on Ni foam substrate with a high mass loading via a CV electrodeposition route for supercapacitor application, Electrochimica Acta, 136 (2014) 189-194.

[14] X. Lu, D. Zheng, T. Zhai, Z. Liu, Y. Huang, S. Xie, Y. Tong, Facile synthesis of large-area manganese oxide nanorod arrays as a high-performance electrochemical supercapacitor, Energy & Environmental Science, 4 (2011) 2915-2921.

[15] W. Li, K. Xu, B. Li, J. Sun, F. Jiang, Z. Yu, R. Zou, Z. Chen, J. Hu, MnO_2 Nanoflower Arrays with High Rate Capability for Flexible Supercapacitors, ChemElectroChem, 1 (2014) 1003-1008.

[16] P. Yang, Y. Li, Z. Lin, Y. Ding, S. Yue, C.P. Wong, X. Cai, S. Tan, W. Mai, Worm-like amorphous MnO_2 nanowires grown on textiles for high-performance flexible supercapacitors, Journal of Materials Chemistry A, 2 (2014) 595-599.

[17] J. Duay, S.A. Sherrill, Z. Gui, E. Gillette, S.B. Lee, Self-Limiting Electrodeposition of Hierarchical MnO_2 and $M(OH)_2/MnO_2$ Nanofibril/Nanowires: Mechanism and Supercapacitor Properties, ACS Nano, 7 (2013) 1200-1214.

[18] B.J. Plowman, L.A. Jones, S.K. Bhargava, Building with bubbles: the formation of high surface area honeycomb-like films via hydrogen bubble templated electrodeposition, Chemical Communications, (2015).

[19] S. Eugénio, T. Silva, M. Carmezim, R. Duarte, M. Montemor, Electrodeposition and characterization of nickel–copper metallic foams for application as electrodes for supercapacitors, J Appl Electrochem, 44 (2014) 455-465.

[20] H.C. Shin, J. Dong, M. Liu, Nanoporous structures prepared by an electrochemical deposition process, Advanced Materials, 15 (2003) 1610-1614.

[21] W.M. Haynes, CRC handbook of chemistry and physics, CRC press2014.

[22] C.-C. Hu, J.-C. Chen, K.-H. Chang, Cathodic deposition of $Ni(OH)_2$ and $Co(OH)_2$ for asymmetric supercapacitors: Importance of the electrochemical reversibility of redox couples, Journal of Power Sources, 221 (2013) 128-133.

[23] T. Nguyen, M. Boudard, L. Rapenne, O. Chaix-Pluchery, M.J. Carmezim, M.F. Montemor, Structural evolution, magnetic properties and electrochemical response of $MnCo_2O_4$ nanosheet films, RSC Adv., 5 (2015) 27844-27852.

[24] Q. Wang, D. O'Hare, Recent advances in the synthesis and application of layered double hydroxide (LDH) nanosheets, Chemical reviews, 112 (2012) 4124-4155.

[25] Y. Yue, H. Liang, Hierarchical micro-architectures of electrodes for energy storage, Journal of Power Sources, 284 (2015) 435-445.

[26] T. Nguyen, S. Eugenio, M. Boudard, L. Rapenne, M.J. Carmezim, T. Moura Silva, M.F. Montemor, Hybrid nickel manganese oxide nanosheets-3D metallic dendrites percolation network electrodes for high-rate electrochemical energy storage, Nanoscale, (2015).

[27] R. Downs, The RRUFF Project: An Integrated Study of The Chemistry, Crystallography, Raman and Infrared Spectroscopy of Minerals, Program and abstracts of the 19th general meeting of the International Mineralogical Association in Kobe, Japan, 2006, pp. O03-13.

[28] T. Gao, H. Fjellvåg, P. Norby, A comparison study on Raman scattering properties of α- and β-MnO_2, Analytica Chimica Acta, 648 (2009) 235-239.

[29] T. Gao, M. Glerup, F. Krumeich, R. Nesper, H. Fjellvåg, P. Norby, Microstructures and Spectroscopic Properties of Cryptomelane-type Manganese Dioxide Nanofibers, J. Phys. Chem. C, 112 (2008) 13134-13140.

[30] C.M. Julien, M. Massot, C. Poinsignon, Lattice vibrations of manganese oxides: Part I. Periodic structures, Spectrochimica Acta Part A: Molecular and Biomolecular Spectroscopy, 60 (2004) 689-700.

[31] Q. Qu, P. Zhang, B. Wang, Y. Chen, S. Tian, Y. Wu, R. Holze, Electrochemical Performance of MnO_2 Nanorods in Neutral Aqueous Electrolytes as a Cathode for Asymmetric Supercapacitors, J. Phys. Chem. C, 113 (2009) 14020-14027.

[32] H. Xia, Y. Wang, J. Lin, L. Lu, Hydrothermal synthesis of MnO_2/CNT nanocomposite with a CNT core/porous MnO_2 sheath hierarchy architecture for supercapacitors, Nanoscale research letters, 7 (2012) 1-10.

[33] T.P. Gujar, V.R. Shinde, C.D. Lokhande, W.-Y. Kim, K.-D. Jung, O.-S. Joo, Spray deposited amorphous RuO_2 for an effective use in electrochemical supercapacitor, Electrochemistry Communications, 9 (2007) 504-510.

[34] A. Bard, L. Faulkner, Electrochemical Methods: Fundamentals and Applications, John Wiley & Sons, Inc2001.

[35] S. Ardizzone, G. Fregonara, S. Trasatti, “Inner” and “outer” active surface of RuO_2 electrodes, Electrochimica Acta, 35 (1990) 263-267.

[36] T. Nguyen, M. Boudard, L. Rapenne, M.J. Carmezim, M.F. Montemor, Morphological changes and electrochemical response of mixed nickel manganese oxides as charge storage electrodes, Journal of Materials Chemistry A, 3 (2015) 10875-10882.

[37] Q. Li, Z.-L. Wang, G.-R. Li, R. Guo, L.-X. Ding, Y.-X. Tong, Design and Synthesis of MnO_2/Mn/MnO_2 Sandwich-Structured Nanotube Arrays with High Supercapacitive Performance for Electrochemical Energy Storage, Nano Lett., 12 (2012) 3803-3807.

[38] L. Huang, D. Chen, Y. Ding, S. Feng, Z.L. Wang, M. Liu, Nickel–Cobalt Hydroxide Nanosheets Coated on $NiCo_2O_4$ Nanowires Grown on Carbon Fiber Paper for High-Performance Pseudocapacitors, Nano Lett., 13 (2013) 3135-3139.

[39] X. Li, J. Shen, W. Sun, X. Hong, R. Wang, X. Zhao, X. Yan, A super-high energy density asymmetric supercapacitor based on 3D core-shell structured NiCo-layered double hydroxide@carbon nanotube and activated polyaniline-derived carbon electrodes with commercial level mass loading, Journal of Materials Chemistry A, 3 (2015) 13244-13253.

3.3. Structural Evolutions, Magnetic Properties and Electrochemical Response of $MnCo_2O_4$ Nanosheet Films[✧]

Tuyen Nguyen[a,b], Michel Boudard[b], Laetitia Rapenne[b], Odette Chaix-Pluchery[b], M. João Carmezim[a,c], M. Fátima Montemor[a]

[a] Centro de Química Estrutural, Instituto Superior Técnico, Universidade de Lisboa, 1049-001 Lisboa, Portugal

[b] Univ. Grenoble Alpes, LMGP, F-38000 Grenoble & CNRS, LMGP, F-38000 Grenoble, France
[c] ESTSetúbal, Instituto Politécnico de Setúbal, 1959-007 Lisboa, Portugal

$MnCo_2O_4$ spinel oxide nanosheets were prepared *via* electrodeposition and post thermal annealing on stainless steel substrates. The structural transformation of an electrodeposited hydroxide phase into a spinel phase was achieved by thermal annealing at different temperatures (250 °C, 350 °C, 450 °C and 650 °C). The surface morphology of the films revealed the presence of a nanosheet percolation network that was converted into nanoplatelets after annealing at 650 °C. The nanosheets composed of nanocrystals and the crystal size of the $MnCo_2O_4$ spinel oxide increased from 10 nm after 250 °C annealing to 100 nm after 650 °C annealing, in which a twinning was observed. The magnetic transition temperature also increased from 101 K to 176 K for the films annealed at 250 °C and 650 °C, respectively. The spinel films displayed specific capacitance values above 400 F g^{-1} at 1 A g^{-1}, making these spinel oxides promising pseudocapacitive materials.

Keywords: transition metal hydroxide, mixed spinel oxide, nanosheets, structural evolution, magnetic properties, pseudocapacitor

---

[✧] **Adapted from RSC Advances, 2015, 5, 27844-27852**

3.3.1. Introduction

Recently, transition metal (TM) oxides and hydroxides have extensively been considered as alternative active materials for redox supercapacitor electrodes thanks to their high charge storage capability and high reversibility [1, 2]. Various TM oxides/hydroxides exhibit a pseudocapacitive behavior because of reversible surface redox reactions with OH^- anions in the alkaline electrolytes [3]. Due to the large interlayer distance in the hydroxide structure, ions in electrolytes can easily diffuse into the electrode material, resulting in increased capacitance. Wet and hydrothermal-based methods are normally used to prepare the TM hydroxides for electrodes [4]. For example, $Co(OH)_2$ was deposited on stainless steel by potentiostatic electrodeposition in the form of a network of nanolayered sheets [5] having specific capacitance values of 860 F g^{-1}. $Ni(OH)_2$ was deposited by a hydrothermal method [6], leading to single crystalline nanoplatelet arrays with an areal capacitance value of 64 mF cm^{-2}. Mixed TM hydroxides, especially double TM hydroxides, are also studied as they benefit from the possibility of multiple redox reactions of the combined TM with OH^-, resulting in enhanced capacitances [7]. Two TMs can be incorporated into a hydroxide structure by co-deposition/precipitation routes [8]. For example, nanostructured porous layered $Co_{1-x}Ni_x(OH)_2$ films were prepared by potentiodynamic electrodeposition [9] showing a specific capacitance value of 1213 F g^{-1}. NiTi layered double hydroxide nanosheets prepared by two hydrothermal steps [10] have an areal capacitance value of 10.37 F cm^{-2}.

At the same time, spinel oxides and mixed (double) spinel oxides have also raised interest in the search of new redox supercapacitor electrodes [11]. Though spinel oxides were studied extensively in the development of secondary batteries [12, 13], there are much less studies for possible use as pseudocapacitive electrodes for redox supercapacitors. For such an application, (mixed) spinel oxide electrodes can be obtained through the synthesis of hydroxides and their subsequent transformation into spinel phases by thermal annealing [14]. Hydroxides have the advantage of high ionic diffusion, but spinel oxides present an increased electrical conductivity [15]. A Co_3O_4 nanowire array prepared by the hydrothermal method with post thermal annealing at 250 °C for 3 hours [16] displays a specific capacitance value of 715 F g^{-1}. A $NiCo_2O_4$ nanosheet film electrodeposited and annealed at 300 °C for 2 hours [17] presents a specific capacitance value of 1450 F g^{-1}. These studies show promising results, however, the structural transformations and electrochemical behavior with annealing temperature are usually not detailed and consequently not fully understood.

The incorporation of manganese into mixed oxides is of high interest due to its low cost, environmental friendliness and the possibility of several reversible redox reactions as a consequence of the multi valence states of manganese in manganese oxides [18]. There is scarce work regarding the electrochemical performance of mixed oxides with manganese. For example, $Ni_{1-x}Mn_xO_y$ nanoflakes deposited on α-MnO_2 nanowires using chemical bath deposition and post annealing at 300 °C [19] display a specific capacitance of 400 F g^{-1}. $MnCo_2O_4$ spinel oxide nanowires were also prepared by the hydrothermal method followed by a thermal annealing at 350 °C [20], and display a specific capacitance value of 349.8 F g^{-1}. But, as for the previous studies, none of these reports have detailed the structural transformations occurring with annealing temperature.

Besides electrochemical properties, spinel oxides also present magnetic properties [21]. The porous nanostructured spinel oxides thermally annealed for supercapacitors can lead to relevant changes in the magnetic properties [21].

The present work aims at detailing the structural changes, evolution of magnetic properties and electrochemical response of a Mn-Co hydroxide converted into a spinel phase after annealing at different temperatures. The films were deposited on stainless steel substrates by galvanostatic electrodeposition, forming a 3D layer composed of nanosheets. The transformation of an electrodeposited hydroxide into a spinel oxide by thermal annealing was studied in detail with respect to the annealing temperature as a tuning parameter for improving structural, physical and electrochemical properties of the resulting pseudocapacitive electrodes. Thus, this work goes beyond the state-of-art, by discussing results focused particularly on structural transformations occurring in

$MnCo_2O_4$ electrodes with annealing temperature. The magnetic properties and the electrochemical response in NaOH electrolyte of the material were also investigated.

3.3.2. Experimental

Materials:

Manganese nitrate $Mn(NO_3)_2$, cobalt nitrate $Co(NO_3)_2$ and sodium hydroxide NaOH from Sigma Aldrich were used for electrodeposition and electrochemical evaluation experiments, respectively. The chemicals were used as received without further purification process. Stainless steel (AISI 304 obtained from Goodfellow) substrates were used for electrodeposition experiments. Steel samples were previously polished with SiC grit papers up to 1000 grits, rinsed with deionized water and ethanol and dried by a jet of compressed air.

Electrodeposition:

The electrodeposition experiments were performed in a conventional electrochemical system under ambient atmosphere at room temperature using a Voltalab PGZ 100 Potentiostat from Radiometer, with the stainless steel as a working electrode, the saturated calomel electrode (SCE) as reference electrode and the platinum foil as counter electrode. All potentials referred in this work are potentials versus the SCE. The depositions were performed in a constant current mode, applying a current density of -0.4 mA cm^{-2} for 2500 seconds. The concentrations of the precursor salts used in the experiments were 0.093M $Mn(NO_3)_2$ and 0.007 M $Co(NO_3)_2$. These concentrations were selected to obtain a Co/Mn ratio close to 2 in the deposited films. The samples were annealed at 250, 350, 450 and 650 ^{o}C for 3 hours.

Characterization:

Field emission gun scanning electron microscopy (FEG-SEM, JEOL 7001F and FEI QUANTA 250 ESEM microscopes) and energy dispersive x-ray spectroscopy were used for analyzing the surface morphology and the composition of the deposited films. Topographic images and surface roughness were obtained with an atomic force microscopy (AFM, Nanosurf Easyscan microscope), working in tapping mode. X-ray diffraction (XRD, Bruker AXS D8 Advance diffractometer) in Bragg-Brentano and grazing incident (GIXRD) configurations with Cu K_α radiation, Fourier transform infrared spectroscopy (FTIR, Digilab Excalibur Series spectrometer) and Raman spectroscopy (Horiba/Jobin Yvon LabRam spectrometer) were used for studying structural characteristics. For Raman measurements, the 632.8 nm He-Ne laser was used for excitation on a spot of 1 μm^2 and the counting time was 400 s. The structural details were studied by transmission electron microscopy (TEM, JEOL JEM-2010 microscope) operating at 200 KeV. TEM samples were prepared by film scratching using a diamond tip, and the resulting powder was collected directly on TEM grids in order to avoid structural transformations induced by sample thinning process. The magnetic characteristics were studied using a SQUID MPMS magnetometer (Quantum Design). Field cool (FC) curves were measured in the 10K-300K temperature range with a magnetic field of 500 Oe.

The electrochemical response was determined by cyclic voltammetry at a scan rate of 20 mV s^{-1}, and chronopotentiometry at a constant current density of 1 A g^{-1} in NaOH electrolytes. All the electrochemical experiments were carried out in the conventional three-electrode system, using steel as working electrode. The specific capacitance of the film has been estimated from the chronopotentiometry curves using the formula:

$$C = \frac{It}{\Delta V}$$

in which, C, I, t, ΔV are the specific capacitance of the deposits (F g^{-1}), the charge/discharge current density (A g^{-1}), the discharge time (s) and the charge/discharge potential windows (V), respectively.

3.3.3. Results and Discussion

FEG-SEM micrographs in Figure 3.3.1 evidence the morphological features of the as-deposited film and films annealed at different temperatures. The as-deposited films (top row) present a porous surface morphology composed of nanosheets, which are still observed after thermal treatment up to

450 °C (middle row; 350 °C not shown). The nanosheets morphology suggest that they were grown almost perpendicularly to the substrate plane (out of plane direction in Figure 3.3.1) and are connected together, forming a percolation network with an open porous structure. Nanosheets have an average thickness of about 10 nm and an average length of approximately 165 nm. The surface morphology of the films annealed at 650 °C (bottom row) is different from that of the as-deposited and low temperature annealed films. The nanosheets are transformed into nanoplatelets, each one of about 46 nm of thickness and 150 nm of average length. The percolation network has almost vanished.

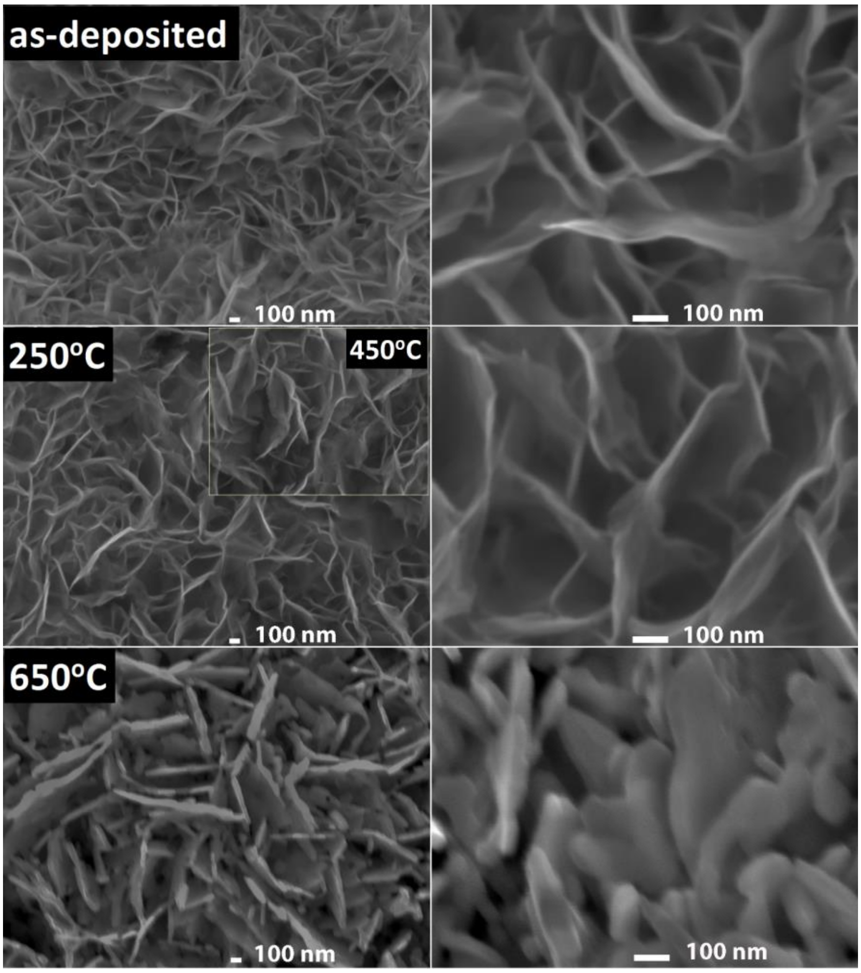

Figure 3.3.1. FEG-SEM images of the film surface at low (left) and high (right) magnifications. Top: as-deposited film. Middle: films annealed at 250 °C. Bottom: films annealed at 650 °C. Inset: FEG-SEM image of films annealed at 450 °C with the same magnification with that of the left images for comparison.

The formation of the nanosheets is based on the preferential growth of the double layer hydroxide structure during the electrodeposition process as proposed in literature [22]. The nanosheet structure is retained after thermal annealing at low temperature, a process in good agreement with a previous work [22]. The hydroxides are formed due to the electrodeposition based on the generation of OH^- ions through the reduction of nitrate ions or water electrolysis, and the reaction of generated OH^- ions with metal cations in the electrolyte [23]. The porous surface morphology composed of the nanosheet percolation network as shown in the FEG-SEM images suggests potential applications as pseudocapacitve electrodes.

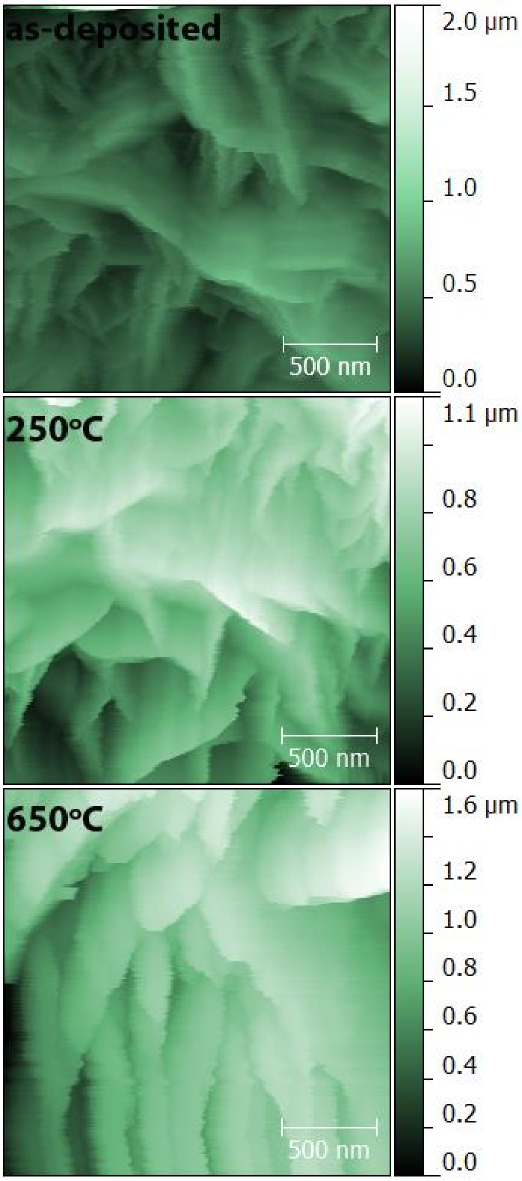

Figure 3.3.2. From top to bottom: tapping mode AFM topography images of the films (in 2 µm x2 µm region): as-deposited, annealed at 250 °C, and annealed at 650 °C. Color scale on the right part indicates the out of plane scale.

The surface topography of the films measured by AFM in a 2 µm x2 µm squared region is shown in Figure 3.3.2. The AFM images evidence the presence of interconnected nanosheets. As already observed in the FEG-SEM micrographs, there is no clear change in the surface topography between the as-deposited and 250 °C annealed films. The average size of the individual nanosheets determined by AFM is about 10 nm in thickness and 200 nm in length. At 650 °C, the surface topography is different and the nanosheets seem to evolve into nanoplatelets as observed previously. The AFM average surface roughness is about 85 nm, 79 nm, and 93nm and the maximum deepness of the films is about 570, 560 and 400 nm for the as-deposited, 250 °C and 650 °C annealed films, respectively. Thus, it shows a deepness decrease after annealing at 650 °C.

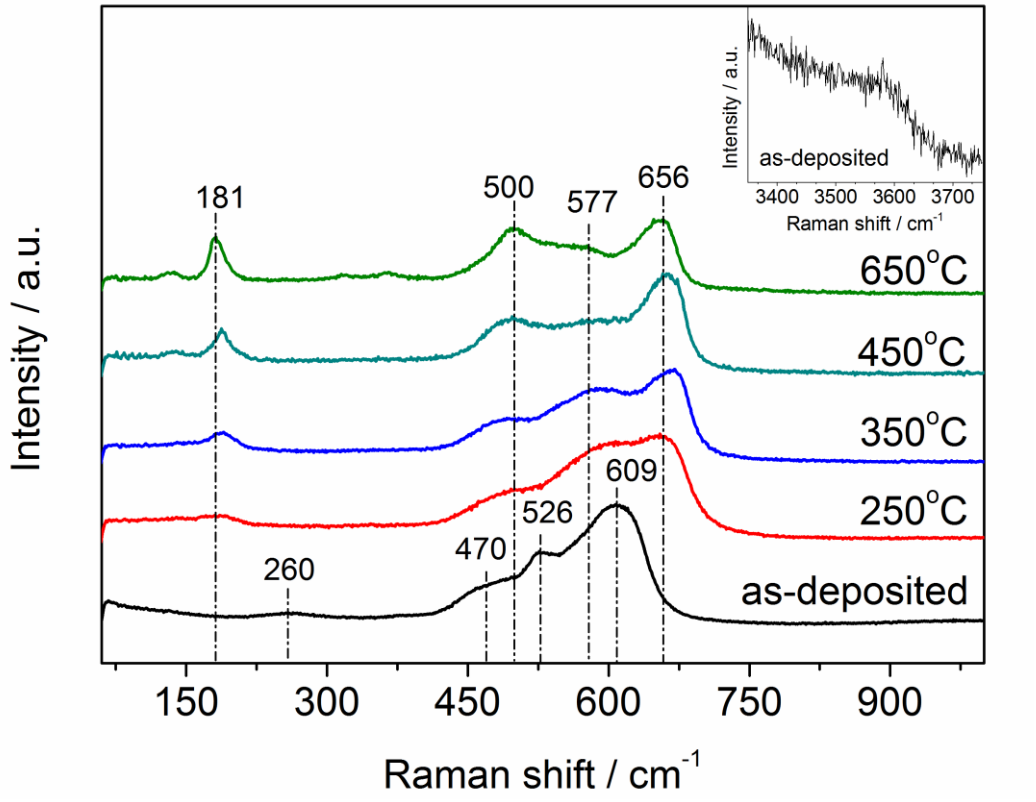

Figure 3.3.3. Raman spectra of the as-deposited film and films annealed at different temperatures. Inset: Raman spectrum of the as-deposited film in a higher wavenumber range. The positions of Raman bands are given in the spectra of the as-deposited and 650 °C annealed films. Vertical lines are only visual guides.

The Raman spectrum of the as-deposited film presents four broad bands at 260, 470, 526 and 609 cm^{-1} (Figure 3.3.3) and a weak band around 3600 cm^{-1} (Figure 3.3.3 inset). The bands at 260 and 609 cm^{-1} match well with the E_g modes reported for $Co(OH)_2$ (space group P-3m1) [25] whereas the band at 470 cm^{-1} can be assigned to A_{1g} mode, despite the shift in wavenumber when compared to $Co(OH)_2$ and $Mn(OH)_2$ (see Figure 3.3.3 and Table 3.3.1). The band at 526 cm^{-1}, assigned to an A_{2u} symmetry mode in literature, is slightly shifted due to its A_{2u} symmetry; this mode is normally IR-active and Raman-inactive following the selection rules and then could be related to structural defects.

Table 3.3.1. Positions (cm^{-1}) of Raman and FITR bands for the as-deposited and 250-650 °C annealed films as compared with bands reported in literature for some brucite-type hydroxides $M(OH)_2$ (M=TM, space group P-3m1) and AB_2O_4 spinel oxides (A, B = TM, space group Fd3m). TW: this work.

	Raman					FTIR		
Hydroxides $M(OH)_2$	E_g	A_{1g}	E_g	A_{2u}	$A_{1g}(\nu_{O-H})$	ν_{M-O}, ν_{M-O-H}	ν_{O-H}	Ref.
$Co(OH)_2$	547	427	250	503				[24]
$Co(OH)_2$	~610	~430	~260	~510				[25]
$Co(OH)_2$						480–540	3637	[26]
$Co(OH)_2$						460, 520	3634	[27]
$Co(OH)_2$				510	3569	433	3630	[28]
$Mn(OH)_2$	645	461	262	367				[29]
$Mn(OH)_2$		401	234	432	3578	386	3625	[28]
$Ni(OH)_2$		445	310	510	3580			[30]
As-deposited	609	470	260	526		594	3573	TW

Spinels AB_2O_4	A_{1g}	F_{2g}	F_{2g}	E_g	F_{2g}	ν_{A-O}	ν_{B-O}	Ref.
$MnCo_2O_4$	~680	~520		~480	~200	667	562	[31]
$MnCo_2O_4$						662	572	[32]
$NiCo_2O_4$	671	523		477	187			[33]
$NiCo_2O_4$	648	504		456	186			[34]
Co_3O_4	690	621	519	482		661	570	[35]
Co_3O_4	691	618	521	482	194			[36]
Co_3O_4	686	616	519	481	194			[37]
250 °C	658	591		490	188	658		TW
350 °C	668	587		492	188	666	567	TW
450 °C	663	587		498	188	672	562, 496	TW
650 °C	656	577		500	181	682	553, 503	TW

The observed band shifts when compared to $Co(OH)_2$ and $Mn(OH)_2$ spectra reported in literature [24, 25] can be explained by either a mixture of $Co(OH)_2$ and $Mn(OH)_2$ and/or the possible formation of a mixed $Co_{1-x}Mn_x(OH)_2$ hydroxide. The broadness of the bands can probably be related to the nanocrystalline nature of the as-deposited film. The week band around 3600 cm^{-1} (Figure 3.3.3 inset) is assigned to the O-H stretching A_{1g} mode of the hydroxide (Table 3.3.1) [28, 30].

After annealing at 250 ^oC, the bands assigned to the hydroxide disappear and new bands arise at 188, 490, 591 and 658 cm^{-1} (Figure 3.3.3). Although the position of these bands do not match exactly with those reported in for $MnCo_2O_4$ [31], the similarity is evident as well as for other spinel oxides depicted in Table 3.3.1, like $NiCo_2O_4$ and Co_3O_4. In these cases, the band shifts are larger due to the presence of a different cation (Ni^{2+} or Co^{2+}) in the A site of the AB_2O_4 spinel structure (space group Fd3m). This favours the structural transformation of the hydroxide into the spinel phase and the new bands, as pointed above, can thus be assigned to F_{2g}, E_g, F_{2g} and A_{1g} symmetry modes of the $MnCo_2O_4$ spinel phase, respectively. Note that the slightly different positions reported for the same material, for example $NiCo_2O_4$ (see Table 3.3.1) [33, 34] can be related to other differences in the material properties such as crystal size and shape or strain state in the films.

When increasing the annealing temperature up to 650 °C, the bands slightly shift and tend to become narrower and more intense, indicating that the thermal treatment favors the crystal growth and improves the crystal quality of the spinel phase.

The FTIR spectrum of the as-deposited film in Figure 3.3.4 presents some very broad vibration bands, particularly the not well-defined OH stretching band at about 3573 cm^{-1}, the weak bending mode of the interlayer water molecule at 1640 cm^{-1}, the bands at 1351 cm^{-1} and 1490 cm^{-1} due to the C=O vibration of absorbed CO_2 and the carbonate ions from the dissolution of CO_2 in water [38, 39] and the band at 594 cm^{-1} arising from the metal-oxygen stretching or metal-hydroxyl bending vibration modes in hydroxides [26, 27] (Table 3.3.1). Thus, it further confirms the formation of the layered hydroxide previously identified.

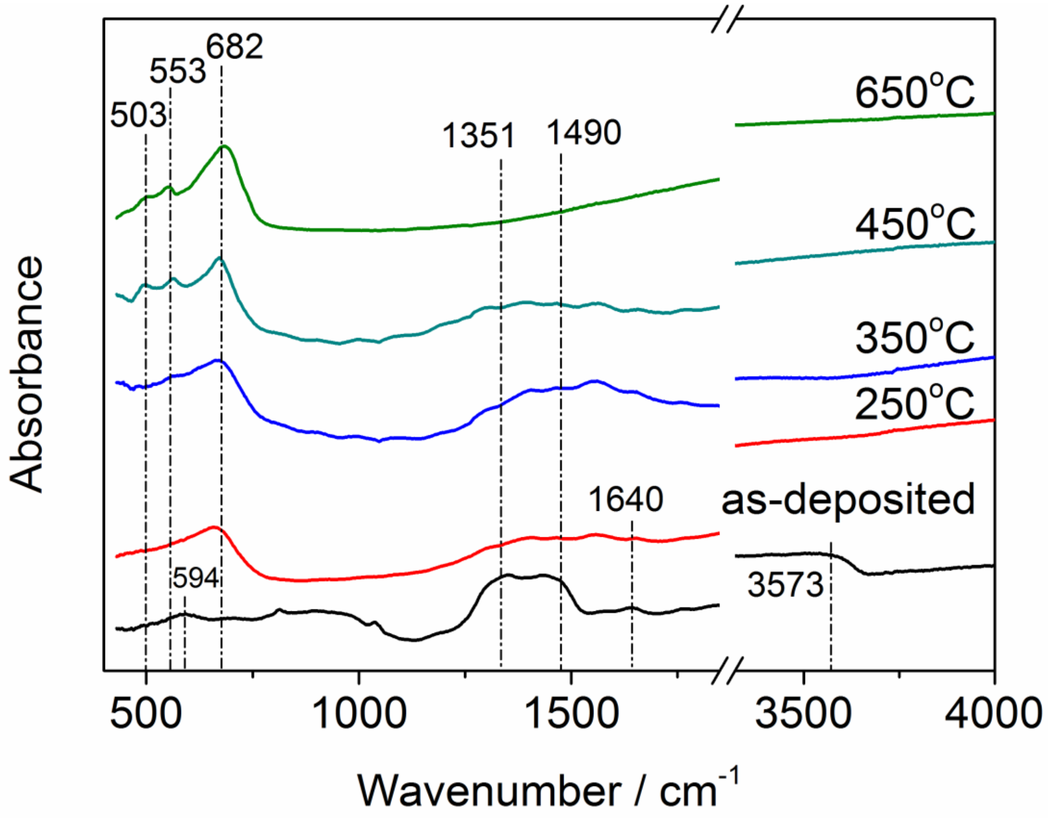

Figure 3.3.4. FTIR spectra of the as-deposited film and films annealed at different temperatures.

These bands vanish after annealing and simultaneously new bands occur indicating the transformation from the hydroxide into a new phase. The bands become narrower and increase in intensity with increasing temperature, in good agreement with the Raman results. They can be found at 682 cm^{-1}, 553 cm^{-1}, and 503 cm^{-1} in the film annealed at 650 °C. The two first ones can be assigned to the metal-oxygen stretching modes associated with Mn^{2+} ions in tetrahedral sites and with Co^{3+} ions in octahedral sites in the spinel structure, respectively [31, 32, 35] (Table 3.3.1). The bands are slightly shifted in comparison with the positions reported in literature, probably due to differences in film composition, strain state, and structural disorder.

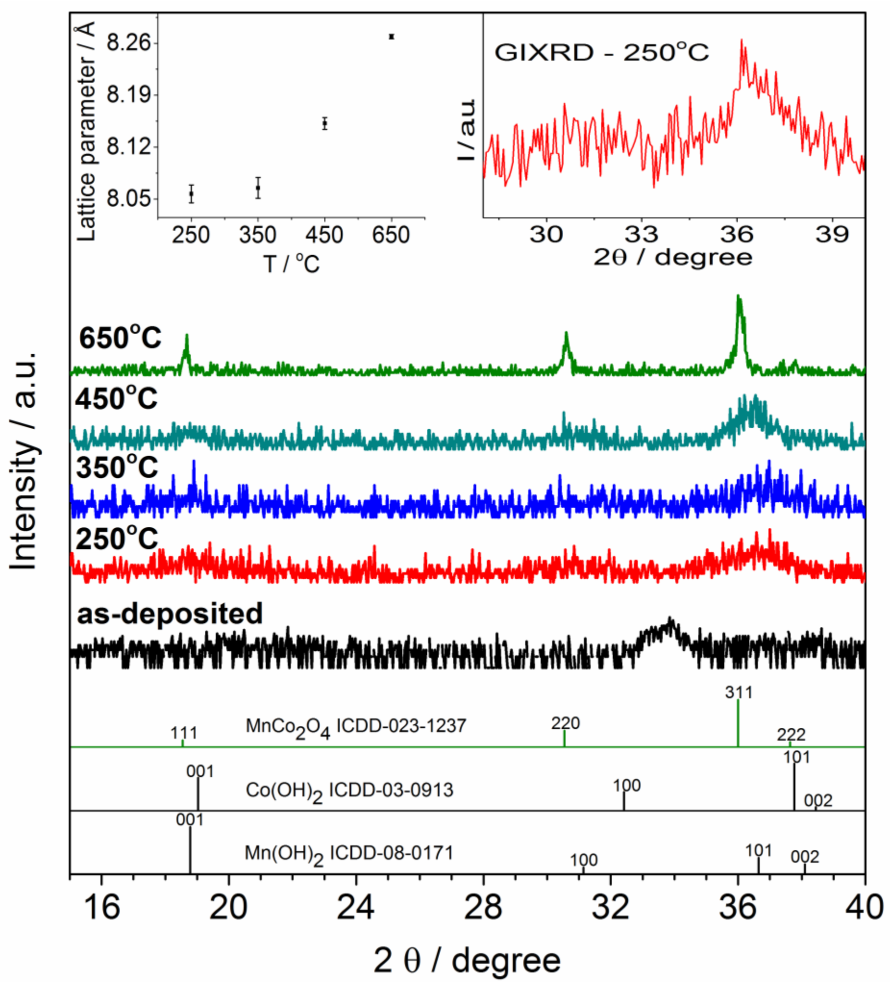

Figure 3.3.5. XRD patterns of the as-deposited film and films annealed at 250 °C, 350 °C, 450 °C and 650 °C in comparison with ICDD cards of $Co(OH)_2$, $Mn(OH)_2$ and $MnCo_2O_4$. Left inset: evolution of the $MnCo_2O_4$ cubic lattice parameter with annealing temperature. Right inset: GIXRD pattern of the film annealed at 250 °C.

XRD measurements were performed to identify the phases present in the films (Figure 3.3.5). XRD patterns of the as deposited and 250 °C, 350 °C and 450 °C annealed films show very broad diffraction lines making difficult any clear phase identification. GIXRD experiments confirm the presence of broad lines and no major enhancement of the signal is achieved. It shows an intrinsic poor XRD of the films related to their structural properties and is in agreement with the presence of small (more or less disordered) nanocrystals in each nanosheet as will be confirmed by the TEM analysis. The correlation length estimated from the full width at half maximum (FWHM) of the lines is 25 nm and 7 nm for the as-deposited and 250 °C annealed films, respectively, giving a rough estimation of the average nanocrystal size. However, despite the weakness and broadness of the diffraction line at 33.9 °2θ in the as-deposited film pattern, seems to be related to (100) planes of $Mn(OH)_2$ (ICDD card n° 08-0171) and/or $Co(OH)_2$ (ICDD card n° 03-0913) (see TEM analysis). It is worthy to note that $Mn(OH)_2$ and $Co(OH)_2$ are miscible as reported elsewhere [40]. The absence of the 001 diffraction line in the XRD patterns of the as-deposited film expected at low angle from the $Mn(OH)_2$ and $Co(OH)_2$ ICDD cards is probably linked to the nanosheets texture. This point will be made clearer in the TEM section.

After annealing a clear transformation arises. Although it is difficult to observe it at 250 °C, it is clear that the broad peak at 33.9 °2θ disappears with annealing and a new peak occurs at about 36.6 °2θ. When increasing the annealing temperature, this peak sharpens and its intensity increases whereas two other peaks can be observed at 19 and 31 °2θ, the whole pattern being in good agreement with the 111, 220 and 311 diffraction lines of the face centered cubic (FCC) $MnCo_2O_4$ spinel structure (ICDD card n° 00-023-1237, lattice parameter = 8.269 Å). Note that 311 diffraction line of the spinel structure is more visible in the pattern of the 250°C annealed film when using GIXRD (right inset of Figure 3.3.5). The cubic lattice parameter calculated from this line is 8.057 Å for the 250 °C annealed film; this value increases with increasing the annealing temperature, reaching the bulk value of 8.269 Å after annealing at 650 °C. This evolution can be related to the increasing nanoscale size of the diffracting particles with increasing temperature as shown by the decrease of FWHM of the diffraction lines indicating correlation lengths changing from a few nm to 40 nm.

XRD results, in good agreement with FEG-SEM, Raman and FTIR results, indicate that the hydroxide phase of the nanosheets transform into the spinel phase after thermal treatment. At low annealing temperature, the broadening and low intensity of the peaks result from the nanocrystalline nature of the diffracting particles distributed in the individual nanosheets as will be shown by TEM analysis. Further increase of the annealing temperature results in peak intensity increase and a sharpening suggesting an increased correlation length. At 650 °C, narrow and more intense peaks are observed that favours the growth of larger well-crystallized crystals in the nanoplatelets, in good agreement with FEG-SEM and AFM results.

TEM images of the as-deposited and annealed films are shown in Figure 3.3.6. Low magnification TEM images show large superimposed particles, evidencing of a nanosheet-like structure, in agreement with FEG-SEM results. The size of the individual nanosheets is about 200 nm, which is comparable with the values determined by FEG-SEM and AFM. Darker areas in the images correspond to thicker areas in the TEM samples due to the preparation by film scratching, directly collected on TEM grids (without solution dispersion and sonication), thereby making difficult to separate the nanosheets.

The selected area electron diffraction (SAED) pattern of the as-deposited film (Figure 3.3.6, top middle) shows continuous diffraction rings indicating the polycrystalline nature of the as-deposited nanosheets. The position of the intense rings in the pattern are comparable with those given in the $Co(OH)_2$ ICDD card (n° 03-0913, a = 0.3179 nm, c = 0.4649 nm). For example, the interplanar distance $d_{100} = 0.25$ nm calculated from the SAED is close to $d_{100} = 0.276$ nm of $Co(OH)_2$. Note that only rings with null c indices (in hexagonal setting) are observed in the SAED. This corresponds to a texture with the [001] 3-fold axis of the trigonal structure of TM hydroxides [41] perpendicular to the surface of the nanosheet. The high resolution transmission electron microscopy (HRTEM) image of the as-deposited film is shown in Figure 3.3.6 (top right) and the inverse fast Fourier transform (FFT) image of the red square part in this image is shown in the bottom inset. This inset shows the continuous lattice planes corresponding to the [001] zone axis of an individual nanocrystal as seen in a superimposed simulated image, this zone axis is in agreement with SAED result. The FFT of the whole HRTEM image depicted in the top right inset reveals two different orientations of the observed nanocrystals, resulting from the rotation of the [001] zone axis by nearly 25 degrees as indicated by the blue and red hexagons. The average size of the nanocrystals is about 20 nm. This indicates that nanocrystals are randomly distributed in the hydroxide nanosheets with their *c*- axis being perpendicular to the nanosheet. This preferential growth clarifies the absence of the 001 diffraction line in the XRD line of the as-deposited film.

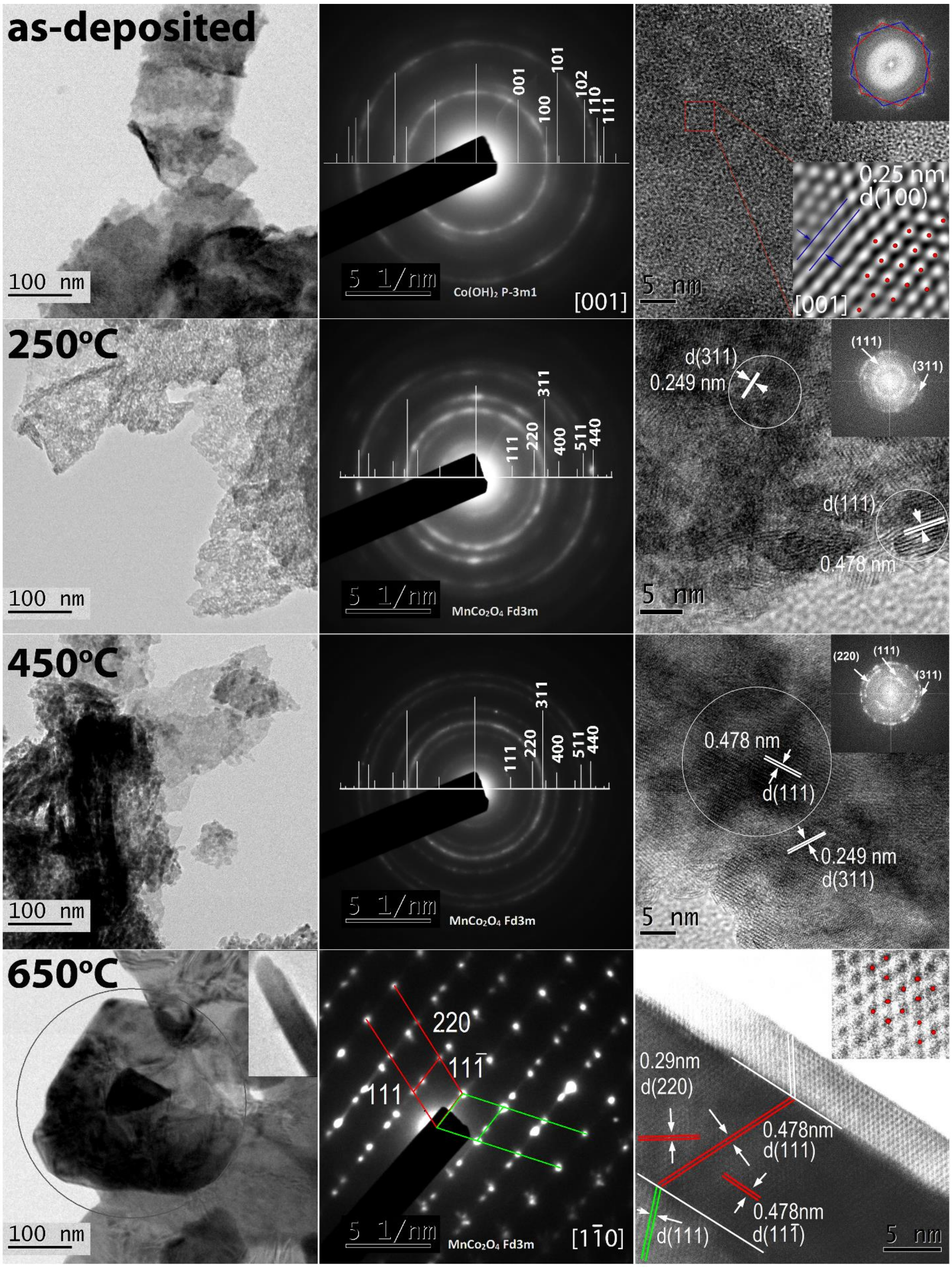

Figure 3.3.6. From top to bottom: TEM images of the as-deposited film and films annealed at 250 °C, 450 °C and 650 °C. From left to right: low magnification TEM images (left), SAED (middle) HRTEM images (right). SAED patterns are indexed from the superposition of the diffraction lines and lattice

planes. Top right inset: FFT of the HRTEM images for as-deposited, 250 °C and 450 °C. The blue and red hexagons in as deposited FFT correspond to two [001] zone axes rotated by nearly 25 degrees. Top right inset in HRTEM 650 ^{o}C image: enlargement with a superimposed projection of a simulated structure of $MnCo_2O_4$. Bottom right inset in the HRTEM image of the as-deposited film: inverse FFT image of the image selected by the red square exhibiting the hexagonal symmetry which results from the projection of the trigonal $Co(OH)_2$ structure along the [001] zone axis (hexagonal setting).

After low temperature thermal annealing (250-450 ^{o}C), the SAED patterns present well-defined diffraction rings, which can be indexed as the FCC $MnCo_2O_4$ phase (ICDD n^{o} 00-023-1237). The rings indicate the polycrystalline nature of the nanosheets and no texture was identified. This demonstrates the transformation of the as-deposited hydroxide(s) into the $MnCo_2O_4$ spinel phase. HRTEM images (Figure 3.3.6, right, 250 °C, 450 °C) show the presence of nanocrystals with different orientations in the nanosheets; lattice fringes with spacings of 0.249, 0.292, 0.478 nm are visible; corresponding to (311), (220) and (111) lattice planes of the $MnCo_2O_4$ structure. The estimation of the crystal size from the HRTEM images (see white circles in the images) indicates a size increase from values around 10 nm for the films annealed at 250 ^{o}C and 350 ^{o}C to values around 20 nm at 450 ^{o}C.

The thick nanoplatelet observed at low magnification in the film annealed at 650 ^{o}C (Figure 3.3.6 bottom left black circle (top view) and inset (side view)) gives evidence of the growth and transformation of the nanosheets during the increase of temperature. The length and thickness of the nanoplatelets are close to 200 nm and 45 nm, respectively, which is comparable with FEG-SEM results. The nanoplatelets visible in films annealed at 650 °C show that large facets develop during the growth of the nanosheets leading to a quasi-hexagonal prism shape of the platelet after thermal annealing at 650 ^{o}C. The normal to the base of the prism is a 3-fold axis ([111] zone axis) and corresponds to a slow growth direction, leading to large facets whereas the fast growth of the nanoplatelets along the $[1\bar{1}0]$ axis explains its hexagonal shape. The inset shows a side view of the platelets along the $[1\bar{1}0]$ zone axis; its SAED pattern (Figure 3.3.6, bottom middle) is composed of sharp diffraction spots indexed as (111) and (220) lattice planes corresponding to two crystals whose reciprocal lattice are represented schematically in the SAED. They present a twinning by reflection across the $(11\bar{1})$ plane. The twinning is also observed in the HRTEM image. The HRTEM image shows lattice fringes with spacings of 4.78 Å and 2.9 Å which correspond to (111) and (220) lattice planes of FCC $MnCo_2O_4$. The lattice can be superimposed to the $MnCo_2O_4$ structure generated by CaRIne software projected along the $[1\bar{1}0]$ zone axis (Figure 3.3.6, inset of bottom right).

The average crystal size as calculated from low magnification TEM images (not shown) is about 100 nm, indicating a significant growth of the crystals after annealing at 650 °C. During the temperature-induced growth process, different nanocrystals with the same orientation, but randomly distributed become connected and these morphological changes at 650 °C as shown by FEG-SEM and AFM result in a porosity decrease and may not be the optimum trend for the application in redox supercapacitors. Meanwhile, $MnCo_2O_4$ has been reported as a material displaying good properties for electrocatalytic reactions, such as oxygen reduction reaction or oxygen evolution reaction [42]. The twinning has been reported as possible active site for electrocatalytic reactions [43].

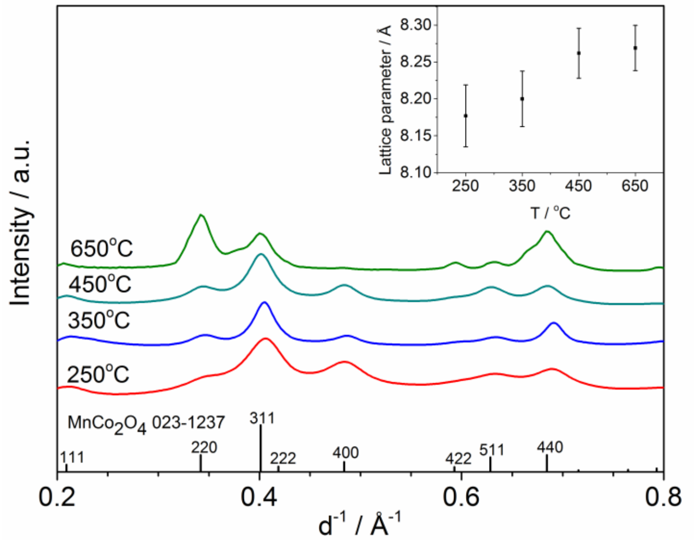

Figure 3.3.7. Integrated SAED profiles of the films annealed at 250 °C, 350 °C, 450 °C, 650 °C compared with diffraction lines given in the $MnCo_2O_4$ ICDD card. Inset: evolution of the calculated $MnCo_2O_4$ lattice parameter with annealing temperature.

The $MnCo_2O_4$ structural evolution resulting from the thermal treatment is shown in Figure 3.3.7, representing electron diffraction profiles obtained by integration of the SAED patterns using the Diffraction Ring Profiler [44]. The line positions match well with those given in the $MnCo_2O_4$ ICDD card. The fact that the 400 line expected at 0.49 $Å^{-1}$ has disappeared and that the relative line intensities have changed in the 650 °C integrated SAED profile can be explained by the preferential orientation of the crystals. The correlation length calculated by Scherrer equation from the 311 line of the integrated SAED profile at 250 °C is 2.6 nm.

As shown in the inset of Figure 3.3.7, the lattice parameter increases from 8.177 Å after annealing at 250 °C to 8.269 Å after annealing at 650 °C. This last value is in agreement with XRD results and corresponds to the bulk value.

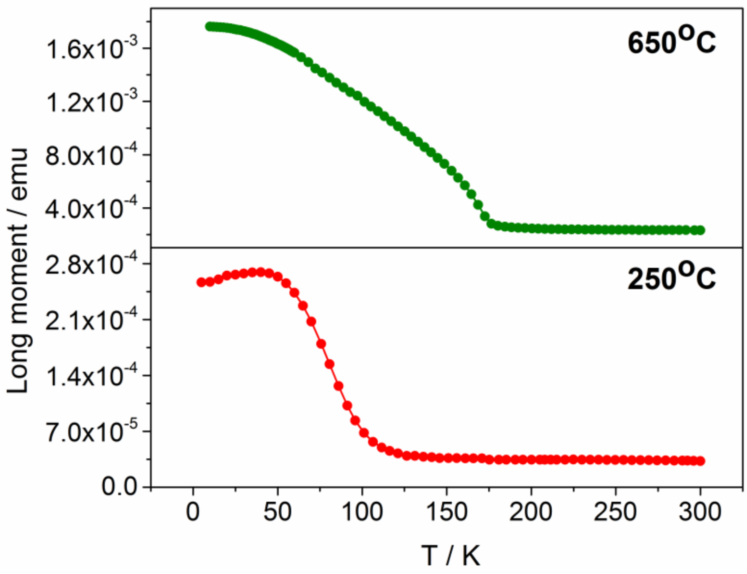

Figure 3.3.8. FC curves of the films annealed at 250 °C (bottom) and 650 °C (top). The applied in-plane field was 500 Oe.

The magnetic properties of the films annealed at different temperatures were studied by performing temperature-dependent magnetic moment measurements. The results are shown in Figure 3.3.8. The magnetic transition temperature determined from the FC curves increases from 101 K to 176 K when the annealing temperature increases from 250 °C to 650 °C, respectively. As reported for other spinel oxides [45], the increase of the transition temperature with annealing temperature is probably correlated to the crystal size increase observed from TEM study.

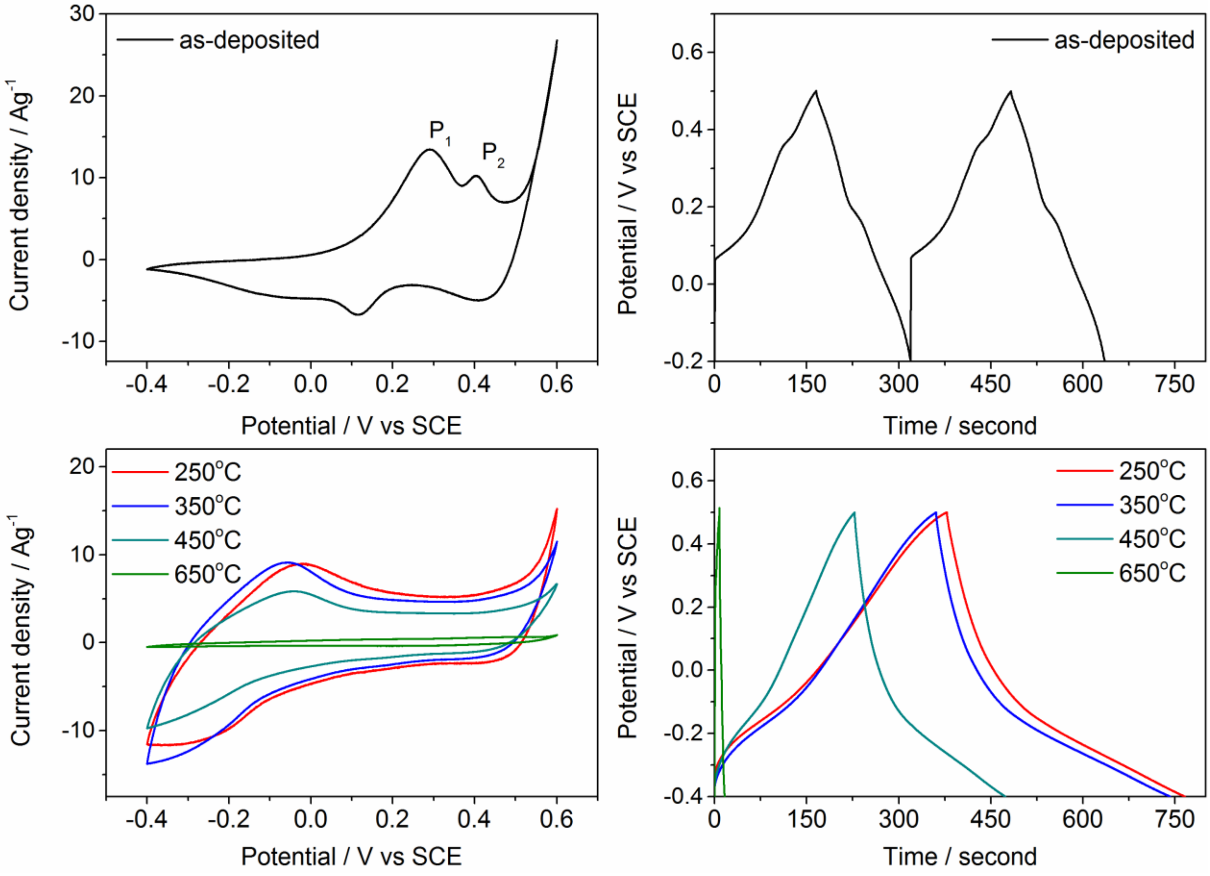

Figure 3.3.9. Cyclic voltammetry (left) and charge-discharge (right) curves for the as-deposited film (top) and films annealed at different temperatures (bottom).

To understand the electrochemical behavior of the deposited films, cyclic voltammetry (CV) and charge-discharge (CD) measurements were carried out. The CV curve of the as-deposited film shown in Figure 3.3.9 (top left) displays two well-defined redox peaks, P_1 and P_2, at 0.25 and 0.42 V, which can be related to the following redox reactions [46, 47]:

P_1: $Mn(OH)_2 + OH^- \leftrightarrow MnOOH + H_2O + e^-$ 0.25 V vs SCE (3.3.1)

$Co(OH)_2 + OH^- \leftrightarrow CoOOH + H_2O + e^-$ (3.3.2)

$MnOOH + OH- \leftrightarrow MnO_2 + H_2O + e-$ (3.3.3)

P_2: $CoOOH + OH^- \leftrightarrow CoO_2 + H_2O + e-$ 0.42 V vs SCE (3.3.4)

The CD curve of the as-deposited film shows a nonlinear behaviour, it is the consequence of several redox reactions identified in CV, which confirm the pseudocapacitive behavior of the prepared electrode in good agreement with the work of Conway et al. [48]. The specific capacitance, as calculated from the charge-discharge curve, is 218 F g^{-1}.

The CV and CD curves of the spinel oxide $MnCo_2O_4$ films are shown in Figure 3.3.9 (bottom). The redox peaks at -0.04/-0.25 V vs SCE can be observed. They could be due to the redox reaction of $MnCo_2O_4$ with OH^- as below [49-51]:

$$MnCo_2O_4 + OH^- + H_2O \leftrightarrow MnOOH + 2CoOOH + e^- \qquad (3.3.5)$$

The capacitive response is enhanced in the more negative potential region. It has been shown that Co_3O_4/MnO_2 core/shell nanowires/nanosheets display an increased capacitive response in the low potential region as compared to Co_3O_4 [52]. This behavior can be due to the contribution of the redox reaction of manganese oxide with hydroxyl anions at more negative potentials [49]. The working potential window also widens compared to the as-deposited hydroxide. The increased area of the CV curves indicates that the capacitive response is enhanced after thermal treatment. CV curves show that the $MnCo_2O_4$ films annealed at 250 ^oC and 350 ^oC display an enhanced capacitive performance compared to the as-deposited ones or to the 450 ^oC annealed films. At 650 ^oC, the current response significantly decreases and this can be explained by the reduced porosity and increased crystal size, observed in the FEGSEM and TEM studies. The specific capacitances calculated from the CD curves (Figure 3.3.9, bottom right) are 430 F g^{-1}, 422 F g^{-1}, 271 F g^{-1} and 9 F g^{-1} for films annealed at 250 ^oC, 350 ^oC, 450 ^oC and 650 ^oC, respectively. Table 3.3.2 summaries the data of the electrochemical performance of the pseudocapacitive electrodes. As the main goal is to understand the effect of temperature, the electrochemical study do not includes longer-term cycling behavior.

When increasing the annealing temperature, the crystal size increases and leads to lower number of active sites for the redox reactions, and thereby to a decrease of the specific capacitance. In terms of enhanced pseudocapacitive response, the results suggest that there is an optimum temperature range for the film annealing.

Table 3.3.2. Specific capacitance and working potential of the as-deposited film and $MnCo_2O_4$ films.

	As-deposited	250 °C	350 °C	450 °C	650 °C
Specific capacitance (F g^{-1})	218	430	422	271	9
Working potential (V)	0.7	0.9	0.9	0.9	0.9

The specific capacitance values of the $MnCo_2O_4$ spinel oxides obtained by thermal annealing at 250–350 °C are increased comparatively to the untreated manganese-based oxides, but are still lower than the values reported for other spinel oxides [14, 17, 23]. Improvement of the specific capacitance could be achieved by increasing the surface area of the films, or by depositing on porous current collectors.

3.3.4. Conclusions

$MnCo_2O_4$ oxide films grown by electrochemical deposition followed by thermal annealing were produced and characterized. The annealing induces the transformation of the as-deposited mixed hydroxide phase into the spinel $MnCo_2O_4$ phase. The analysis of the surface morphology indicates the formation of a nanosheet percolation network in the as-deposited films that is preserved at low annealing temperatures. Detailed structural studies show that the as-deposited nanosheets are composed of nanocrystals with preferential orientations. These preferential orientations are suppressed with annealing at 250 °C and random distributed nanocrystals about 10 nm in size are observed, preserving the shape and size of the nanosheets. The nanocrystal size is further increased with subsequent annealing at higher temperature and large platelets with maximum size of 200 nm are formed after annealing at 650 °C. They are mainly composed of twin crystals in hexagonal prisms resulting in a decrease of the porosity and a drastic decrease of the electrochemical properties. The increase of the magnetic transition temperature with annealing temperature is directly related to the increased crystal size and crystalline quality. Electrochemical results detailed the redox reactions of the films with OH^- anions. The specific capacitance value is 217.8 F g^{-1} at 1 A g^{-1} in the as-deposited film. It increases to more than 400 F g^{-1} at 1 A g^{-1} in the $MnCo_2O_4$ film annealed at 250 ^oC-350 ^oC.

Acknowledgements

We would like to thank Fundação para a Ciência e Tecnologia (FCT) for the funding under the contract PTDC/CTM-MET/119411/2010, IDS-FunMat Erasmus Mundus PhD School, and the European COST Action MP1004. We also thank E. Eyraud (Institut Néel), C. Jimenez and H. Roussel (LMGP) for their supports for SQUID, FTIR and (GI)XRD experiments.

References

[1] L. Wang, Z.H. Dong, Z.G. Wang, F.X. Zhang, J. Jin, Layered α-$Co(OH)_2$ Nanocones as Electrode Materials for Pseudocapacitors: Understanding the Effect of Interlayer Space on Electrochemical Activity, Advanced Functional Materials, 23 (2013) 2758-2764.

[2] X. Guo, F. Zhang, D.G. Evans, X. Duan, Layered Double Hydroxide Films: Synthesis, Properties and Applications, Chemical Communications, 46 (2010) 5197-5210.

[3] C. Shang, S. Dong, S. Wang, D. Xiao, P. Han, X. Wang, L. Gu, G. Cui, Coaxial $Ni_xCo_{2x}(OH)_{6x}$/TiN Nanotube Arrays as Supercapacitor Electrodes, ACS Nano, 7 (2013) 5430–5436.

[4] G. Wang, L. Zhang, J. Zhang, A Review of Electrode Materials for Electrochemical Supercapacitors, Chem. Soc. Rev., 41 (2012) 797-828.

[5] V. Gupta, T. Kusahara, H. Toyama, S. Gupta, N. Miura, Potentiostatically Deposited Nanostructured α-$Co(OH)_2$: A High Performance Electrode Material for Redox-Capacitors, Electrochemistry Communications, 9 (2007) 2315-2319.

[6] J. Li, W. Zhao, F. Huang, A. Manivannan, N. Wu, Single-Crystalline $Ni(OH)_2$ and NiO Nanoplatelet Arrays as Supercapacitor Electrodes, Nanoscale, 3 (2011) 5103-5109.

[7] C. Yuan, J. Li, L. Hou, X. Zhang, L. Shen, X.W.D. Lou, Ultrathin Mesoporous $NiCo_2O_4$ Nanosheets Supported on Ni Foam as Advanced Electrodes for Supercapacitors, Advanced Functional Materials, 22 (2012) 4592-4597.

[8] Q. Yang, Z. Lu, J. Liu, X. Lei, Z. Chang, L. Luo, X. Sun, Metal Oxide and Hydroxide Nanoarrays: Hydrothermal Synthesis and Applications as Supercapacitors and Nanocatalysts, Progress in Natural Science: Materials International, 23 (2013) 351-366.

[9] S.B. Kulkarni, A.D. Jagadale, V.S. Kumbhar, R.N. Bulakhe, S.S. Joshi, C.D. Lokhande, Potentiodynamic Deposition of Composition Influenced $Co_{1-x}Ni_x$ LDHs Thin Film Electrode for Redox Supercapacitors, International Journal of Hydrogen Energy, 38 (2013) 4046-4053.

[10] Y. Gu, Z. Lu, Z. Chang, J. Liu, X. Lei, Y. Li, X. Sun, NiTi Layered Double Hydroxide Thin Films for Advanced Pseudocapacitor Electrodes, J. Mater. Chem. A, 1 (2013) 10655-10661.

[11] H.-C. Chien, W.-Y. Cheng, Y.-H. Wang, S.-Y. Lu, Ultrahigh Specific Capacitances for Supercapacitors Achieved by Nickel Cobaltite/Carbon Aerogel Composites, Advanced Functional Materials, 22 (2012) 5038-5043.

[12] V. Etacheri, R. Marom, R. Elazari, G. Salitra, D. Aurbach, Challenges in The Development of Advanced Li-ion Batteries: A Review, Energy & Environmental Science, 4 (2011) 3243-3262.

[13] C.M. Hayner, X. Zhao, H.H. Kung, Materials for Rechargeable Lithium-Ion Batteries, Annual Review of Chemical and Biomolecular Engineering, 3 (2012) 445-471.

[14] G. Zhang, X.W. Lou, Controlled Growth of $NiCo_2O_4$ Nanorods and Ultrathin Nanosheets on Carbon Nanofibers for High-performance Supercapacitors, Sci Rep, 3 (2013).

[15] Z. Wu, Y. Zhu, X. Ji, $NiCo_2O_4$-based Materials for Electrochemical Supercapacitors, Journal of Materials Chemistry A, 2 (2014) 14759-14772.

[16] Q. Yang, Z. Lu, Z. Chang, W. Zhu, J. Sun, J. Liu, X. Sun, X. Duan, Hierarchical Co_3O_4 Nanosheet@Nanowire Arrays with Enhanced Pseudocapacitive Performance, RSC Adv., 2 (2012) 1663-1668.

[17] C. Yuan, J. Li, L. Hou, X. Zhang, L. Shen, X.W. Lou, Ultrathin Mesoporous $NiCo_2O_4$ Nanosheets Supported on Ni Foam as Advanced Electrodes for Supercapacitors, Advanced Functional Materials, 22 (2012) 4592-4597.

[18] W. Wei, X. Cui, W. Chen, D.G. Ivey, Manganese Oxide-based Materials as Electrochemical Supercapacitor Electrodes, Chem. Soc. Rev., 40 (2011) 1697-1721.

[19] H.-Y. Wang, F.-X. Xiao, L. Yu, B. Liu, X.W. Lou, Hierarchical α-MnO_2 Nanowires@$Ni_{1-x}Mn_xO_y$ Nanoflakes Core–Shell Nanostructures for Supercapacitors, Small, 10 (2014) 3181-3186.

[20] L. Li, Y.Q. Zhang, X.Y. Liu, S.J. Shi, X.Y. Zhao, H. Zhang, X. Ge, G.F. Cai, C.D. Gu, X.L. Wang, J.P. Tu, One-dimension $MnCo_2O_4$ Nanowire Arrays for Electrochemical Energy Storage, Electrochimica Acta, 116 (2014) 467-474.

[21] K. Uusi-Esko, E.L. Rautama, M. Laitinen, T. Sajavaara, M. Karppinen, Control of Oxygen Nonstoichiometry and Magnetic Property of $MnCo_2O_4$ Thin Films Grown by Atomic Layer Deposition, Chemistry of Materials, 22 (2010) 6297-6300.

[22] Q. Wang, D. O’Hare, Recent advances in the synthesis and application of layered double hydroxide (LDH) nanosheets, Chemical reviews, 112 (2012) 4124-4155.

[23] Q. Yang, Z. Lu, X. Sun, J. Liu, Ultrathin Co_3O_4 Nanosheet Arrays with High Supercapacitive Performance, Sci Rep, 3 (2013).

[24] S.R. Shieh, T.S. Duffy, Raman Spectroscopy of $Co(OH)_2$ at High Pressures: Implications for Amorphization and Hydrogen Repulsion, Phys. Rev. B, 66 (2002) 134301.

[25] J.A. Koza, C.M. Hull, Y.-C. Liu, J.A. Switzer, Deposition of β-$Co(OH)_2$ Films by Electrochemical Reduction of Tris(ethylenediamine)cobalt(III) in Alkaline Solution, Chemistry of Materials, 25 (2013) 1922-1926.

[26] M. Aghazadeh, S. Dalvand, M. Hosseinifard, Facile Electrochemical Synthesis of Uniform β-$Co(OH)_2$ Nanoplates for High Performance Supercapacitors, Ceramics International, 40 (2014) 3485-3493.

[27] M. Aghazadeh, H.M. Shiri, A.-A.M. Barmi, Uniform β-Co(OH)2 Disc-like Nanostructures Prepared by Low-temperature Electrochemical Route as an Electrode Material for Supercapacitors, Applied Surface Science, 273 (2013) 237-242.

[28] H. Lutz, H. Möller, M. Schmidt, Lattice Vibration Spectra. Part LXXXII. Brucite-type Hydroxides $M(OH)_2$(M= Ca, Mn, Co, Fe, Cd)—IR and Raman spectra, neutron diffraction of $Fe(OH)_2$, Journal of Molecular Structure, 328 (1994) 121-132.

[29] R. Downs, The RRUFF Project: An Integrated Study of The Chemistry, Crystallography, Raman and Infrared Spectroscopy of Minerals, Program and abstracts of the 19th general meeting of the International Mineralogical Association in Kobe, Japan, 2006, pp. O03-13.

[30] S. Deabate, F. Fourgeot, F. Henn, X-ray Diffraction and Micro-Raman Spectroscopy Analysis of New Nickel Hydroxide Obtained by Electrodialysis, Journal of Power Sources, 87 (2000) 125-136.

[31] N. Padmanathan, S. Selladurai, Mesoporous MnCo2O4 Spinel Oxide Nanostructure Synthesized by Solvothermal Technique for Supercapacitor, Ionics, 20 (2014) 479-487.

[32] T. Nissinen, M. Leskelä, M. Gasik, J. Lamminen, Decomposition of Mixed Mn and Co Nitrates Supported on Carbon, Thermochimica Acta, 427 (2005) 155-161.

[33] Z.-Q. Liu, K. Xiao, Q.-Z. Xu, N. Li, Y.-Z. Su, H.-J. Wang, S. Chen, Fabrication of Hierarchical Flower-like Super-structures Consisting of Porous $NiCo_2O_4$ Nanosheets and Their Electrochemical and Magnetic Properties, RSC Adv., 3 (2013) 4372-4380.

[34] L. Huang, D. Chen, Y. Ding, S. Feng, Z.L. Wang, M. Liu, Nickel–Cobalt Hydroxide Nanosheets Coated on $NiCo_2O_4$ Nanowires Grown on Carbon Fiber Paper for High-Performance Pseudocapacitors, Nano Lett., 13 (2013) 3135-3139.

[35] C.-W. Tang, C.-B. Wang, S.-H. Chien, Characterization of Cobalt Oxides Studied by FT-IR, Raman, TPR and TG-MS, Thermochimica Acta, 473 (2008) 68-73.

[36] V. Hadjiev, M. Iliev, I. Vergilov, The Raman Spectra of Co_3O_4, Journal of Physics C: Solid State Physics, 21 (1988) L199.

[37] J. Yang, H. Liu, W.N. Martens, R.L. Frost, Synthesis and Characterization of Cobalt Hydroxide, Cobalt Oxyhydroxide, and Cobalt Oxide Nanodiscs, J. Phys. Chem. C, 114 (2010) 111-119.

[38] L. Xu, Y.-S. Ding, C.-H. Chen, L. Zhao, C. Rimkus, R. Joesten, S.L. Suib, 3D Flowerlike α-Nickel Hydroxide with Enhanced Electrochemical Activity Synthesized by Microwave-assisted Hydrothermal Method, Chemistry of Materials, 20 (2007) 308-316.

[39] H.B. Li, M.H. Yu, F.X. Wang, P. Liu, Y. Liang, J. Xiao, C.X. Wang, Y.X. Tong, G.W. Yang, Amorphous Nickel Hydroxide Nanospheres with Ultrahigh Capacitance and Energy Density as Electrochemical Pseudocapacitor Materials, Nat Commun, 4 (2013).

[40] E.D. McLaughlin, L.A. Breaux, Chemical Mineralogy, Smelting and Metallization, (2009).

[41] R. Ma, K. Takada, K. Fukuda, N. Iyi, Y. Bando, T. Sasaki, Topochemical Synthesis of Monometallic (Co^{2+}–Co^{3+}) Layered Double Hydroxide and Its Exfoliation into Positively Charged $Co(OH)_2$ Nanosheets, Angewandte Chemie International Edition, 47 (2008) 86-89.

[42] M. Hamdani, R. Singh, P. Chartier, Co_3O_4 and Co-based Spinel Oxides Bifunctional Oxygen Electrodes, Int. J. Electrochem. Sci, 5 (2010) 556-577.

[43] N.T. Khi, J. Yoon, H. Baik, S. Lee, D.J. Ahn, S.J. Kwon, K. Lee, Twinning Boundary-Elongated Hierarchical Pt Dendrites with An Axially Twinned Nanorod Core for Excellent Catalytic Activity, CrystEngComm, 16 (2014) 8312-8316.

[44] L. Zhang, C.M. Holt, E.J. Luber, B.C. Olsen, H. Wang, M. Danaie, X. Cui, X. Tan, V. W. Lui, W.P. Kalisvaart, High Rate Electrochemical Capacitors from Three-Dimensional Arrays of Vanadium Nitride Functionalized Carbon Nanotubes, J. Phys. Chem. C, 115 (2011) 24381-24393.

[45] N. Zhao, W. Nie, X. Liu, S. Tian, Y. Zhang, X. Ji, Shape ‐ and Size ‐ Controlled Synthesis and Dependent Magnetic Properties of Nearly Monodisperse Mn_3O_4 Nanocrystals, Small, 4 (2008) 77-81.

[46] L. Cao, F. Xu, Y.Y. Liang, H.L. Li, Preparation of the Novel Nanocomposite $Co(OH)_2$/Ultra-Stable Y Zeolite and Its Application as a Supercapacitor with High Energy Density, Advanced materials, 16 (2004) 1853-1857.

[47] S.H. Kim, Y.I. Kim, J.H. Park, J.M. Ko, Cobalt-Manganese Oxide/Carbon-nanofiber Composite Electrodes for Supercapacitors, Int. J. Electrochem. Sci, 4 (2009) 1489-1496.

[48] T.-C. Liu, W. Pell, B. Conway, Stages in The Development of Thick Cobalt Oxide Films Exhibiting Reversible Redox Behavior and Pseudocapacitance, Electrochimica Acta, 44 (1999) 2829-2842.

[49] B. Messaoudi, S. Joiret, M. Keddam, H. Takenouti, Anodic Behaviour of Manganese in Alkaline Medium, Electrochimica Acta, 46 (2001) 2487-2498.

[50] T. Zhou, S. Mo, S. Zhou, W. Zou, Y. Liu, D. Yuan, Mn_3O_4/Worm-like Mesoporous Carbon Synthesized via A Microwave Method for Supercapacitors, J Mater Sci, 46 (2011) 3337-3342.

[51] K. Deori, S.K. Ujjain, R.K. Sharma, S. Deka, Morphology Controlled Synthesis of Nanoporous Co_3O_4 Nanostructures and Their Charge Storage Characteristics in Supercapacitors, ACS Appl. Mater. Interfaces, 5 (2013) 10665-10672.

[52] L. Yu, G. Zhang, C. Yuan, X.W.D. Lou, Hierarchical $NiCo_2O_4$@MnO_2 Core–Shell Heterostructured Nanowire Arrays on Ni Foam as High-performance Supercapacitor Electrodes, Chemical Communications, 49 (2013) 137-139.

3.4. Morphological changes and electrochemical response of mixed nickel manganese oxides as charge storage electrodes✧

Tuyen Nguyen[a,b], Michel Boudard[b], Laetitia Rapenne[b], M. João Carmezim[a,c], M. Fátima Montemor[a]

[a] CQE - Centro de Química Estrutural, Insituto Superior Técnico, Universidade de Lisboa, 1049-001 Lisboa, Portugal.

[b] LMGP, Univ. Grenoble Alpes, CNRS, F-38000 Grenoble, France.

[c] ESTSetúbal, Instituto Politécnico de Setúbal, 1959-007 Lisboa, Portugal.

Nickel manganese (Ni-Mn) oxides films were prepared by potentiostatic electrodeposition over stainless steel and post thermal annealing at 250 ^oC. Morphological and structural changes were observed depending upon the Ni to Mn ratio in the electrolyte. Single-phase $Ni_{1-x}Mn_xO$ oxide was formed with low Mn content, whereas two-phases composed of $Ni_{1-x}Mn_xO$ and $Ni_xMn_{3-x}O_4$ were formed at high Mn content. Electrochemical studies revealed an increase of the specific capacitance of the mixed Ni-Mn electrodes compared to the single metal oxides, thus pin-pointing a synergistic effect. The Ni-Mn oxides film displayed specific capacitances of about 300 F g^{-1} in a potential window of 0.5 V at an applied current density of 1 A g^{-1}. The rate capability of the oxides was 58% when the applied current was increased from 1 A g^{-1} to 10 A g^{-1}. The Ni-Mn oxide film exhibits excellent cycling stability with 100% capacitance retention after 1500 cycles.

Keywords: mixed oxide, nickel manganese oxide, redox supercapacitors, electrodeposition, morphological changes

---

✧ **Adapted from Journal of Materials Chemistry A, 2015,3, 10875-10882**

3.4.1. Introduction

Transition metal oxides (TMOs), such as RuO_2 and Co oxides were formerly studied by B. Conway who evaluated their pseudocapacitance and ability to be used as charge storage electrodes for application in redox supercapacitors [1, 2]. Presently, some mixed TMOs regained interest for charge storage electrodes and have been intensively studied as new redox materials with potential application in asymmetric supercapacitors. Mixed TMOs show enhanced electrochemical performance when compared to single metallic oxides [3], due to (i) increased electrical conductivity [4] and (ii) the combined contribution of different transition metals to the reversible redox reactions [5]. Examples of mixed TMOs found in recent literature include $NiCo_2O_4$ [6], $NiMoO_4$ [7], and $CoFe_2O_4$ [8].

Generally, mixed TMOs are prepared by solution based methods such as hydrothermal [9], sol-gel [10], chemical bath deposition [11], or electrodeposition [12]. The good electrochemical properties of the mixed TMOs depend not only on the stoichiometries of the oxides [13] but also on the presence of highly porous nanostructures such as nanowires and/or nanoneedles [14], nanosheets [15], and nanotubes [16] that can be obtained *via* an optimal preparation process.

Among mixed TMOs, nickel manganese (Ni-Mn) oxides are of great interest due to advantages resulting from the combination of Ni and Mn oxides. By one hand, Ni oxides have the advantage of reaching high theoretical specific capacitance values [17] of 2584 F g^{-1}. On the other hand, Mn oxides have the advantage of low cost, various valences and multiple redox reactions [18]. However, very few works addressing the electrochemical response of mixed Ni-Mn oxides for redox supercapacitors have been reported up to now. The published work show that spinel $NiMn_2O_4$ oxides prepared by epoxide-driven sol−gel process and thermal treatment [19] exhibited specific capacitance of 243 F g^{-1} at 5 mV s^{-1}. Porous $NiMn_2O_4$ with various morphologies including bipyramid, fusiform and plates, were prepared by thermal decomposition and transformation from oxalate precursors [20], showing specific capacitances of 180 F g^{-1} at 0.25 A g^{-1}. $Ni_yMn_{1-y}O_x$ with granular morphology were synthesized by *in situ* inclusion of Ni during the growth of Mn oxide [21] and the resulting electrodes showed a specific capacitance of 380 F g^{-1} at 5 mV s^{-1}.

Electrochemical deposition is a simple, low cost route and a one-step process that allows preparing self-sustained active materials directly on current collectors. It has been widely reported that surface morphology of films prepared by electrodeposition can be turned by varying current, potential, temperature, and additives [22]. However, the possibility of turning the surface morphology by varying chemical compositions is rarely reported. In this work, Ni-Mn oxides films were grown directly on stainless steel substrates, via electrodeposition followed by thermal annealing. The study highlights the effect of the Ni:Mn ratio on the morphology of the films produced and a correlation with the electrochemical performance.

3.4.2. Experimental

All chemical reagents were high purity grades and were obtained from Sigma- Aldrich. Stainless steel (AISI 304) obtained from Goodfellow was used as substrate for the electrodeposition.

The electrodeposition experiments were performed in electrolytes containing Mn nitrate $Mn(NO_3)_2$ and Ni nitrate $Ni(NO_3)_2$ using a conventional electrochemical system (Voltalab PGZ100 Potentiostat from Radiometer) at room temperature using the stainless steel as working electrode, saturated calomel electrode (SCE) as reference electrode and a platinum foil as counter electrode. All potentials referred in this work are referred to the SCE.

The depositions were performed in potentiostatic mode, applying a potential of -1.1 V with total passed charge of -600 mC cm^{-2}. The molar ratio of $Ni(NO_3)_2$ and $Mn(NO_3)_2$ was varied in the electrolyte, keeping a total concentration of 0.1 M. The $Ni(NO_3)_2$:$Mn(NO_3)_2$ ratios tested were: 1:0, 3:1, 1:1, 1:3, 1:6, 1:9 and 0:1 and the corresponding films are denoted as NM-1:0, NM-3:1, NM-1:1, NM-1:3, NM-1:6, NM-1:9 and NM-0:1 as shown in Table 3.4.1, respectively. After electrodeposition, all the specimens were annealed at 250°C for 3 hours. The masses of the films were carefully weighed and are shown in Table 3.4.1.

Table 3.4.1. Ni:Mn ratio in the electrolytes used for electrodepositions, corresponding film notation and mass.

Ni:Mn	1:0	3:1	1:1	1:3	1:6	1:9	0:1
Film	NM-1:0	NM-3:1	NM-1:1	NM-1:3	NM-1:6	NM-1:9	NM-0:1
Mass (mg cm^{-2})	0.32	0.29	0.30	0.30	0.28	0.26	0.23

Field emission gun scanning electron microscopy (FEG-SEM, JEOL 7001F microscope) equipped with energy disperse x-ray spectroscopy (EDX) was used for morphological investigation and elemental analysis. Raman spectroscopy (Horiba/Jobin Yvon LabRam spectrometer) with He-Ne laser beam of 632.8 nm was used for the structural studies. The structural details were studied by transmission electron microscopy (TEM, JEOL JEM-2010 microscope) operating at an acceleration voltage of 200 keV.

To evaluate electrochemical response, cyclic voltammetry (CV) and charge-discharge (CD) tests were carried out in a conventional three-electrode electrochemical cell using 1 M KOH as electrolytes and the Ni-Mn oxide films as working electrode.

3.4.3. Results and Discussion

Figure 3.4.1a shows the elemental composition of the electrodeposited films, obtained by EDX elemental analysis in terms of Ni to Mn ratios and compares it with the electrolyte composition. Figure 3.4.1b-h shows the FEG-SEM images of the films deposited from electrolytes containing different Ni:Mn ratios and subsequently annealed. Figure 3.4.1a reveals that the Ni:Mn ratio in the electrodeposited films is higher than the corresponding ratio in the electrolyte. The ratios in the films are of 5.9, 2.9, 0.67, 0.27 and 0.14 for the corresponding values in the solutions of 3, 1, 0.33, 0.16 and 0.11. The film deposition is based on the reaction of the metallic cations (Ni^{2+}, Mn^{2+}) in the electrolyte with the hydroxyl anions generated through nitrate reduction or water electrolysis on the electrode to form $Ni(OH)_2$/$Mn(OH)_2$, being transformed into the oxide phases by thermal annealing.

The solubility constant of $Mn(OH)_2$ is higher than that of $Ni(OH)_2$, leading to a decreased Mn content in the electrodeposited films [23].

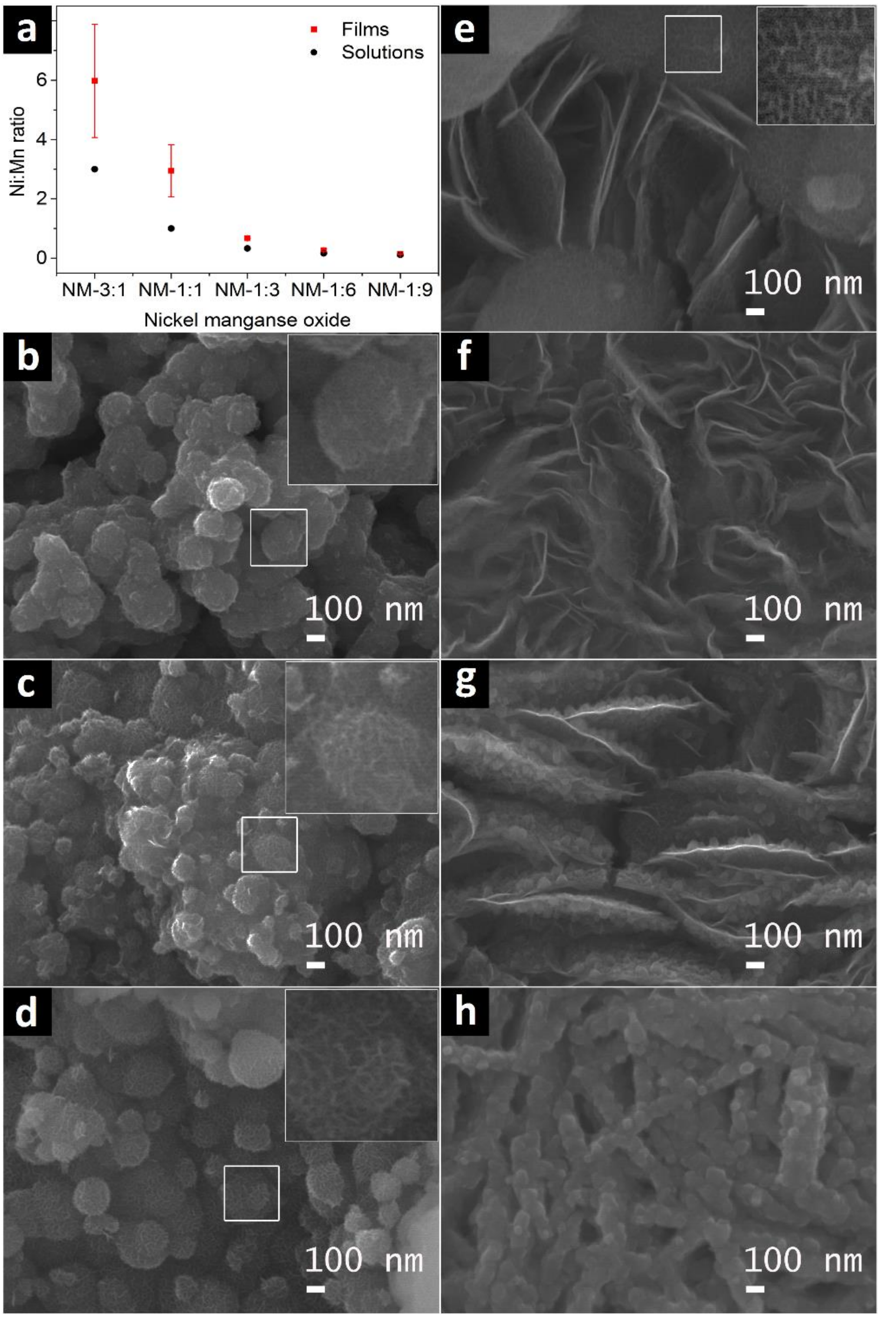

Figure 3.4.1. Composition and surface morphology of the electrodeposited films. Ni:Mn ratio in the films (measured by EDX) *vs.* the ratio in the electrolyte (a). FEG-SEM images of the NM-1:0 (b), NM-3:1 (c), NM-1:1 (d), NM-1:3 (e), NM-1:6 (f), NM-1:9 (g) and NM-0:1 (h) films. Insets: enlargement of white squares marked in the corresponding images.

The FEG-SEM images in Figure 3.4.1 show the morphological changes when varying the Ni:Mn ratios in the electrolyte. The single metal oxides revealed particles agglomerates for single the Ni oxide (NM-1:0) and interconnected worm-like nanostructures for the single Mn oxide (NM-0:1), respectively. The co-deposition of Ni and Mn in the NM-3:1 and NM-1:1 films results in the formation of surface morphologies similar to that of the NM-1:0 film and creates texture on the agglomerated particles (insets) due to thin layers of nanosheets. Further increase of Mn content favours the growth of larger 2D nanosheets, leading to the creation of a unique surface morphology constituted of nanosheets connected with texture particles as observed in the NM-1:3 film. The surface morphologies of the NM-1:6 and NM-1:9 films reveal the presence of nanosheets and nanosheets containing of attached nanoparticles, respectively. The morphologies that characterize the NM-1:3 oxides are, for the best of our knowledge, reported for the first time in this work. Thus the porous morphology of the produced films depends upon the electrolyte and resulting film composition.

It has been reported that the surface morphology of $Ni_xCo_{3-x}O4$ films [13] is constituted of nanosheets without significant changes when varying the Ni to Co ratio. The surface morphology of Co_3O_4 and $Ni_xCo_{3-x}O_4$ at high Ni content is also composed of nanosheets. On the other hand, Ni-Fe oxide films have shown relevant morphological changes [24] when varying the Ni to Fe ratio. The Ni oxide film and Fe oxide film exhibit different surface morphologies, which are composed of thin nanobelts and of big particles with step terrace surface, respectively. When compared to literature [13, 24], the morphological changes observed in this work can be explained assuming different preferential growth of the Ni oxide and Mn oxide as suggested in the corresponding FEG-SEM images. Thus, the results highlight the possibility of turning the surface morphology of electrodeposited Ni-Mn electrodes by varying the composition of the electrolyte.

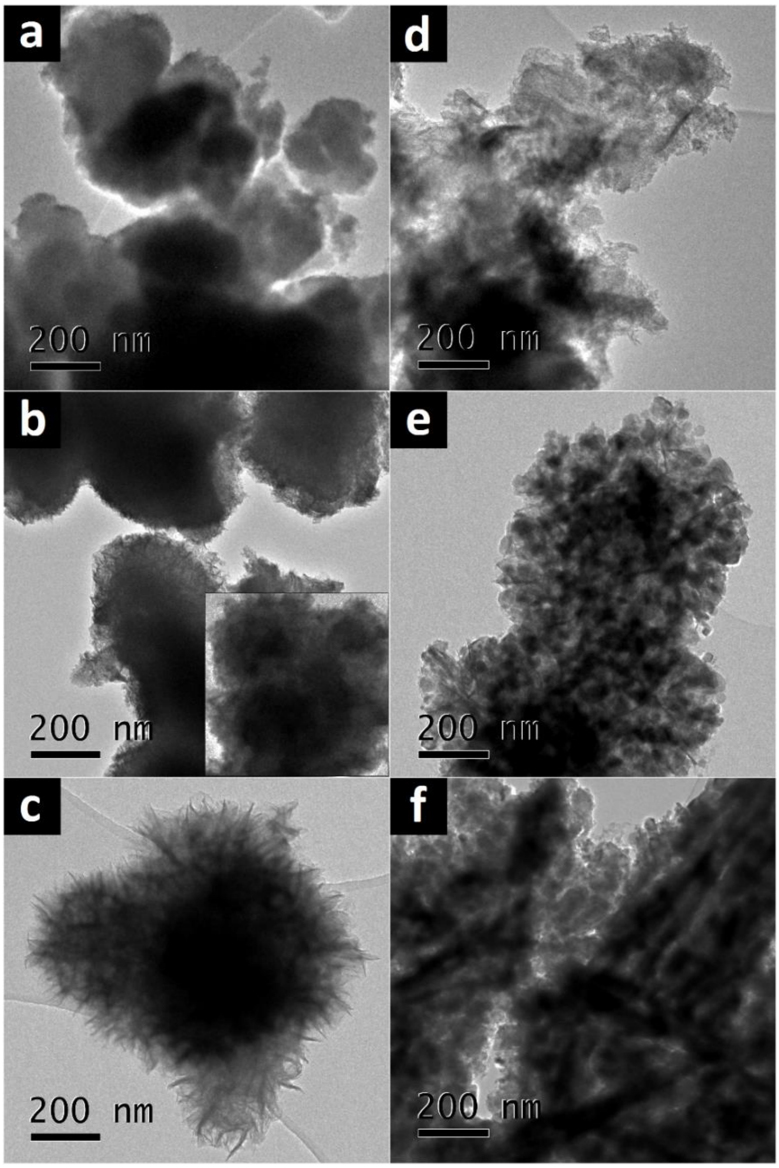

Figure 3.4.2. TEM images of the NM-1:0 (a), NM-3:1 (b inset), NM-1:1 (b), NM-1:3 (c), NM-1:6 (d), NM-1:9 (e) and NM-0:1 (f) films. The inset is in the same magnification with that of other images.

The TEM images depicted in Figure 3.4.2 show the presence of particles and wire-like structures in the NM-1:0 and NM-0:1 films. Thin layers of nanosheets start forming on the surface of the particles present in the NM-3:1 film and become more evident in NM-1:1 film, indicating the particles develop more texture by adding Mn. Large nanosheets grown on the texture particles are present in the NM-1:3 film. Nanosheets and nanoparticles attached to nanosheets can be observed in NM-1:6 and NM-1:9. This is in agreement with the FEG-SEM observations, evidencing the morphological changes of the films containing different Ni:Mn ratios.

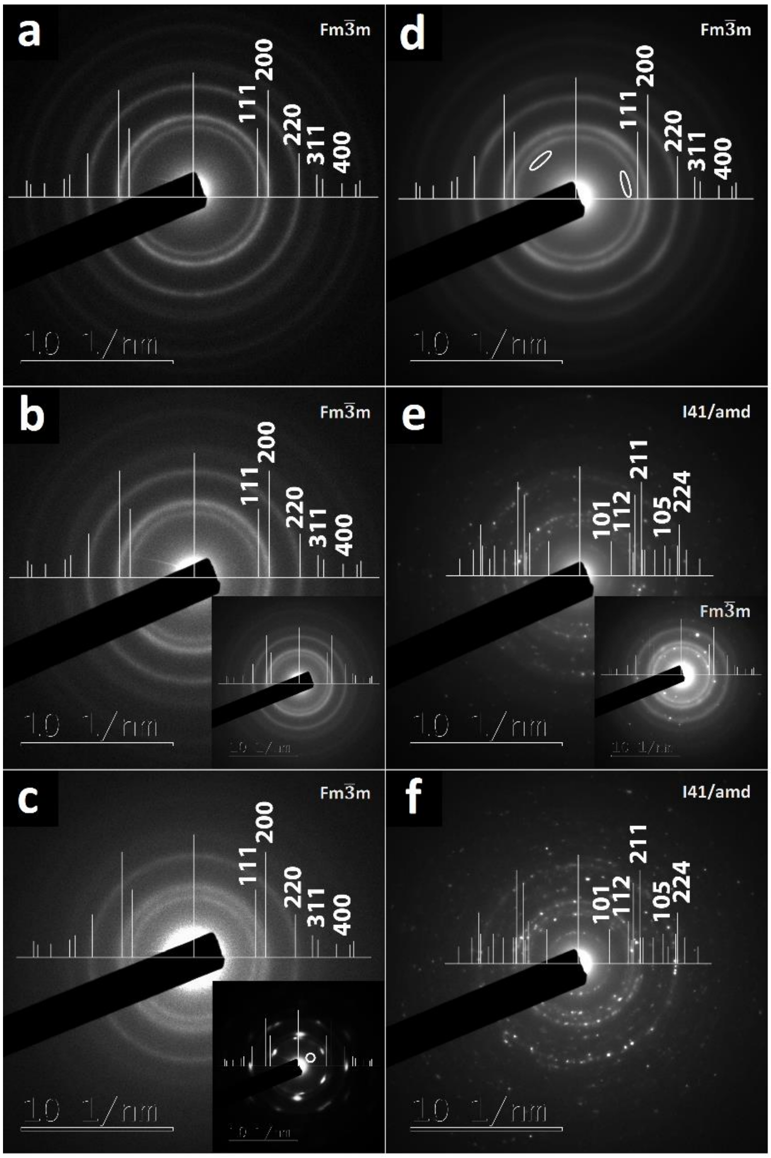

Figure 3.4.3. SAED patterns of NM-1:0 (a), NM-3:1 (b inset), NM-1:1 (b), NM-1:3 (c), NM-1:6 (d), NM-1:9 (e) and NM-0:1 (f). Insets in NM-1:3 (c) and NM-1:9 (e) SAED: SAED patterns measured at different areas of the samples. White circle and ellipsoids marked in SAED patterns (c inset and d) correspond to the diffraction from another phase.

The SAED patterns of the NM-1:0, NM-3:1, NM-1:1, NM-1:3, and NM-1:6 films (Figure 3.4.3) present well-defined diffraction rings, indicating the polycrystalline nature of the formed films. The broadening of the rings accounts for the nanocrystalline nature of the films. The SAED patterns of the NM-1:9 and NM-0:1 films are composed of diffraction spots, forming discrete rings, which are probably due to the presence of large nanocrystals. Diffraction rings in the SAED patterns of NM-1:0

(Figure 3.4.3a) and NM-0:1 (Figure 3.4.3f) films well match with the diffraction patterns of the face-centred cubic (FCC) NiO (ICDD card n° 00-047-1049, a = 4.177 Å, space group Fm-3m) and of the body-centred tetragonal Mn_3O_4 (ICDD card n° 00-024-0734, a = 5.76210 Å, c =9.46960 Å, space group I41/amd). The intense rings indicated in the figures correspond to the diffractions from (111), (200), (220) and (311) lattice planes of NiO and from (101), (112), (200), (103) and (211) lattice planes of Mn_3O_4. The NM-3:1, NM-1:1, NM-1:3 and NM-1:6 mixed oxide films present SAED patterns similar to that of NM-1:0, thus suggesting the substitution of Mn into the NiO lattice forming mixed $Ni_{1-x}Mn_xO$ oxides. Indeed, the cubic lattice parameter of the solid solutions $Ni_{1-x}Mn_xO$, calculated from the SAED patterns, increases when increasing Mn content, which are 4.1094, 4.1094, 4.1368, 4.2333, 4.2916, and 4.2916 Å for NM-1:0, NM-3:1, NM-1:1, NM-1:3, NM-1:6 and NM-1:9 films, respectively. The deviation of the lattice parameter of NM-1:0 films from the reference value can be due to the nanocrystalline nature of the film. It is worth to note that NiO structures with 75% Mn in cation sites has been reported (ICDD card n° 01-078-0427). Additionally, weak diffraction spots can be found at lattice distances close to 0.49 nm and 0.27 nm (marked by white circle and ellipsoids in the corresponding patterns) in NM-1:3 (Figure 3.4.3c inset) and NM-1:6 (Figure 3.4.3d) patterns, which seem to correspond to diffractions from the (101) and (103) lattice planes of Mn_3O_4. Moreover, the possibility of Ni substitution in Mn_3O_4 phase cannot be excluded. This result can be due to phase separation and will be further clarified by the Raman analysis. The NM-1:9 patterns (Figure 3.4.3e) show Mn_3O_4 or NiO (inset) diffraction characteristics, depending on the area under measurement, pointing out the phase separation. The lattice parameter (a = 5.691 Å, c = 9.595 Å) of Mn_3O_4 phase in NM-1:9 film is different from that (a = 5.716 Å, c = 9.497 Å) of the NM-0:1 film, which can be due to the substitution of Ni in the Mn_3O_4, forming $Ni_xMn_{3-x}O_4$.

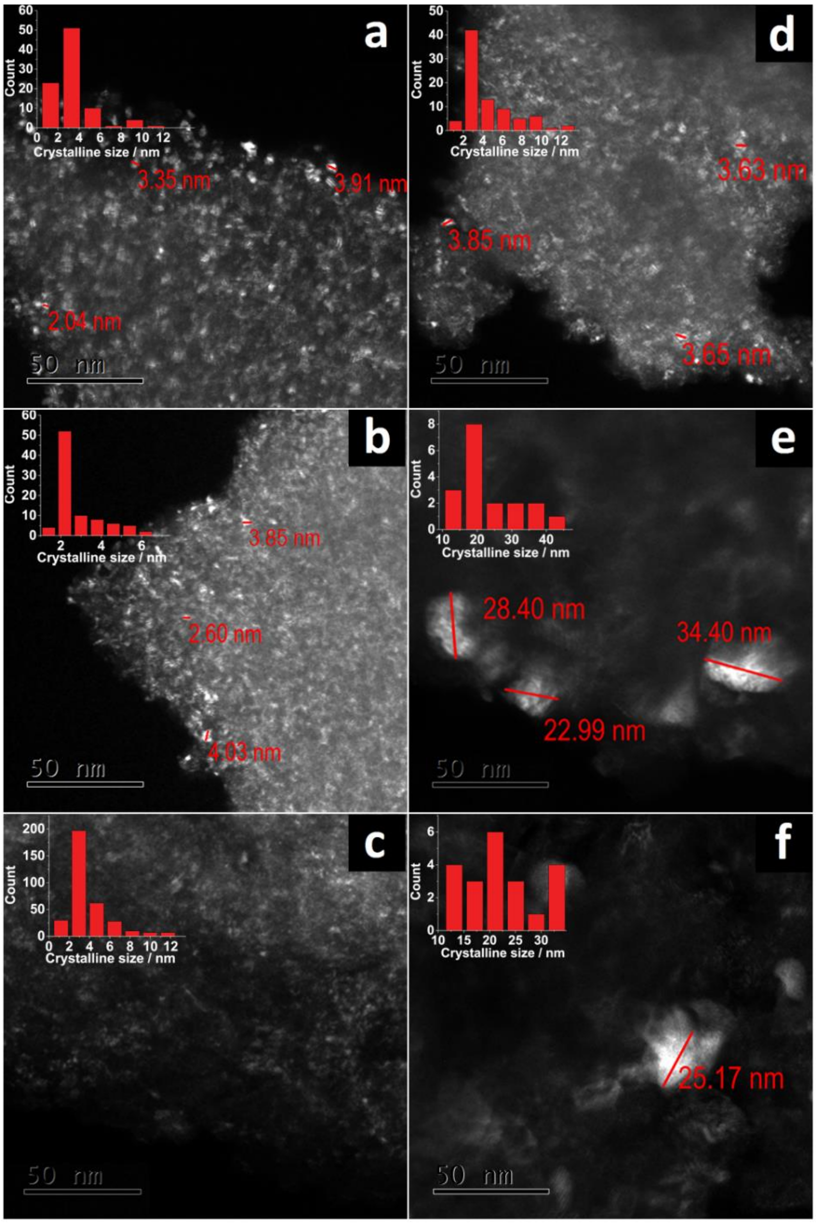

Figure 3.4.4. DFTEM images of NM-1:0 (a), NM-1:1 (b), NM-1:3 (c), NM-1:6 (d), NM-1:9 (e) and NM-0:1 (f) films. Insets: crystal size distributions. The crystal size distributions of NM-1:9 and NM-0:1 films were calculated from lower magnification images (not shown), DFTEM images with the same magnification with that of the other images were used for comparison.

To detail crystal size and its distribution, dark-field TEM (DFTEM) observations were carried out. DFTEM images were recorded by selecting a part of the two first rings of SAED patterns with the objective aperture and results are shown in Figure 3.4.4. The images show that the films are composed of nanocrystals and the crystal size and distribution is shown in the inset of DF images.

The average and range of the crystal sizes are approximately 2 nm and 1-12 nm for NM-1:0, NM-3:1, NM-1:1, NM-1:3 and NM-1:6 films and about 20 nm and 10-40 nm for NM-1:9 and NM-0:1 films. The large crystal sizes in NM-1:9 and NM-0:1 films result in the discrete diffraction rings in the SAED patterns as previously shown in Figure 3.4.3e and f. These results are in good agreement with the size of the nanoparticles surrounding the nanosheets and forming nanoworms as observed in the FEG-SEM images (Figure 3.4.1g and h).

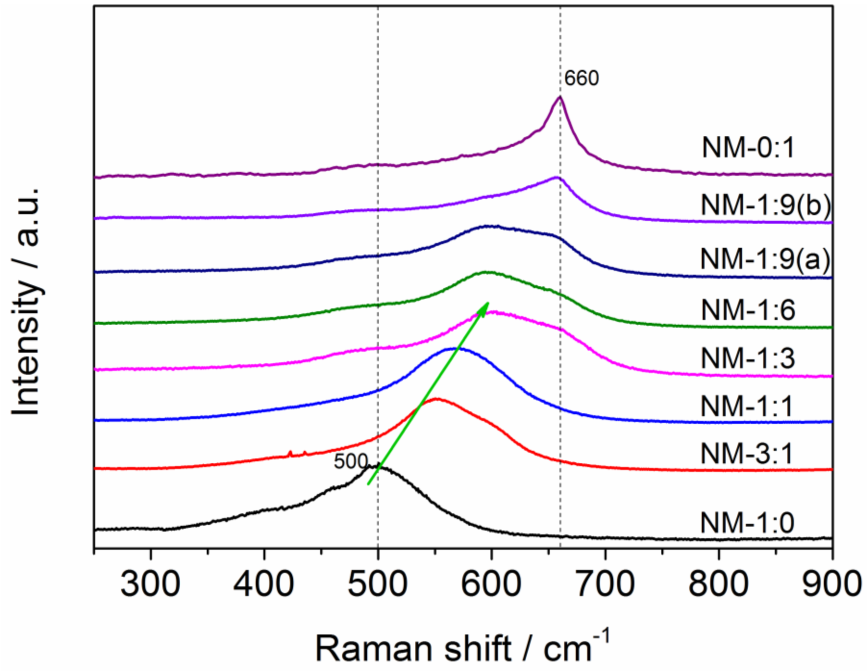

Figure 3.4.5. Raman spectra of the deposited films with different Ni:Mn ratios. NM-1:9(a) and NM-1:9(b) are Raman spectra measured at different spots on the NM-1:9 film. Important Raman bands are marked. Vertical and arrow lines are only visual guides.

The Raman spectra of the films deposited with different Ni:Mn ratios are shown in Figure 3.4.5. The Raman spectra of the nickel oxide (NM-1:0) and of the manganese oxide (NM-0:1) shows intense bands at approximately 500 cm^{-1} and 660 cm^{-1}, which can correspond to the Ni-O stretching mode of NiO [25] and Mn-O breathing mode of Mn_3O_4 [26]. The broadening of the Raman bands is due to the nanocrystalline nature of the films [27]. The Raman spectra of the mixed oxides show a blue shift of the Ni-O stretching band to 550, 571 cm^{-1} for NM-3:1, NM-1:1 films and to 598 cm^{-1} for NM-1:3, NM-

1:6, NM-1:9 films. The shift of the bands can be explained by the formation of mixed $Ni_{1-x}Mn_xO$, as shown in the TEM results. The NM-1:3, NM-1:6, NM-1:9 Raman spectra depict a band at 660 cm^{-1} at a position similar to the Mn-O breathing band in Mn_3O_4, probably due to the co-existing phases. The Raman spectra of the NM-1:9 film show differences in the band intensities, depending on the measuring spots on the same film. NM-1:9(a) and NM-1:9(b) are Raman spectra measured at different spots on the NM-1:9 film. The spectrum of NM-1:9(a) shows an intense band similar to the one expected for the mixed $Ni_{1-x}Mn_xO$ oxide and the spectrum of NM-1:9(b) shows an intense band similar to Mn_3O_4, in good agreement with TEM observations.

To assess the electrochemical behavior of the deposited films, CV and CD measurements were carried out. The CVs were performed at a scan rate of 20 mV s^{-1} in a potential window between 0 and 0.6 V and CDs were performed at constant current of 1 A g^{-1} in a potential window between 0 and 0.5 V. The CV results are depicted in Figure 3.4.6a and it is possible to observe that both single oxides, the Ni oxide (NM-1:0) and the Mn oxide (NM-0:1), do not display defined redox peaks. However there is a weak broadened wave that contributes to the increase of the current density. These shoulders are probably due to the redox reactions (Ni^{2+}/Ni^{3+} and Mn^{2+}/Mn^{3+}) with the hydroxyl (OH^-) anions in the alkaline electrolyte as below [17, 28, 29]:

$Mn_3O_4 + 2H_2O + OH^- \leftrightarrow 2MnOOH + Mn(OH)_3 + e^-$ 0-0.2V (3.4.1)

$2(2MnOOH+Mn(OH)_3)+ 3OH^- \leftrightarrow (6MnO_2).5H_2O + 3H^+ + 6e^-$ (3.4.2)

$NiO + OH^- \leftrightarrow NiOOH + e^-$ 0.4-0.6V (3.4.3)

For the mixed Ni-Mn oxide films, the redox peaks become more evidenced in the CV curves. The peak position is shifted to lower potentials when the Mn content increases. The broad redox peaks are likely to include the contributions of the redox reactions of Ni oxide and Mn oxide with OH^-. Moreover, the current response of the redox peak increases for the NM-1:0, NM-3:1, and NM-1:1 films, and reaches a maximum value for the NM-1:3 one. Then it decreases when the Mn content increases. These results evidence a synergistic effect on the redox reactions of the mixed oxides.

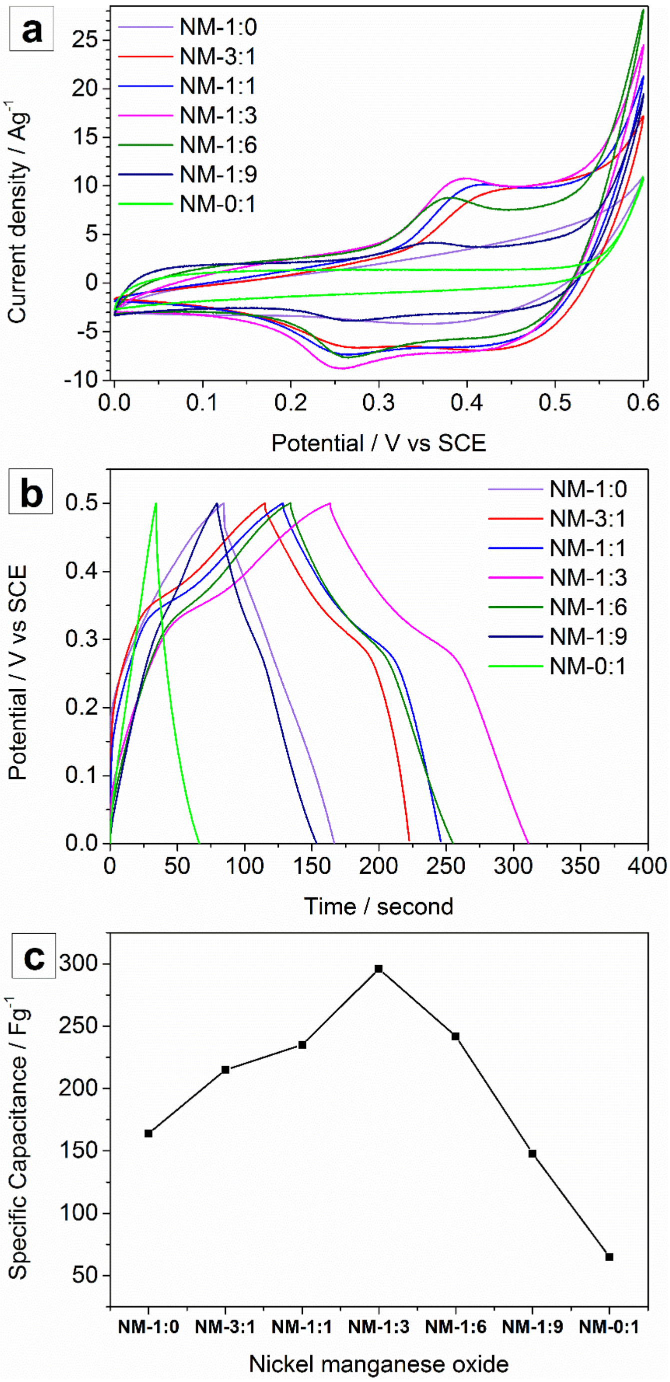

Figure 3.4.6. Cyclic Voltammetry curves at a scan rate of 20 mV s^{-1} (a) and charge-discharge curves at a current density of 1 A g^{-1} (b) for the films with different Ni:Mn ratio and specific capacitance of the films (c).

The CD results are presented in Figure 3.4.6b. The deviations from a non-linear slope in the CD curves is characteristic of materials that display a pseudocapacitive behavior [2] due to multiple redox reactions. The discharge time is the highest for the NM-1:3 films, in good agreement with the high current density response observed in the CV results. The specific capacitance of the films was calculated from the CD curves using the formula:

$$C = \frac{It}{\Delta V} \qquad (3.4.4)$$

where I, t, ΔV are the CD current density (A g^{-1}), the discharge time (s) and the working potential range (V), respectively.

Figure 3.4.6c depicts the specific capacitances of the electrodeposited films. The values obtained for the single metal oxides are 164 F g^{-1} and 65 F g^{-1} for the Ni oxide and for the Mn oxide, respectively. The specific capacitances of the mixed oxides are 215 F g^{-1}, 235 F g^{-1}, 296 F g^{-1}, 242 F g^{-1} and 148 F g^{-1} for NM-3:1, NM-1:1, NM-1:3, NM-1:6 and NM-1:9 films, respectively. The specific capacitance values increase in the mixed oxides, thus confirming the synergistic effect for the mixed electrodes compared to the single metal oxides. The highest values observed for the NM-1:3 film can be due to a cooperative result of an enhanced redox response combined with an increased surface area, resulting from the presence of interconnected nanosheets-dimpled texture spherical particles shown in the FEG-SEM and TEM analysis.

The NM-1:3 mixed oxides display the highest specific capacitance values amongst the electrodeposited films and its electrochemical behaviour was further studied. The effect of the scan rate on the capacitive response of the NM-1:3 film was assessed by varying the scan rate from 5 mV s^{-1} to 100 mV s^{-1}. The CV results obtained at different scan rates are presented in Figure 3.4.7a. The results show that the main redox peaks shifts and that the current density increases with the scan rate, indicating the good reversibility of the redox reactions and thus the good pseudocapacitive behavior [30]. The potential difference, between the anodic peak and the cathodic peak, increases due to polarization of the electrode at increased scan rates. The potential difference between the anodic/cathodic peaks at scan rates of 5 mV s^{-1} and 100 mV s^{-1} is approximately 100 mV, indicating the low polarization of the electrode. The shape of the cyclic voltamograms is almost preserved up to the highest scan rate (100 mV s^{-1}), indicating the easy diffusion of ions in the electrolyte into the film.

The anodic and cathodic current density peak vs. the square root of the scan rate are plotted in Figure 3.4.7b. The linear relation indicates that the redox reactions are diffusion-controlled processes [31].

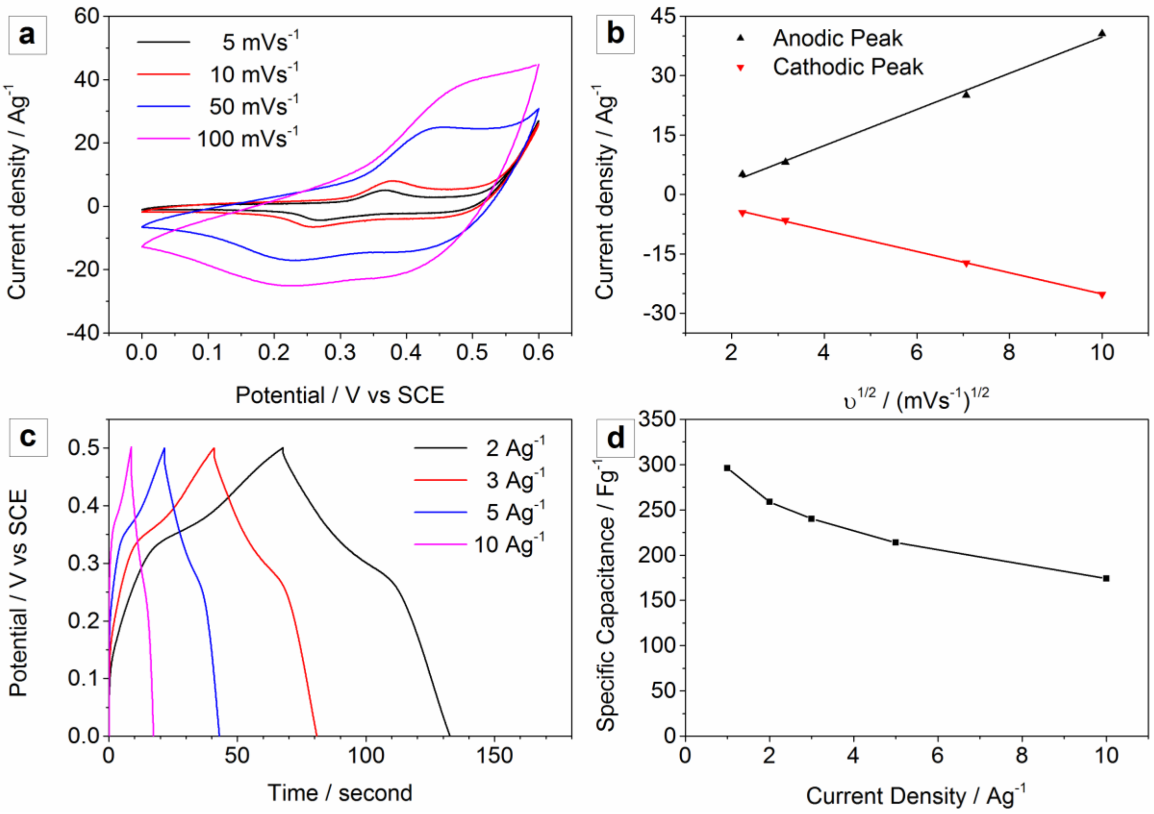

Figure 3.4.7. Electrochemical performance of the NM-1:3 film. Cyclic voltammetry curves obtained at different scan rates (a), the relation of current density with the square root of scan rate (b), charge-discharge curves with different current densities (c) and evolution of the specific capacitance *vs.* the applied current density (d).

Rate capability, which is an important parameter for evaluating the suitability of a material to work as an electrode for energy storage, was also assessed by performing CD measurements with applied currents up to 10 A g^{-1} (Figure 3.4.7c). The results show that the potential drop is more marked and the discharge time decreased when the current density increases, thereby reducing the specific capacitance. The specific capacitance depends upon the applied current density, Figure 3.4.7d, and shows a reduction of 42% when the current increases from 1 A g^{-1} to 10 A g^{-1}, highlighting the good rate capability of the film. The specific capacitance reduction is probably consequence of inaccessible active sites at high applied current densities.

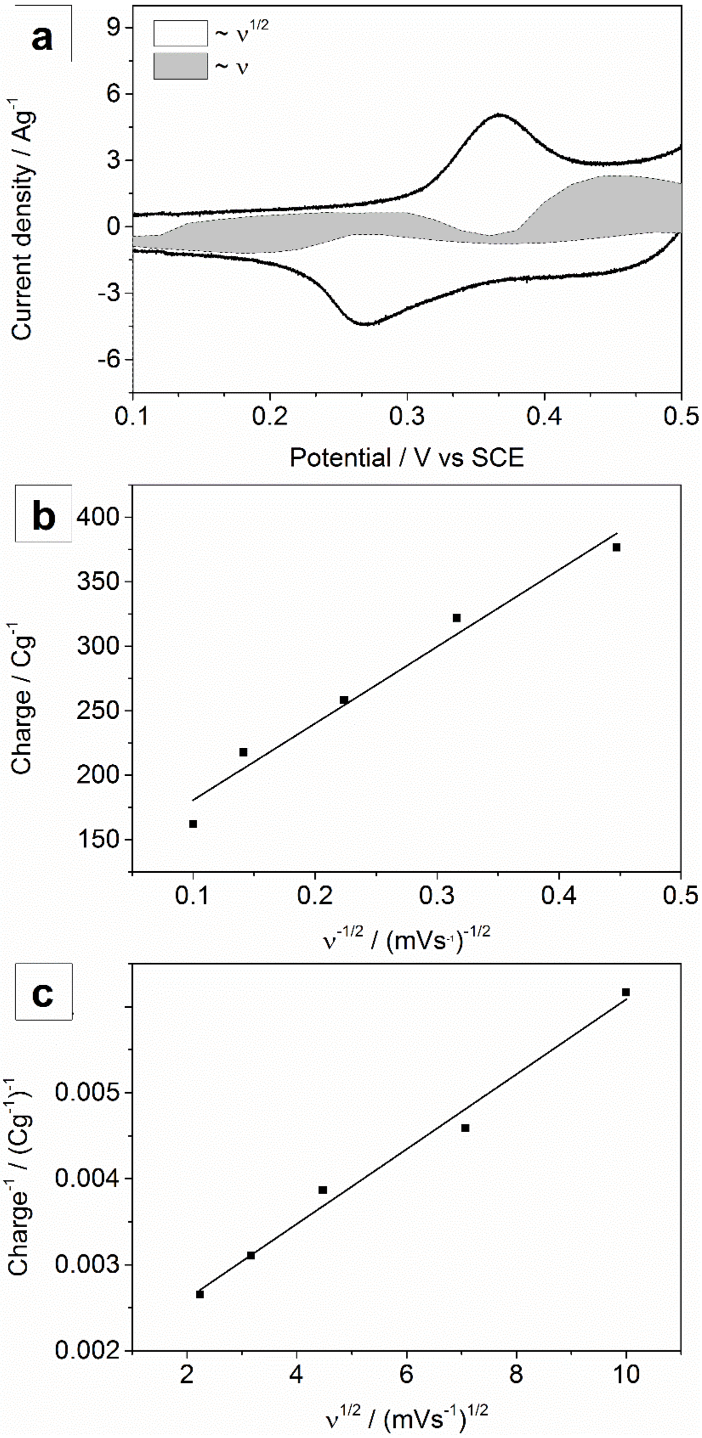

Figure 3.4.8. Kinetic analysis of the NM-1:3 films. Contributions of double layer capacitance (varying with v) and diffusion controlled redox capacitance (varying with $v^{1/2}$) to the total capacitance (a). The relation of charge (Q) vs. $v^{-1/2}$ (b) and of Q^{-1} vs. $v^{1/2}$ (c).

The results show that the redox reactions in the mixed oxide films are essentially diffusion-controlled processes. The total specific capacitance includes the contribution of the non-faradic double layer and the contribution of the diffusion-controlled redox processes. To better understand the mechanisms of charge storage and the contribution of the diffusion-controlled redox capacitive response to the total capacity, the cyclic voltamograms with different scan rates were fitted with kinetic models [32-34].

The results show that the current response from the double layer capacitance is proportional (k_1) to the scan rate (v), and the diffusion-controlled redox capacitance is proportional (k_2) to the square root of the scan rate ($v^{1/2}$). The total current response (i) from the two processes is described as [32, 33]:

$$i = k_1 v + k_2 v^{1/2} \tag{3.4.5}$$

Thereby, by determining k_1 and k_2 it is possible to separate the current response from the two contributions, and to calculate the contribution of the double layer capacitance and the contribution of the diffusion-controlled redox capacitance to the total capacitance, Figure 3.4.8a. The results indicate that the diffusion controlled-redox capacitance contribution is about 62% of the total capacitance.

The relationship between charge ($Q/Coulomb$) and the scan rate in cyclic voltamograms is described by the equations (6) and (7) as reported elsewhere [34]

$$Q = Q_{v=\infty} + constant\left(v^{-1/2}\right) \tag{3.4.6}$$

or

$$Q^{-1} = Q_{v=0}^{-1} + constant(v^{1/2}) \tag{3.4.7}$$

with $Q_{v=\infty}$ is the double layer charge, which is the value at $v = \infty$. $Q_{v=0}$ is the total charge, which is the value at $v = 0$. Therefore, by plotting Q *vs.* $v^{-1/2}$, and Q^{-1} *vs.* $v^{1/2}$, the double layer capacitance and the total capacitance can be retrieved from the y-axis intercepts, Figure 3.4.8b and c. The calculation indicates that the contribution from the double layer capacitance is about 20%; the remaining capacitance of about 80% is the contribution from the diffusion controlled-redox capacitance. Thus, both methods show that diffusion-controlled redox reactions are the main contributors for the total charge storage of the electrode.

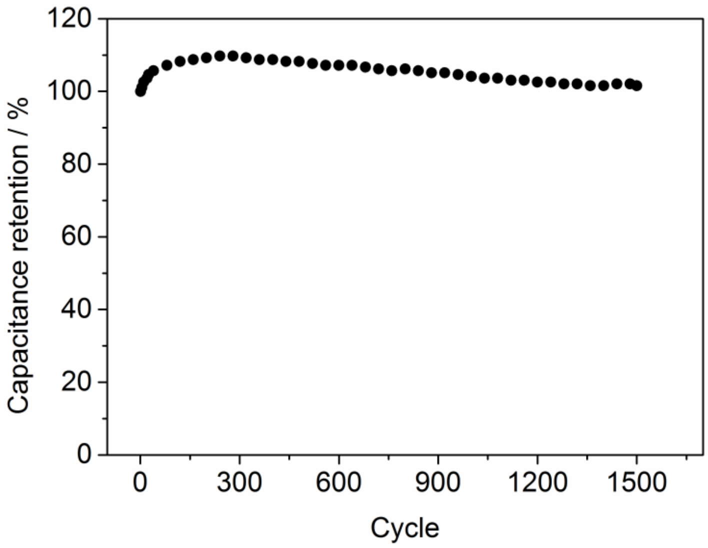

Figure 3.4.9. Cycling stability of the NM-1:3 film for 1500 cycles at constant current of 3 A g^{-1}.

For application as energy storage electrodes, the cycling stability of the material is one of the most important parameters. Therefore, the cycling stability of the NM-1:3 film was tested under charge-discharge cycling under an applied current density of 3 A g^{-1} for 1500 cycles. The capacitance retention *vs.* the number of cycle is shown in Figure 3.4.9. The specific capacitance retention shows an increase of approximately 5% during the first 50 cycles and reaches a maximum value of 108% after 100 cycles; then it is slowly decreases. After 1500 cycles, the capacitance retention is still as high as 101% compared to the initial specific capacitance, indicating a remarkable cycling stability. The excellent cycling stability after 1500 cycles specifies the good electrochemical reversibility of the deposited Ni-Mn oxide, making this material an interesting candidate for application as charge storage material in redox supercapacitors.

3.4.4. Conclusions

Mixed Ni-Mn oxides were grown by co-electrodeposition on stainless steel from electrolytes containing different Ni to Mn ratios and submitted to post thermal annealing. The composition of the electrolyte determines the chemical composition of the mixed oxides and affects the surface morphology, the structure and the electrochemical response. The presence of particles with and without surface texture, mixed nanosheets-dimpled texture spherical particles, nanosheets, nanoparticles attached to nanosheets and worm-like nanostructures were observed depending on the Ni:Mn ratio in the electrolyte.

The phases observed in the single metal oxides were NiO and Mn_3O_4, respectively. Mixed $Ni_{1-x}Mn_xO$ were formed at low Mn contents and two phases, composed of $Ni_{1-x}Mn_xO$ and $Ni_xMn_{3-x}O_4$, occurred at higher Mn contents. The $Ni_{1-x}Mn_xO$ phases were composed of small nanocrystals with an average size of 2 nm, and the $Ni_xMn_{3-x}O_4$ phase contained large nanocrystals with an average size of 20 nm.

The electrochemical studies revealed that the mixed Ni and Mn oxides generate a synergistic effect compared to the single metal oxides, being possible to attain specific capacitances of approximately 300 F g^{-1} for the films with Ni to Mn ratio of 1:3. Kinetic analysis revealed that the redox capacitance was the main contributor for the total capacitive response of the electrode. The mixed oxide films showed good rate capability and the capacitance retention was 58% when current increased from 1 A g^{-1} to 10 A g^{-1}. The mixed oxide films also showed excellent cycling stability that was kept above 100% under an applied current of 3 A g^{-1} for 1500 cycles.

Acknowledgements

We would like to thank Fundação para a Ciência e Tecnologia (FCT) for the funding under the contract PTDC/CTM-MET/119411/2010 & UID/QUI/00100/2013, IDS-FunMat Erasmus Mundus PhD School, and the European COST Action MP1004. We also thank O. Chaix (LMGP, Univ. Grenoble Alpes & CNRS) for Raman measurements.

References

[1] B.E. Conway, Transition from “supercapacitor” to “battery” behavior in electrochemical energy storage, Journal of the Electrochemical Society, 138 (1991) 1539-1548.

[2] T.-C. Liu, W. Pell, B. Conway, Stages in The Development of Thick Cobalt Oxide Films Exhibiting Reversible Redox Behavior and Pseudocapacitance, Electrochimica Acta, 44 (1999) 2829-2842.

[3] C. Yuan, H.B. Wu, Y. Xie, X.W.D. Lou, Mixed Transition‐Metal Oxides: Design, Synthesis, and Energy‐Related Applications, Angewandte Chemie International Edition, 53 (2014) 1488-1504.

[4] H. Wang, Q. Gao, L. Jiang, Facile Approach to Prepare Nickel Cobaltite Nanowire Materials for Supercapacitors, Small, 7 (2011) 2454-2459.

[5] V. Gupta, S. Gupta, N. Miura, Electrochemically synthesized nanocrystalline spinel thin film for high performance supercapacitor, Journal of Power Sources, 195 (2010) 3757-3760.

[6] H. Jiang, J. Ma, C. Li, Hierarchical porous $NiCo_2O_4$ nanowires for high-rate supercapacitors, Chemical Communications, 48 (2012) 4465-4467.

[7] D. Guo, P. Zhang, H. Zhang, X. Yu, J. Zhu, Q. Li, T. Wang, $NiMoO_4$ nanowires supported on Ni foam as novel advanced electrodes for supercapacitors, Journal of Materials Chemistry A, 1 (2013) 9024-9027.

[8] V.S. Kumbhar, A.D. Jagadale, N.M. Shinde, C.D. Lokhande, Chemical synthesis of spinel cobalt ferrite ($CoFe_2O_4$) nano-flakes for supercapacitor application, Applied Surface Science, 259 (2012) 39-43.

[9] M. Jayalakshmi, M.M. Rao, N. Venugopal, K.-B. Kim, Hydrothermal synthesis of SnO_2–V_2O_5 mixed oxide and electrochemical screening of carbon nano-tubes (CNT), V_2O_5, V_2O_5–CNT, and SnO_2/V_2O_5–CNT electrodes for supercapacitor applications, Journal of Power Sources, 166 (2007) 578-583.

[10] T.Y. Wei, C.H. Chen, H.C. Chien, S.Y. Lu, C.C. Hu, A cost‐effective supercapacitor material of ultrahigh specific capacitances: spinel nickel cobaltite aerogels from an epoxide‐driven sol–gel process, Advanced materials, 22 (2010) 347-351.

[11] R.R. Salunkhe, K. Jang, H. Yu, S. Yu, T. Ganesh, S.-H. Han, H. Ahn, Chemical synthesis and electrochemical analysis of nickel cobaltite nanostructures for supercapacitor applications, Journal of Alloys and Compounds, 509 (2011) 6677-6682.

[12] J. Du, G. Zhou, H. Zhang, C. Cheng, J. Ma, W. Wei, L. Chen, T. Wang, Ultrathin porous $NiCo_2O_4$ nanosheet arrays on flexible carbon fabric for high-performance supercapacitors, ACS Appl. Mater. Interfaces, 5 (2013) 7405-7409.

[13] X. Lu, X. Huang, S. Xie, T. Zhai, C. Wang, P. Zhang, M. Yu, W. Li, C. Liang, Y. Tong, Controllable synthesis of porous nickel-cobalt oxide nanosheets for supercapacitors, Journal of Materials Chemistry, 22 (2012) 13357-13364.

[14] L. Huang, D. Chen, Y. Ding, S. Feng, Z.L. Wang, M. Liu, Nickel–Cobalt Hydroxide Nanosheets Coated on $NiCo_2O_4$ Nanowires Grown on Carbon Fiber Paper for High-Performance Pseudocapacitors, Nano Lett., 13 (2013) 3135-3139.

[15] C. Yuan, J. Li, L. Hou, X. Zhang, L. Shen, X.W.D. Lou, Ultrathin mesoporous $NiCo_2O_4$ nanosheets supported on Ni foam as advanced electrodes for supercapacitors, Advanced Functional Materials, 22 (2012) 4592-4597.

[16] Z. Yin, S. Zhang, Y. Chen, P. Gao, C. Zhu, P. Yang, L. Qi, Hierarchical nanosheet-based $NiMoO_4$ nanotubes: synthesis and high supercapacitor performance, Journal of Materials Chemistry A, 3 (2015) 739-745.

[17] G. Wang, L. Zhang, J. Zhang, A Review of Electrode Materials for Electrochemical Supercapacitors, Chem. Soc. Rev., 41 (2012) 797-828.

[18] W. Wei, X. Cui, W. Chen, D.G. Ivey, Manganese Oxide-based Materials as Electrochemical Supercapacitor Electrodes, Chem. Soc. Rev., 40 (2011) 1697-1721.

[19] M. Zhang, S. Guo, L. Zheng, G. Zhang, Z. Hao, L. Kang, Z.-H. Liu, Preparation of $NiMn_2O_4$ with large specific surface area from an epoxide-driven sol–gel process and its capacitance, Electrochimica Acta, 87 (2013) 546-553.

[20] H. Pang, J. Deng, S. Wang, S. Li, J. Du, J. Chen, J. Zhang, Facile synthesis of porous nickel manganite materials and their morphology effect on electrochemical properties, RSC Adv., 2 (2012) 5930-5934.

[21] P. Ahuja, S.K. Ujjain, R.K. Sharma, G. Singh, Enhanced supercapacitor performance by incorporating nickel in manganese oxide, RSC Adv., 4 (2014) 57192-57199.

[22] K.-S. Choi, Shape control of inorganic materials via electrodeposition, Dalton Trans., (2008) 5432-5438.

[23] A. Clifford, The Prediction of Solubility Product Constants1, J. Am. Chem. Soc., 79 (1957) 5404-5407.

[24] L. Zhang, H. Gong, Improvement in flexibility and volumetric performance for supercapacitor application and the effect of Ni-Fe ratio on electrode behaviour, Journal of Materials Chemistry A, 3 (2015) 7607-7615.

[25] K.-W. Nam, K.-B. Kim, A study of the preparation of NiO_x electrode via electrochemical route for supercapacitor applications and their charge storage mechanism, Journal of the Electrochemical Society, 149 (2002) A346-A354.

[26] M. Kim, X. Chen, X. Wang, C. Nelson, R. Budakian, P. Abbamonte, S. Cooper, Pressure and field tuning the magnetostructural phases of Mn_3O_4: Raman scattering and x-ray diffraction studies, Phys. Rev. B, 84 (2011) 174424.

[27] J. Zuo, C. Xu, Y. Liu, Y. Qian, Crystallite size effects on the Raman spectra of Mn_3O_4, Nanostructured Materials, 10 (1998) 1331-1335.

[28] B. Messaoudi, S. Joiret, M. Keddam, H. Takenouti, Anodic behaviour of manganese in alkaline medium, Electrochimica Acta, 46 (2001) 2487-2498.

[29] J. Jiang, A. Kucernak, Electrochemical supercapacitor material based on manganese oxide: preparation and characterization, Electrochimica Acta, 47 (2002) 2381-2386.

[30] T.P. Gujar, V.R. Shinde, C.D. Lokhande, W.-Y. Kim, K.-D. Jung, O.-S. Joo, Spray deposited amorphous RuO_2 for an effective use in electrochemical supercapacitor, Electrochemistry Communications, 9 (2007) 504-510.

[31] A. Bard, L. Faulkner, Electrochemical Methods: Fundamentals and Applications, John Wiley & Sons, Inc2001.

[32] J. Wang, J. Polleux, J. Lim, B. Dunn, Pseudocapacitive Contributions to Electrochemical Energy Storage in TiO_2 (Anatase) Nanoparticles, J. Phys. Chem. C, 111 (2007) 14925-14931.

[33] T. Brezesinski, J. Wang, J. Polleux, B. Dunn, S.H. Tolbert, Templated Nanocrystal-Based Porous TiO_2 Films for Next-Generation Electrochemical Capacitors, J. Am. Chem. Soc., 131 (2009) 1802-1809.

[34] S. Ardizzone, G. Fregonara, S. Trasatti, “Inner” and “outer” active surface of RuO_2 electrodes, Electrochimica Acta, 35 (1990) 263-267.

3.5. Hybrid nickel manganese oxide nanosheet-3D metallic dendrite percolation network electrodes for high-rate electrochemical energy storage✧

Tuyen Nguyen[a,b], Sónia Eugénio[a], Michel Boudard[b], Laetitia Rapenne[b], M. João Carmezim[a,c], M. Fátima Montemor[a]

[a] CQE - Centro de Química Estrutural, Insituto Superior Técnico, Universidade de Lisboa, 1049-001 Lisboa, Portugal.

[b] LMGP, Univ. Grenoble Alpes, CNRS, F-38000 Grenoble, France.

[c] ESTSetúbal, Instituto Politécnico de Setúbal, 1959-007 Setúbal, Portugal.

This work reports the fabrication, by electrodeposition and post-thermal annealing, of hybrid electrodes for high rate electrochemical energy storage composed of nickel manganese oxide ($Ni_{0.86}Mn_{0.14}O$) nanosheets over 3D open porous dendritic NiCu foams. The hybrid electrodes are made of two different percolation networks of nanosheets and dendrites, and exhibit specific capacitance values of 848 F g^{-1} at 1 A g^{-1}. The electrochemical tests revealed that the electrodes display an excellent rate capability, characterized by capacitance retention of approximately 83% when the applied current density increases from 1 A g^{-1} to 20 A g^{-1}. The electrodes also evidenced high charge-discharge cycling stability, which attained 103 % after 1000 cycles.

Keywords: double metal oxides, nickel manganese oxides, supercapacitors, hybrid structures, rate capability

---

✧ **Adapted from Nanoscale, 2015,7, 12452-12459**

3.5.1. Introduction

Supercapacitors are presently considered as one of the most important devices for energy storage solutions, due to the increased power density and cycling stability. However, these systems still lack energy density, a crucial issue for its widespread use. Thus, efforts have been directed towards transition metal oxide (TMO) based pseudocapacitors (or redox supercapacitors) to achieve higher energy densities. In this perspective, double TMOs, such as $NiCo_2O_4$ or $NiFe_2O_4$ have been highlighted as promising materials for energy storage due to their superior pseudocapacitive performance compared to the corresponding single metal oxides like NiO, Co_3O_4 and Fe_3O_4 [1-4]. The main advantage of using double TMOs is to explore the multiple redox reactions due to the presence of two different transition metals. The ultimate goal is to enhance the pseudocapacitive response [5-7].

In this context, nickel manganese oxides (NMOs) are of great interest due to the combined advantages of both oxides. On the one hand, manganese oxides have natural abundance, present low cost, are environmental benign and display multiple redox reactions [8, 9]. On the other hand, nickel oxides have the advantage of reaching high theoretical specific capacitance values (2573 F g^{-1}) [10, 11]. However, very few studies concerning the morphological, structural and compositional features of NMOs and its relation to the pseudocapacitive performance have been reported up to date.

It is known that for good pseudocapacitive response, the active electrode material must possess increased interfacial area, to promote the contact with the electrolyte ions and to enhance the redox activity. Previous work reports the growth of nanostructured TMOs materials such as nanowires [10, 11] or nanosheets [12, 13] on three dimensional (3D) conducting current collectors such as nickel/carbon foam [14, 15] and carbon paper [16, 17] for improved pseudocapacitive performance. The effect has been attributed to the continuous conducting network of the current collectors that results in an increased electrical conductivity. Moreover, the open porous structure can be easily covered and/or filled with the nanostructured active material, resulting in enhanced surface area and reduced ionic diffusion length. Although high specific capacitance values have been obtained, the rate capability is still rather poor, and typically below 70% when the current density increases from 1 A g^{-1} up to 20 A g^{-1} [20, 21]. Acceptable rate capability values are usually in the range 40-60% when the current densities increase from 1 A g^{-1} to 20 A g^{-1} (but most of the reported values are measured at the highest current density of 10 A g^{-1}) [18]. Thus, rate capability values above this typical range are an acknowledged need.

Recently, we reported that NMOs electrodeposited on stainless steel collectors for charge storage electrodes have a synergistic effect compared to the single nickel oxide and single manganese oxide [19]. Moreover, this material displayed very good pseudocapacitive response and excellent cycling stability, making it a very interesting candidate for application in redox supercapacitor electrodes. Following these interesting results it is very likely that the pseudocapacitive performance can be significantly improved by depositing the NMOs onto 3D open porous current collectors with continuous conducting pathways. Thus, the present work aims at developing a novel hybrid electrode based on NMOs for high rate electrochemical energy storage, with rate capability above 80% when the current density is increased up to 20 A g^{-1}. This objective was achieved by designing electrodes with a nano-architecture composed of a 3D pseudocapacitive NMO nanosheets percolation network grown over the 3D conducting dendrites percolation network of the open porous metallic foam. These novel hybrid nano-architectured electrodes, prepared via a facile electrodeposition route and post-thermal annealing, displayed superior pseudocapacitive performance with enhanced specific capacitance, excellent rate capability and cycling stability.

3.5.2. Experimental

Electrodeposition

The NiCu foams were electrodeposited on stainless steel (AISI 304) in a solution containing $NiSO_4·7H_2O$ (0.5 M), H_2SO_4 (1.5 M), HCl (1 M) and $CuSO_4·5H_2O$ (0.01 M). The foams were electrodeposited under galvanostatic mode, by applying a constant current of 1.8 A cm^{-2} for 90 seconds and 180 seconds in a two-electrode cell (Kikusui Electronics, Model PAB 32-3) [20]; the resulting foams were denoted as F1 and F2, respectively.

The NMO films electrodeposition was performed in a conventional three-electrode electrochemical system (Voltalab PGZ 100 Potentiostat from Radiometer), at room temperature, using the NiCu foams (F1, F2) as working electrode, the saturated calomel electrode (SCE) as reference electrode and a platinum foil as counter electrode. An electrolyte containing $Mn(NO_3)_2$ (0.075 M) and $Ni(NO_3)_2$ (0.025 M) was used for the electrodeposition experiments. The depositions were performed in galvanostatic mode, applying a current density of -1 mA cm^{-2} for 10 minutes. After that the films were annealed at 250 ^{o}C for 3 hours.

Characterization

Field emission gun scanning electron microscopy (FEG-SEM, JEOL 7001F microscope) was used to study the surface morphology of the films. X-ray diffraction (XRD, Bruker AXS D8 Advance diffractometer) in Bragg-Brentano configuration with Cu K_α radiation and Raman spectroscopy (Horiba/Jobin Yvon LabRam spectrometer) were used to study the structural features. The structural details were also studied by transmission electron microscopy (TEM, JEOL JEM-2010 microscope), working at an acceleration voltage of 200 keV. Energy dispersive X-ray spectroscopy (EDX) mappings were performed by scanning transmission electron microscopy (STEM, JEOL JEM-2010F microscope).

To evaluate electrochemical response, cyclic voltammetry (CV) and charge-discharge (CD) measurements were carried out in a conventional three-electrode electrochemical cell using the NMO films as working electrode and 1 M KOH as electrolyte. All potentials referred in this work are potentials versus SCE.

3.5.3. Results and discussion

FEG-SEM images of the F1 and F2 foams taken at different magnifications are depicted in Figure 3.5.1. In agreement with previous work [20], the foams show an open porous 3D morphology with randomly distributed micrometric size pores (Figure 3.5.1a and d) .The pore walls, themselves, are constituted of randomly interconnected dendrites forming an open porous 3D percolation network (Figure 3.5.1b-c and e-f), thus creating a good electron conducting pathway. The F2 foams, electrodeposited for longer time, present a lower surface pore density (approximately 417 pores mm^{-2}) and a larger average pore diameter (approximately 20 µm) than F1 foams (approximately 855 pores mm^{-2} and 14 µm, respectively). It should also be taken into consideration that the foams have the interconnected volumetric porosity [20], thus it is expected that the pore density in volume will have a much higher value. In this context, as F2 that is deposited for a longer time and presents a higher thickness (approximately 100 µm), it will present a higher areal surface area compared to the F1 foam.

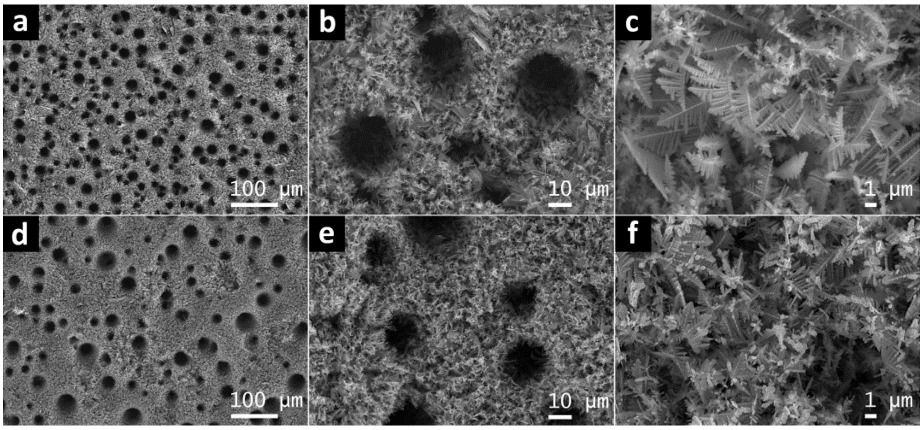

Figure 3.5.1. FEG-SEM images of (a-c) F1 and (d-f) F2 foams at different magnifications.

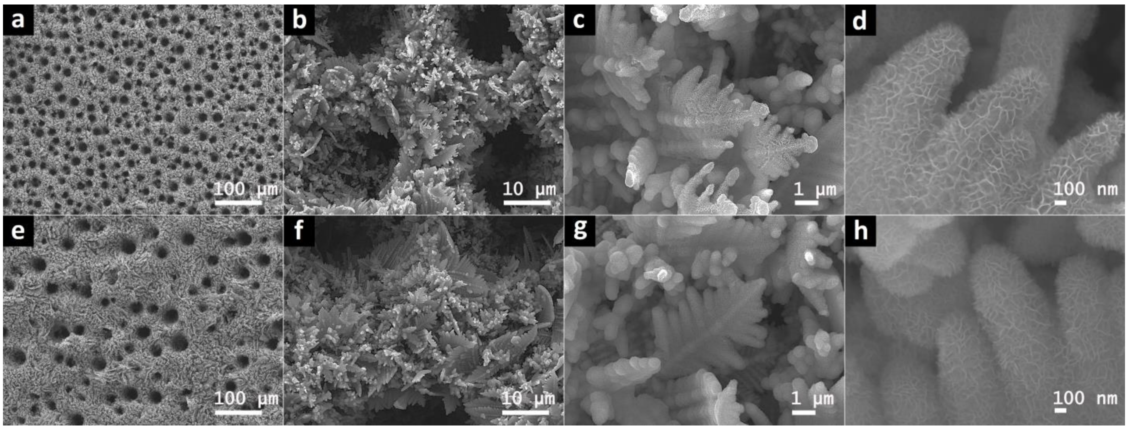

Figure 3.5.2. FEG-SEM images of nickel manganese oxide films deposited on NiCu foams at different magnifications. (a-d) F1-NMO film, (e-h) F2-NMO film.

NMO was electrodeposited on the F1 and F2 foams, and denoted as F1-NMO and F2-NMO, respectively. Figure 3.5.2 shows the FEG-SEM images of the F1-NMO (a-d) and F2-NMO (e-h) films at different magnifications. At low magnification (Figure 3.5.2a and e), the surface morphology of F1-NMO and F2-NMO is similar to the surface morphology of the pristine foams, indicating that the electrodeposited NMO oxide homogeneously mimics the original 3D morphology of the foams. Higher magnification FEG-SEM images show that the each Ni-Cu dendrite is uniformly covered by the NMO oxides that display nanosheets-like morphologies with an average thickness of approximately 10 nm. The nanosheets grow almost vertically on the dendrites surface and each nanosheet is interconnected with others, forming a 3D percolation network with a fine porous structure. Thereby, a 3D hierarchical hybrid material composed of two different 3D percolation networks, nanosheets and dendrites, is constructed. This architecture is expected to display an increased interfacial area, promoting the closer contact of the NMO film with the electrolyte ions and enhancing the redox reactions and electron transfer.

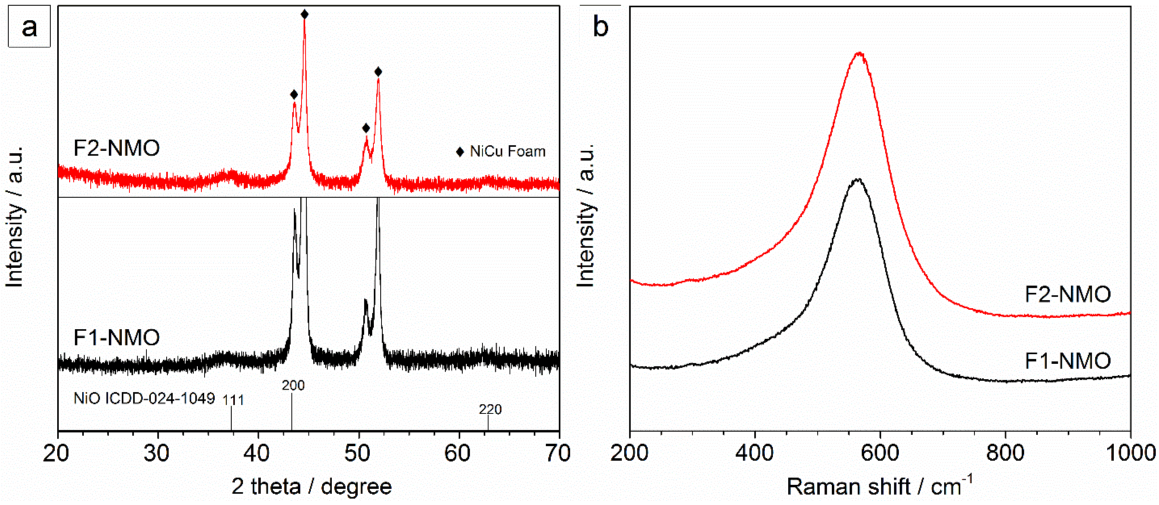

Figure 3.5.3. (a) XRD patterns and (b) Raman spectra of F1-NMO and F2-NMO films.

XRD patterns and Raman spectra of the deposited NMO films are shown in Figure 3.5.3a and b, respectively. The intense lines in the XRD patterns correspond to the NiCu foams [20]. The broad and weak diffraction lines at 37.5° and 62° are close to the (111) and (220) diffraction lines of face-centred cubic (FCC) NiO (ICDD card n° 00-047-1049, a = 4.177 Å, space group Fm-3m). There are no evident lines from manganese oxide, thus suggesting the substitution of Mn into the NiO, forming $Ni_{1-x}Mn_xO$ oxide [21]. The broadening of the peaks accounts for the nanocrystalline nature of the films. The Raman spectra in Figure 3.5.3b show a broad and intense band at 580 cm^{-1}, which can be assigned to M-O (M = Ni/Mn) stretching mode of the $Ni_{1-x}Mn_xO$ oxide nanocrystals as reported in our previous work [19]. Hence, combining with FEG-SEM observation, the results reveal the formation of $Ni_{1-x}Mn_xO$ nanosheets.

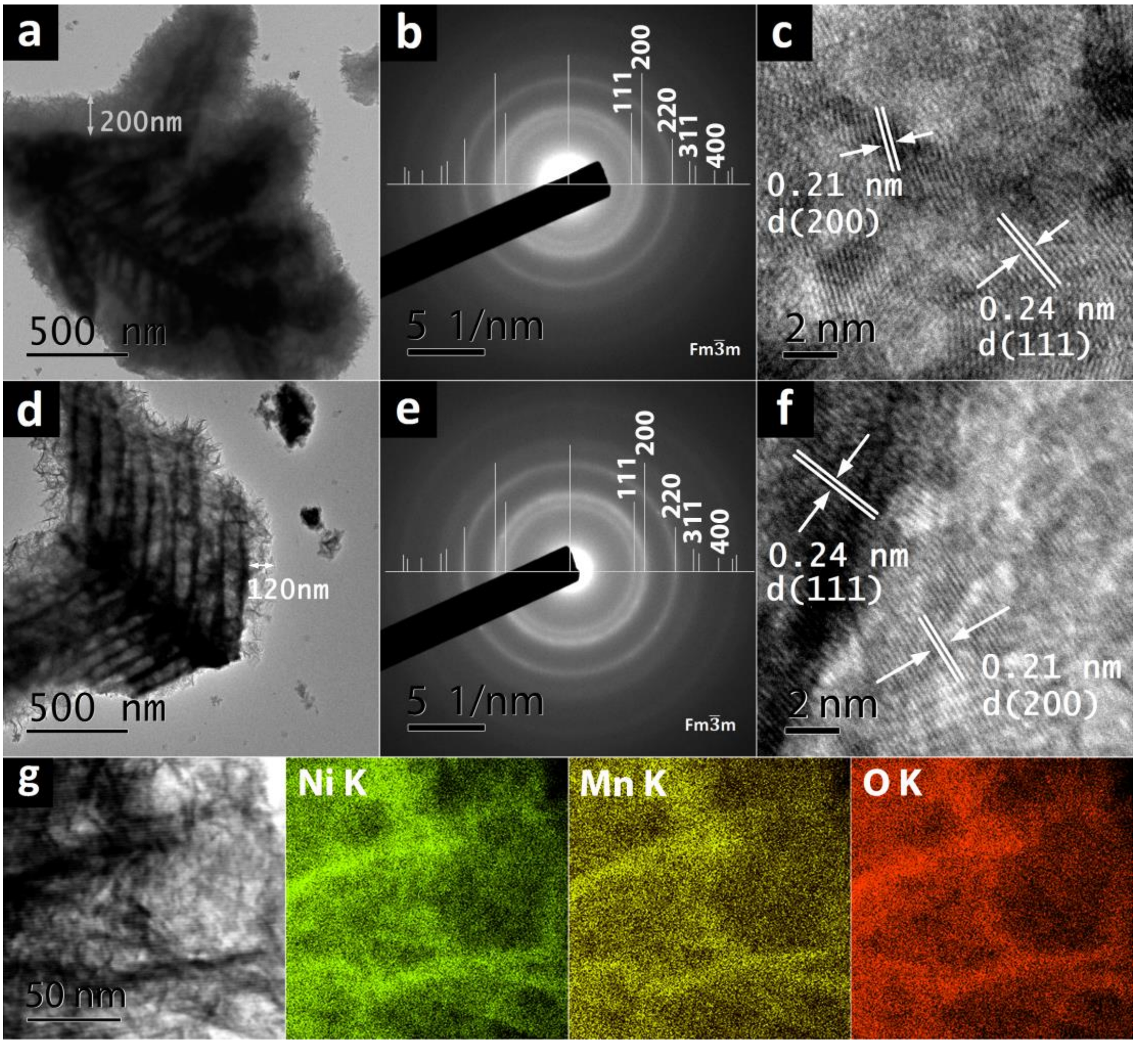

Figure 3.5.4. Low magnification TEM, SAED and HRTEM images of (a-c) F1-NMO and (d-f) F2-NMO. (g) STEM image and elemental mappings of Ni, Mn and O of the representative nanosheet.

TEM results are shown in Figure 3.5.4. Low magnification TEM images (Figure 3.5.4a and d) evidence the dendritic structure covered by a layer of crumpled nanosheets. The nanosheets layer is denser in the F1-NMO film. The nominal thickness of the nanosheets layers is about 200 nm and 120 nm for F1-NMO and F2-NMO films, respectively. Thus, the results reveal the formation of a thinner oxide layer on the foam electrodeposited for longer time (180 s).

Selected area electron diffraction (SAED) patterns (Figure 3.5.4b and e) of the NMO nanosheets present well-defined diffraction rings, revealing the polycrystalline nature of the nanosheets. The diffraction rings well match with (111), (200) and (220) diffraction lines of the NiO structure. Furthermore, EDX analysis evidence the presence of nickel and manganese. Thus, in good agreement with XRD and Raman results, the results suggest the formation of $Ni_{1-x}Mn_xO$. High resolution TEM (HRTEM) images (Figure 3.5.4c and f) show lattice fringes with distances of approximately 0.24 and 0.21 nm, corresponding to (111) and (200) lattice planes of the NMO oxide nanosheets. A representative STEM image and the elemental distribution of the nanosheets are shown in Figure 3.5.4g. The STEM study was performed on NMO nanosheets detached from the dendrites after scratching the foam to avoid interference from the foam material. The STEM image reveals the existence of crumpled nanosheets and the elemental mapping of Ni, Mn and O K-edges shows identical distribution for Ni, Mn and O. The Ni to Mn ratio determined from the STEM-EDX analysis is about 6:1. Thus, the results confirm the formation of homogenously deposited $Ni_{0.86}Mn_{0.14}O$ oxide nanosheets over the 3D dendrites percolation network.

Figure 3.5.5a and b shows the CV curves, obtained at different scan rates in a potential window ranging from 0 to 0.6 V, for the F1-NMO and F2-NMO films. The CV curves for blank foams obtained at 50 mV s^{-1} are also depicted. The voltammograms evidence a pair of redox peaks, which can be assigned to the redox reaction M-O/M-OOH (M is Ni/Mn in NMOs) of the NMO oxide with the OH^- anions in the alkaline electrolyte [19]. The comparison of the CV response at 50 mV s^{-1} for the blank foams and for the deposited NMO film on the corresponding foams indicates a negligible contribution from the foams to the total pseudocapacitive response.

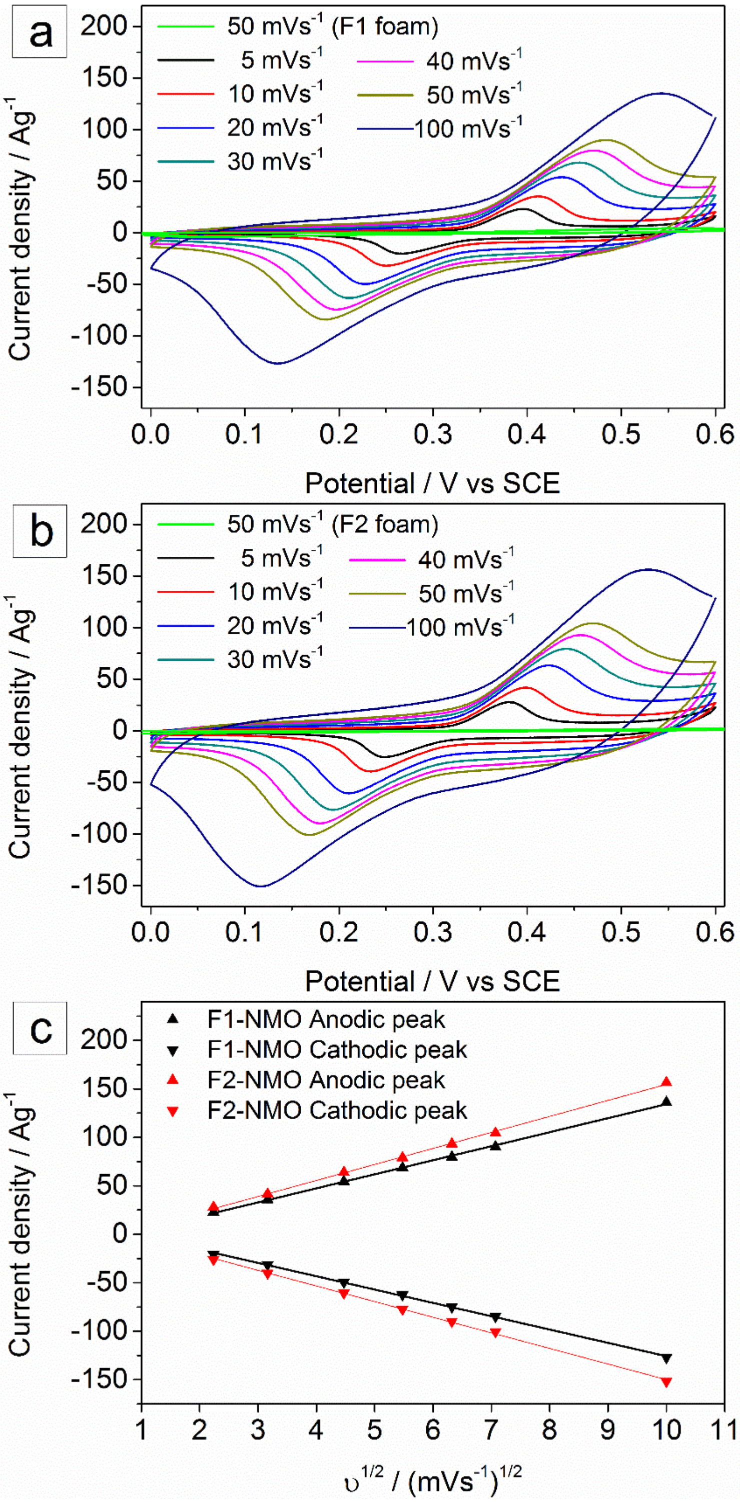

Figure 3.5.5. CV curves of (a) the F1-NMO, (b) F2-NMO at different scan rates and of the corresponding blank foams at 50 mV s^{-1}, respectively. (c) The relation of peak current with the square root of scan rate.

The shift of the redox peaks with increasing scan rate and the large separation between them indicates the quasi reversibility of the redox reactions [22]. The potential difference between the anodic and the cathodic peak increases due to the polarization of the electrode at increased scan rates. The shape of the cyclic voltamograms is preserved when increasing the scan rate up to 100 mV s^{-1}, indicating good ionic diffusion as result of the double percolation network structure. The evolution of the anodic and cathodic peaks current densities with the square root of the scan rate is depicted in Figure 3.5.5c. The linear relation indicates that the redox reactions are essentially diffusion-controlled processes. The current response of the redox peaks is higher in the F2-NMO film, indicating a better pseudocapacitive response of the NMO film deposited on the foam prepared for longer deposition time. This effect is probably related to the formation of a thinner NMO layer as observed in TEM analysis.

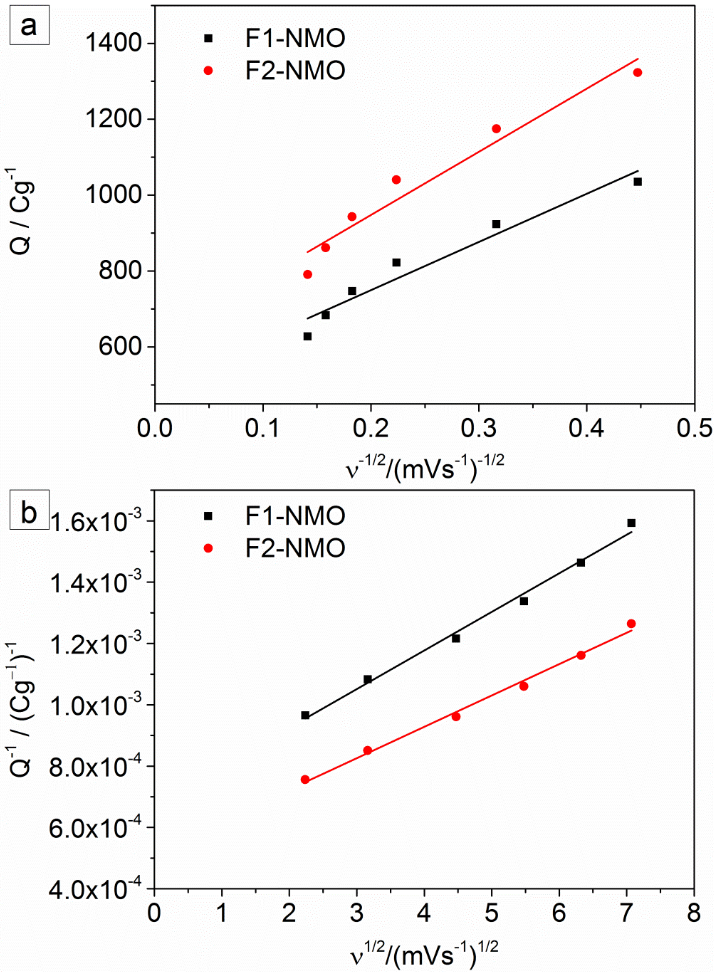

Figure 3.5.6. The relation of (a) charge Q *vs.* $v^{-1/2}$ and (b) Q^{-1} *vs.* $v^{1/2}$.

The total specific capacitance includes the contributions from the double layer and the diffusion-controlled redox processes. To detail the mechanisms of charge storage and the contribution of the diffusion-controlled redox capacitive response to the total capacity of the electrode, the cyclic voltammetry data obtained at different scan rates were fitted with kinetic models [23]. The relationship between the charge ($Q/Coulomb$) and the scan rate can be described by equations (6) and (7) [23]:

$$Q = Q_{v=\infty} + constant\left(v^{-1/2}\right) \tag{3.5.1}$$

or

$$Q^{-1} = Q_{v=0}^{-1} + constant(v^{1/2}) \tag{3.5.2}$$

where: $Q_{v=\infty}$ is the double layer charge, which is the value at $v = \infty$. $Q_{v=0}$ is the total charge, which is the value at $v = 0$. Therefore, by plotting Q *vs.* $v^{-1/2}$, and Q^{-1} *vs.* $v^{1/2}$, the double layer capacitance and the total capacitance can be retrieved from the y-axis intercepts in Figure 3.5.6. The calculations show that the diffusion-controlled redox capacitive contribution is approximately 75%-80% of the total specific capacitance of the electrode.

The CD measurements were carried out in a potential window ranging from 0 to 0.5 V, under applied current densities increasing from 1 A g^{-1} up to 20 A g^{-1}. The results are shown in Figure 3.5.7. The plateau in the CD curves, in the potential range around 0.25-0.35 V, is consequence of the redox reactions identified in the CV curves that contribute to the enhanced pseudocapacitive response [24]. The discharge time is longer in the F2-NMO film compared to the F1-NMO film, indicating higher specific capacitance for the first. The specific capacitance of the NMO film was calculated from the CD curves using the formula:

$$C = \frac{It}{\Delta V} \tag{3.5.3}$$

where: *I*, *t*, *ΔV* are the CD current density (A g^{-1}), the discharge time (s) and the CD potential window (V), respectively.

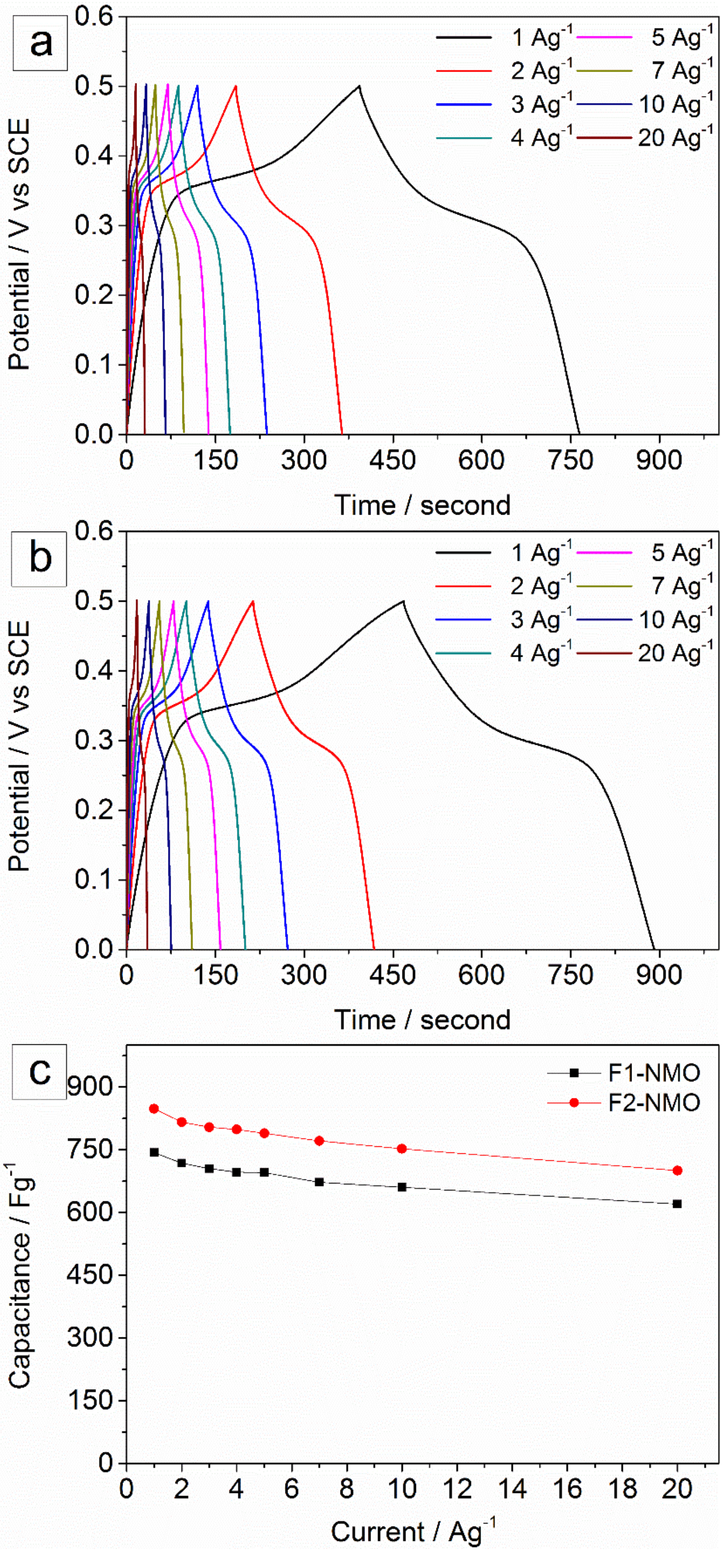

Figure 3.5.7. Charge-discharge curves of (a) the F1-NMO and (b) F2-NMO at different currents. (c) Specific capacitance versus the applied current density.

The specific capacitance values calculated at 1 A g^{-1} are 743 F g^{-1} and 848 F g^{-1} for F1-NMO and F2-NMO films, respectively. The increased specific capacitance of F2-NMO compared to F1-NMO is probably due to the formation of a thinner NMO layer over the higher areal surface area of the thicker foam deposited for a longer time, resulting in an increase in the volume/mass fraction of the pseudocapacitive NMO layers. Thus, the results suggest that the specific capacitance of the NMO nanosheets films can be increased by increasing their volume/mass fraction in the foam.

Rate capability is an important parameter for assessing the electrochemical performance of electrodes for charge storage and was assessed by performing CD tests at current densities up to 20 A g^{-1}. The results show that when the current density increases, the potential drop is more marked and the discharge time decreases, thereby decreasing the specific capacitance. The decreased capacitance is probably due to increased Ohmic contributions and less accessible surface regions, which become progressively excluded as the reaction rate is enhanced by the increasing high current density. The capacitance retentions are about 83% when the current density increases from 1 A g^{-1} to 20 A g^{-1} for both films, confirming an excellent rate capability. Previous work report that $NiCo_2S_4$ nanosheets on nitrogen-doped carbon foam [25] revealed capacitance retention of 71% when the current density increased from 2 A g^{-1} to 20 A g^{-1}. $NiCo_2O_4$ nanorods and nanosheets on carbon nanofibers [18] display capacitance retention of 48.8% and 51.9% respectively when current density increased from 1 A g^{-1} to 20 A g^{-1}, while, nickel-cobalt-aluminum layered hydroxides proposed for high rate supercapacitors [26] display capacitance retention of approximately 72% when the current density increased from 1 A g^{-1} to 20 A g^{-1}. The high rate capability of the electrodes proposed in this work can be attributed to the formation of a hierarchical architecture composed of double 3D percolation networks of NMO oxide nanosheets and of dendrites that enhances the interfacial area of the active material, facilitating the accessibility of the ions and hence, the charge transfer.

The charge-discharge cycling stability of the electrode is another important parameter for practical application of the electrode in redox supercapacitors. Thus, a cycling stability test (continuous charge-discharge) under an applied current density of 5 A g^{-1} was performed for 1000 cycles. The F2-NMO electrode, the one displaying the highest specific capacitance values, was chosen to perform this stability test. The capacitance retention (Figure 3.5.8) increases to approximately 122% after 40 cycles, and reaches a maximum value of 134% after 200 cycles corresponding to specific capacitance values of 1057 F g^{-1}. Then, it slowly decreases to approximately 103% after 1000 cycles.

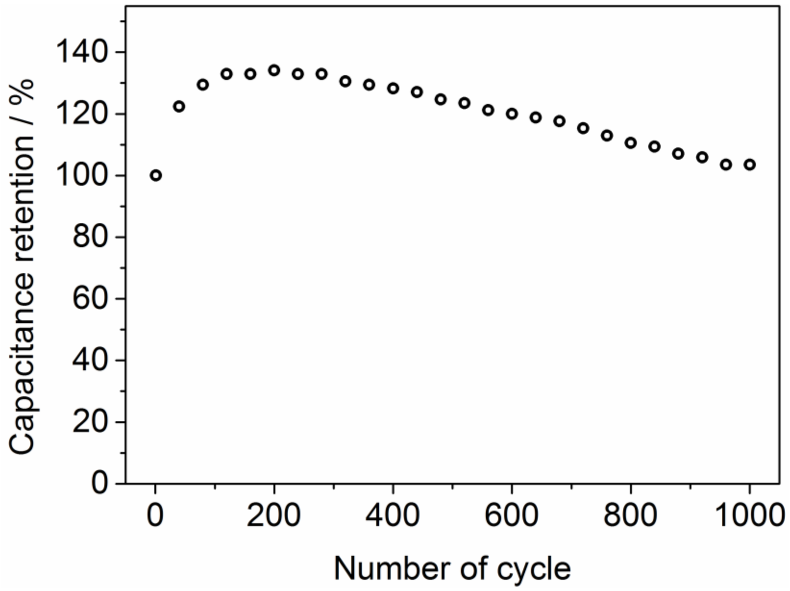

Figure 3.5.8. Charge-discharge cycling stability of the F2-NMO at 5 A g^{-1} for 1000 cycles.

This stable behaviour is similar to that of NMO deposited directly on stainless steel reported in our previous work [19], thus confirming the main contribution of NMO nanosheets to the pseudocapacitive response. The result indicates an excellent cycling stability of the NMO film. Along with its high specific capacitance and especially high rate capability, the NMO deposited on 3D foam can be considered as a very promising material for electrochemical energy storage electrodes for redox supercapacitors.

3.5.4. Conclusions

In summary, this work reports the fabrication of a hybrid electrode consisting on NMO nanosheets over 3D open porous dendritic foams forming double percolation networks. This hybrid 3D architecture displays unique physic-chemical properties that make this material an interesting option for high rate electrochemical energy storage electrodes. The active materials are composed of polycrystalline $Ni_{86}Mn_{0.14}O$ nanosheets forming a network that mimics the dendritic foam architecture.

The hybrid electrode showed a maximum specific capacitance of 1057 F g^{-1} at 5 A g^{-1} after continuous cycling. High rate capability, with 83% specific capacitance retention, was achieved when the current density increased from 1 A g^{-1} to 20 A g^{-1}. The electrodes display excellent cycling stability, with specific capacitance retention close to 103% after 1000 charge-discharge cycles. The high pseudocapacitive performance and the remarkable rate capability result from the double percolation network nano-architecture that makes this electrode a promising material for application in high rate pseudocapacitors.

Acknowledgements

The authors thank Fundação para a Ciência e Tecnologia (FCT) for the funding under the contract PTDC/CTM-MET/119411/2010 & UID/QUI/00100/2013 (CQE Funding), IDS-FunMat Erasmus Mundus PhD School, and the European COST Action MP1004. H. Roussel (LMGP, Univ. Grenoble Alpes) is acknowledged for XRD measurements.

References

[1] D.P. Dubal, P. Gomez-Romero, B.R. Sankapal, R. Holze, Nickel cobaltite as an emerging material for supercapacitors: An overview, Nano Energy, 11 (2015) 377-399.

[2] Z.-Y. Yu, L.-F. Chen, S.-H. Yu, Growth of $NiFe_2O_4$ nanoparticles on carbon cloth for high performance flexible supercapacitors, Journal of Materials Chemistry A, 2 (2014) 10889-10894.

[3] C. Yuan, H.B. Wu, Y. Xie, X.W.D. Lou, Mixed Transition ‐ Metal Oxides: Design, Synthesis, and Energy ‐ Related Applications, Angewandte Chemie International Edition, 53 (2014) 1488-1504.

[4] T.Y. Wei, C.H. Chen, H.C. Chien, S.Y. Lu, C.C. Hu, A cost ‐ effective supercapacitor material of ultrahigh specific capacitances: spinel nickel cobaltite aerogels from an epoxide ‐ driven sol–gel process, Advanced materials, 22 (2010) 347-351.

[5] V. Gupta, S. Gupta, N. Miura, Electrochemically synthesized nanocrystalline spinel thin film for high performance supercapacitor, Journal of Power Sources, 195 (2010) 3757-3760.

[6] Y. Zhang, L. Li, H. Su, W. Huang, X. Dong, Binary metal oxide: advanced energy storage materials in supercapacitors, Journal of Materials Chemistry A, 3 (2015) 43-59.

[7] Z. Wu, Y. Zhu, X. Ji, $NiCo_2O_4$-based materials for electrochemical supercapacitors, Journal of Materials Chemistry A, 2 (2014) 14759-14772.

[8] W. Wei, X. Cui, W. Chen, D.G. Ivey, Manganese Oxide-based Materials as Electrochemical Supercapacitor Electrodes, Chem. Soc. Rev., 40 (2011) 1697-1721.

[9] M.-K. Song, S. Cheng, H. Chen, W. Qin, K.-W. Nam, S. Xu, X.-Q. Yang, A. Bongiorno, J. Lee, J. Bai, Anomalous pseudocapacitive behavior of a nanostructured, mixed-valent manganese oxide film for electrical energy storage, Nano Lett., 12 (2012) 3483-3490.

[10] Z. Sun, S. Firdoz, E.Y.-X. Yap, L. Li, X. Lu, Hierarchically structured MnO_2 nanowires supported on hollow Ni dendrites for high-performance supercapacitors, Nanoscale, 5 (2013) 4379-4387.

[11] X.-h. Xia, J.-p. Tu, Y.-q. Zhang, Y.-j. Mai, X.-l. Wang, C.-d. Gu, X.-b. Zhao, Freestanding Co_3O_4 nanowire array for high performance supercapacitors, RSC Adv., 2 (2012) 1835-1841.

[12] L. Huang, D. Chen, Y. Ding, S. Feng, Z.L. Wang, M. Liu, Nickel–Cobalt Hydroxide Nanosheets Coated on $NiCo_2O_4$ Nanowires Grown on Carbon Fiber Paper for High-Performance Pseudocapacitors, Nano Lett., 13 (2013) 3135-3139.

[13] Q. Yang, Z. Lu, X. Sun, J. Liu, Ultrathin Co_3O_4 nanosheet arrays with high supercapacitive performance, Sci. Rep., 3 (2013).

[14] G.-W. Yang, C.-L. Xu, H.-L. Li, Electrodeposited nickel hydroxide on nickel foam with ultrahigh capacitance, Chem. Commun., (2008) 6537-6539.

[15] X.-C. Dong, H. Xu, X.-W. Wang, Y.-X. Huang, M.B. Chan-Park, H. Zhang, L.-H. Wang, W. Huang, P. Chen, 3D Graphene–Cobalt Oxide Electrode for High-Performance Supercapacitor and Enzymeless Glucose Detection, ACS Nano, 6 (2012) 3206-3213.

[16] L. Huang, D. Chen, Y. Ding, Z.L. Wang, Z. Zeng, M. Liu, Hybrid composite $Ni(OH)_2@NiCo_2O_4$ grown on carbon fiber paper for high-performance supercapacitors, ACS Appl. Mater. Interfaces, 5 (2013) 11159-11162.

[17] R.B. Rakhi, W. Chen, D. Cha, H.N. Alshareef, Substrate Dependent Self-Organization of Mesoporous Cobalt Oxide Nanowires with Remarkable Pseudocapacitance, Nano Lett., 12 (2012) 2559-2567.

[18] G. Zhang, X.W. Lou, Controlled Growth of $NiCo_2O_4$ Nanorods and Ultrathin Nanosheets on Carbon Nanofibers for High-performance Supercapacitors, Sci. Rep., 3 (2013) 1470.

[19] T. Nguyen, M. Boudard, L. Rapenne, M.J. Carmezim, M.F. Montemor, Morphological changes and electrochemical response of mixed nickel manganese oxides as charge storage electrodes, Journal of Materials Chemistry A, 3 (2015) 10875-10882.

[20] S. Eugénio, T. Silva, M. Carmezim, R. Duarte, M. Montemor, Electrodeposition and characterization of nickel–copper metallic foams for application as electrodes for supercapacitors, J Appl Electrochem, 44 (2014) 455-465.

[21] P. Mallick, C. Rath, A. Rath, A. Banerjee, N.C. Mishra, Antiferro to superparamagnetic transition on Mn doping in NiO, Solid State Communications, 150 (2010) 1342-1345.

[22] A. Bard, L. Faulkner, Electrochemical Methods: Fundamentals and Applications, John Wiley & Sons, Inc2001.

[23] S. Ardizzone, G. Fregonara, S. Trasatti, "Inner" and "outer" active surface of RuO_2 electrodes, Electrochimica Acta, 35 (1990) 263-267.

[24] T.-C. Liu, W. Pell, B. Conway, Stages in The Development of Thick Cobalt Oxide Films Exhibiting Reversible Redox Behavior and Pseudocapacitance, Electrochimica Acta, 44 (1999) 2829-2842.

[25] L. Shen, J. Wang, G. Xu, H. Li, H. Dou, X. Zhang, $NiCo_2S_4$ Nanosheets Grown on Nitrogen-Doped Carbon Foams as an Advanced Electrode for Supercapacitors, Advanced Energy Materials, 5 (2015) 1400977.

[26] X. Wang, C. Yan, A. Sumboja, J. Yan, P.S. Lee, Achieving High Rate Performance in Layered Hydroxide Supercapacitor Electrodes, Advanced Energy Materials, 4 (2014) 1301240.

3.6. Layered $Ni(OH)_2$-$Co(OH)_2$ electrodes prepared by electrodeposition for redox supercapacitors

Tuyen Nguyen[a,b], Michel Boudard[b], M. João Carmezim[a,c], M. Fátima Montemor[a]

[a] CQE - Centro de Química Estrutural, Instituto Superior Técnico, Universidade de Lisboa, 1049-001 Lisboa, Portugal.

[b] LMGP, Univ. Grenoble Alpes, CNRS, F-38000 Grenoble, France.

[c] ESTSetúbal, Instituto Politécnico de Setúbal, 1959-007 Setúbal, Portugal.

In this work, an electrode composed of two layers $Ni(OH)_2$ and $Co(OH)_2$ was designed and prepared by electrodeposition on stainless steel current collectors for application as a high specific capacitance material for redox supercapacitors. The studies were performed on single layer films of $Ni(OH)_2$, $Co(OH)_2$, $Ni_{1/2}Co_{1/2}(OH)_2$ and two layers films of $Ni(OH)_2$ on $Co(OH)_2$ and $Co(OH)_2$ on $Ni(OH)_2$ to highlight the advantages of the new electrode architecture. The microscopy studies revealed the formation of nanosheets in the $Co(OH)_2$ films and of particles agglomerates in the $Ni(OH)_2$ films. Important morphological changes were also observed in the double hydroxides films and two layers films. The new architecture composed of two layers films of $Ni(OH)_2$ on $Co(OH)_2$ displayed a redox response characterized by the presence of two peaks in the cyclic voltammograms, which could be assigned to the redox reactions of the metallic species present in the two layers film. The electrodes revealed a specific capacitance of 1580 F g^{-1} at the current density of 1 A g^{-1}.

Keywords: hydroxides, nanosheets, nickel, cobalt, redox capacitors, layer by layer, electrodeposition

3.6.1. Introduction

Transition metal hydroxides (TMHs) are attractive materials for application as charge storage materials due to its high charge storage capacity, or high specific capacitance, resulting from Faradaic redox reactions with hydroxyl anions in alkaline electrolytes [1-3]. The high specific capacitance values associated to the redox activity is due to the layered structure of the material that is characterized by a large interlayer distance, favoring the diffusion of electrolyte ions into the bulk, leading to additional bulk redox reactions besides the surface ones [4]. The charge storage performance of TMHs based electrodes [5] is less dependent on their surface area, compared to metal oxides based electrodes, due to the contribution from the bulk redox reactions. Nevertheless, for enhanced charge storage capacity and the enhanced electrochemical response, a rational design of TMHs based electrodes is still needed and is attracting a lot of interest in the research community [5]. For example, $Co(OH)_2$ was deposited on stainless steel by potentiostatic electrodeposition, in the form of a network of nanolayered sheets [6], having specific capacitance values of 860 F g^{-1}. $Ni(OH)_2$ was deposited by a hydrothermal method [7], leading to single crystal nanoplatelet arrays with an areal capacitance value of 64 mF cm^{-2}.

Double TMHs are also studied for high charge storage electrodes for redox supercapacitors due to advantages compared to the corresponding single TMHs [1, 8]. Due to the presence of two transition metal (TM) ions in the double TMHs, the redox response can be further enhanced as compared to their corresponding single TMHs, owing to the combination of redox reactions with two TMs[9, 10]. For example, nanostructured porous layered $Co_{1-x}Ni_x(OH)_2$ films were prepared by potentiodynamic electrodeposition [11] showing a specific capacitance value of 1213 F g^{-1}. NiTi layered double hydroxide nanosheets prepared by two hydrothermal steps [12] displayed an areal capacitance value of 10.37 F cm^{-2}. More recently, Ni^{3+} doped NiTi hydroxide monolayer nanosheets were reported [13], presenting very high specific capacitance values of 2310 F g^{-1}.

Among the double TMHs that have been reported in literature, Ni-Co hydroxides are considered as the most promising double TMHs as materials for redox supercapacitor electrodes [8]. Their pseudocapacitive mechanism has been proposed [8, 14-16], similar to the mechanism proposed in literature for their oxide derivatives $NiCo_2O_4$, that is based on the synergic redox reaction with OH^- in KOH or NaOH electrolytes, involving the oxidation states of Ni^{2+}/Ni^{3+} and Co^{2+}/Co^{3+}. The redox response of Ni^{2+}/Ni^{3+} in $Ni(OH)_2$ or NiO occurs at potentials of approximately 0.4-0.6 V vs SCE [17]. The corresponding response of Co^{2+}/Co^{3+} in $Co(OH)_2$ or Co_3O_4 occurs at potentials of approximately 0-0.2 V vs SCE [18]. Their synergistic redox response occurs at approximately 0.2-0.4 V vs SCE [19], resulting in enhanced pseudocapacitive response in the Ni-Co hydroxides.

Most of studies performed on double Ni-Co hydroxides have been focused on its synergistic redox response compared to the single TMHs. Thus, it is expectable that electrodes composed of single $Ni(OH)_2$ and single $Co(OH)_2$ hydroxides designed in a way that combines the redox response from the single Ni^{2+}/Ni^{3+} and Co^{2+}/Co^{3+} redox reactions, will display enhanced electrochemical response.

Thus, in this study an electrode architecture composed of layered films of $Ni(OH)_2$ on $Co(OH)_2$ and $Co(OH)_2$ on $Ni(OH)_2$ (here after denominated $Ni(OH)_2$-$Co(OH)_2$ and $Co(OH)_2$-$Ni(OH)_2$) was designed via a facile two steps electrodeposition route. For comparative purposes the single layer hydroxides $Ni(OH)_2$, $Co(OH)_2$ and their double hydroxide $Ni_{1/2}Co_{1/2}(OH)_2$ were also prepared and studied.

3.6.2. Experimental

Electrodeposition

The potentiostatic electrodeposition was performed in a conventional three-electrode electrochemical cell, at room temperature, using Radiometer Voltalab PGZ 100 Potentiostat with stainless steel (AISI 304, Goodfellow) as a substrate (working electrode), platinum foil as counter electrode and the saturated calomel electrode (SCE) as reference electrode. Prior the electrodeposition, steel samples were polished with SiC grit papers up to 1000 grits, rinsed with deionized water and ethanol and dried by a jet of compressed air. The electrolytes used for the deposition were 0.1 M $Ni(NO_3)_2$, 0.1 M $Co(NO_3)_2$ and [0.05 M $Ni(NO_3)_2$ + 0.05 M $Co(NO_3)_2$] for the electrodeposition of $Ni(OH)_2$, $Co(OH)_2$ and $Ni_{1/2}Co_{1/2}(OH)_2$, respectively. All films were electrodeposited at a constant potential of -1.1 V vs SCE. Single layer films of $Ni(OH)_2$, $Co(OH)_2$ and $Ni_{1/2}Co_{1/2}(OH)_2$ were deposited with total applied charge of -1 C cm^{-2}. Layered films of $Ni(OH)_2$-$Co(OH)_2$ and $Co(OH)_2$-$Ni(OH)_2$ were prepared by depositing each layer, separately, following the order in the films, with the total applied charge for the deposition of each layer of -0.5 C cm^{-2}. All the potentials referred in this work are *vs.* SCE.

Characterization

Field emission gun scanning electron microscopy (FEG-SEM, JEOL 7001F and FEI QUANTA 250 ESEM microscopes) was used for studying the surface morphology (top view and cross section) of the deposited films. Cross-section measurements were done by scratching part of the films away from the substrate and observed on 75^o tilted sample holder.

The structural details were studied by transmission electron microscopy (TEM, JEOL JEM-2010 microscope) operating at 200 KeV. TEM samples were prepared by film scratching using a diamond tip, and the resulting powder was collected directly on TEM grids in order to avoid structural transformations induced by sample thinning process.

The electrochemical performance of the electrodes was studied by cyclic voltammetry (CV) and charge-discharge (CD) in 1 M KOH alkaline electrolytes. All the electrochemical tests were carried out in the conventional three-electrode cell using the films deposited on steel as working electrodes.

The specific capacitance of the films was calculated from the CD curves using the formula:

$$C = \frac{It}{\Delta V} \tag{3.6.1}$$

where I, t, ΔV are the CD current density (A g^{-1}), the discharge time (s) and the working potential range (V), respectively.

3.6.3. Results and Discussion

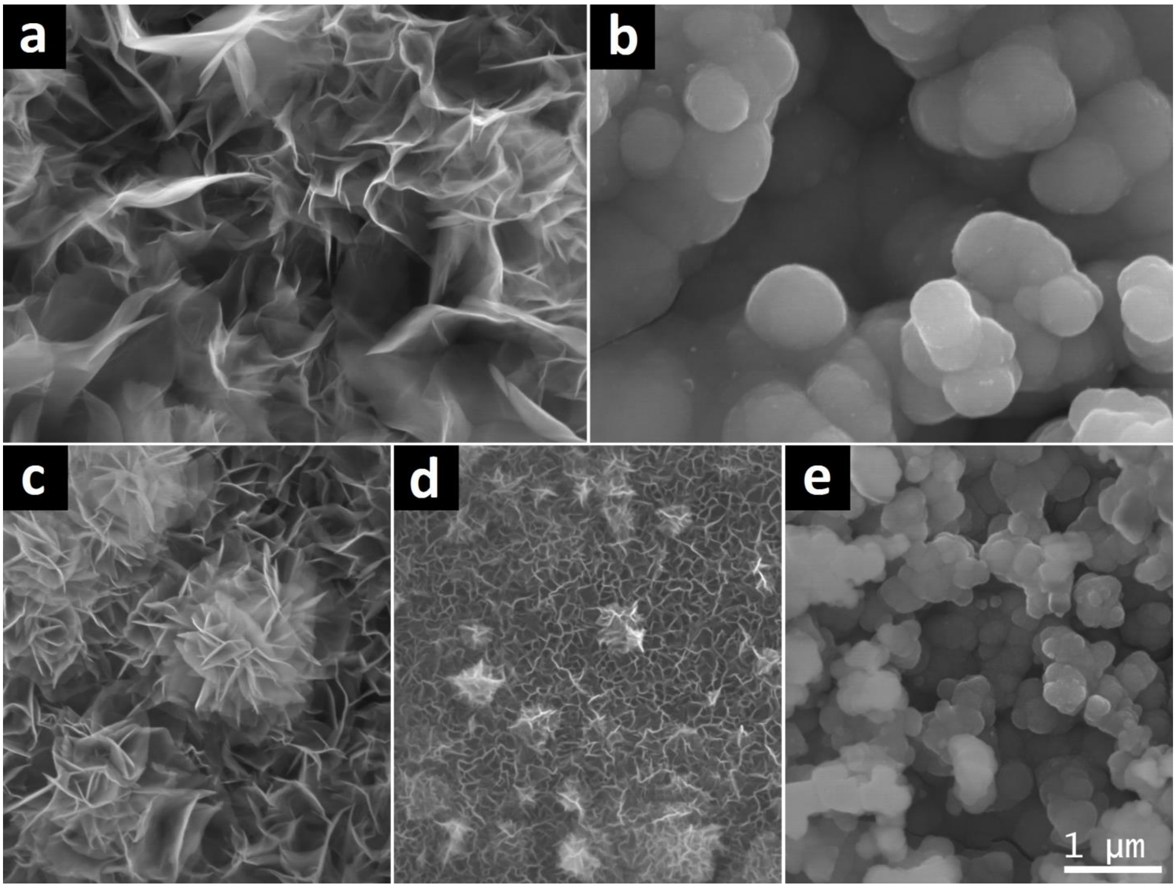

Figure 3.6.1. Top-view FEG-SEM images of the (a) $Co(OH)_2$, (b) $Ni(OH)_2$, (c) $Co(OH)_2$-$Ni(OH)_2$, (d) $Ni_{1/2}Co_{1/2}(OH)_2$ and (e) $Ni(OH)_2$-$Co(OH)_2$ films. The same scale bar is applied for all images in the figure.

Figure 3.6.1 shows top-view FEG-SEM images of the hydroxide films with different architectures electrodeposited on stainless steel substrates. The film electrodeposition is based on the generation of hydroxyl OH^- anions through the nitrate reduction and the reactions of metal ions in the electrolyte with the generated OH^- anions, leading to the formation of the hydroxide films deposited on stainless steel. FEG-SEM images of $Co(OH)_2$ and $Ni(OH)_2$ films, Figure 3.6.1a and b, show the presence crumpled nanosheets and agglomerated nanoparticles. This is in agreement with surface morphologies of Co_3O_4 and NiO films obtained by electrodeposition of their corresponding hydroxides, based on the same deposition mechanism with this work, and post thermal transformation (with the preservation of the surface morphology) to the oxides [20, 21]. The surface morphology of the $Ni_{1/2}Co_{1/2}(OH)_2$ film, Figure 3.6.1d, reveals the presence of nanosheets, which are almost vertically grown on the substrate and interconnected together, forming a percolation network. On top of the nanosheets network, dendrites are formed and randomly distributed over the surface. The surface morphology characterized for $Ni_{1/2}Co_{1/2}(OH)_2$ film is different from that of the corresponding single oxides, and probably due to the different preferential growth of the single oxides as reported previously [21]. The surface morphologies of $Co(OH)_2$-$Ni(OH)_2$ and $Ni(OH)_2$-$Co(OH)_2$ films, Figure 3.6.1c and e, reveal the presence of a flower-like architecture composed of nanosheets and of agglomerated particles. The nanosheets architecture in $Co(OH)_2$-$Ni(OH)_2$ is slightly different from that of $Co(OH)_2$ film and the particle size in $Ni(OH)_2$-$Co(OH)_2$ film is smaller than the corresponding size in $Ni(OH)_2$ film (300 nm vs. 1 μm). This difference can be due to the fact that $Co(OH)_2$ and $Ni(OH)_2$ were grown on other hydroxides layers rather than on the stainless steel, resulting in the differences in the nucleation process, and thus in distinct surface morphology. It should be noted that, due to low electron conductivity of the bottom hydroxides layer, the top hydroxides layer favors the grow of a new layer rather than the coverage with nanosheets as reported in previous work [22] for $NiCo_2O_4$/$NiCo_2O_4$ system. It is expected that the features of the morphological architecture and the differences in the composition of each electrode, will result in distinct electrochemical response. This issue will be discussed below.

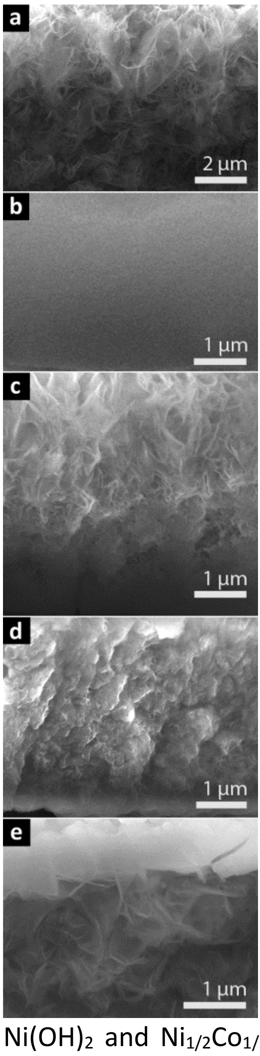

Figure 3.6.2. (left side). Cross-section FEG-SEM images of the (a) $Co(OH)_2$, (b) $Ni(OH)_2$, (c) $Co(OH)_2$-$Ni(OH)_2$, (d) $Ni_{1/2}Co_{1/2}(OH)_2$ and (e) $Ni(OH)_2$-$Co(OH)_2$ films.

The morphology of the films cross section was studied by FEG-SEM and the results are shown in Figure 3.6.2. The cross-section images of $Co(OH)_2$, $Ni(OH)_2$ and $Ni_{1/2}Co_{1/2}(OH)_2$ (Figure 3.6.2a, b and d) show the presence of a crumpled nanosheets layer, a dense layer and interconnected nanosheets, respectively. This is in a good agreement with the top-view FEG-SEM images, indicating the homogeneity of the film morphologies. The images of the two layer films, Figure 3.6.2c and e, revealed the presence of two layers with different morphologies. Each of them revealed morphologies quite similar to that of the single layer films. The thickness of the $Co(OH)_2$ layer is thicker than that of the $Ni(OH)_2$ layer. This can be due to the nanosheets morphology of the $Co(OH)_2$ layer that displays higher porosity compared to the $Ni(OH)_2$ layer, which composed of dense particles, leading to the high volume/area in the $Co(OH)_2$ film. Therefore, it results in the formation of thick $Co(OH)_2$ layers.

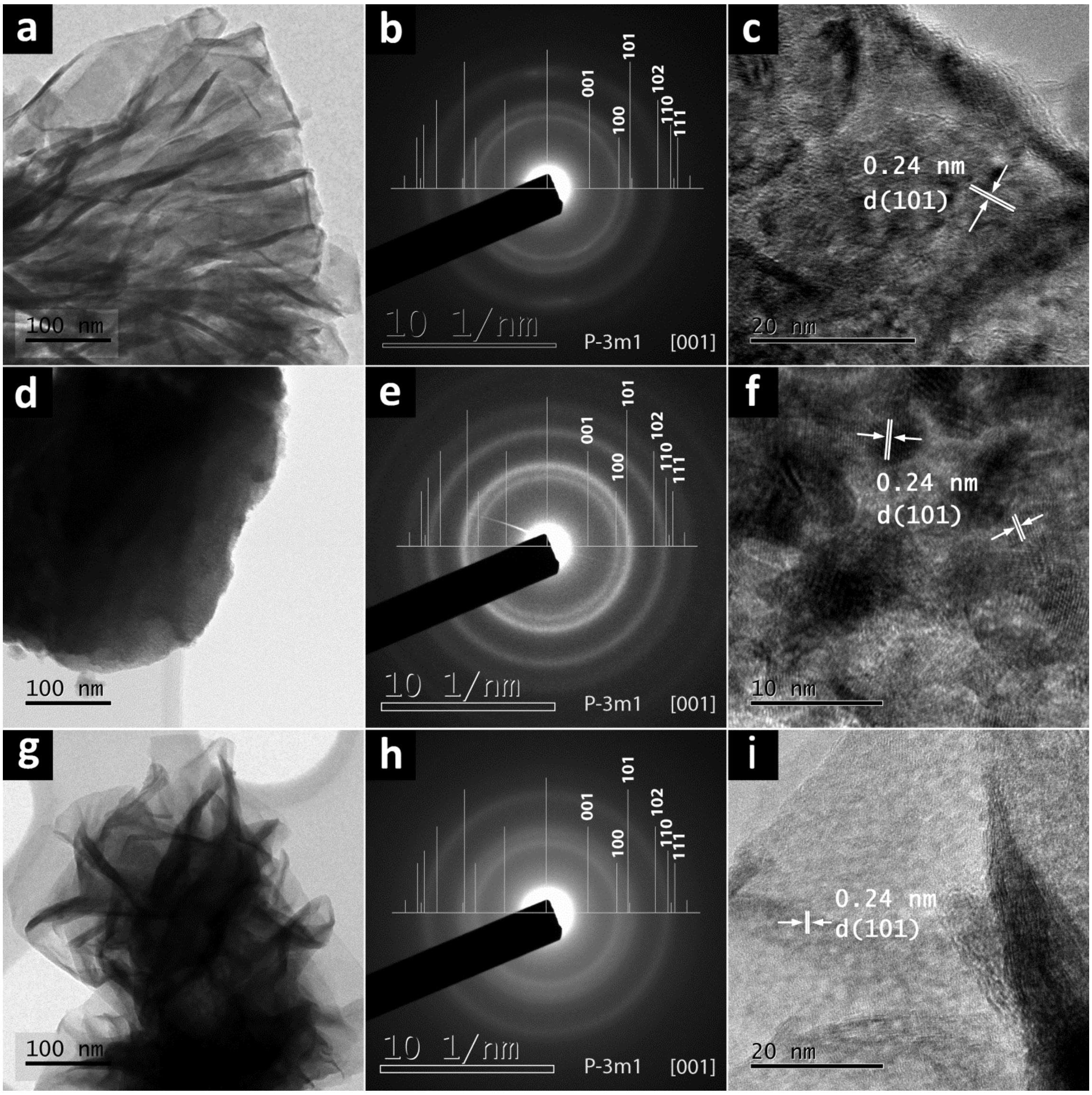

Figure 3.6.3. TEM results. From left to right: low magnified TEM images, SAED patterns and HRTEM images. (a-c) $Co(OH)_2$, (d-f) $Ni(OH)_2$ and (g-i) $Ni_{1/2}Co_{1/2}(OH)_2$ films.

TEM results the $Co(OH)_2$, $Ni(OH)_2$ and $Ni_{1/2}Co_{1/2}(OH)_2$ films are depicted in Figure 3.6.3. The $Co(OH)_2$ layer and the $Ni(OH)_2$ layer in the layered films can be represented by the TEM results of the single layers $Co(OH)_2$ and $Ni(OH)_2$ films, and thus TEM measurement was not performed on the two layers films. Low magnified TEM images revealed the presence of thin and crumpled nanosheets in the $Co(OH)_2$ and $Ni_{1/2}Co_{1/2}(OH)_2$ films (Figure 3.6.3a and g) and a dense particle in the $Ni(OH)_2$ film (Figure 3.6.3d). This is in agreement with FEG-SEM observations. The selected area electron diffractions (SAED) of these films (Figure 3.6.3b, e and h) show well-defined diffractions rings, revealing the polycrystalline nature of the films. The broadening of the rings indicates the formation of nanocrystals or low crystallinity in the films. These rings can be indexed to (100), (101), and (110) lattice planes of the trigonal hydroxide structures (space group P-3m1). Notes that the diffraction from (001) plane is missed, probably due to the preferential growth of hydroxides in [001] direction as reported previously [23]. The d_{101} values are of 2.45 nm, 2.43 nm and 2.44 nm for $Co(OH)_2$ $Ni(OH)_2$ and $Ni_{1/2}Co_{1/2}(OH)_2$ films, respectively. The d_{101} value of $Ni_{1/2}Co_{1/2}(OH)_2$ films is lower than that of $Co(OH)_2$ film and higher than that of $Ni(OH)_2$ film, indicating the formation of the mixed hydroxide $Ni_{1/2}Co_{1/2}(OH)_2$. High resolution TEM (HRTEM) results (Figure 3.6.3c, f and i) evidenced the lattice fringes with distances of approximately 0.24 nm, which are randomly oriented and correspond to the lattice spacing of (101) planes, thus in agreement with the SAED results.

The electrochemical response of the deposited films was assessed by CV measurements in a potential window ranging from -0.2 V to 0.6 V with the scan rate of 20 mV s^{-1} in 1 M KOH electrolytes; the results are shown in Figure 3.6.4a. The CV curves of $Co(OH)_2$ and $Ni(OH)_2$ show the presence of a broad anodic peaks at approximately 0.22 V and 0.54, which can be assigned to the redox reactions of the films with OH^- in alkaline electrolytes as below [23]:

For $Co(OH)_2$

$$Co(OH)_2 + OH^- \leftrightarrow CoOOH + H_2O + e^- \qquad (3.6.2)$$

$$CoOOH + OH^- \leftrightarrow CoO_2 + H_2O + e^- \qquad (3.6.3)$$

For $Ni(OH)_2$

$$Ni(OH)_2 + OH^- \leftrightarrow NiOOH + H_2O + e^- \quad (3.6.4)$$

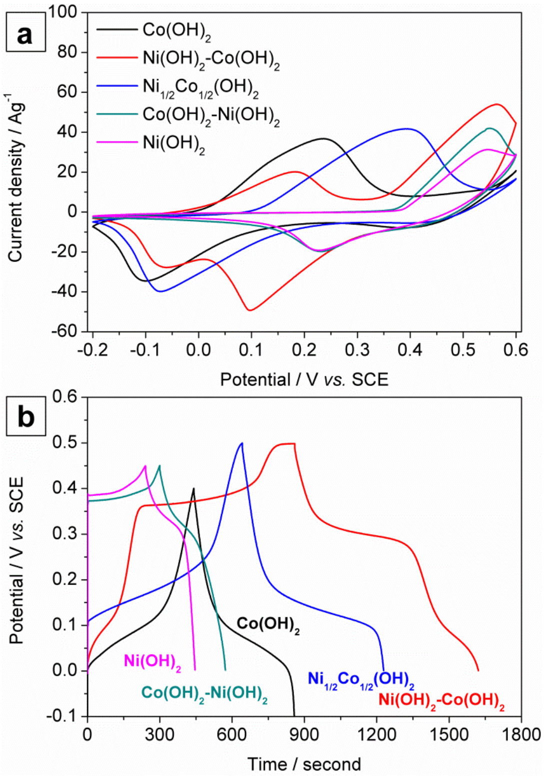

Figure 3.6.4. (a) Cyclic voltammetry curves at a scan rate of 20 mV s^{-1} and (b) galvanostatic charge-discharge curves at a constant current of 1 A g^{-1} of $Ni(OH)_2$, $Co(OH)_2$, $Co(OH)_2$-$Ni(OH)_2$, $Ni_{1/2}Co_{1/2}(OH)_2$ and $Ni(OH)_2$-$Co(OH)_2$ films.

The CV curve of $Ni_{1/2}Co_{1/2}(OH)_2$ reveals the presence of a broad anodic peak. The redox peak potential is approximately 0.38 V, which is in the middle of the redox peak potentials of its corresponding single oxides $Co(OH)_2$ and $Ni(OH)_2$. Furthermore, the current response increase compared to $Co(OH)_2$ and $Ni(OH)_2$. This is an indication of the synergistic redox reaction in $Ni_{1/2}Co_{1/2}(OH)_2$, leading to an increased electrochemical response.

The CV curves of the $Ni(OH)_2$-$Co(OH)_2$ films evidence the presence of two redox peaks, which are approximately at the same potential of the redox response of $Co(OH)_2$ and $Ni(OH)_2$ films. Thus, it indicates the redox contribution of both layers in the two layers film. The current response corresponding to the redox reaction of $Co(OH)_2$ is lower than that of $Co(OH)_2$ film due to the formation of thinner $Co(OH)_2$ layer. The current response corresponding to the redox reaction of $Ni(OH)_2$ increases compared to those of $Ni(OH)_2$ and $Ni_{1/2}Co_{1/2}(OH)_2$ films.

The CV curve of $Co(OH)_2$-$Ni(OH)_2$ film presents a redox peak at a similar potential to that of $Ni(OH)_2$ films. The current response at the peaks increases compared to $Ni(OH)_2$ film. It can also be observed that the onset potential of the anodic peak in $Co(OH)_2$-$Ni(OH)_2$ film shifted to a negative potential as compared to the anodic peak in $Ni(OH)_2$, thus indicating the contribution of $Co(OH)_2$. The contribution of $Co(OH)_2$ layer, however, is rather small, probably due to the lower conductivity [24] of $Ni(OH)_2$ layer compared to $Co(OH)_2$ leading to the reduced contribution from $Co(OH)_2$ layer.

Overall, with the separated contribution of the two redox reactions in $Ni(OH)_2$-$Co(OH)_2$ film, this film is expected to display the highest specific capacitance values amongst the ones prepared in this work.

To determine the specific capacitance values, CD measurements were carried out with the constant current of 1 A g^{-1}. The potential windows used to measure specific capacitance values of each film were optimized in order to obtain the highest specific capacitance value in the corresponding films. It can be clearly observed a presence of two plateaus in the CD curves of $Ni(OH)_2$-$Co(OH)_2$ film. The CD results of the other films present one plateau in the curves. This is in a good agreement with the redox response previously identified in the CV curves. The specific capacitance values calculated at 1 A g^{-1} are 834 F g^{-1}, 1524 F g^{-1}, 1172 F g^{-1}, 606 F g^{-1} and 457 F g^{-1} for $Co(OH)_2$, $Ni(OH)_2$-$Co(OH)_2$, $Ni_{1/2}Co_{1/2}(OH)_2$ and $Co(OH)_2$-$Ni(OH)_2$ and $Ni(OH)_2$ films, respectively. The specific capacitance value of $Ni_{1/2}Co_{1/2}(OH)_2$ increases compared to its corresponding single oxides due to the synergistic redox reaction. The highest specific capacitance value of $Ni(OH)_2$-$Co(OH)_2$ film is due to the separated contribution of the two redox reactions. Thus, this results clearly evidences the advantage of multiple redox reaction in the layered $Ni(OH)_2$-$Co(OH)_2$ film. It should be noted that the specific capacitance value of $Ni(OH)_2$-$Co(OH)_2$ film is very high, considering that it is deposited on stainless steel which is a flat current collector without any porous channels.

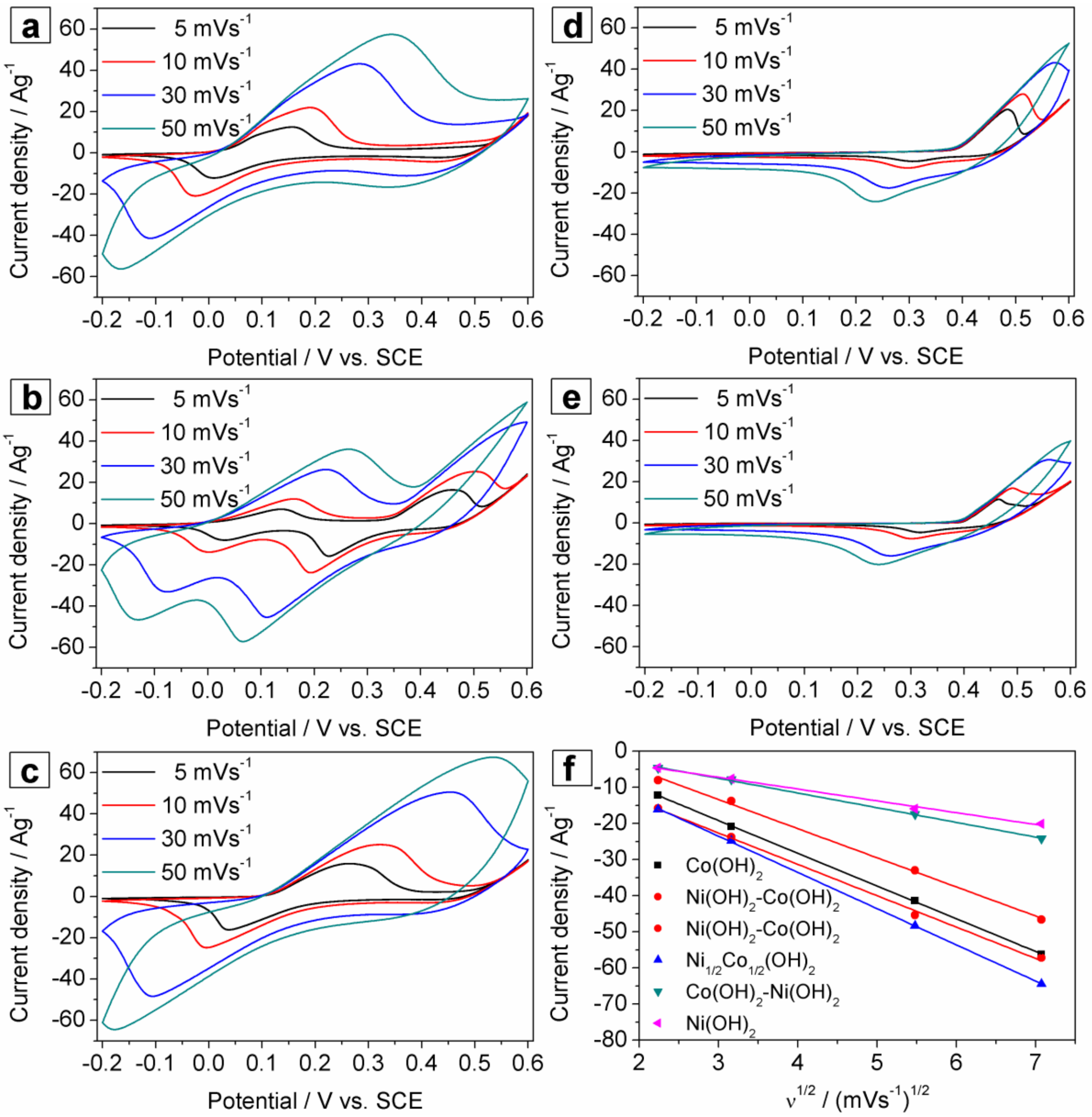

Figure 3.6.5. Cyclic voltammograms at different scan rates of 5 mV s^{-1}, 10 mV s^{-1}, 30 mV s^{-1} and 50 mV s^{-1} of (a) $Co(OH)_2$, (b) $Ni(OH)_2$-$Co(OH)_2$, (c) $Ni_{1/2}Co_{1/2}(OH)_2$, (d) $Co(OH)_2$-$Ni(OH)_2$ and (e) $Ni(OH)_2$. (f) Relation of current density peaks with the square root of scan rates.

The electrochemical capacitive response of the electrodeposited films was further assessed by performing CV measurements with varying the scan rate from 5 mV s^{-1} to 50 mV s^{-1}. The CV results obtained at different scan rates are presented in Figure 3.6.5a-e. The results show that in all deposited films the main redox peaks shifts, the large separation between them and the current density increases with the scan rate, indicating the quasi reversibility of the redox reactions and thus the good pseudocapacitive behavior [25]. The potential difference, between the anodic peak and the cathodic peak, increases due to polarization of the electrode at increased scan rates. The shape of the cyclic voltamograms is almost preserved up to the highest scan rate indicating the easy diffusion of ions in the electrolyte into the film. This is probably due to characteristics of hydroxides, favoring the diffusion of ions. The cathodic current density peaks vs. the square root of the scan rate are depicted in Figure 3.6.5f. The linear relation indicates that the redox reactions are diffusion-controlled processes [26].

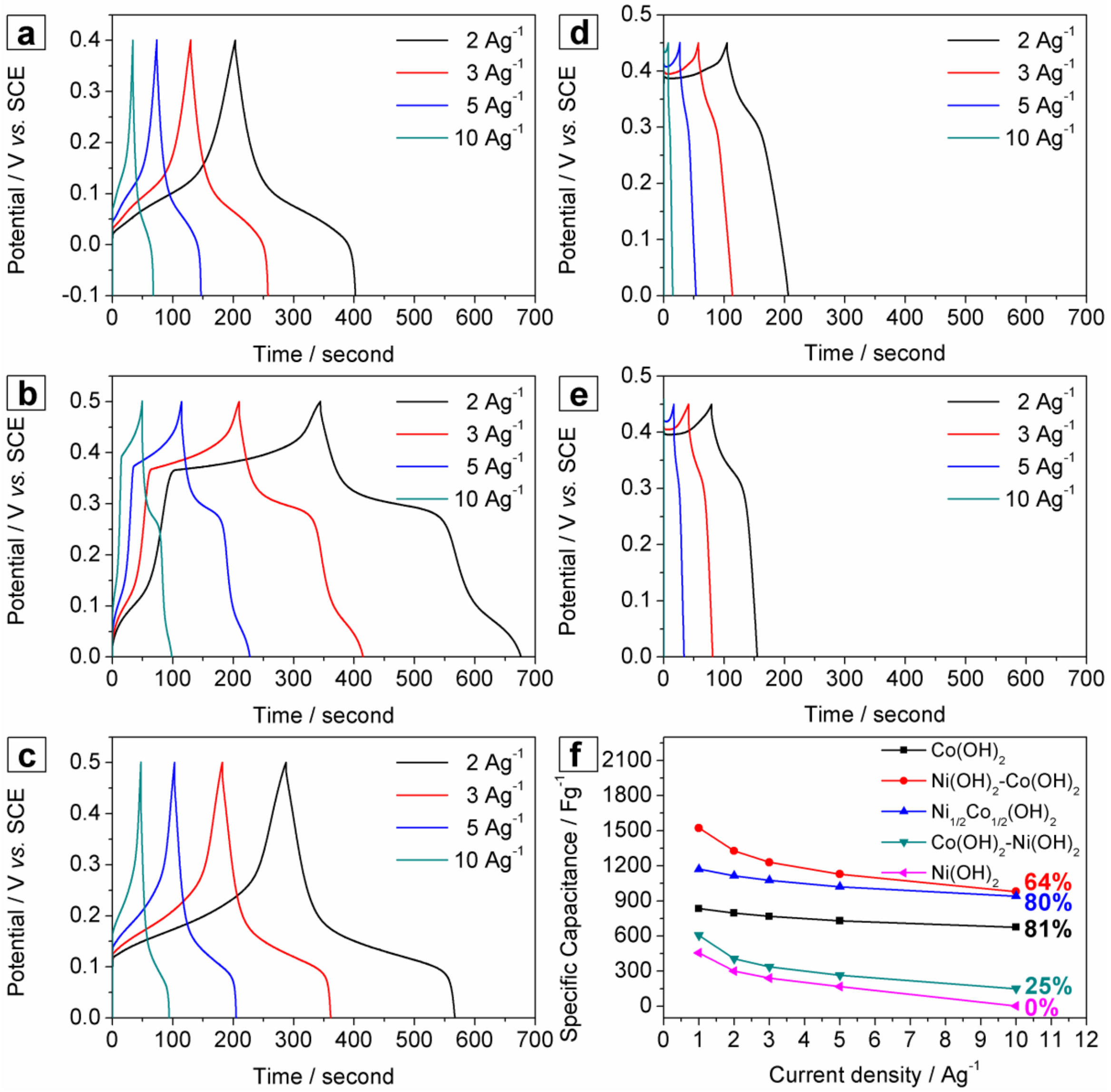

Figure 3.6.6. Charge-discharge at different constant currents of 2 A g^{-1}, 3 A g^{-1}, 5 A g^{-1} and 10 A g^{-1} of (a) $Co(OH)_2$, (b) $Ni(OH)_2$-$Co(OH)_2$, (c) $Ni_{1/2}Co_{1/2}(OH)_2$, (d) $Co(OH)_2$-$Ni(OH)_2$ and (e) $Ni(OH)_2$. (f) The relation of specific capacitance values with increasing current density of the prepared films.

Rate capability, which is an important parameter for evaluating the suitability of a material to work as an electrode for electrochemical energy storage, was also assessed by performing CD measurements with applied currents increasing up to 10 A g^{-1} (Figure 3.6.6a-e). The results show that the potential drop is more marked and the discharge time decreased when the current density increases, thereby reducing the specific capacitance. Notably, the response time of $Ni(OH)_2$ dropped to zero when applying current density of 10 A g^{-1}. This indicates the intrinsic poor rate of $Ni(OH)_2$ as reported elsewhere in literature[2]. The specific capacitance depends upon the applied current density, Figure 3.6.6f, and shows capacitance retentions of 81%, 64%, 80%, 25% and 0% when the current increases from 1 A g^{-1} to 10 A g^{-1} for $Co(OH)_2$, (b) $Ni(OH)_2$-$Co(OH)_2$, (c) $Ni_{1/2}Co_{1/2}(OH)_2$, (d) $Co(OH)_2$-$Ni(OH)_2$ and (e) $Ni(OH)_2$, respectively. The specific capacitance reduction in all the films is probably consequence of inaccessible active sites at high applied current densities. $Co(OH)_2$ and $Ni_{1/2}Co_{1/2}(OH)_2$ present highest rate capability, while $Ni(OH)_2$ and $Co(OH)_2$-$Ni(OH)_2$ present very poor rate capability. The value of $Ni(OH)_2$-$Co(OH)_2$ is lower than that of $Co(OH)_2$ and $Ni_{1/2}Co_{1/2}(OH)_2$, probably due to the presence of $Ni(OH)_2$ layer with low rate capability. However, considering the specific capacitance values obtained at 10 A g^{-1} of 667 F g^{-1}, 949 F g^{-1} and 975 F g^{-1} for $Co(OH)_2$ and $Ni_{1/2}Co_{1/2}(OH)_2$ and $Ni(OH)_2$-$Co(OH)_2$, this two layers film still displayed the highest specific capacitance values.

The total specific capacitance includes the contributions from the double layer and the diffusion-controlled redox processes. To detail the mechanisms of charge storage and the contribution of the diffusion-controlled redox capacitive response to the total capacity of the electrode, the cyclic voltammetry data obtained at different scan rates were fitted with kinetic models [27]. The relationship between the charge ($Q/Coulomb$) and the scan rate can be described by equations (3.6.5) and (3.6.6) [27]:

$$Q = Q_{v=\infty} + constant\left(v^{-1/2}\right) \quad (3.6.5)$$

$$Q^{-1} = Q_{v=0}^{-1} + constant(v^{1/2}) \quad (3.6.6)$$

where: $Q_{v=\infty}$ is the double layer charge, which is the value at $v = \infty$. $Q_{v=0}$ is the total charge, which is the value at $v = 0$. Therefore, by plotting Q *vs.* $v^{-1/2}$, and Q^{-1} *vs.* $v^{1/2}$, the double layer capacitance and the total capacitance can be retrieved from the y-axis intercepts in Figure 3.6.7a and b. The calculation results are presented as the contribution of diffusion-controlled redox capacitive and of double layer capacitive to the total specific capacitance of the deposited films in Figure 3.6.7c.

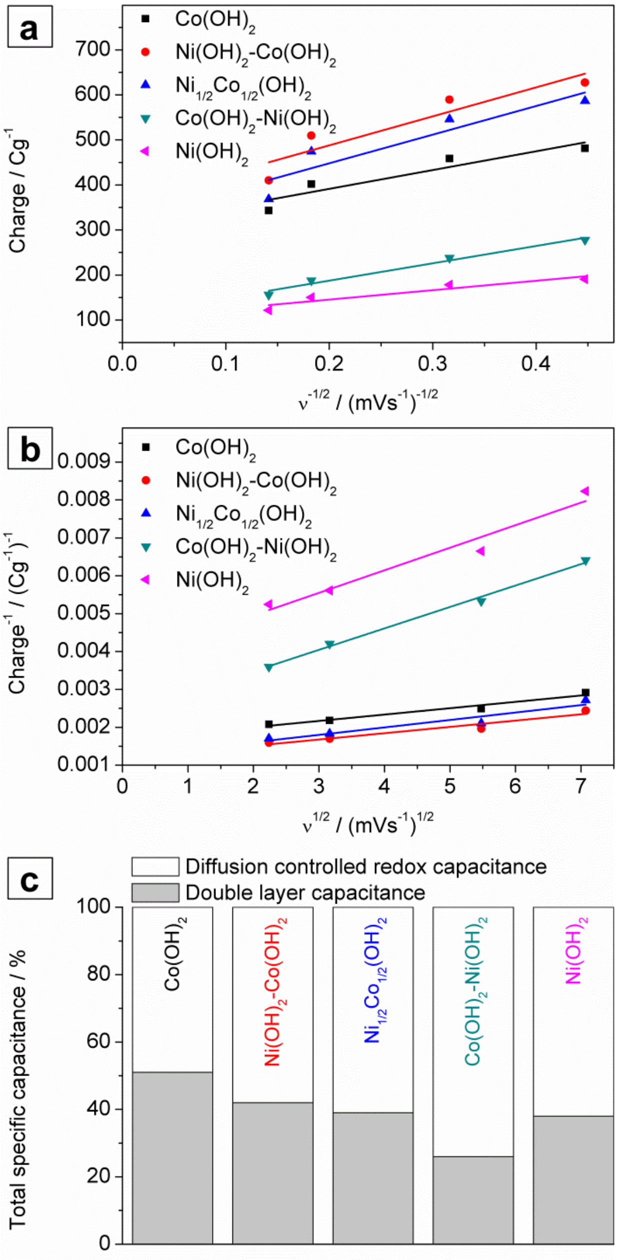

Figure 3.6.7. The relation of (a) charge (Q) vs. $v^{-1/2}$, (b) of Q^{-1} vs. $v^{1/2}$ and (c) contributions of double layer capacitance and diffusion controlled redox capacitance to the total capacitance of the deposited films.

As shown in Figure 3.6.7c, in most films, except $Co(OH)_2$, the contribution of the diffusion-controlled redox processes to the capacitive response is higher than the double layer ones, thus indicating that the diffusion-controlled redox processes are the main contributors to the total specific capacitance. The higher contribution of the double layer capacitance in the $Co(OH)_2$ film can be explained by the formation of thin crumpled nanosheets, leading to an increased surface area and therefore increasing double layer contribution.

This analysis shows that the diffusion-controlled redox contribution of 74% in $Co(OH)_2$-$Ni(OH)_2$ film is higher than that of $Ni(OH)_2$ film of 62%. Thus, it indicates that the $Co(OH)_2$ layer also contribute to the total capacitive response.

The contribution of the diffusion-controlled redox processes to the total capacitance is similar for the individual $Ni(OH)_2$-$Co(OH)_2$ and $Ni_{1/2}Co_{1/2}(OH)_2$ films, and there is a marked synergistic effect in the layered film.

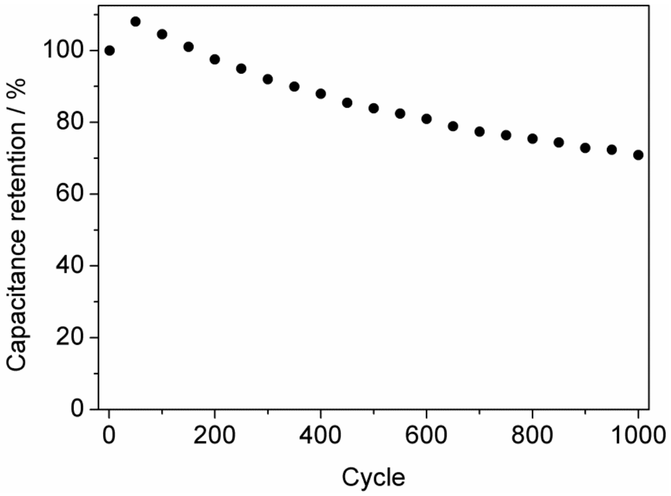

Figure 3.6.8. Charge-discharge cycling stability of the $Ni(OH)_2$-$Co(OH)_2$ film at constant current of 10 A g^{-1} for 1000 cycles.

The CD cycling stability of the electrode is another important parameter for its practical application as electrode in redox supercapacitors. The $Ni(OH)_2$-$Co(OH)_2$ electrodes, displaying the highest specific capacitance values were selected for the stability test. The cycling stability test (continuous charge and discharge) under an applied current density of 10 A g^{-1} was performed for 1000 cycles. The capacitance retention (Figure 3.6.8) increases to approximately 108% after 50 cycles. Then, it slowly decreases to approximately 71% after 1000 cycles. Even though, the final value is not so high, this stability is comparable to the values reported for $Ni_xCo_{2-x}(OH)_6/NiCo_2O_4$ grown on carbon paper [19]. It should also be noted that the stability test was performed at a high-applied current of 10 A g^{-1}. The similar stability test for $Ni(OH)_2$ on 3D ultrathin graphite foam [28] presented the capacitance retention of 66 % after 1000 cycles. The specific capacitance value after 1000 cycles is 692 F g^{-1} at 10 A g^{-1}, revealing a high specific capacitance value after cycling.

Overall, the reported results suggested that new electrodes architectures composed of two TM hydroxides layers can display enhanced specific capacitance values compared to the corresponding DTMH electrodes. Thus, this work opens a new way of designing TMHs electrodes for an enhanced pseudocapacitive response.

3.6.4. Conclusions

In summary, the new two layers hydroxides $Ni(OH)_2$-$Co(OH)_2$ electrodes prepared by electrodeposition on stainless steel were studied towards application in redox supercapacitors. Comparative studies of this electrode with $Co(OH)_2$, $Ni_{1/2}Co_{1/2}(OH)_2$, $Co(OH)_2$-$Ni(OH)_2$ and $Ni(OH)_2$ revealed its enhanced pseudocapacitive response with high specific capacitance values, 1580 F g^{-1}. The high specific capacitance is due to the contribution of the two hydroxides layers to the redox response of the electrode, leading to the presence of two redox peaks in the cyclic voltammogram. The contribution of the two hydroxide layers to the total pseudocapacitive response results from an architecture composed of agglomerated particles $Ni(OH)_2$ (top layer) over nanosheets $Co(OH)_2$ (bottom layer) with high ionic diffusion, allowing the diffusion of electrolyte into both layers of the electrodes. It displays a good rate capability with a specific capacitance value at 10 A g^{-1} of 975 F g^{-1}. The specific capacitance value at 10 A g^{-1} after continuous CD cycling for 1000 cycles is 692 F g^{-1}.

Acknowledgements

The authors would like to thank Fundação para a Ciência e Tecnologia (FCT) for the funding under the contract PTDC/CTM-MET/119411/2010 & UID/QUI/00100/2013, IDS-FunMat Erasmus Mundus PhD School and the European COST Action MP1004. L. Rapenne (LMGP) is acknowledged for TEM measurements.

References

[1] J.P. Cheng, J. Zhang, F. Liu, Recent development of metal hydroxides as electrode material of electrochemical capacitors, RSC Adv., 4 (2014) 38893-38917.

[2] G.-W. Yang, C.-L. Xu, H.-L. Li, Electrodeposited nickel hydroxide on nickel foam with ultrahigh capacitance, Chemical Communications, (2008) 6537-6539.

[3] W.-j. Zhou, J. Zhang, T. Xue, D.-d. Zhao, H.-l. Li, Electrodeposition of ordered mesoporous cobalt hydroxide film from lyotropic liquid crystal media for electrochemical capacitors, Journal of Materials Chemistry, 18 (2008) 905-910.

[4] M.-S. Wu, K.-C. Huang, Fabrication of nickel hydroxide electrodes with open-ended hexagonal nanotube arrays for high capacitance supercapacitors, Chemical Communications, 47 (2011) 12122-12124.

[5] Q. Yang, Z. Lu, J. Liu, X. Lei, Z. Chang, L. Luo, X. Sun, Metal Oxide and Hydroxide Nanoarrays: Hydrothermal Synthesis and Applications as Supercapacitors and Nanocatalysts, Progress in Natural Science: Materials International, 23 (2013) 351-366.

[6] V. Gupta, T. Kusahara, H. Toyama, S. Gupta, N. Miura, Potentiostatically Deposited Nanostructured α-$Co(OH)_2$: A High Performance Electrode Material for Redox-Capacitors, Electrochemistry Communications, 9 (2007) 2315-2319.

[7] J. Li, W. Zhao, F. Huang, A. Manivannan, N. Wu, Single-Crystalline $Ni(OH)_2$ and NiO Nanoplatelet Arrays as Supercapacitor Electrodes, Nanoscale, 3 (2011) 5103-5109.

[8] H. Chen, L. Hu, M. Chen, Y. Yan, L. Wu, Nickel–Cobalt Layered Double Hydroxide Nanosheets for High-performance Supercapacitor Electrode Materials, Advanced Functional Materials, 24 (2014) 934-942.

[9] V. Gupta, S. Gupta, N. Miura, Potentiostatically Deposited Nanostructured Co_xNi_{1-x} Layered Double Hydroxides as Electrode Materials for Redox-Supercapacitors, Journal of Power Sources, 175 (2008) 680-685.

[10] R.R. Salunkhe, K. Jang, S.-w. Lee, H. Ahn, Aligned nickel-cobalt hydroxide nanorod arrays for electrochemical pseudocapacitor applications, RSC Adv., 2 (2012) 3190-3193.

[11] S.B. Kulkarni, A.D. Jagadale, V.S. Kumbhar, R.N. Bulakhe, S.S. Joshi, C.D. Lokhande, Potentiodynamic Deposition of Composition Influenced $Co_{1-x}Ni_x$ LDHs Thin Film Electrode for Redox Supercapacitors, International Journal of Hydrogen Energy, 38 (2013) 4046-4053.

[12] Y. Gu, Z. Lu, Z. Chang, J. Liu, X. Lei, Y. Li, X. Sun, NiTi Layered Double Hydroxide Thin Films for Advanced Pseudocapacitor Electrodes, J. Mater. Chem. A, 1 (2013) 10655-10661.

[13] Y. Zhao, Q. Wang, T. Bian, H. Yu, H. Fan, C. Zhou, L.-Z. Wu, C.-H. Tung, D. O'Hare, T. Zhang, Ni^{3+} doped monolayer layered double hydroxide nanosheets as efficient electrodes for supercapacitors, Nanoscale, 7 (2015) 7168-7173.

[14] L. Xie, Z. Hu, C. Lv, G. Sun, J. Wang, Y. Li, H. He, J. Wang, K. Li, Co_xNi_{1-x} double hydroxide nanoparticles with ultrahigh specific capacitances as supercapacitor electrode materials, Electrochimica Acta, 78 (2012) 205-211.

[15] X. Wang, A. Sumboja, M. Lin, J. Yan, P.S. Lee, Enhancing electrochemical reaction sites in nickel–cobalt layered double hydroxides on zinc tin oxide nanowires: a hybrid material for an asymmetric supercapacitor device, Nanoscale, 4 (2012) 7266-7272.

[16] Y. Tao, L. Zaijun, L. Ruiyi, N. Qi, K. Hui, N. Yulian, L. Junkang, Nickel–cobalt double hydroxides microspheres with hollow interior and hedgehog-like exterior structures for supercapacitors, Journal of Materials Chemistry, 22 (2012) 23587-23592.

[17] C.-C. Hu, J.-C. Chen, K.-H. Chang, Cathodic deposition of $Ni(OH)_2$ and $Co(OH)_2$ for asymmetric supercapacitors: Importance of the electrochemical reversibility of redox couples, Journal of Power Sources, 221 (2013) 128-133.

[18] C. Zhao, W. Zheng, X. Wang, H. Zhang, X. Cui, H. Wang, Ultrahigh capacitive performance from both $Co(OH)_2$/graphene electrode and $K_3Fe(CN)_6$ electrolyte, Sci. Rep., 3 (2013).

[19] L. Huang, D. Chen, Y. Ding, S. Feng, Z.L. Wang, M. Liu, Nickel–Cobalt Hydroxide Nanosheets Coated on $NiCo_2O_4$ Nanowires Grown on Carbon Fiber Paper for High-Performance Pseudocapacitors, Nano Lett., 13 (2013) 3135-3139.

[20] C. Yuan, L. Yang, L. Hou, L. Shen, X. Zhang, X.W. Lou, Growth of ultrathin mesoporous Co_3O_4 nanosheet arrays on Ni foam for high-performance electrochemical capacitors, Energy & Environmental Science, 5 (2012) 7883-7887.

[21] T. Nguyen, M. Boudard, L. Rapenne, M.J. Carmezim, M.F. Montemor, Morphological changes and electrochemical response of mixed nickel manganese oxides as charge storage electrodes, Journal of Materials Chemistry A, 3 (2015) 10875-10882.

[22] X. Liu, S. Shi, Q. Xiong, L. Li, Y. Zhang, H. Tang, C. Gu, X. Wang, J. Tu, Hierarchical $NiCo_2O_4$@$NiCo_2O_4$ Core/Shell Nanoflake Arrays as High-Performance Supercapacitor Materials, ACS Appl. Mater. Interfaces, 5 (2013) 8790-8795.

[23] T. Nguyen, M. Boudard, L. Rapenne, O. Chaix-Pluchery, M.J. Carmezim, M.F. Montemor, Structural evolution, magnetic properties and electrochemical response of $MnCo_2O_4$ nanosheet films, RSC Adv., 5 (2015) 27844-27852.

[24] K. Nogi, M. Naito, T. Yokoyama, Nanoparticle technology handbook, Elsevier2012.

[25] T.P. Gujar, V.R. Shinde, C.D. Lokhande, W.-Y. Kim, K.-D. Jung, O.-S. Joo, Spray deposited amorphous RuO_2 for an effective use in electrochemical supercapacitor, Electrochemistry Communications, 9 (2007) 504-510.

[26] A. Bard, L. Faulkner, Electrochemical Methods: Fundamentals and Applications, John Wiley & Sons, Inc2001.

[27] S. Ardizzone, G. Fregonara, S. Trasatti, “Inner” and “outer” active surface of RuO_2 electrodes, Electrochimica Acta, 35 (1990) 263-267.

[28] J. Ji, L.L. Zhang, H. Ji, Y. Li, X. Zhao, X. Bai, X. Fan, F. Zhang, R.S. Ruoff, Nanoporous $Ni(OH)_2$ Thin Film on 3D Ultrathin-Graphite Foam for Asymmetric Supercapacitor, ACS Nano, 7 (2013) 6237-6243.

3.7. Current transient and *in-situ* AFM studies of initial growth stages of electrochemically deposited nickel cobalt hydroxide nanosheet films

Tuyen Nguyen[a], M. João Carmezim[a,b], M. Fátima Montemor[a]

[a] CQE - Centro de Química Estrutural, Insituto Superior Técnico, Universidade de Lisboa, Lisbon 1049-001, Portugal.

[b] ESTSetúbal, Instituto Politécnico de Setúbal, 1959-007 Setúbal, Portugal.

Current transient's evolution and *in-situ* electrochemical AFM were used to study the initial stages of growth of electrochemically deposited nickel cobalt hydroxide films for energy storage applications Current transient were taken at constant potentials, from -700 mV to -1000 mV with a step of 50 mV. The current transients were fitted with three different nucleation models: Scharifker-Hill, Scharifker-Mostany and Mirkin-Nilov-Heerman-Tarallo and the results revealed a 3D spontaneous nucleation mechanism. *In-situ* electrochemical AFM studies confirmed the spontaneous nucleation mechanism, which led to the early stage formation of nanosheets. The in-situ AFM results were further supported by ex-situ FEG-SEM results, showing the formation of nanoneedles at the first stages of nucleation and the growth into nanosheets with the increasing deposition time.

Keywords: *in-situ* AFM, film growth, double layered hydroxide, nickel, cobalt, supercapacitors.

3.7.1. Introduction

Double nickel cobalt hydroxides (DNCHs) are currently receiving considerable attention as electrode materials for high energy density storage, namely as materials for redox-based supercapacitor applications [1, 2]. The layered structure of DNCHs, with high interlayer distances, facilitates the bulk ionic diffusion, resulting in enhanced charge storage capacity since the redox reactions are not limited only to the surface of the electrodes, but can also take place in the bulk [3]. On the other hand, due to the presence of two transition metals (TMs) ions, nickel and cobalt, in the electrodes, the redox reactions involve both TMs ions, leading to an enhanced electrochemical response [4]. For example, nanostructured porous layered $Co_{1-x}Ni_x(OH)_2$ films were prepared by potentiodynamic electrodeposition [5] showing a specific capacitance value of 1213 F g^{-1}. Ultrathin Ni-Co hydroxides nanosheets electrodes [1] prepared by surfactant assisted hydrothermal deposition exhibited a specific capacitance value of 2682 F g^{-1}. Hybrid $Co_{1-x}Ni_x(OH)_2/NiCo_2O_4$ prepared via two steps of hydrothermal and electrodeposition route exhibited high areal capacitance values ranging from 0.61 F cm^{-2} to 2.17 F cm^{-2} depending on the stoichiometry of nickel and cobalt in the DNCHs [6].

DTMHs are also a regular precursor to prepare nickel cobalt spinel oxides (NCSOs) $NiCo_2O_4$, an emerging material for redox supercapacitors [7, 8], through thermal transformation [9]. The $NiCo_2O_4$ electrodes normally maintain the architecture of its parent DTMHs and present a good pseudocapacitive response resulting from its increased electron conductivity [10]. For example, $NiCo_2O_4$ nanosheets film electrodeposited and annealed at 300 °C for 2 hours [11] presented a specific capacitance value of 1450 F g^{-1}. $NiCo_2O_4$ nanosheets and nanorods supported carbon nanofibers [12] were prepared by hydrothermal method exhibiting high specific capacitance values of 1002 F g^{-1} and 1023 F g^{-1}, respectively.

Electrodeposition is a facile route to prepare DNCHs either as electrodes for redox supercapacitors or as precursors for thermal transformation to NCSOs among other solution-based routes such as hydrothermal, chemical bath deposition and sol-gel [13]. The electrodeposition of DNCHs is generally based on the generation of hydroxyl ions near the electrode/electrolyte interface, through the reduction of nitrate ions in the electrolyte followed by the reactions of metal ions, in the solution, with the generated hydroxyls to form DNCHs deposited on substrates[13]. DNCH nanosheets are normally formed, regardless the substrate used for electrodeposition, either on non-pseudocapacitive current collectors such as stainless steel [5, 14], nickel foam [15], graphene covered nickel foam [16] or on other pseudocapacitive materials such as $NiCo_2O_4$ nanowires array [6] and TiN nanotubes array [17]. This versatility suggests a similar nucleation and growth mechanism for the electrodeposited DNCHs on different substrates.

Nevertheless, the nucleation mechanism of the electrodeposited DNCHs nanosheets films is still not understood and never reported in literature, to the best of authors' knowledge. Thus, this work aims at understanding this fundamental issue, by combining current transient studies with *in-situ* electrochemical atomic force microscope (AFM) and *ex-situ* field emission gun scanning electron microscope (FEG-SEM) measurements. The nucleation mechanism elucidated from these studies will be discussed in detail.

3.7.2. Experimental

Materials

Nickel nitrate $Ni(NO_3)_2$ and cobalt nitrate $Co(NO_3)_2$ from Sigma Aldrich were used as precursors for the electrodeposition of the films. The chemicals were used as received without further purification process. Stainless steel (AISI 304 obtained from Goodfellow) was used as substrate for the films electrodeposition. Steel samples were previously polished with SiC grit papers up to 1000 grits, rinsed with deionized water and ethanol and dried by a jet of compressed air.

Current transient measurements

The current transient measurements were performed in a conventional electrochemical system under ambient atmosphere, at room temperature, using a Voltalab PGZ 100 Potentiostat from

Radiometer, with the stainless steel as a working electrode, the saturated calomel electrode (SCE) as reference electrode and the platinum foil as counter electrode. The concentrations of the precursors used in the experiments were 0.033 M $Ni(NO_3)_2$ and 0.066 M $Co(NO_3)_2$. The deposition potentials used to measure the current transients were selected after performing linear sweep voltammetry measurements in the same electrolyte.

In-situ **atomic force microscope (AFM) measurements**

In-situ electrochemical AFM were performed in an electrochemical cell, controlled by the Autolab Mini Potentiostat, designed for this measurement, using stainless steels as working electrode, a platinum ring as counter electrode and a platinum wire as quasi reference electrode. The *in-situ* topographic images were recorded by AFM microscope (Easyscan microscope) from Nanosurf. The *in-situ* measurement were performed by applying a pulsed potential of -1200 mV vs Pt (-800 mV vs SCE) with potential-on of 5 seconds to 10 seconds and potential-off of 5 minutes; tapping mode AFM scans were taken during the potential-off time.

Ex-situ **surface morphology measurements**

FEG-SEM (JEOL 7001F microscope) was used for *ex-situ* observation of the surface morphology of the electrodeposited films at the early growth stages. *Ex-situ* topographic images were also obtained with *ex-situ* AFM working in tapping mode.

3.7.3. Results and Discussion

The selection of the cathodic potentials for the current transient measurements, was made by carrying out linear sweep voltammetry (LSV) measurements, in the cathodic regime, with a scan rate of 10 mV s^{-1}. The results are presented in Figure 3.7.1a. The curves evidence a first onset potential at approximately -680 mV, which corresponds to the nitrate reduction reaction to generate hydroxyl anions and the simultaneous reactions of metal cations (Ni^{2+} and Co^{2+}) with the generated hydroxyls to form metal hydroxides deposited onto the stainless steel substrate as below:

$$NO_3^-+7H_2O+8e^-\rightarrow NH_4+10OH^- \quad (3.7.1)$$

$$xNi^2+2xCo^{2+}+6xOH^-\rightarrow Ni_xCo_{2x}(OH)_{6x} \quad (3.7.2)$$

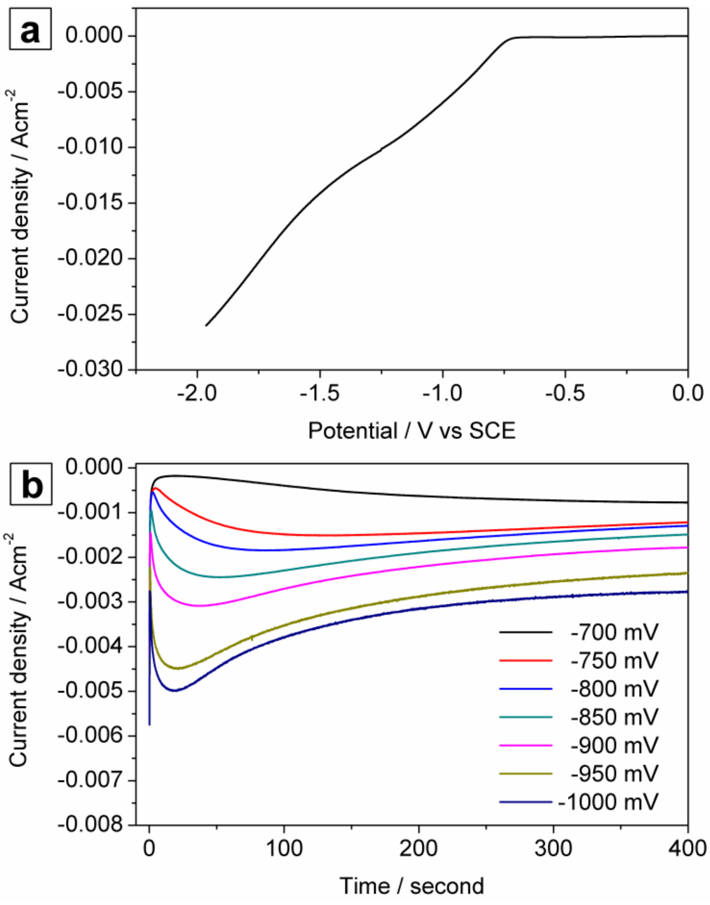

Figure 3.7.1. (a) Linear sweep voltammetry with the potential sweep from 0 V to -2 V and scan rate of 10 mV s^{-1}. (b) Current transient curves obtained at different applied potential determined from linear weep voltammetry result.

At potentials more negative than the first onset potential, the current response continuously increases and the second onset potential occurs at approximately -1350 mV, which corresponds to the hydrogen evolution reaction. From the LSV results, potentials in the range from -700 mV to -1000 mV were selected for the current transient measurement and the applied potentials were separated by an interval of -50 mV. The results are shown in Figure 3.7.1b. Generally, in all the curves, the current response increases and drops quickly when applying potential, then it slowly increases and decreases again after reaching the current maxima. This trend is not very well defined in the CT curve at applied potential of -700 mV, probably due to the slow growing process of the film at the potential close to the onset potential. There are four processes that control the current response during the application of the potential. The first increasing/decaying current results from the double layer formation or adsorption/desorption processes [18-20]. The current response increases after the decay may be related to the growth of nuclei size, and/or the increase in number of nuclei. During the growing process, the growth of each nucleus occurs under diffusion control, forming diffusion zones around each nucleus until these zones overlap and linear mass-transfer starts like on a planar electrode surface, leading to the decrease of current [18-20].

To understand the nucleation process, the experimental current transients obtained at different potentials were fitted with various nucleation models. One of these is the Scharifker-Hills (SH) nucleation model [18], which is based on the analysis of potentiostatic current transients. The SH model describes a mechanism involving three dimensions (3D) multiple nucleations with the growth rate of hemispherical nuclei, being controlled by semi-infinite linear diffusion that depend upon the potential used for electrodeposition [18]. The current response during the electrodeposition process is described for the two-limit cases: instantaneous nucleation and progressive nucleation. The former first one is a fast nucleation process with a high number of nuclei grown at the beginning of electrodeposition, which remain unchanged during the growing time. The second one is a slow nucleation process, in which the number of nuclei increases during the electrodeposition time. The current responses are described as [18]:

Instantaneous nucleation:

$$I = \frac{zFD^{1/2}c}{\pi^{1/2}t^{1/2}}[1 - \exp(N\pi kDt)] \qquad (3.7.3)$$

$$k = \left(\frac{8\pi cM}{\rho}\right)^{1/2} \qquad (3.7.4)$$

Progressive nucleation:

$$I = \frac{zFD^{1/2}c}{\pi^{1/2}t^{1/2}}[1 - \exp(-AN_x\pi k'Dt^2/2)] \qquad (3.7.5)$$

$$k' = \frac{4}{3}\left(\frac{8\pi cM}{\rho}\right)^{1/2} \qquad (3.7.6)$$

where z is number of electrons transferred during the deposition process, F is Faraday constant (96500 Cmol^{-1}), D is the diffusion coefficient, c is the concentration of the precursor in the solution, M is the molecular weight, ρ is the density of the electrodeposited layer, k and k' are material constants and N is nucleus number, respectively.

Equations (3.7.3) and (3.7.5) can be transformed into non-dimensional equations (3.7.7-9) and (3.7.10-12) describing the dependence of $(I/I_m)_2$ vs. t/t_m, with I_m is current maximum and t_m is the time at current maximum.

Instantaneous nucleation:

$$\frac{I^2}{I_m^2} = \frac{1.9542}{t/t_m}\{1 - exp[-1.2564(t/t_m)]\}^2 \qquad (3.7.7)$$

$$I_m^2 t_m = 0.1629(zFc)^2 D \qquad (3.7.8)$$

$$I_m = 0.632zFDc(kN)^{1/2} \qquad (3.7.9)$$

Progressive nucleation:

$$\frac{I^2}{I_m^2} = \frac{1.2254}{t/t_m}\{1 - exp[-2.3367(t/t_m)]\}^2 \qquad (3.7.10)$$

$$I_m^2 t_m = 0.1629(zFc)^2 D \qquad (3.7.11)$$

$$I_m = 0.632zFDc(kN)^{1/2} \qquad (3.7.12)$$

By transforming the experimental current transient curves into this non-dimensional form and comparing it to the theoretical curves (equations 3.7.7 and 10), the nucleation mechanism can be extracted. Furthermore, the nuclear number and the diffusion coefficient can be calculated from equation (3.7.8 and 11) and (3.7.9 and 12), respectively.

Based on the deposition mechanism presented in the reaction 3.7.1 and 2. The number of electron transfer during the deposition process is 8, the atomic weight of $NiCo_2(OH)_6$ is 278.619 g mol^{-1} and assuming that the density of $NiCo_2(OH)_6 = 2Co(OH)_2 + Ni(OH)_2$ is 11.292 g cm^{-3}, those were used in the SH model discussed above for the fitting and the results will be presented in the following part.

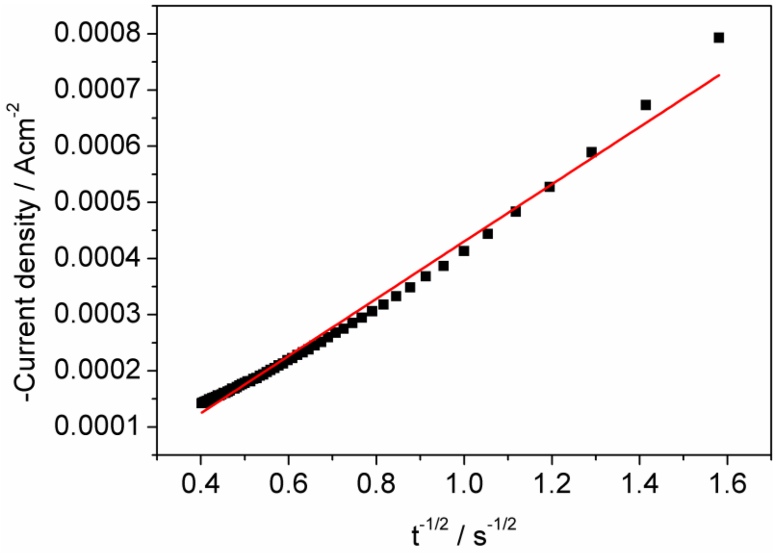

Figure 3.7.2. The relation of current density with $t^{-1/2}$ of obtained by changing the x-axis from t to $t^{-1/2}$ in the current transient measured at -700 mV.

At potential of -700 mV, the current transient does not present a well-defined current maximum, making difficult to fit it with the SH nucleation model described above. Alternatively, the study of the underlying electrochemical deposition at -700 mV was done by fitting with the Cottrell equation:

$$-j = \frac{zFD^{1/2}c}{\pi^2 t^{1/2}} \tag{3.7.13}$$

Figure 3.7.2 shows the current density vs. $time^{-1/2}$ plot at the applied potential of -700 mV, which was obtained by changing the x-axis from t to $t^{-1/2}$ in the current transient curve. The red line in Figure 3.7.2 is the fitting of the experimental curve with the Cottrell equation. The diffusion coefficient D can be retrieved from this fitting, being 2.18365 x 10^{-9} cm^2 s^{-1}.

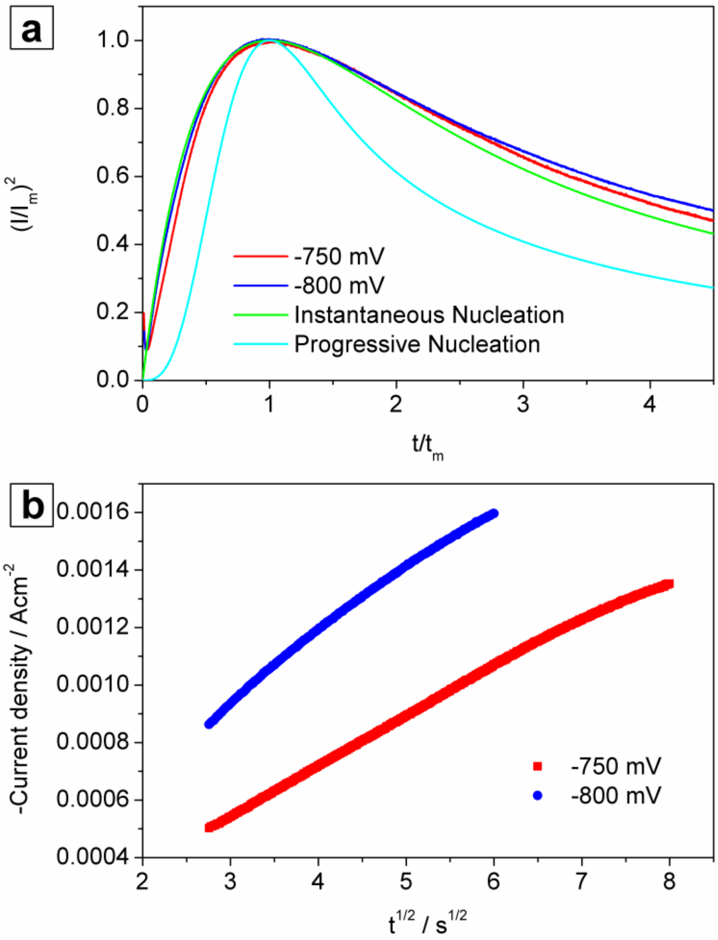

Figure 3.7.3. (a) $(I/I_m)^2$ vs t/t_m relationship and (b) current density vs. time$^{1/2}$ obtained by changing the coordination of the corresponding current transient at -750 mV and -800 mV.

For potentials ranging from -750 mV to -1000 mV, the current transient curves were transformed into the non-dimensional form and compared to the theoretical curves. The results are presented in Figure 3.7.3a and Figure 3.7.4.

It can be clearly observed that at potential of -750 mV and -800 mV, the $(I/I_m)^2$ vs t/t_m curves can be fitted with the theoretical instantaneous nucleation model, revealing that the nucleation mechanism is based on the instantaneous formation of nuclei. The diffusion coefficients and the nuclear numbers were also calculated (Table 3.7.1). The results demonstrated that the nuclei number increases when increasing applied potential.

Table 3.7.1. The diffusion coefficient and the nuclei numbers of films prepared by electrodeposition at -750 mV and -800 mV.

Potential	D (cm^2s^{-1})	N
- 750 mV	1.804 x 10^{-6}	6817
- 800 mV	1.799 x 10^{-6}	10215

The earlier and simple description of multiple nucleation detailed by Hills, Schiffrin and Thompson [19, 20] was also applied to study the nucleation mechanism at potentials of -750 mV and -800 mV. This theory simply assumes that in multiples nucleation, the growth of each nucleus is non-interactive with other nuclei, being an independent process. And in case of instantaneous nucleation, the current response $I_{N,t}$ is simply a product of the number of nuclei with the current response from the growth of single nuclei [19]:

$$I_{N,t} = NI_{1,t} \qquad \text{with} \qquad I_{1,t} = \frac{zF\pi(2Dc)^{3/2}M^{1/2}Nt^{1/2}}{\rho^{1/2}} \tag{3.7.14}$$

where the growth of single nuclei $I_{1,t}$ describes by localized spherical diffusion.

The linear relationship of current density vs. time$^{1/2}$ at potentials of -750 mV and -800 mV evidences the instantaneous nucleation at these potentials, in agreement with the SH fitting.

The $(I/I_m)^2$ vs t/t_m curves at potential of -850 mV to -1000 mV, Figure 3.7.4, does not match with the progressive nucleation curves and were fitted with the instantaneous nucleation curves. However, the fitting goodness is not as good as the one observed for potentials of -750 mV and -800 mV. Furthermore, the SH model can only be applied to the two limit cases of nucleation, and uses only current maxima to describe the current response. The Scharifker-Mostany (SM) model [21] was then applied to further clarify the nucleation mechanism at these applied potentials.

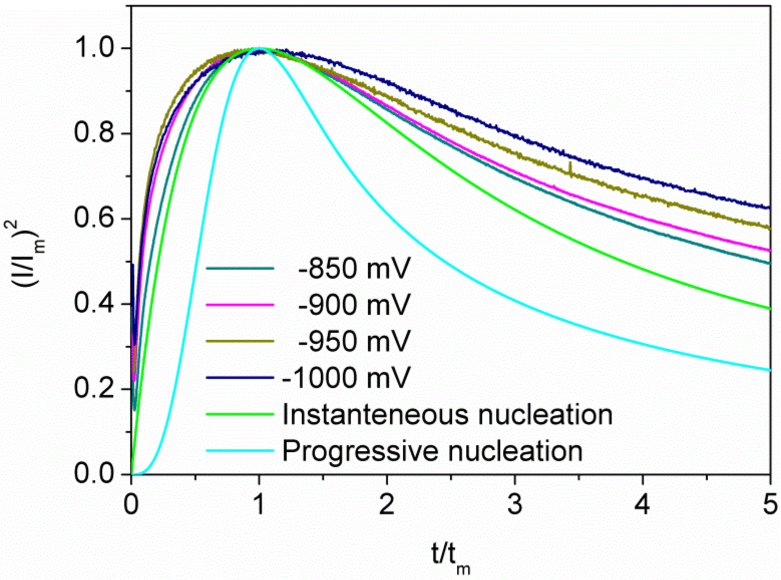

Figure 3.7.4. $(I/I_m)^2$ vs t/t_m relationship obtained by changing the coordination of the corresponding current transient at -850 mV and -1000 mV.

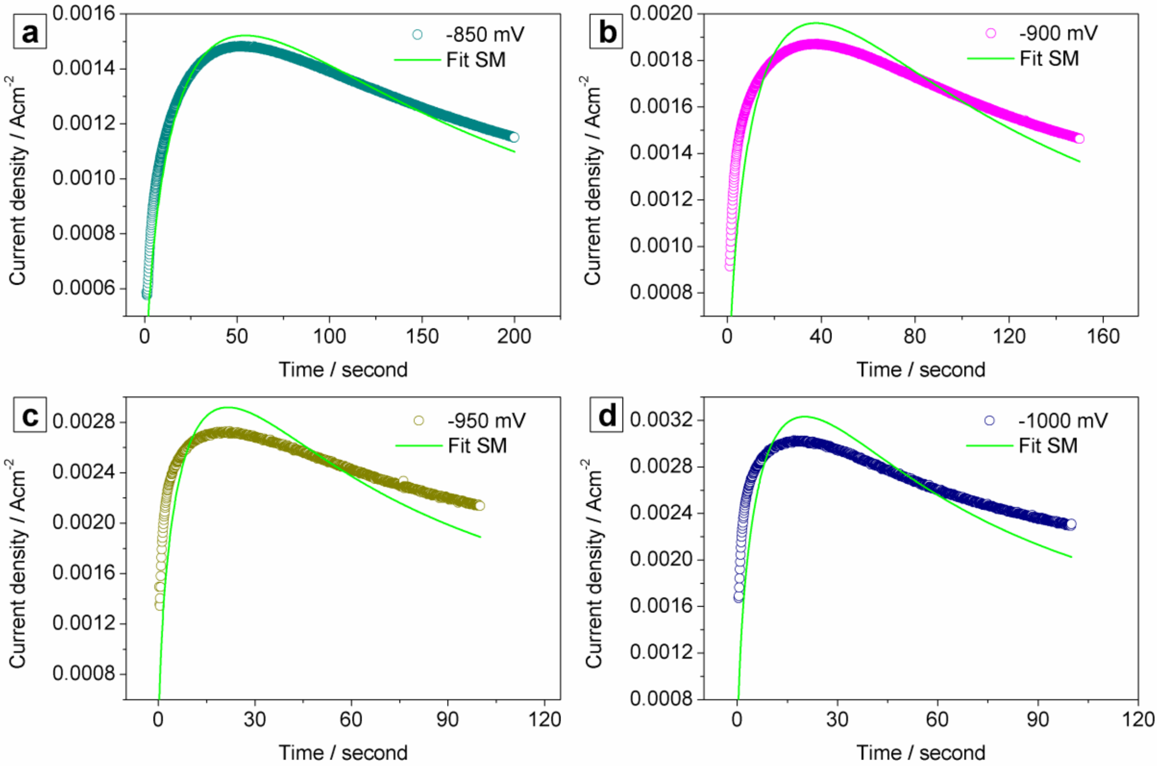

Figure 3.7.5. Fitting of current transient curves at potentials ranging from -850 mV to -1000 mV with Scharifker-Mostany model.

The SM model describes the current response in potentiostatic electrodeposition as

$$I = \frac{zFD^{1/2}c}{\pi^{1/2}t^{1/2}}\left(1 - exp\left\{-N_0\pi kD\left[t - \frac{1-e^{-At}}{A}\right]\right\}\right) \quad (3.7.15)$$

This model overcomes some limitations of the previous SH model, therefore the fitting is not limited to the two cases of instantaneous nucleation and progressive nucleation. The nucleation rate, the nuclei number and the diffusion coefficient can be retrieved by fitting the experimental current transient curves with the current response as proposed in the SM model.

Table 3.7.2. The nucleation rate, the nuclei numbers and the diffusion coefficient obtained from the fitting results with Scharifker-Mostany model of films prepared by electrodeposition at -850 mV to -1000 mV.

Potential / mV	**A (s^{-1})**	**N**	**D ($cm^2 s^{-1}$)**
-850	3.107×10^{19}	14228	2.073×10^{-6}
-900	4.018×10^{24}	17839	2.386×10^{-6}
-950	1.016×10^{17}	24610	3.025×10^{-6}
-1000	5.489×10^{17}	22973	3.467×10^{-6}

The fitting results of the current transient in the potentials ranging from -850 mV to -1000 mV are presented in Figure 3.7.5. Overall, the model can be used to fit the current transient curves. Even though, the fitting curves show some deviations from the experimental curves. The nucleation rate, the nuclei number and the diffusion coefficient were calculated from the fitting and are presented in Table 3.7.1. The nuclei number and the diffusion coefficient increased as compared to the values calculated at potentials of -700 mV to -850 mV. This can be due to the increase of the electromotive force at higher potential. The high nuclei number estimated for the films formed at more cathodic potentials compared to the previous ones (-800 and -750 mV) indicates that the nucleation mechanism is also an instantaneous process.

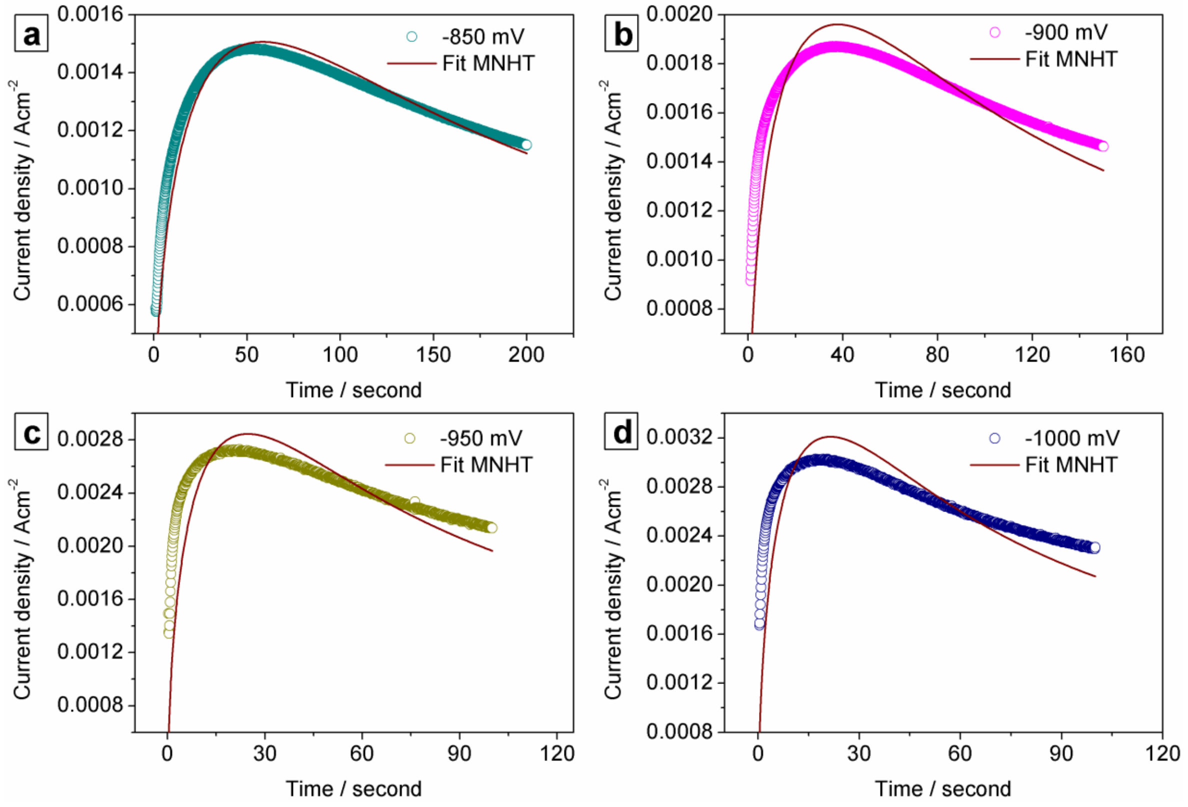

Figure 3.7.6. Fitting of current transient curves at potentials ranging from -850 mV to -1000mV with the MNHT model.

Table 3.7.3. The nucleation rate, the nuclei numbers and the diffusion coefficient obtained from the fitting results with MNHT model of films prepared by electrodeposition at -850 mV to -1000 mV.

Potential / mV	**A (s^{-1})**	**N**	**D ($cm^2 s^{-1}$)**
-850	8.106 x 10^{15}	12658	2.177 x 10^{-6}
-900	7.845 x 10^{43}	17839	2.386 x 10^{-6}
-950	5.564 x 10^{24}	19726	3.294 x 10^{-6}
-1000	9.995 x 10^{43}	20663	3.630 x 10^{-6}

The current transient curves at potentials in the range from -850 mV to -1000 mV were also fitted with the Mirkin-Nilov and Heerman-Tarallo (MNHT) nucleation model [22, 23]. While the thickness of the diffusion layer calculated in SM model is a function of time, in the MNHT model the thickness of the diffusion layer is not only a function of time but also has the contribution of nucleation rate. This results in the current response described by MNHT is as follows [22, 23]:

$$I = \frac{zFD^{1/2}c}{\pi^{1/2}t^{1/2}} \frac{0.520893At-1.206814A^{3/2}t^{3/2}+1.185724A^{2}t^{2}-0.051314A^{1/2}t^{1/2}}{[At-1+exp(-At)](1-1.206814A^{1/2}t^{1/2}+1.185724At)} \left[1 - exp\left(-N_0 \pi k D \left(1 - \frac{1-exp(-At)}{At}\right) t\right)\right] \tag{3.7.16}$$

The fitting results of the experimental current transient curves with the current response proposed by MNHT model are presented in Figure 3.7.6. The fitting results were similar to the ones obtained with the SM model and the fitting curves show a reasonable match with the experimental ones, however some deviations are still observed. The nucleation rate, nuclei number and diffusion coefficient were also obtained from the fitting results, being depicted in Table 3.7.3. It is clearly shown that the nuclear number and diffusion coefficient increase with the applied potential. Moreover, the nuclei numbers suggest instantaneous nucleation, being in good agreement with the results from SM model.

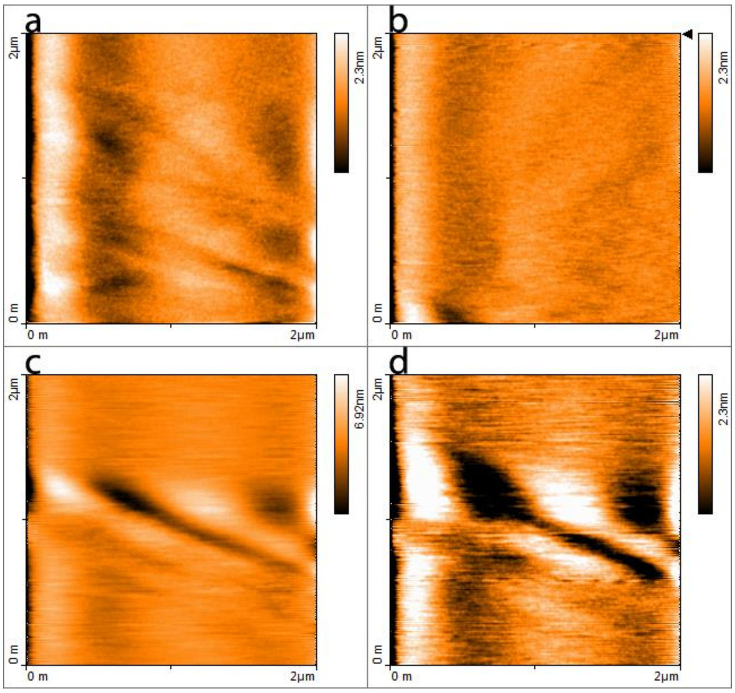

Figure 3.7.7. *In-situ* AFM results of the film deposited at -1200 mV vs Pt. The AFM images were measured in the area of 2 x 2 µm^2 during the potential-off time (a) before applying potential and after applying potential for (b) 5 seconds, (c) 15 seconds and (d) 20 seconds.

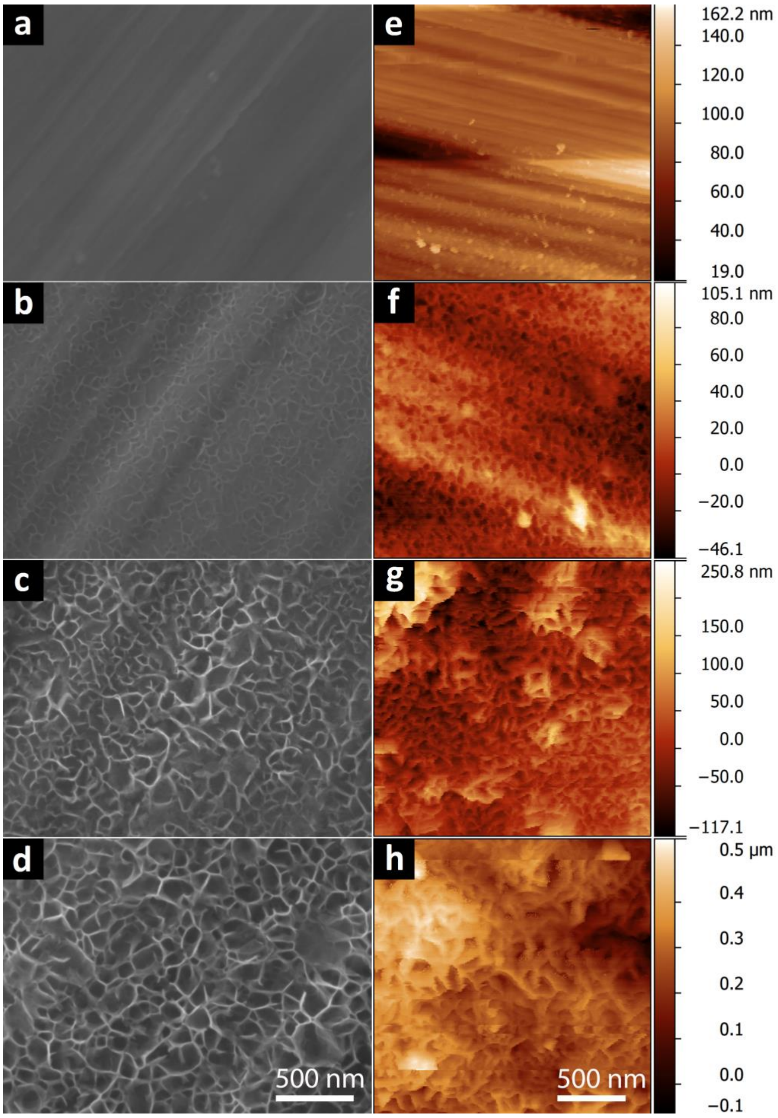

Figure 3.7.8. *Ex-situ* FEG-SEM and AFM measured in the area of 2 x 2 μm^2 (a, e) before electrodeposition and after electrodeposition for (b, f) 5 seconds, (c, g) 15 second and (d, h) 25 seconds. The color scale bars on the right correspond to the out-of-plane scale of AFM images. The scale bars at the bottom left and bottom right are applied for all the FEG-SEM images and AFM images in the figure, respectively.

To further understand the nucleation mechanisms and the results obtained from the fitting of the experimental curves with the different nucleation growth models, *in-situ* electrochemical AFM were carried out. AFM images were obtained during the potential-off time after applying potential of -1200 mV *vs.* Pt (800 mV *vs.* SCE) for 5 seconds, 15 seconds and 25 seconds. The results are shown in Figure 3.7.7. Although the low resolution of the AFM images that were taken in liquid environment, the images suggest an increase in the number of particles, corresponding to nuclei, after applying potential for 5 seconds. This is in agreement with the previous fitting results, confirming the instantaneous nucleation. After applying the potential for 15 seconds, deep valleys seem to develop and seem to be further developed after 25 seconds, probably due to the growth of interconnected nanosheets.

Ex-situ FEG-SEM and AFM measurements were performed to confirm the above hypothesis and the formation of interconnected nanosheets. The results are shown in Figure 3.7.8. The growth of nanoneedles homogeneously distributed over the substrate was observed for the film deposited in 5 seconds, as shown in both *ex-situ* FEG-SEM and AFM images (Figure 3.7.8b and f). This is in agreement with the formation of homogenously distributed nuclei observed with *in-situ* AFM measurements. After deposition times of 15 seconds and 25 seconds, *ex-situ* FEG-SEM and AFM images (Figure 8c and d, g and h) revealed the presence of interconnected nanosheets with large gaps between them, confirming the hypothesis proposed previously in the *in-situ* AFM results.

3.7.4. Conclusions

In summary, nucleation studies based on current transient analysis, *in-situ* AFM, *ex-situ* AFM and FEG-SEM of nickel cobalt hydroxide films prepared by electrodeposition have been reported. Current transients fitted with Scharifker-Hill, Scharifker-Mostany and Mirkin-Nilov-Heerman-Tarallo models revealed the film growth is based on instantaneous nucleation regardless in the applied potentials ranging from -700 mV to -1000 mV. Nuclei number and diffusion coefficient increases as a function of applied potentials. *In-situ* AFM results suggested the instantaneous nucleation and revealed the growth of nanosheets, a mechanism that was further confirmed by *ex-situ* AFM and FEG-SEM imaging.

Acknowledgements

The authors thank Fundação para a Ciência e Tecnologia (FCT) for the funding under the contract PTDC/CTM-MET/119411/2010 & UID/QUI/00100/2013, IDS-FunMat Erasmus Mundus PhD School, the European COST Action MP1004. We also thank Pedro Nolasco and Yegor Morozov (IST Lisboa) for their support with the *in-situ* AFM and Mini Potentiostat setup.

References

[1] H. Chen, L. Hu, M. Chen, Y. Yan, L. Wu, Nickel–Cobalt Layered Double Hydroxide Nanosheets for High-performance Supercapacitor Electrode Materials, Advanced Functional Materials, 24 (2014) 934-942.

[2] J.P. Cheng, J. Zhang, F. Liu, Recent development of metal hydroxides as electrode material of electrochemical capacitors, RSC Adv., 4 (2014) 38893-38917.

[3] Y. Tao, L. Zaijun, L. Ruiyi, N. Qi, K. Hui, N. Yulian, L. Junkang, Nickel–cobalt double hydroxides microspheres with hollow interior and hedgehog-like exterior structures for supercapacitors, Journal of Materials Chemistry, 22 (2012) 23587-23592.

[4] X. Wang, A. Sumboja, M. Lin, J. Yan, P.S. Lee, Enhancing electrochemical reaction sites in nickel–cobalt layered double hydroxides on zinc tin oxide nanowires: a hybrid material for an asymmetric supercapacitor device, Nanoscale, 4 (2012) 7266-7272.

[5] S.B. Kulkarni, A.D. Jagadale, V.S. Kumbhar, R.N. Bulakhe, S.S. Joshi, C.D. Lokhande, Potentiodynamic Deposition of Composition Influenced $Co_{1-x}Ni_x$ LDHs Thin Film Electrode for Redox Supercapacitors, International Journal of Hydrogen Energy, 38 (2013) 4046-4053.

[6] L. Huang, D. Chen, Y. Ding, S. Feng, Z.L. Wang, M. Liu, Nickel–Cobalt Hydroxide Nanosheets Coated on $NiCo_2O_4$ Nanowires Grown on Carbon Fiber Paper for High-Performance Pseudocapacitors, Nano Lett., 13 (2013) 3135-3139.

[7] Y. Zhang, L. Li, H. Su, W. Huang, X. Dong, Binary metal oxide: advanced energy storage materials in supercapacitors, Journal of Materials Chemistry A, 3 (2015) 43-59.

[8] Z. Wu, Y. Zhu, X. Ji, $NiCo_2O_4$-based materials for electrochemical supercapacitors, Journal of Materials Chemistry A, 2 (2014) 14759-14772.

[9] G. Zhang, X.W. Lou, Controlled Growth of $NiCo_2O_4$ Nanorods and Ultrathin Nanosheets on Carbon Nanofibers for High-performance Supercapacitors, Sci. Rep., 3 (2013).

[10] V. Gupta, S. Gupta, N. Miura, Electrochemically synthesized nanocrystalline spinel thin film for high performance supercapacitor, Journal of Power Sources, 195 (2010) 3757-3760.

[11] C. Yuan, J. Li, L. Hou, X. Zhang, L. Shen, X.W. Lou, Ultrathin Mesoporous $NiCo_2O_4$ Nanosheets Supported on Ni Foam as Advanced Electrodes for Supercapacitors, Advanced Functional Materials, 22 (2012) 4592-4597.

[12] G. Zhang, X.W. Lou, Controlled Growth of $NiCo_2O_4$ Nanorods and Ultrathin Nanosheets on Carbon Nanofibers for High-performance Supercapacitors, Sci Rep, 3 (2013).

[13] X. Xia, Y. Zhang, D. Chao, C. Guan, Y. Zhang, L. Li, X. Ge, I.M. Bacho, J. Tu, H.J. Fan, Solution synthesis of metal oxides for electrochemical energy storage applications, Nanoscale, 6 (2014) 5008-5048.

[14] V. Gupta, S. Gupta, N. Miura, Potentiostatically Deposited Nanostructured Co_xNi_{1-x} Layered Double Hydroxides as Electrode Materials for Redox-Supercapacitors, Journal of Power Sources, 175 (2008) 680-685.

[15] M. Yang, H. Cheng, Y. Gu, Z. Sun, J. Hu, L. Cao, F. Lv, M. Li, W. Wang, Z. Wang, Facile electrodeposition of 3d concentration-gradient Ni-Co hydroxide nanostructures on nickel foam as high performance electrodes for asymmetric supercapacitors, (2015).

[16] Y. Bai, W. Wang, R. Wang, J. Sun, L. Gao, Controllable synthesis of 3D binary nickel-cobalt hydroxide/graphene/nickel foam as a binder-free electrode for high-performance supercapacitors, Journal of Materials Chemistry A, (2015).

[17] C. Shang, S. Dong, S. Wang, D. Xiao, P. Han, X. Wang, L. Gu, G. Cui, Coaxial $Ni_xCo_{2x}(OH)_{6x}$/TiN Nanotube Arrays as Supercapacitor Electrodes, ACS Nano, 7 (2013) 5430–5436.

[18] B. Scharifker, G. Hills, Theoretical and experimental studies of multiple nucleation, Electrochimica Acta, 28 (1983) 879-889.

[19] G.J. Hills, D.J. Schiffrin, J. Thompson, Electrochemical nucleation from molten salts—I. Diffusion controlled electrodeposition of silver from alkali molten nitrates, Electrochimica Acta, 19 (1974) 657-670.

[20] G.A. Gunawardena, G.J. Hills, I. Montenegro, Potentiostatic studies of electrochemical nucleation, Electrochimica Acta, 23 (1978) 693-697.

[21] B.R. Scharifker, J. Mostany, Three-dimensional nucleation with diffusion controlled growth: Part I. Number density of active sites and nucleation rates per site, Journal of Electroanalytical Chemistry and Interfacial Electrochemistry, 177 (1984) 13-23.

[22] L. Heerman, A. Tarallo, Theory of the chronoamperometric transient for electrochemical nucleation with diffusion-controlled growth, Journal of Electroanalytical Chemistry, 470 (1999) 70-76.

[23] M.V. Mirkin, A.P. Nilov, Three-dimensional nucleation and growth under controlled potential, Journal of Electroanalytical Chemistry and Interfacial Electrochemistry, 283 (1990) 35-51.

Chapter 4. General discussion

Overall, this PhD dissertation addressed several aspects concerning morphological, structural and electrochemical properties of novel electrodes for charge storage based on single transition metal oxides and on double/mixed oxides containing Mn-Co, Mn-Ni and Ni-Co (Figure 4.1). Thus, manganese oxides (Mn_3O_4 and MnO_2), $MnCo_2O_4$, Ni-Mn oxides and Ni-Co hydroxides were prepared by electrodeposition and studied aiming its application as electrode materials for redox supercapacitors.

Mn_3O_4 electrodes were electrodeposited from nitrate-based electrolytes and the hydrogen bubbling template-assisted electrodeposition was applied to fabricate the novel MnO_2 electrodes. $MnCo_2O_4$ films were prepared by electrodeposition from nitrate-based electrolytes and submitted to thermal annealing. The evolution of the structural properties with the thermal annealing was studied in detail for the $MnCo_2O_4$ electrodes. The surface morphology and composition of Ni-Mn oxides were tuned by electrodepositing films with different Ni:Mn ratio. Moreover, a novel architecture composed on Ni-Mn oxide films electrodeposited on Ni-Cu foams was developed, exhibiting superior pseudocapacitive response. Ni-Co hydroxides were designed in a two layers architecture composed of $Ni(OH)_2$ over $Co(OH)_2$ and revealed an enhanced specific capacitance compared to that of the mixed Ni-Co hydroxides. And finally, the nucleation mechanism was revealed for the case of Ni-Co hydroxide electrodeposition.

This chapter discusses the most important achievements of the results obtained in this work, compares it to the state-of-art and highlights the contributions beyond it.

The electrodeposition route was chosen to fabricate TMO electrodes because it is a simple and one-step route, allowing depositing TMO films directly on the current collector, providing excellent adhesion without needing binders or other foreign additives. This has an important impact because the active material will present a lower electrical equivalent resistance that is typical of binders. Moreover, it opens a wide array of possibilities in what concerns current collectors. In this study, stainless steel was chosen as current collector because it displays good electron conductivity and high corrosion resistance.

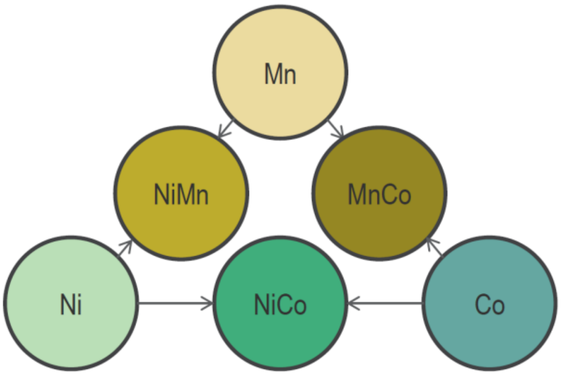

Figure 4.1. The general scheme evidencing the combination of metallic oxides/hydroxides studied in this PhD thesis.

The first step was the electrodeposition of manganese oxide from nitrate-based electrolytes. The process was thoroughly studied by varying the electrodeposition parameters such as applied potentials (ranging from -1.0 V to -1.5 V), electrolyte concentrations (0.1 M, 0.25 M and 0.5 M), and applied charge (-0.3 C cm^{-2}, -0.6 C cm^{-2} and -0.9 C cm^{-2}). In nitrate-based electrolytes, electrodeposition involves the reduction of nitrate to form hydroxyl anions that react with Mn^{2+} to form $Mn(OH)_2$. This hydroxide can be transformed into oxide phases by annealing. Thus, the effect of the post thermal annealing process at different temperatures (from 200 ^{o}C to 400 ^{o}C) was investigated too. Thermal annealing at 200 ^{o}C resulted in an enhanced specific capacitance, and further increasing of the annealing temperature resulted in a decrease of the specific capacitance. The variation of the deposition parameters (applied potential, electrolyte concentration and applied charge) resulted in the morphological changes, which induced relevant porosity changes, thereby affecting directly the electrochemical response of the films. The optimal deposition parameters resulted in the formation of hierarchical face-centered tetragonal (FCT) Mn_3O_4 nanoparticles/nanoflakes morphologies (Figure 4.2, left) exhibiting specific capacitance values of 416 F g^{-1} at 1 A g^{-1} in 1 M NaOH electrolyte. In comparison with recent work, reporting a two steps electrodeposition process for fabricating hierarchical structures of nanoflakes/nanoflakes [1], the results obtained in this thesis reveal that a simple one step electrodeposition route allows the fabrication of an hierarchical structure based on nanoflakes (Figure 4.2, left). The electrode exhibited quite poor capacitance retention - 46% after a continuous charge-discharge test for 1000 cycles. The specific capacitance obtained after 1000 cycles at 1 A g^{-1} was 196 F g^{-1} and this value is comparable to values reported for manganese oxide before cycling, working in neutral electrolyte [2]. The high initial specific capacitance values, the low retention and the poor stability can be due to the high redox activity and irreversible redox reactions of manganese oxide (relating to the phase transformation from Mn_3O_4 to MnO_2 [3]), respectively, in alkaline electrolyte [2]. A large number of published work reports the pseudocapacitive performance of manganese oxide in neutral electrolyte; however, the present results highlighted the redox response of manganese oxide in alkaline electrolytes for pseudocapacitors. This opens a route to explore its mixing with nickel or cobalt oxides (which are well- known for their pseudocapacitive response in alkaline electrolytes [4-6]) for supercapacitor electrodes working in alkaline electrolyte. Moreover, while some work addresses the cathodic electrodeposition of manganese oxide from chloride and permanganate based electrolyte [7, 8], detailed studies concerned to cathodic electrodeposition from nitrate-based electrolytes were never reported up to the present date (to the best of the author’s knowledge). Thus, this work also provides new insights, concerning the influence of key electrodeposition parameters as stated above, on the cathodic electrodeposition of manganese oxides from nitrate-based electrolyte.

Manganese oxides with hierarchical porous structure or morphological architecture such as nanowires, nanofibril/nanowires and sandwich-structured nanotube arrays [9-11] have shown a good pseudocapacitive performance. The high pseudocapacitive performance achieved can be due to the formation of hierarchical architectures that facilitate the redox reactions. Nevertheless, the hierarchical architecture was rather limited to that based on 1D nanowires [9-13], thereby novel designed hierarchical electrodes with good pseudocapacitive performance are still a target to be searched. In the above discussion, it was shown that the hierarchical morphology of manganese oxide can be obtained *via* optimization of electrodeposition parameters; besides those that can be obtained *via* the two step deposition routes reported in literature. The morphology of manganese oxide electrodes was further engineered by optimizing electrodeposition in sulfate-based electrolytes using hydrogen bubbling as a dynamic template (hydrogen gas evolves as the result of applying high cathodic potentials [14]). The electrodeposition was based on the hydrogen evolution reaction that released hydroxyl anions, which reacted with Mn^{2+} to form $Mn(OH)_2$ to be transformed to oxide phases by electro-oxidation. Electro-oxidation was chosen because these films were unstable by thermal annealing. Hydrogen evolution ($2H_2O + 2e^- \rightarrow H_2 + 2OH^-$) acted both as a dynamic template and as source of hydroxyl anions. The obtained electrodes showed well-distributed micro-holes, with an average diameter of approximately 18 µm and depth of approximately 2.2 µm over a continuous nanosheet network, forming the hierarchical architecture electrode (Figure 4.2, right).

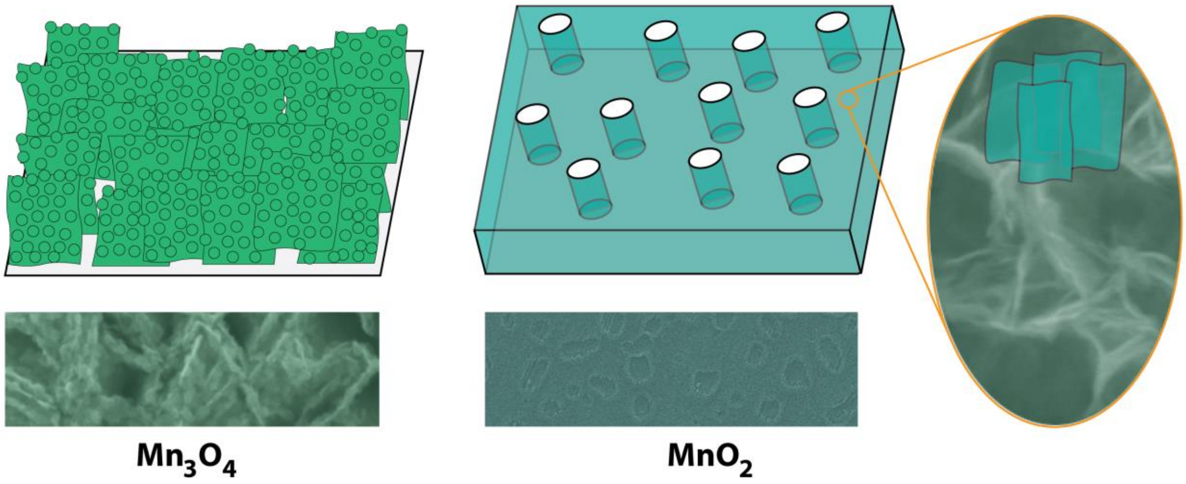

Figure 4.2. Schematic images of the hierarchical Mn_3O_4 nanoparticle/nanoflake and micro/nano porous MnO_2.

Each nanosheet displayed a low crystalline MnO_2 phase. The specific capacitance at 1 A g^{-1} was 667 F g^{-1} in 1 M NaOH electrolyte. The enhanced specific capacitance compared to those discussed above can be due to an increased surface area, resulting from the novel hierarchical structure composed of micro-holes and fine nanosheets (Figure 4.2, right). Furthermore, it can result from the formation of the poorly crystalized MnO_2 phase, which has been reported to display better redox activity compared to the Mn_3O_4 phase [2]. The specific capacitance value in 1 M Na_2SO_4 was 305 F g^{-1} at 1 A g^{-1}. The specific capacitance is lower than that obtained in NaOH electrolyte probably because of the decreased ability to store electrons and to release them in the redox process [2, 3, 15]. Because the stability of manganese oxides (electrodeposited at the potential of -1.3 V, electrolyte concentration of 0.25 M, applied charge of -0.6 C cm^{-2} and annealing at 200 ^{o}C in 1 hour) in 1 M NaOH is quite poor, further electrochemical tests were carried out in 1 M Na_2SO_4. Rate capability of the electrode was 61% when increasing current densities from 1 to 10 A g^{-1}, and capacitance retention was 67% after 1000 charge-discharge cycles at 5 A g^{-1}, revealing the good pseudocapacitive performance of the novel designed manganese oxide electrode deposited directly on stainless steel. Recent literature reported that the hierarchical MnO_2 nanofibril/nanowire array prepared using anodized aluminum oxide as a hard template [10] displayed specific capacitance values of 298 F g^{-1} at 1 A g^{-1} and that hierarchical MnO_2/carbon nanotubes [16] displayed specific capacitance values of 223 F g^{-1} at 1 A g^{-1}. Thus, compared to the state-of-art, the novel MnO_2 micro/nano porous architecture prepared by hydrogen bubbling templated electrodeposition is a promising route to fabricate MnO_2 based supercapacitor electrodes. Nevertheless, the capacitance retention of 67% after 1000 charge-discharge cycles was not fully satisfactory; this response was probably due to the decreased adhesion of the films on the current collector, which could be originated from the hydrogen evolution.

The MnO_2 electrode prepared by hydrogen bubbling templated electrodeposition presented novel surface morphologies and displayed a good pseudocapacitive performance, this route could be very interesting to prepare mixed TMOs oxides based on Mn oxide combined with Co/Ni oxides. However, the standard reduction potential (SRP) of Co^{2+} and Ni^{2+} are −0.25 and −0.28 V *vs.* the standard hydrogen electrode (SHE), whereas the SRP of hydrogen evolution reaction is −0.827 V *vs.* (SHE), thus in sulfate-based electrolyte, the one applied to prepare MnO_2 as stated above, metallic Co and Ni would deposit preferentially. Thus, the deposition of mixed TMO electrode was carried out in nitrate-based electrolyte. Furthermore, electrodeposition of mixed TM hydroxide film precursors and their post-thermal transformation into mixed TMO films has been recently reported [17, 18] as an interesting route to fabricate electrodes for supercapacitors. Despite these studies, the effect of annealing on the structural evolution and its correlation with the electrochemical response was not sufficiently detailed as previously stated in the Chapter 3.3. Thus, in this thesis, $MnCo_2O_4$ spinel oxide nanosheet films were prepared by electrodeposition of Mn-Co hydroxides and post-thermal transformation into the spinel phase, and the correlation between structural evolution and electrochemical response at each stage of annealing was studied into detail. Structural studies at different annealing temperatures using Raman & FTIR spectroscopy were performed and their vibration bands were investigated and assigned. Face centered cubic (FCC) $MnCo_2O_4$ spinel oxides were obtained after thermal annealing. The higher symmetry of $MnCo_2O_4$ compared to FCT Mn_3O_4 obtained in the above work was probably due to the presence of Co favoring the growth into FCC structure [19, 20]. Moreover, the $MnCo_2O_4$ spinel nanosheets (thickness of approximately 10 nm) were much thinner than that of Mn_3O_4 nanoflakes (thickness of approximately 14 nm) and displayed surface morphology similar to Co_3O_4 prepared by electrodeposition and thermal annealing [21, 22], suggesting that Co acted as structural and morphological directing agent during the growth of the films. The detailed structural transformation was studied by TEM showing that annealing at temperatures of 250 ^{o}C favored the growth from the *c*-axis preferentially grown hydroxide nanocrystals into randomly oriented spinel nanocrystals with average size of approximately 5 nm in the nanosheets, Figure 4.3, leading to an enhanced pseudocapacitive performance with the specific capacitance value of 430 F g^{-1} at 1 A g^{-1} in 1 M NaOH. This enhanced response after thermal annealing at 250ºC was in agreement with the results obtained for manganese oxides. Annealing at higher temperatures resulted in increasing crystal size, Figure 4.3, changing surface morphology from percolating nanosheet network to nanoflakes that did not display a long-range interconnectivity, leading to a decreased porosity, and therefore to a poor pseudocapacitive performance. Though, the transformation from hydroxide films to spinel films has been usually applied to prepare mixed oxide based electrodes for supercapacitors [17, 23], the detailed structural transformation from electrodeposited hydroxide phase into the spinel phase by thermal annealing and correlation with the electrochemical response have been scarcely reported in literature [17, 23], thus this work goes beyond the state-of-the art by reporting in detail these aspects.

The Mn_3O_4 and $MnCo_2O_4$ based electrodes exhibited good specific capacitances values in 1 M NaOH, which were above 400 F g^{-1} at 1 A g^{-1}. However, their long-term stabilities were rather poor, being 46% and 7% after 1000 cycles and 2000 cycles of the initial specific capacitance values for Mn_3O_4 and $MnCo_2O_4$, respectively. It is worth to noting that the stability of $MnCo_2O_4$ was worst compared to that of Mn_3O_4 electrodes. Most probably, because of the finer morphology of $MnCo_2O_4$, the redox processes resulted in increased irreversible redox reactions, leading to poor stability [2].

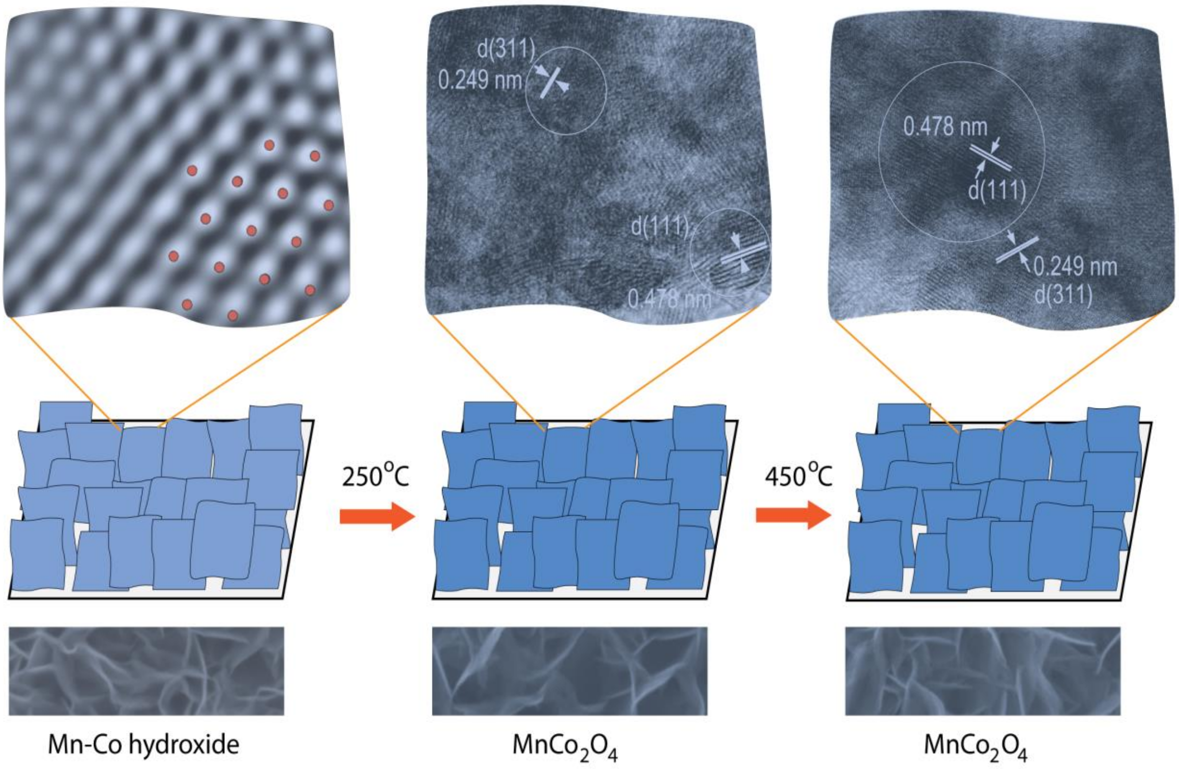

Figure 4.3. A schematic image of the structural evolution from the Mn-Co hydroxide to the spinel $MnCo_2O_4$ by thermal annealing. Circles indicate nanocrystals with different orientations.

Ni-Mn oxides (NMO) were the next double oxides fabricated, that were electrodeposited with different Ni to Mn ratio of 1:0, 3:1, 1:1, 1:3, 1:6, 1:9 and 0:1 and post-thermal annealed at 250 ^{o}C for three hours, learning from the previous results obtained with $MnCo_2O_4$. Varying the Ni to Mn ratio in the electrolyte, and hence in the films, resulted in relevant changes in the structure (crystalline phases) and surface morphology. The surface morphologies showed the presence of particles (Ni:Mn of 1:0), textured particles (Ni:Mn of 3:1 and 1:1), textured particle-nanosheets (Ni:Mn of 1:3), nanosheets (Ni:Mn of 1:6 and 1:9) and nanowires (Ni:Mn of 0:1). Single-phase $Ni_{1-x}Mn_xO$ oxide was formed at low Mn content, whereas two-phases composed of $Ni_{1-x}Mn_xO$ and $Ni_xMn_{3-x}O_4$ were formed at high Mn content. The maximum specific capacitance of about 300 F g^{-1} at 1 A g^{-1} in 1 M KOH was obtained at Ni:Mn ratio of 1:3 in the solution (corresponding to the ratio in the film of approximately 2:3). This oxide showed excellent pseudocapacitive performance, displaying 103% capacitance retention after 1500 cycles, evidencing the synergistic redox reaction when combining two TMOs. This revealed the advantage of combining different transition metal oxides, compared to the single Ni and Mn oxides. Often, in many reports about mixed oxides, the comparison studies with single oxides were not addressed (e.g. $NiMoO_4$ [24]) or were addressed, but showing a worst pseudocapacitive response (e.g. Ni-Fe oxides [25]). Therefore the advantage of using mixed oxides for energy storage *vs.* the corresponding single metal oxides was not sufficiently evidenced [24] or even eliminated [25]. Recent works (*e.g.* Ni-Zn oxides) have addressed only the contribution from one oxide in the mixed oxides, excluding the contribution from the other oxide to the redox response and no comparison studies with single oxides have been published [26, 27]. Thus, these points highlighted the promising use of mixed NMO based electrodes for supercapacitors. The presence of co-existing phases of $Ni_{1-x}Mn_xO$ and $Ni_xMn_{3-x}O_4$ with crystal sizes of approximately 2 nm and 20 nm, respectively, and the synergistic redox response suggested that the enhanced redox response is the result of mixing oxides at nano scale besides incorporating them in the single phase [28, 29]. The enhanced specific capacitance of NMOs at Ni:Mn of 1:3 could partially result from enhanced porosity due to the presence of texture particle-nanosheets morphology (Figure 4.4, left). However, to the author knowledge, the redox contribution and morphology contribution cannot be separated. The morphological changes depended upon the Ni to Mn ratio used in the deposition electrolytes. Even though literature does not provide a concise explanation for the possible origin (mechanism) of the morphological changes observed when varying the transition metal ratio as reported for $NiCo_2O_4$ [30] and Ni-Fe oxides [25] prepared by electrodeposition and hydrothermal methods, respectively. It can be concluded that the surface morphology of the double TMOs can be tuned if the two single metal oxides are controlled to grow in different ways under the same deposition conditions. Thereby, the surface area or porosity of the films can be tailored to improve the electrochemical performance.

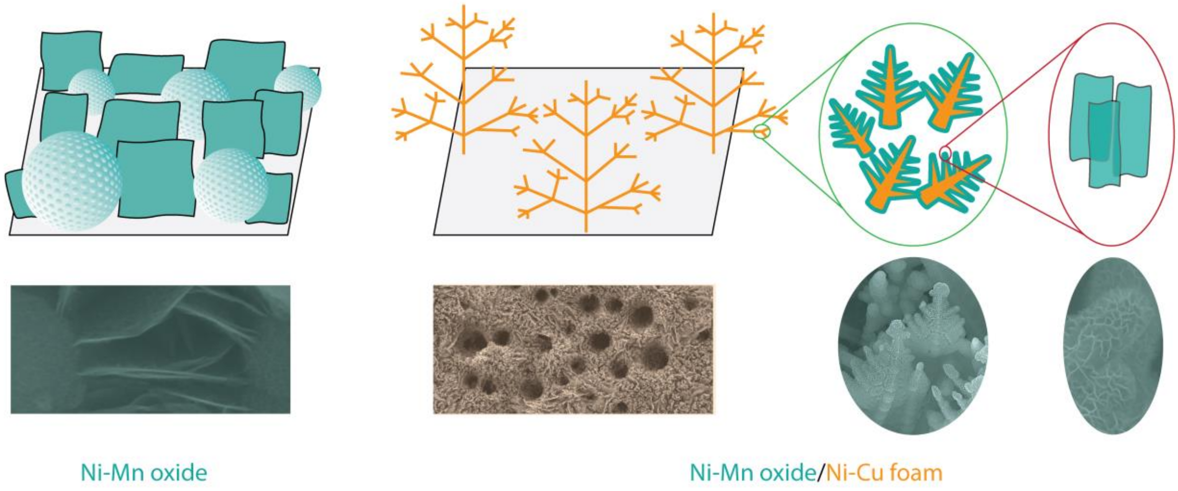

Figure 4.4. Schematic images of the texture particle-nanosheet Ni-Mn oxide, and Ni-Mn oxide on Ni-Cu foam.

The NMOs showed a very interesting redox response and pseudocapacitive performance. However, when the maximum specific capacitance values of NMOs are compared with $NiCo_2O_4$ oxides, this value was rather low [18, 31, 32]. Note that the high specific capacitance values of $NiCo_2O_4$ [33, 34] reported in literature resulted from their deposition on open porous current collectors such as carbon papers and nickel foams. To further improve the storage capacity of NMOs, the films were deposited on 3D conducting Ni-Cu foams with open porous structure (which was also prepared by electrodeposition). The resulting architecture displayed a hierarchical morphology composed of NMO nanosheets over Ni-Cu dendrites with long-range interconnectivity (Figure 4.4, right) of high porosity. Each nanosheet displayed the $Ni_{0.86}Mn_{0.14}O$ phase. High specific capacitance values of 1057 F g^{-1} at 5 A g^{-1} in 1 M KOH after 200 continuous charge-discharge cycling were obtained, which could result from the high porosity of the electrode and the enhanced redox response of the mixed $Ni_{0.86}Mn_{0.14}O$ nanosheets. Interestingly, very high rate capability could be achieved, with 83% capacitance retention when increasing the current densities from 1 A g^{-1} to 20 A g^{-1}. The remarkable rate capability was the result of the novel hierarchical electrode's architecture composed of pseudocapacitive Ni-Mn oxide nanosheet percolation network grown over 3D conducting Ni-Cu dendrite percolation network (Figure 4.4, right). Moreover, the system presented a very good cycling stability behavior, with 103% capacitance retention after 1000 charge-discharge cycles, which is similar to the behavior of the corresponding oxide films deposited on stainless steel. The results suggested that the pseudocapacitive response was mainly originated from the oxide phase.

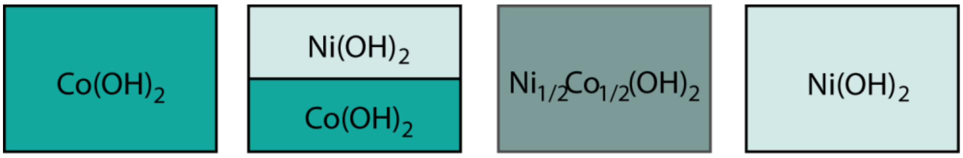

Figure 4.5. A schematic approach of depositing TM hydroxide films including one TM hydroxide layer films and two TM hydroxide layer films.

The thesis also addressed a novel Ni-Co oxide/hydroxide electrode architecture, considering that the mixed oxides with Ni have shown very good pseudocapacitive performance and considering that this system is currently emerging as a promising electrode for supercapacitors, with an increasing number of papers and reviews [18, 31, 32, 35]. This work contributed to the development of this system by designing a new electrode architecture composed of layered hydroxides, in which the single Ni and Co hydroxides were deposited, separately into consecutive layers, over stainless steel via two steps electrodeposition, namely $Ni(OH)_2$ over $Co(OH)_2$, Figure 4.5. The surface morphologies of Co, Ni and Ni-Co hydroxides films showed the presence of crumpled nanosheets, agglomerated dense nanoparticles and interconnected nanosheets, whereas that of two layer films displayed properties closer to the films deposited in one layer. The summing contribution of the individual hydroxide layers in the $Ni(OH)_2$-$Co(OH)_2$ films originates cyclic voltammograms displaying two distinct redox peaks, each of them represented for the redox reaction of the corresponding hydroxide layers.

Considering that $Ni(OH)_2$ formed a dense layer on the top of $Co(OH)_2$ nanosheet layer, the contribution of $Co(OH)_2$ layer was quite pronounced in the cyclic voltammogram, probably due to the high ionic diffusion in the layered hydroxide film. This layered architecture exhibited very high specific capacitance values of 1580 F g^{-1} at an applied current density of 1 A g^{-1} in 1 M KOH. This value was higher than that obtained in Ni-Co hydroxide with synergistic redox reactions and single Co, Ni hydroxides of 1172 F g^{-1} and 834 F g^{-1}, 457 F g^{-1} at 1 A g^{-1}, respectively. Note that the values obtained for Ni-Co hydroxide and $Co(OH)_2$ were similar to values obtained for the same materials deposited on stainless steel, which displayed similar surface morphologies, reported in literature [36, 37]. Also, it is worth to note that this value, obtained by depositing the film directly on the non-porous current collector (stainless steel), was almost in the same order of values reported for pseudocapacitive materials deposited on porous current collectors [38-40]. The capacitance retention after 1000 charge-discharge cycles at 10 A g^{-1} was 71%, corresponding to the specific capacitance value of 985 F g^{-1}, indicating a remarkable pseudocapacitive performance of the material over stainless steel. Literature reports that Ni-Co hydroxide/$NiCo_2O_4$/carbon paper [39], $Co(OH)_2$/stainless steel [37] and $Ni(OH)_2$/nickel foam [41] prepared by electrodeposition displayed capacitance retention of 72% after 2000 cycles, 94% after 1000 cycles and 52% after 300 cycles, respectively. Thus, the stability of new designed electrode exhibited similar response to that of mixed Ni-Co hydroxides, and similar to the average values of single hydroxides reported in previous work. The higher specific capacitance values obtained in the new layered electrodes, goes beyond the state-of-the-art for the single hydroxide and mixed hydroxides, suggesting a promising material to be used as redox supercapacitor electrodes.

Table 4.1 and Figure 4.6 summarize the morphologies, structures and pseudocapacitive performance including specific capacitance, contribution of the diffusion controlled redox capacitance, rate capability and cycling stability of the representative film in each system (which displayed highest performance) studied in this work.

Table 4.1. Morphologies and structures of the pseudocapacitive electrodes reported in this work.

Systems	Morphology	Structure
Mn_3O_4	Nanoparticles/nanoflakes (Figure 4.2, left)	Spinel
MnO_2	Micro-hole distributed over the nanosheet network (Figure 4.2, right)	MnO_2
$MnCo_2O_4$	Nanosheets (Figure 4.3)	Spinel
NMO	Nanosheets-texture particles (Figure 4.4, left)	NiO and Mn_3O_4
NMO/Ni-Cu foam	Nanosheets/dendrites (Figure 4.4, right)	$Ni_{0.86}Mn_{0.14}O$
$Ni(OH)_2$-$Co(OH)_2$	Dense layer/Nanosheet layer (Figure 4.5)	$Ni(OH)_2/Co(OH)_2$

As shown in Figure 4.6, specific capacitance values of $Ni(OH)_2$-$Co(OH)_2$ and Ni-Mn oxides/NiCu foam electrodes were the highest ones achieved in this work. The formation of a dense $Ni(OH)_2$ layer over $Co(OH)_2$ nanosheet layer with high specific capacitance revealed that the charge storage capacity of materials with layered-structure is less dependent on the surface area. The enhancement of the specific capacitance when depositing Ni-Mn oxide on Ni-Cu foam revealed that the high surface area is an important parameter to enhance the specific capacitance of TMO electrodes. Formation of nanocrystals distributed in a nanostructure also accounted for the enhanced charge storage ability.

The specific capacitance values obtained for the electrodes studied in this work, as shown in Figure 4.6, were still far from the theoretical specific capacitance values calculated in the introduction part (in Chapter 1). For example, calculated theoretical specific capacitance of MnO_2 and $MnCo_2O_4$ are 1110 F g^{-1} and 1810 F g^{-1}, respectively and that of $Ni_{0.86}Mn_{0.14}O$ can be calculated as 2966 F g^{-1}, whereas those corresponding values obtained experimentally were 305 F g^{-1}, 420 F g^{-1} and 848 F g^{-1} at 1 A g^{-1}. The decreased specific capacitance values experimentally obtained compared to the theoretical specific capacitance values suggest that the redox reactions are only partially occurring in the active materials. It can probably be due to the fact that the bulk part of the materials was not accessible to the electrolyte, and that the electron conductivity of the materials was low [6], leading to the reduction of the number of active reaction sites.

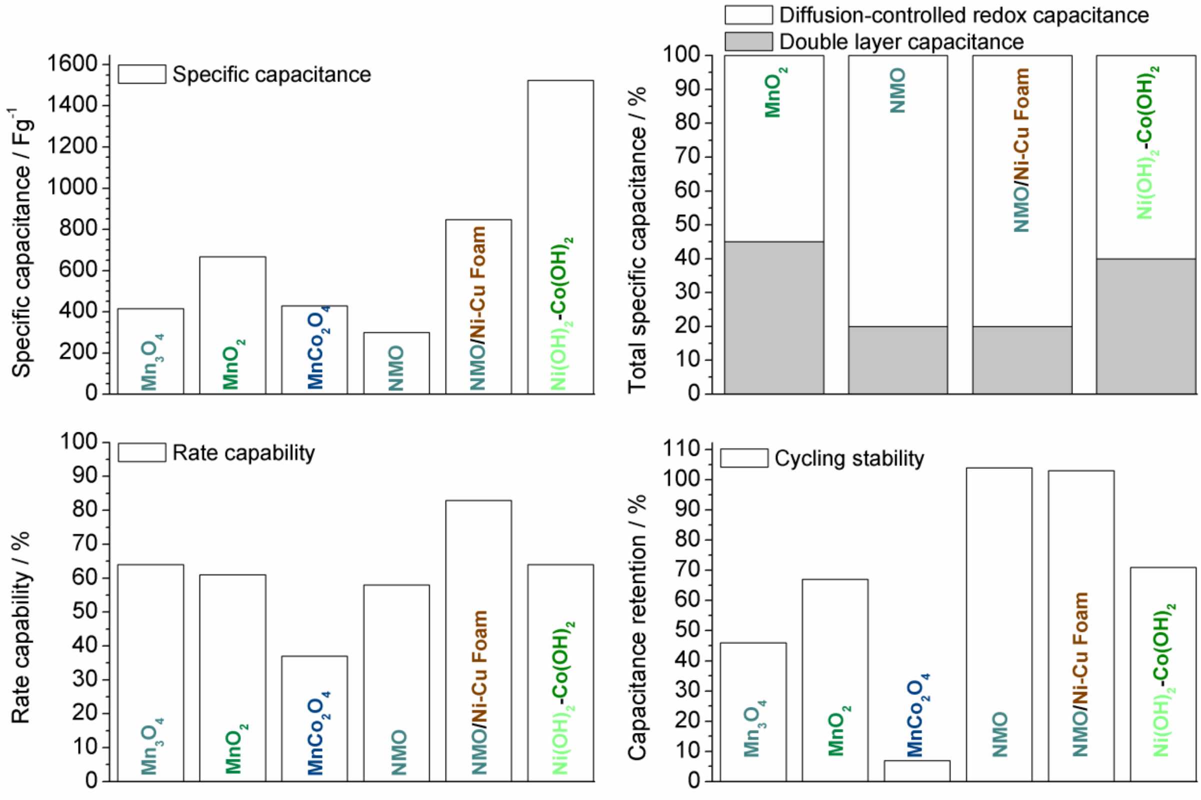

Figure 4.6. Pseudocapacitive performance including specific capacitance at 1 A g^{-1}, contribution of the diffusion-controlled redox capacitance, rate capability when current densities increase from 1 to 10 A g^{-1} (to 20 A g^{-1} for NMO/Ni-Cu foam) and cycling stability after 1000 cycles (200 cycles for $MnCo_2O_4$) of the electrodes reported in this work.

Due to the high surface area of TMO electrode, the contribution of capacitive process (double layer formation) is also present and sums up to the redox contribution, thus leading to increased specific capacitances. The pseudocapacitive response includes an important contribution from diffusion-controlled redox reactions of TMO electrodes with hydroxyl anions in electrolyte, giving rise to enhanced charge storage. The contribution of the diffusion-controlled redox capacitance was about 80% for Ni-Mn oxide based electrodes, which was the highest values contributed from the diffusion controlled redox capacitance in this work (Figure 4.6), suggesting a synergistic redox response in the mixed oxide. The low contribution of the diffusion-controlled redox capacitance - 55% in MnO_2 electrodes, leaded to the pseudocapacitive response with rectangular cyclic voltammogram that mimics those of carbon materials. As the main aim of this work was to design novel coatings for supercapacitor electrodes, deeper understanding about the redox process (mechanism) that governs the pseudocapacitive performance was not carried out, but is an interesting topic to be carried out in future work.

Rate capability was exceptionally high for Ni-Mn oxides/Ni-Cu foam (which was 83%) compared to the other electrodes in this work (Figure 4.6), which accounts for the potential of these novel electrodes composed of double percolation networks as pseudocapacitive material and of the support conducting material that displayed multi-scale porosity, resulting in an enhanced redox performance at high reaction rates.

The high charge-discharge cycling stability of the Ni-Mn oxide films (Figure 4.6) accounted for the reversible redox reactions whereas the low stability of Mn_3O_4 and $MnCo_2O_4$ was probably due to irreversible redox reactions. Understanding the mechanisms that affect the stability response can be an interesting topic for further studies.

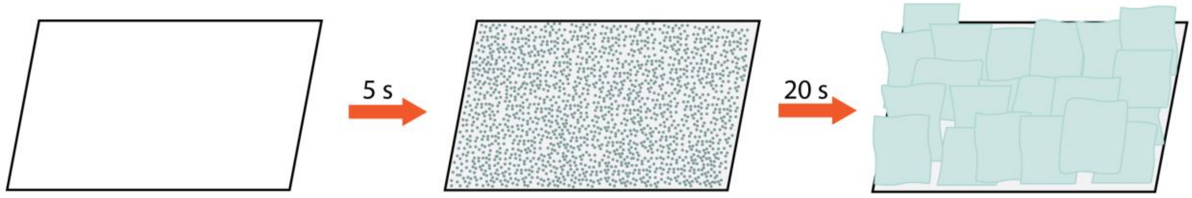

Figure 4.7. Nucleation processes during the electrodeposition of Ni-Co hydroxides.

Finally, the nucleation mechanism of the films prepared by electrodeposition was studied on Ni-Co hydroxide films since these exhibited the highest specific capacitance value obtained in the thesis. Literature reports the electrodeposition of Ni-Co hydroxide either as pseudocapacitive electrodes or as precursors to be transformed into Ni-Co spinel oxide, but the nucleation mechanism was still unclear. Current transient (with applied potentials ranging from -700 mV to -1000 mV) analysis with different growing models including Scharifker-Hill for the applied potentials of -750 mV and -800 mV, Scharifker-Mostany and Mirkin-Nilov-Heerman-Tarallo for the applied potentials ranging from -850 mV to -1000 mV and *in-situ* AFM studies revealed the 3D instantaneous nucleation mechanism in all potentials applied in this work (Figure 4.7). Furthermore, *ex-situ* AFM and *ex-situ* FEG-SEM revealed that the films tend to grow into interconnected nanoflakes (Figure 4.7) after short deposition time (20s). Thus, the results contribute to the fundamental understanding of the film growth process.

Overall, this PhD dissertation overcomes the state-of-the-art in developing novel materials for redox supercapacitors, contributing to further developments in the field.

References

[1] X. Liu, S. Shi, Q. Xiong, L. Li, Y. Zhang, H. Tang, C. Gu, X. Wang, J. Tu, Hierarchical $NiCo_2O_4$@ $NiCo_2O_4$ Core/shell Nanoflake Arrays as High-Performance Supercapacitor Materials, ACS Appl. Mater. Interfaces, 5 (2013) 8790-8795.

[2] W. Wei, X. Cui, W. Chen, D.G. Ivey, Manganese Oxide-based Materials as Electrochemical Supercapacitor Electrodes, Chem. Soc. Rev., 40 (2011) 1697-1721.

[3] B. Messaoudi, S. Joiret, M. Keddam, H. Takenouti, Anodic Behaviour of Manganese in Alkaline Medium, Electrochimica Acta, 46 (2001) 2487-2498.

[4] J.P. Cheng, J. Zhang, F. Liu, Recent development of metal hydroxides as electrode material of electrochemical capacitors, RSC Adv., 4 (2014) 38893-38917.

[5] X. Xia, Y. Zhang, D. Chao, C. Guan, Y. Zhang, L. Li, X. Ge, I.M. Bacho, J. Tu, H.J. Fan, Solution synthesis of metal oxides for electrochemical energy storage applications, Nanoscale, 6 (2014) 5008-5048.

[6] G. Wang, L. Zhang, J. Zhang, A Review of Electrode Materials for Electrochemical Supercapacitors, Chem. Soc. Rev., 41 (2012) 797-828.

[7] N. Nagarajan, H. Humadi, I. Zhitomirsky, Cathodic electrodeposition of MnO_x films for electrochemical supercapacitors, Electrochimica Acta, 51 (2006) 3039-3045.

[8] J. Wei, N. Nagarajan, I. Zhitomirsky, Manganese oxide films for electrochemical supercapacitors, Journal of materials processing technology, 186 (2007) 356-361.

[9] P. Yang, Y. Li, Z. Lin, Y. Ding, S. Yue, C.P. Wong, X. Cai, S. Tan, W. Mai, Worm-like amorphous MnO_2 nanowires grown on textiles for high-performance flexible supercapacitors, Journal of Materials Chemistry A, 2 (2014) 595-599.

[10] J. Duay, S.A. Sherrill, Z. Gui, E. Gillette, S.B. Lee, Self-Limiting Electrodeposition of Hierarchical MnO_2 and $M(OH)_2/MnO_2$ Nanofibril/Nanowires: Mechanism and Supercapacitor Properties, ACS Nano, 7 (2013) 1200-1214.

[11] Q. Li, Z.-L. Wang, G.-R. Li, R. Guo, L.-X. Ding, Y.-X. Tong, Design and Synthesis of $MnO_2/Mn/MnO_2$ Sandwich-Structured Nanotube Arrays with High Supercapacitive Performance for Electrochemical Energy Storage, Nano Lett., 12 (2012) 3803-3807.

[12] J. Liu, J. Jiang, C. Cheng, H. Li, J. Zhang, H. Gong, H.J. Fan, Co_3O_4 Nanowire@MnO_2 Ultrathin Nanosheet Core/Shell Arrays: A New Class of High-Performance Pseudocapacitive Materials, Advanced Materials, 23 (2011) 2076-2081.

[13] L. Yu, G. Zhang, C. Yuan, X.W.D. Lou, Hierarchical $NiCo_2O_4$@MnO_2 core–shell heterostructured nanowire arrays on Ni foam as high-performance supercapacitor electrodes, Chemical Communications, 49 (2013) 137-139.

[14] A. Bard, L. Faulkner, Electrochemical Methods: Fundamentals and Applications, John Wiley & Sons, Inc2001.

[15] T. Zhou, S. Mo, S. Zhou, W. Zou, Y. Liu, D. Yuan, Mn_3O_4/Worm-like Mesoporous Carbon Synthesized via A Microwave Method for Supercapacitors, J Mater Sci, 46 (2011) 3337-3342.

[16] H. Xia, Y. Wang, J. Lin, L. Lu, Hydrothermal synthesis of MnO_2/CNT nanocomposite with a CNT core/porous MnO_2 sheath hierarchy architecture for supercapacitors, Nanoscale research letters, 7 (2012) 1-10.

[17] C. Yuan, J. Li, L. Hou, X. Zhang, L. Shen, X.W. Lou, Ultrathin Mesoporous $NiCo_2O_4$ Nanosheets Supported on Ni Foam as Advanced Electrodes for Supercapacitors, Advanced Functional Materials, 22 (2012) 4592-4597.

[18] Z. Wu, Y. Zhu, X. Ji, $NiCo_2O_4$-based materials for electrochemical supercapacitors, Journal of Materials Chemistry A, 2 (2014) 14759-14772.

[19] S.K. Meher, G.R. Rao, Ultralayered Co_3O_4 for High-Performance Supercapacitor Applications, J. Phys. Chem. C, 115 (2011) 15646-15654.

[20] S.K. Meher, G.R. Rao, Effect of Microwave on the Nanowire Morphology, Optical, Magnetic, and Pseudocapacitance Behavior of Co_3O_4, J. Phys. Chem. C, 115 (2011) 25543-25556.

[21] C. Yuan, L. Yang, L. Hou, L. Shen, X. Zhang, X.W. Lou, Growth of ultrathin mesoporous Co_3O_4 nanosheet arrays on Ni foam for high-performance electrochemical capacitors, Energy & Environmental Science, 5 (2012) 7883-7887.

[22] Q.-c. Liu, J.-j. Xu, Z.-w. Chang, X.-b. Zhang, Direct electrodeposition of cobalt oxide nanosheets on carbon paper as free-standing cathode for Li-O_2 battery, Journal of Materials Chemistry A, 2 (2014) 6081-6085.

[23] Q. Yang, Z. Lu, Z. Chang, W. Zhu, J. Sun, J. Liu, X. Sun, X. Duan, Hierarchical Co_3O_4 Nanosheet@Nanowire Arrays with Enhanced Pseudocapacitive Performance, RSC Adv., 2 (2012) 1663-1668.

[24] S. Peng, L. Li, H.B. Wu, S. Madhavi, X.W.D. Lou, Controlled growth of $NiMoO_4$ nanosheet and nanorod arrays on various conductive substrates as advanced electrodes for asymmetric supercapacitors, Advanced Energy Materials, 5 (2015).

[25] L. Zhang, H. Gong, Improvement in flexibility and volumetric performance for supercapacitor application and the effect of Ni-Fe ratio on electrode behaviour, Journal of Materials Chemistry A, 3 (2015) 7607-7615.

[26] C. Wei, H. Pang, C. Cheng, J. Zhao, P. Li, Y. Zhang, Mesoporous 3D ZnO-NiO architectures for high-performance supercapacitor electrode materials, CrystEngComm, 16 (2014) 4169-4175.

[27] H. Pang, Y. Ma, G. Li, J. Chen, J. Zhang, H. Zheng, W. Du, Facile synthesis of porous ZnO-NiO composite micropolyhedrons and their application for high power supercapacitor electrode materials, Dalton Trans., 41 (2012) 13284-13291.

[28] V. Gupta, S. Gupta, N. Miura, Electrochemically synthesized nanocrystalline spinel thin film for high performance supercapacitor, Journal of Power Sources, 195 (2010) 3757-3760.

[29] T.-Y. Wei, C.-H. Chen, H.-C. Chien, S.-Y. Lu, C.-C. Hu, A Cost-Effective Supercapacitor Material of Ultrahigh Specific Capacitances: Spinel Nickel Cobaltite Aerogels from an Epoxide-Driven Sol–Gel Process, Advanced Materials, 22 (2010) 347-351.

[30] X. Lu, X. Huang, S. Xie, T. Zhai, C. Wang, P. Zhang, M. Yu, W. Li, C. Liang, Y. Tong, Controllable synthesis of porous nickel-cobalt oxide nanosheets for supercapacitors, Journal of Materials Chemistry, 22 (2012) 13357-13364.

[31] Y. Zhang, L. Li, H. Su, W. Huang, X. Dong, Binary metal oxide: advanced energy storage materials in supercapacitors, Journal of Materials Chemistry A, 3 (2015) 43-59.

[32] D.P. Dubal, P. Gomez-Romero, B.R. Sankapal, R. Holze, Nickel cobaltite as an emerging material for supercapacitors: An overview, Nano Energy, 11 (2015) 377-399.

[33] L. Shen, Q. Che, H. Li, X. Zhang, Mesoporous $NiCo_2O_4$ Nanowire Arrays Grown on Carbon Textiles as Binder-Free Flexible Electrodes for Energy Storage, Advanced Functional Materials, 24 (2014) 2630-2637.

[34] G. Zhang, X.W.D. Lou, General Solution Growth of Mesoporous $NiCo_2O_4$ Nanosheets on Various Conductive Substrates as High-Performance Electrodes for Supercapacitors, Advanced Materials, 25 (2013) 976-979.

[35] D. Chen, Q. Wang, R. Wang, G. Shen, Ternary oxide nanostructured materials for supercapacitors: a review, Journal of Materials Chemistry A, 3 (2015) 10158-10173.

[36] S.B. Kulkarni, A.D. Jagadale, V.S. Kumbhar, R.N. Bulakhe, S.S. Joshi, C.D. Lokhande, Potentiodynamic Deposition of Composition Influenced $Co_{1-x}Ni_x$ LDHs Thin Film Electrode for Redox Supercapacitors, International Journal of Hydrogen Energy, 38 (2013) 4046-4053.

[37] V. Gupta, T. Kusahara, H. Toyama, S. Gupta, N. Miura, Potentiostatically Deposited Nanostructured α-$Co(OH)_2$: A High Performance Electrode Material for Redox-Capacitors, Electrochemistry Communications, 9 (2007) 2315-2319.

[38] C. Shang, S. Dong, S. Wang, D. Xiao, P. Han, X. Wang, L. Gu, G. Cui, Coaxial $Ni_xCo_{2x}(OH)_{6x}$/TiN Nanotube Arrays as Supercapacitor Electrodes, ACS Nano, 7 (2013) 5430–5436.

[39] L. Huang, D. Chen, Y. Ding, S. Feng, Z.L. Wang, M. Liu, Nickel–Cobalt Hydroxide Nanosheets Coated on $NiCo_2O_4$ Nanowires Grown on Carbon Fiber Paper for High-Performance Pseudocapacitors, Nano Lett., 13 (2013) 3135-3139.

[40] Y. Bai, W. Wang, R. Wang, J. Sun, L. Gao, Controllable synthesis of 3D binary nickel-cobalt hydroxide/graphene/nickel foam as a binder-free electrode for high-performance supercapacitors, Journal of Materials Chemistry A, 3 (2015) 12530-12538.

[41] G.-W. Yang, C.-L. Xu, H.-L. Li, Electrodeposited nickel hydroxide on nickel foam with ultrahigh capacitance, Chemical Communications, (2008) 6537-6539.

Chapter 5. Conclusions and outlook

Conclusions

In conclusion, this PhD dissertation reported the development of an electrodeposition route to produce new metal oxide (and hydroxide architectures) for application as charge storage electrodes in redox supercapacitors. Moreover, the work studied the physico-chemical and electrochemical properties of single manganese oxides (Mn_3O_4 and MnO_2) and mixed oxides/hydroxides ($MnCo_2O_4$, Ni-Mn oxides and Ni-Co hydroxides) as new redox supercapacitor electrodes.

The influence of potential, electrolyte concentration, applied charge and temperature on the surface morphology and electrochemical response were revealed for electrodeposited manganese oxide (Mn_3O_4) electrodes from nitrate-based electrolytes. Morphological changes depend upon the deposition parameters and the electrochemical response was correlated the surface morphologies of the films. Of those, the film with the hierarchical nanoparticle/nanoflake morphology exhibited specific capacitance value of 416 F g^{-1} at 1 A g^{-1} in 1 M NaOH electrolyte. After 1000 cycles the same electrode exhibited specific capacitances of 196 F g^{-1}, suggesting a possible application of manganese oxides as supercapacitor electrodes working in alkaline electrolyte.

Using hydrogen bubbling as a dynamic template during the electrodeposition process from sulfate-based electrolytes, low crystalline manganese oxide (MnO_2) electrode with well-distributed micro-holes surrounding by a nanosheet network over the surface of the electrode was obtained. The obtained films displayed a specific capacitance of 305 F g^{-1} at 1 A g^{-1} in 1 M Na_2SO_4 electrolyte, rate capability of 61% when increasing the current density from 1 A g^{-1} to 10 A g^{-1}, and capacitance retention of 67% after 1000 cycle. Thus, it suggested a potential application of the hydrogen bubbling as a dynamic template to fabricate electrodes for redox supercapacitors.

$MnCo_2O_4$ spinel oxide nanosheet films were prepared by electrodeposition of Mn-Co hydroxide and post-thermal transformation into the spinel phase. The detailed structural transformation by thermal annealing revealed the transformation from *c*-axis oriented Mn-Co hydroxide nanocrystals to randomly oriented $MnCo_2O_4$ nanocrystals inside nanosheets after thermal annealing at 250 ^{o}C, leading to an enhanced specific capacitance (from 218 F g^{-1} to 420 F g^{-1} at 1 A g^{-1}). Annealing at higher temperatures (450 °C and 650 °C) resulted in increased nanocrystal size and decreasing porosity, leading to poorer specific capacitance (271 F g^{-1} to 9 F g^{-1} at 1 A g^{-1}, respectively).

Ni-Mn oxides showed excellent pseudocapacitive performance, with a specific capacitance 300 F g^{-1}, rate capability of 58% when current densities increased from 1 to 10 A g^{-1}, and capacitance retention of 101% after 1000 cycles for the films with the Ni:Mn ratio of 2:3. The double TMO films evidenced a synergistic redox response when compared to the corresponding single TMOs. $Ni_{1-x}Mn_xO$ phases and two phases (composed of $Ni_{1-x}Mn_xO$ and $Ni_xMn_{3-x}O_4$) were formed at low Mn contents and at high Mn contents, respectively. The morphological changes were depend upon the Ni to Mn ratio used in the electrolytes for electrodeposition whereas Ni and Mn oxides displayed different surface morphologies, suggesting that the surface morphology of the double TMOs can be tuned if the two single metal oxides could be controlled to grow in different ways. This route is a promising way to tailor surface morphology of double TMOs.

The Ni-Mn oxide/3D conducting metallic foams displayed high specific capacitance values (848 F g^{-1} at 1 A g^{-1}), superior rate capability (80% when the current density increases from 1 A g^{-1} to 20 A g^{-1}) and excellent cycling stability with 103% capacitance retention after 1000 cycles. The enhanced pseudocapacitive performance is the result of the novel architecture of the electrode, which is composed of the pseudocapacitive $Ni_{86}Mn_{0.14}O$ nanosheet network formed over 3D Ni-Cu conducting dendrite network. Thus, the results indicated that Ni-Mn oxide based electrodes are very promising candidates for redox supercapacitors.

Layered $Ni(OH)_2$-$Co(OH)_2$ hydroxide electrodes composed of a $Ni(OH)_2$ layer grown over a $Co(OH)_2$ layer, deposited by a two steps electrodeposition process, on stainless steel, showed an exceptionally high specific capacitance - 1580 F g^{-1} at 1 A g^{-1}. This high value is the result of the summative contribution of each hydroxide layer to the total redox response of the electrode. The electrode exhibited high specific capacitance values that were 985 F g^{-1} at 10 A g^{-1} and 692 F g^{-1} (at 10

A g^{-1}) after 1000 cycles. Thus, the results revealed a new possible way to design hydroxide-based pseudocapacitive electrodes for application in redox supercapacitors.

The nucleation mechanism of the Ni-Co hydroxide films prepared by electrodeposition was studied by analyzing the current transient curves at different applied potentials and performing *in-situ* electrochemical AFM measurements. The results revealed that the film formation was based on a 3D instantaneous nucleation mechanism, matching well with the Scharifker-Hill, Scharifker-Mostany and Mirkin-Nilov-Heerman-Tarallo 3D growth models. The films tend to grow into interconnected nanosheets after short deposition time as revealed by *ex-situ* AFM and *ex-situ* FEG-SEM studies. Thus, the results provided the fundamental understanding of the film nucleation and growth.

Outlook

Following by the results achieved in this PhD dissertation, the following areas can be promising for further advance of the state-of-art and are relevant recommendations for future work.

- Optimization of the micro-pore size formation in hierarchical micro/nano porous MnO_2 electrodes and extend this approach to deposit other TMO based electrodes to further improve the pseudocapacitive performance and design novel TMO electrodes for supercapacitors.

- Tailoring the surface morphology of other double TMO electrodes by electrodeposition, in which the morphologies of the corresponding single oxides will be controlled to grow into different forms under the same deposition parameter, to tune their porosity toward an enhanced pseudocapacitive performance.

- Considering the high weight of transition metal foams used in the thesis, if the total mass of the electrode is used to calculate the specific capacitance, the value can be drastically decreased. Thereby, the use of lightweight foam can be improved the total specific capacitance of the whole electrode. In this perspective, lightweight foams such as graphene foam or boron nitride foams can be good candidates for further study as 3D porous current collector to deposit the mixed oxides reported in the thesis.

- Performing fundamental studies about redox response (mechanism) of the mixed oxides with *in-situ* electrochemical approach such as *in-situ* Raman spectroscopy, or *in-situ* measurement with more advanced techniques such as extended x-ray absorption fine structure (EXAFS) and x-ray absorption near edge structure (XANES).

- Understanding ageing of the electrodes by combining different electrochemical and physico-chemical characterizations.

Chapter 6. Résumé en français de la thèse

Ce résumé présente le contenu principal de la version anglaise de la thèse. Les chapitres 1 et 2 de la version anglaise sont résumés dans les sections 1 et 2 (Introduction et techniques expérimentales). Les chapitres 3 et 4 sont résumés dans la section 3 (Résultats et discussions). La section 4 (Conclusion et perspectives) du résumé en français est adaptée du chapitre 5 de la version anglaise.

1. Introduction

Les supercondensateurs sont actuellement considérés comme l'un des dispositifs les plus importants pour les solutions de stockage d'énergie, en raison de la densité de puissance accrue et la stabilité pendant les cycles. Traditionnellement, les supercondensateurs sont utilisés en combinaison avec des batteries pour fournir une puissance supplémentaire pour les applications nécessitant une densité de puissance élevée. Leur faible densité énergétique est un obstacle, et donc les supercondensateurs sont normalement pas utilisé comme un dispositif de stockage unique de l'énergie. Cependant, compte tenu des avantages des supercondensateurs en termes de densité de puissance et de durée de vie [1] (**Figure 1**), et le fait que leur densité d'énergie peut être améliorée, il peut en résulter un dispositif de stockage d'énergie très prometteur.

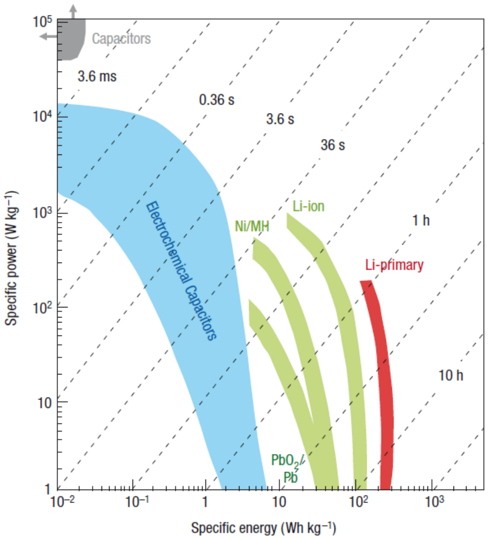

Figure 1. La densité de puissance par rapport à la densité d'énergie de plusieurs dispositifs de stockage de l'énergie électrique: condensateurs, les supercondensateurs et les batteries [1].

La clé pour la densité d'énergie accrue de supercondensateurs réside sur le matériau d'électrode. Des carbones poreux avec une grande surface et une bonne conductivité y compris les charbons actifs, les aérogels de carbone, et les nanotubes de carbone, sont souvent étudiés pour les supercondensateurs

[2-8]. Leur mécanisme de stockage de charge se base sur le processus rapide de formation d'une double couche (processus non-Faradique) et mène à la haute densité de puissance du dispositive. Cependant, la capacité est assez limitée, car elle est totalement régie par la surface spécifique des électrodes, et donc la (capacité spécifique) densité d'énergie est très faible (5-10 Wh kg^{-1}, avec des valeurs spécifiques de capacitance qui sont typiquement inférieures à 200 F g^{-1}) [9, 10]. Ceci a mené à diriger les efforts de recherche vers des pseudo-supercondensateurs basés sur des oxyde de métaux de transition (TMO) (supercondensateurs à oxydo-réduction) afin d'obtenir des densités d'énergie élevées. Des électrodes à base d'oxydes, comme RuO_x, MnO_x, CoO_x et NiO_x, affichent des capacités spécifiques plus élevées en raison de l'accumulation de charge accrue résultant de la réaction Faradique d'oxydo-réduction.

Au cours des dernières années, des études sur les oxydes mixtes, principalement des oxydes doubles de métaux de transition et de phase spinelle, ont retenu beaucoup d'attention pour les supercondensateurs à haute densité d'énergie en raison de leur capacité de stockage d'énergie électrochimique extraordinaire par rapport aux oxydes simple de métaux de transition. Parmi ceux-ci, les oxydes spinelles $NiCo_2O_4$ sont les électrodes les plus connus. Les études sur $NiCo_2O_4$ comme matériau pour les électrodes de pseudo- supercondensateurs ont été lancées après le travail par Hu et al. [11], signalant un aérogel $NiCo_2O_4$ préparé par un procédé sol-gel. Cet aerogel présente par rapport aux oxydes simples des métaux correspondants, plusieurs réactions d'oxydo-réduction due aux contributions des cations Ni et Co. Il en est résulte une réaction capacitive électrochimique améliorée, caractérisé par des valeurs spécifiques de capacitance allant jusqu'à 1400 F g^{-1} à 25 mV s^{-1} à 1 M dans un électrolyte de NaOH et dans une fenêtre de potentiel à partir de 0.04 à 0.52 V après 650 cycles d'activation. En outre, les tests électrochimiques ont révélé une décroissance de la capacité de 9% par rapport à la capacité maximale spécifique après 2000 cycles, indiquant une très bonne performance pseudo-capacitive du matériau $NiCo_2O_4$. Ce résultat a insité de nouvelles électrodes d'oxydes mixtes (par exemple, $NiMoO_4$ [12], $NiFe_2O_4$ [13]) pour les supercondensateurs à haute densité d'énergie. Des approches de préparation différents, tels que l'optimisation des paramètre de dépôt [14] ou le dépôt sur des collecteurs de courant poreux (tels que le papier fait de carbone [15, 16] et les mousse de nickel [17]), ont également été développés pour améliorer la capacité de stockage de charge de $NiCo_2O_4$.

L' électrodéposition est une voie simple et en une seule étape, ce qui permet le dépôt de films TMO directement sur le collecteur de courant, et ce en fournissant une excellente adhérence et sans avoir besoin de liants ou d'autres additifs étrangers. Cela a un impact important parce que la matière active présentera une résistance électrique équivalent inférieure a celle, en général élevé, des liants. La surface et la porosité des matériaux actifs sont les facteurs importants pour l'amélioration des performances de pseudocondensateur. En contrôlant les paramètres de dépôt, il est possible d'adapter la morphologie de surface, sa porosité et la composition chimique des électrodes, ce qui maximise la capacité de stockage de charge. L' électrodéposition ouvre également un large éventail de possibilités en ce qui concerne les collecteurs de courant. La production industrielle peut être effectuée à grande échelle en raison de l'adaptation à différentes échelles du procédé.

Cette thèse de doctorat vise à étudier et à améliorer le comportement électrochimique d'oxydes simples - oxydes de manganèse et à développer de nouvelles électrodes à doubles TMOS adaptés pour le stockage d'énergie dans des superccondensaterurs redox, en déposant les matières actives directement sur l'acier inoxydable collecteur de courant via une route d'électrodéposition flexible et de bas coût. D'une part, cette voie permet d'éviter la nécessité de liants et d'additifs supplémentaires qui introduisent des résistances dans le matériau actif et assure une adhérence à long terme ainsi que la résistance à la corrosion. D'autre part, en contrôlant les paramètres de dépôt, il est possible d'adapter la morphologie de surface et la composition chimique des électrodes, ce qui maximise la capacité de stockage de charge. A cet effet, le travail porte sur le développement d'électrodes d'oxyde doubles (mixtes) sur la base de la combinaison d'oxydes de Mn, Co et Ni par électrodéposition pour des applications dans les supercondensateurs d'oxydo-réduction. Pour étudier ces électrodes, leurs propriétés physico-chimiques ont été caractérisées par les microscopies électroniques à balayage et trasmission (SEM et TEM), la spectroscopie aux rayons X à dispersion d'énergie (EDX), la diffraction des rayons X (XRD), la spectroscopie Raman et infrarouge (FTIR), la microscopie à force atomique (AFM) et par magnétométrie en utilisant un SQUID. Leurs propriétés électrochimiques ont été caractérisés par voltamétrie cyclique et chronopotentiométrie.

Les oxydes mixtes à base de Mn ont d'abord été mis au point. Ainsi, la première étape a consisté en l'électrodéposition d'oxydes de Mn et l'étude de leurs propriétés physico-chimiques et leur réponse électrochimiques. En même temps, du fait que les oxydes de nickel et de Co affichent un effet pseudo-capacitif dans un électrolyte alcalin, ils ont été utilisés avec le Mn pour fabriquer des double

TMO. La réaction électrochimique de l'électrode d'oxyde de manganèse électrodéposé dans un électrolyte alcalin a été étudiée également.

Sur la base des résultats précédents une nouvelle route a été proposée pour concevoir des électrodes d'oxyde de manganèse avec une meilleure réponse électrochimique. La méthode de fabrication est basé sur la formation de bulles d'hydrogène (assistée par l'électrodéposition), conduisant à la formation des électrodes d'oxyde de Mn micro-nano hiérarchiques. Les résultats ont montré que les nouveaux micro-nano films MnO_2 structurés affichent de bonnes performances pseudo-capacitives, ce qui rend cette approche un moyen prometteur pour fabriquer des électrodes d' oxyde métallique à haute performance pour des supercondensateurs redox.

La partie suivante de ma thèse porte sur la fabrication et l'étude de double TMO. Les calculs théoriques montrent que $MnCo_2O_4$ peut offrir des capacités spécifiques très élevés par rapport au divers TMO doubles possibles. Ainsi, je décidai de préparer une série d'électrodes $MnCo_2O_4$. Le processus de dépôt a été basée sur la formation d'hydroxydes TM électrodéposés qui sont transformés en une phase spinelle par recuit thermique. L'évolution des phases électrolytiques d'hydroxyde TM dans la phase spinelle par recuit thermique et en particulier sa corrélation avec la réponse électrochimique n'est pas clairement étudié jusqu'à maintenant et par conséquent il a été adressé. Ainsi, ce chapitre a étudié en détail la composition chimique, la structure, l'évolution morphologique et les propriétés électrochimiques à chaque étape du recuit thermique. Les électrodes $MnCo_2O_4$ révélent une stabilité à des cycles successifs pauvre, mais néanmoins les résultats fournissent des conclusions intéressantes liées à l'effet de la température de recuit.

Suite aux résultats précédents un nouvel oxide double TMO à base de Ni et Mn a été électrodéposé. Les résultas précédents ont permis la sélection d'une température de recuit de 250 °C. En outre, le rapport Mn à Ni a été modifié afin d'étudier les variations correspondantes des propriétés morphologiques, structurelles et électrochimiques. Les résultats ont révélé que ceux-ci sont très sensibles au rapport de Ni:Mn, la valeur optimale étant de 1:3. Les résultats électrochimiques ont démontré un effet synergique de réactions d'oxydoréduction dans les oxydes doubles de Ni-Mn. En outre, les électrodes avec un taux Ni:Mn de 1:3 présentent une stabilité au cyclage remarquable, ce qui en fait un matériau pseudo-capacitif très prometteur.

Dans le but d'augmenter la capacité de stockage de charge des électrodes à base d'oxyde de Ni- Mn, relié aux performances d'oxydo-réduction très prometteuses, cet oxyde a été électrodéposé sur des mousses métalliques préparés par bullage 3D d'hydrogène électrolytiquement assisté. Les nouvelles électrodes composées de nanofeuillets d'oxyde de Ni -Mn sur les mousses métalliques, présentent une performance améliorée pseudo-capacitives par rapport aux oxydes correspondants déposés directement sur l'acier inoxydable.

Du fait que les oxydes mixtes à base d'oxyde de Ni affichent une bonne performance pseudo-capacitive et que les oxydes/hydroxydes de Ni-Co ont été proposés comme matériaux actifs redox pour le stockage de la charge due à la contribution synergique des oxydes/hydroxydes de Ni et de Co, ils ont également été électrodéposés sur des collecteurs de courant en acier inoxydable. L'électrode a été conçu de telle façon qu'il est possible de déposer deux couches consécutives de $Ni(OH)_2$ et $Co(OH)_2$. Cette stratégie est censé sommer les contributions des hydroxydes individuels à la réponse redox totale. En fait, ces électrodes présentent des des valeurs de capacités spécifiques 30% supérieures à celles résultant de la contribution redox synergique dans hydroxydes mixtes Ni-Co.

Dans ce travail, l'électrodéposition a été utilisée pour préparer les électrodes parce qu'il n'y a pas besoin d'utiliser des liants ou additifs étrangers pour préparer les couches actives. Compte tenu de la pertinence de cette approche, la dernière partie de cette thèse porte sur la compréhension fondamentale des processus de croissance, qui sont encore peu discutés. Par conséquent, les mécanismes de formation de films ont été étudiée en ajustant les régimes transitoires de courant avec différents modèles de croissance 3D. L'étude a été complétée par des etudes électrochimiques in-situ par AFM. Un mécanisme de croissance basée sur une nucléation instantanée a été identifié à partir de ces études.

L'ensemble, des résultats ont détaillé la croissance, et les caractérisations physico-chimiques et électrochimiques d’oxydes de Mn, oxydes Mn-Co, Ni-Mn oxydes et hydroxydes de Ni-Co préparés par électrodéposition. L’adaptation de la morphologie et l'architecture de ces électrodes et la création de surfaces présentant une grande aire de surface sont des paramètres clés pour améliorer la performance pseudo-capacitive. Dans le détail, le travail de recherche a contribué au développement de nouveaux oxydex (et hydroxydes) en tant que matériaux pour les supercondensateurs redox par:

- La synthèse de nouvelles électrodes avec de bonnes performances (oxydes Mn, Ni-Mn oxydes, hydroxydes Ni-Co) pseudo capacitives.

- Bien comprendre l'effet du recuit sur la transformation d'hydroxydes mixtes électrodéposés en oxyde mixte et la corrélation avec les propriétés électrochimiques pour des électrodes à base l'oxyde Mn-Co.

- Détailler les mécanismes de croissance de films d'oxyde de Mn électrodéposés à partir d'électrolyte à base de nitrate.

- Révéler un moyen prometteur d'adapter la morphologie de surface des oxydes mixtes électrodéposés par contrôle de la croissance d'oxydes simples.

- Comprendre le mécanisme de nucléation des hydroxydes préparés par électrodéposition (hydroxydes Ni-Co).

2. Experimental

2.1. Fabrication de films par électrodéposition

Les expériences d'électrodéposition ont été réalisées dans un système électrochimique classique sous atmosphère ambiante à la température ambiante en utilisant un VoltaLab PGZ 100 potentiostat de Radiometer, avec l'acier inoxydable comme électrode de travail, une électrode au calomel saturé (SCE) comme électrode de référence et une feuille de platine comme contre- électrode (**Figure 2**). Tous les potentiels décrits dans cet ouvrage sont des potentiels par rapport à la SCE. Des électrolytes à base de nitrate ($Mn(NO_3)_2$, $Co(NO_3)_2$ et $Ni(NO_3)_2$) ont été utilisés pour l'électrodéposition. La température de recuit a été optimisée afin d'obtenir des films présentant une bonne réponse pseudo-capacitives.

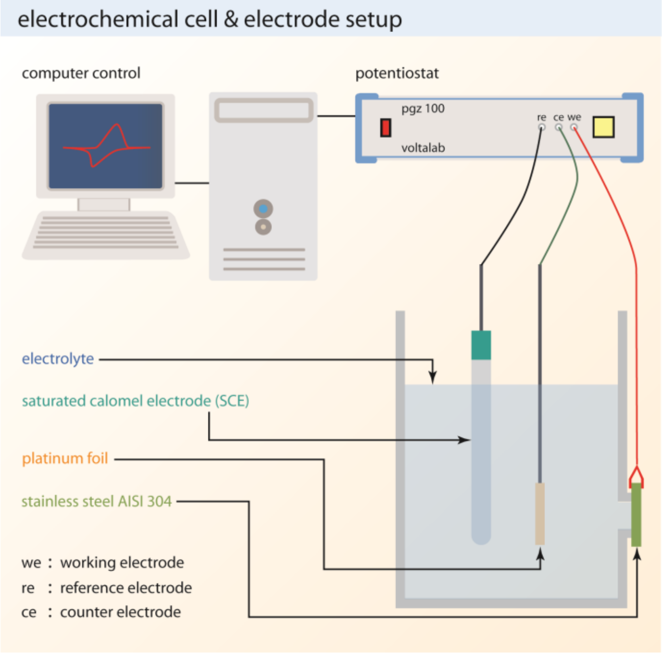

Figure 2. Schéma de la cellule à trois électrodes controlée par le potentiostat.

2.2. Caractérisations

2.2.1. Caractérisation structurale

La microscopie électronique à balayage à effet de champ (microscopes FEG-SEM, JEOL 7001F et FEI QUANTA 250 ESEM) et la spectroscopie par rayons X à dispersion d'énergie (EDX) ont été utilisées pour analyser la morphologie de surface et la composition des couches déposées. Des cartographies EDX ont été réalisées par microscopie électronique à balayage en transmission (microscope STEM, JEOL JEM-2010F). Des images topographiques et de rugosité de surface ont été obtenues avec un microscope à force atomique (microscope AFM, Nanosurf Easyscan), travaillant en mode ‘tapping’. La diffraction des rayons X (XRD, Bruker AXS D8 Advance diffractomètre) en géomètrie Bragg-Brentano et en incidance rasante (GIXRD) avec un rayonnement Cu Kalpha, la spectroscopie infrarouge à transformée de Fourier (FTIR, spectromètre Digilab Excalibur Series) et la spectroscopie Raman (Horiba/Jobin Yvon LabRam Spectromètre) ont été utilisées pour l'étude des caractéristiques structurelles. Pour les mesures Raman, un laser 632.8 nm He-Ne a été utilisé pour l'excitation avec un spot de 1 µm^2 et un temps de comptage de 400 s. Les détails de la structure ont été étudiés par microscopie électronique à transmission (TEM, microscope JEOL JEM-2010) fonctionnant à 200 kV. Les caractéristiques magnétiques ont été étudiées à l'aide d'un magnétomètre SQUID MPMS

(Quantum Design). La dépendeance de l'aimantation sous champ (FC) avec la temperature a été mesurée dans le rang de température 10 K-300 K avec un champ magnétique de 500 Oe.

2.2.2. Caractérisation electrochimique

La réponse électrochimique a été déterminé par voltamétrie cyclique (CV) à différentes vitesses de balayage et de charge-décharge (CD) à différentes densités de courant. Soit 1 M NaOH ou 1 M KOH ont été utilisés comme electrolytes. Toutes les expériences électrochimiques ont été effectuées dans le système classique à trois électrodes comme décrit dans la section de fabrication de films, en utilisant des films déposés sur de l'acier inoxydable comme électrode de travail. La capacité spécifique des films a été calculée à partir des courbes de CD à l'aide de la formule:

$$C = \frac{It}{\Delta V} \qquad (1)$$

où I, t, ΔV sont la densité de courant CD (A g^{-1}), le temps de décharge (s) et la plage de travail du potentiel (V), respectivement.

3. Results and discussion

La première étape a été l'électrodéposition d'oxyde de manganèse à partir d'électrolytes à base de nitrate. Le procédé a été étudié à fond en faisant varier les paramètres d'électrodéposition tel que les potentiels appliqués (allant de -1.0 V à -1.5 V), les concentrations d'électrolyte (0.1 M, 0.25 M et 0.5 M), et la charge appliquée (-0.3 C cm^{-2}, -0.6 C cm^{-2} and -0.9 C cm^{-2}). Les films électrodéposés à partir de bains de nitrate dans le régime cathodique impliquent une generation, soit par la réduction des nitrates ou l'électrolyse de l'eau, de l'anion hydroxyle OH- près du substrat, qui élèvent la valeur du pH à l'interface substrat/électrolyte. Les ions Mn^{2+} dans l'électrolyte réagissent ensuite avec des anions OH^- générés à l'interface substrat/électrolyte, formant $Mn(OH)_2$ qui précipite au niveau du substrat.

$$2H_2O + 2e^- \rightarrow H_2 + 2OH^- \qquad (2)$$

$$NO_3^- + 7H_2O + 8e^- \rightarrow NH_4^+ + 10OH^- \qquad (3)$$

$$Mn^{2+} + 2OH^- \rightarrow Mn(OH)_2 \qquad (4)$$

$$Mn(OH)_2 + \frac{x-1}{2}O_2 \rightarrow MnO_x + H_2O \qquad (5)$$

Cet hydroxyde peut être transformé en oxyde par recuit. Ainsi, l'effet du processus de recuit thermique à différentes températures (de 200 °C à 400 °C) a été étudié. Un recuit thermique à 200 °C a donné lieu à une capacité spécifique accrue, et l'augmentation supplémentaire de la température de recuit a entraîné une diminution de cette capacité spécifique (**Figure 3**).

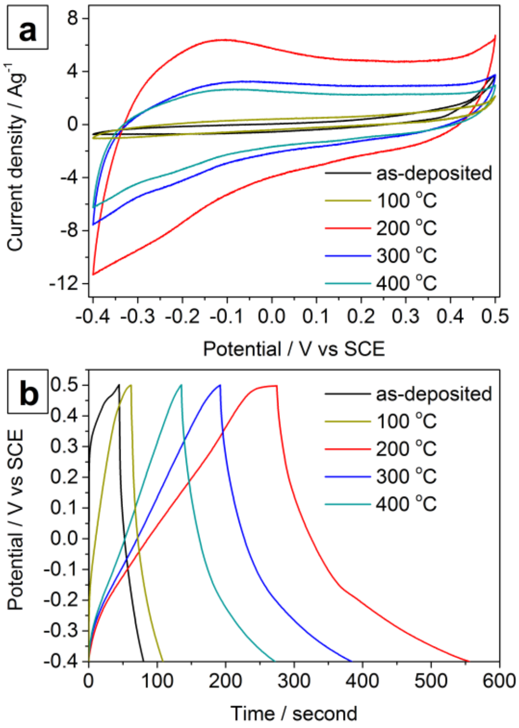

Figure 3. (a) Voltamétrie cyclique à vitesse de balayage de 20 mV s^{-1} et (b) ourbes de charge-décharge à densité de courant de 1 A g $^{-1}$ de films deposes à -1.5 V et après un traitement thermique à 100 °C, 200 °C, 300 °C et 400 °C pendant 1 heure.

La variation des paramètres de dépôt (potentiel appliqué, concentration de l'électrolyte (**Figure 4**) et la charge appliquée) a entraîné des changements morphologiques (**Figure 4**), avec création de porosité importantes, ce qui affecte directement la réponse électrochimique des films. Les paramètres de dépôt optimals ont abouti à la formation de morphologies hiérarchiques de nanoparticules/nanoflakes de face centrée quadratique (FCT) Mn_3O_4 avec des valeurs de capacité spécifiques de 416 F g^{-1} at 1 A g^{-1} dans un électrolyte 1 M NaOH (**Figure 4**). L'électrode a une assez pauvre rétention de capacité - 46% après un test de charge-décharge continue pour 1000 cycles. La capacité spécifique obtenue après 1000 cycles à 1 A g^{-1} est 196 F g^{-1} et cette valeur est comparable aux valeurs rapportées pour l'oxyde de manganèse avant cyclage, travaillant dans un électrolyte neutre [18]. Les valeurs élevées de capacité initiales spécifiques, la faible rétention et la mauvaise stabilité peut être due à l'activité d'oxydo-réduction élevé et les réactions d'oxydoréduction irréversibles de l'oxyde de manganèse (transformation de Mn_3O_4 en MnO_2 [19]), dans un électrolyte alcalin [18].

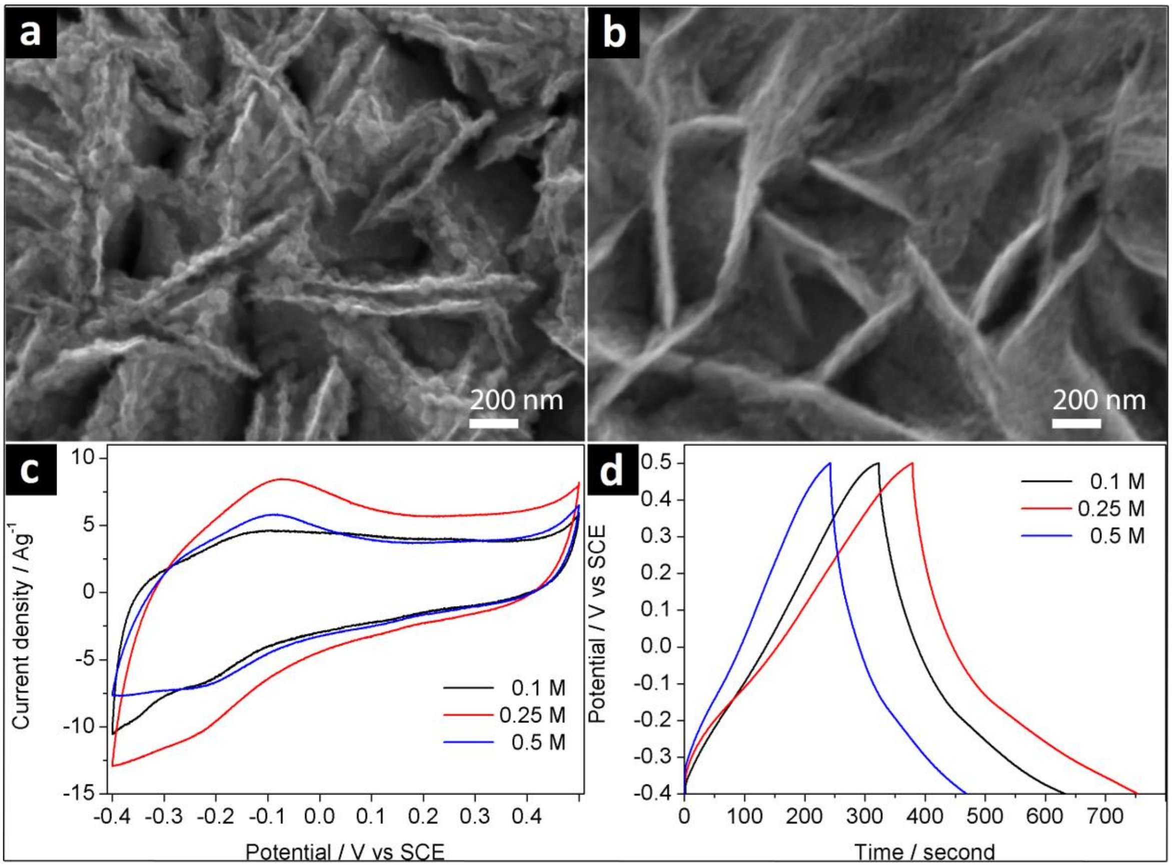

Figure 4. Images MEB-FEG des films déposés avec des concentrations de $Mn(NO_3)_2$ de (a) 0.25 M et (b) 0.5 M avec un potentiel de -1.3 V et une charge appliquée de -0.6 C cm^{-2}. (c) Courbes de voltampérométrie cyclique à une vitesse de balayage de 20 mV s^{-1} et (d) courbes de charge-décharge à densité de courant de 1 A g^{-1} des films deposés avec différentes concentrations de $Mn(NO_3)_2$.

Les présents résultats ont mis en évidence la réponse redox d'oxyde de manganèse dans des électrolytes alcalins. Cela ouvre une voie à explorer par mélange avec des oxydes de cobalt ou nickel (qui sont bien connus pour leur réponse pseudo-capacitive en électrolytes alcalins [20-22]) pour être utilisé comme électrodes pour des supercondensateurs avec des électrolytes alcalins. Ce travail fournit également de nouvelles perspectives, concernant l'influence des paramètres d'électrodéposition clés, sur l’électrodéposition cathodique d'oxydes de manganese à partir d'électrolyte sà base de nitrate. Ce travail a été publié dans le **International Journal of Hydrogen Energy**.

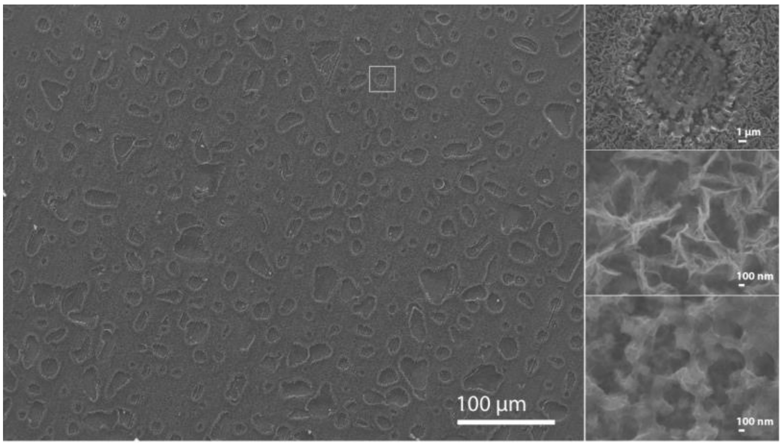

Figure 5. MnO_2 films micro/nano poreux préparés par électrodéposition par evolution d'hydrogène.

Les oxydes de manganèse avec une structure poreuse hiérarchique ou des architectures morphologiques tels que des nanofils, nanofibrilles / nanofils et arrangements sandwich structures de nanotubes [23-25] ont montré une bonne performance pseudo-capacitive. La haute performance pseudo-capacitive atteinte peut être due à la formation d'architectures hiérarchiques qui facilitent les réactions d'oxydoréduction. L'étude d'architectures hiérarchiques a été plutôt limitée à des nanofils 1D [23-27], et des etudes d'autres types d'électrodes hiérarchiques avec de bonnes performances pseudo-capacitives sont toujours une cible à rechercher. Dans la discussion ci-dessus, il a été montré que la morphologie de l'oxyde de manganèse hiérarchique peut être controllée via l'optimisation des paramètres d'électrodéposition; ceci offre une alternative par rapport à ceux que l'on peut obtenir via des dépôts en deux étapes rapportées dans la littérature. La morphologie des électrodes d'oxyde de manganèse peu être optimisé par dépôt dans un électrolyte à base de sulfate en utilisant un barbotage d'hydrogène (l'évolution de l'hydrogène gazeux résulte de l'application des potentiels cathodiques élevées [28]). Le dépôt électrolytique est basée sur le dégagement d'hydrogène qui libère des anions hydroxyle, qui réagissent avec Mn^{2+} pour former $Mn(OH)_2$ et qui se transforme en oxyde par électro-oxydation. L'électro-oxydation a été choisie parce que ces films étaient instables par recuit thermique. Le dégagement d'hydrogène ($2H_2O + 2e^- \rightarrow H_2 + 2OH^-$) a assuré à la fois une matrice dynamique et une source d'anions hydroxyle. Les électrodes obtenus ont constitutes de micro-trous bien répartis, avec un diamètre moyen d'environ 18 µm et une profondeur d'environ 2.2 µm sur un réseau de nanofeuilles continu, formant ainsi l'architecture hiérarchique de l'électrode (**Figure 5**).

Chaque nanofeuille montre une phase MnO_2 mal cristallisé. La capacité spécifique à 1 A g^{-1} était de 667 F g^{-1} avec l'électrolyte 1 M NaOH. La capacité spécifique accrue par rapport à ceux décrit ci-dessus peut être due à une augmentation de la surface, résultant de la nouvelle structure hiérarchique composée de micro-trous et nanofeuillets (Figure 5). En outre, il peut résulter de la formation de la phase MnO_2 mal cristallisé, qui a été rapporté comme ayant une meilleure activité d'oxydo-réduction par rapport à la phase Mn_3O_4 [18]. La valeur de la capacité spécifique avec 1 M Na_2SO_4 était de 305 F g^{-1} à 1 A g^{-1}. La capacité spécifique est inférieure à celle obtenue dans l'électrolyte NaOH et ce probablement en raison de la diminution de la capacité de stocker des électrons et de les libérer dans le processus d'oxydo-réduction [18, 19, 29]. Étant donné que la stabilité des oxydes de manganèse (déposés par électrolyse à potentiel de -1.3 le V, concentration de l'électrolyte de 0.25 M, charge appliquée de -0.6 C cm^{-2} et recuit à 200 ° C en 1 heure) dans du NaOH 1 M est tout à fait faible, plus d'essais électrochimique ont été réalisés dans 1 M de Na_2SO_4. La capacité de charge ('rate capability') de l'électrode était de 61% lors de l'augmentation des densités de courant entre 1 et 10 A g^{-1}, et le maintien de la capacité était de 67% après 1000 cycles de charge-décharge à 5 A g^{-1}, révélant la bonne performance pseudo-capacitive du nouvel électrode d'oxyde de manganèse déposé directement sur de l'acier inoxydable. La littérature récente a indiqué que les arrangements hiérarchique de nanofibres/nanofil de MnO_2 préparé en utilisant de l'oxyde d'aluminium anodisé en tant que matrice dure [24] affichent des valeurs de capacité spécifiques de 298 F g^{-1} à 1 A g^{-1} et que des distributions hiérarchiques MnO_2/nanotubes de carbone [30] affichent des valeurs de capacité spécifiques de 223 F g^{-1} à 1 A g^{-1}. Par rapport à l'état de l'art, l'architecture poreuse innovante de micro/nano MnO_2 préparé par barbotage d'hydrogène électrolytique en tant que matrice dynamique est une voie prometteuse pour fabriquer des électrodes de supercondensateurs à base de MnO_2. Néanmoins, le maintien de la capacité de 67% après 1000 cycles de charge-décharge n'est pas pleinement satisfaisant; cette réponse est probablement due à la diminution de l'adhérence des films sur le collecteur de courant, qui peuvent être du au dégagement d'hydrogène.

L'électrodéposition de nouvelles électrode à base de TMO mixte a été effectuée dans un électrolyte à base de nitrate. En outre, l'électrodéposition de film précurseurs d'hydroxyde de TM mixte et de leur transformation post-thermique en films mixte TMO a été récemment signalée [31, 32] comme une voie intéressante pour fabriquer des électrodes pour des supercondensateurs. En dépit de ces études, l'effet du recuit sur l'évolution structurelle et sa corrélation avec la réponse électrochimique n'est pas à ce jour suffisamment détaillée [31, 32]. Ainsi, dans ce projet, des films de $MnCo_2O_4$ (oxyde spinelle) sous forme de nanofeuilles ont été préparés par électrodéposition d'hydroxydes mixte Mn-Co et leur postérieure transformation par recuit thermique dans la phase spinelle. La corrélation entre l'évolution structurelle et la réponse électrochimique à chaque étape de recuit a été étudié en détail. Les dépôts ont été effectués dans un mode de courant constant, avec l'application d'une densité de courant de -0.4 mA cm^{-2} pendant 2500 secondes. Les concentrations des sels précurseurs utilisés dans les expériences étaient de 0.093M $Mn(NO_3)_2$ et de 0.007 M $Co(NO_3)_2$. Ces concentrations ont été optimisées pour obtenir un ratio Co/Mn voisin de 2 dans les films déposés.

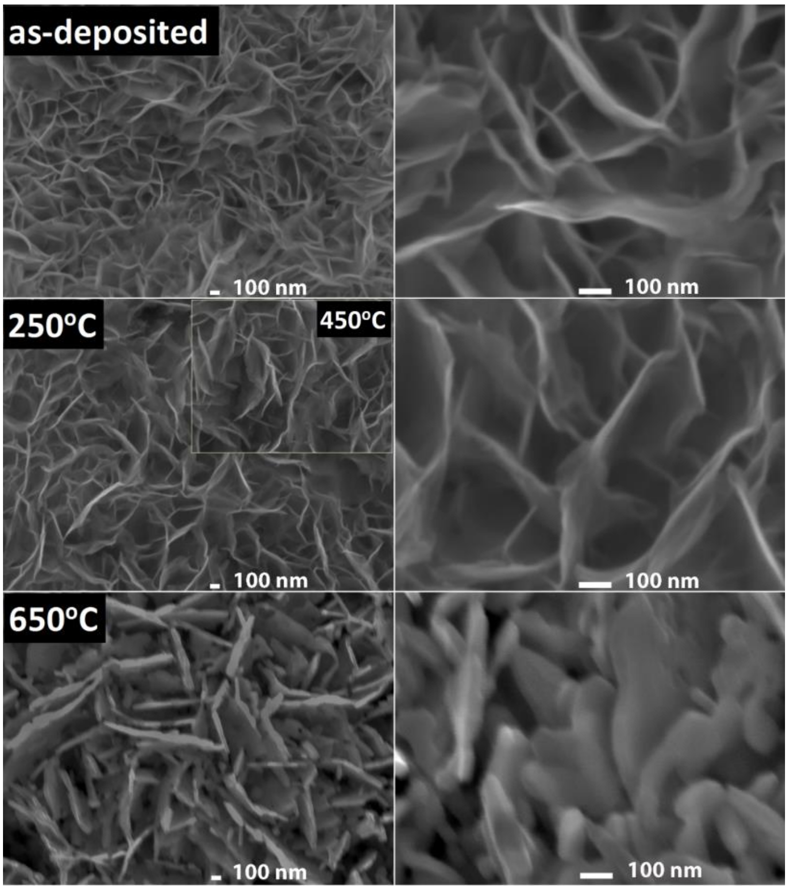

Figure 6. Images FEG-MEB de la surface des films à faible (gauche) et haut (droite) grandissementss. En haut: film tel qu'il a été déposé. Milieu: films recuit à 250 °C. En bas: films recuit à 650 °C. Encart: image FEG-MEB du film recuit à 450 °C avec le même grandissement que les images de gauche pour comparison.

Des études structurales pour différentes températures de recuit et en utilisant la spectroscopie Raman et FTIR ont été effectuées et leurs bandes de vibration ont été étudiées et identifiées. Des oxydes spinelles $MnCo_2O_4$ cubique à face centrée (FCC) ont été obtenus après- recuit thermique. La presence d'une symétrie supérieure FCC de $MnCo_2O_4$ comparé à FCT pour Mn_3O_4 (travail ci-dessus) est probablement due à la présence de Co [33, 34]. Après le dépôt les films (**Figure 6**) présentent une surface poreuse composée de nanofeuillets, qui sont encore observés après traitement thermique jusqu'à 450 °C (**Figure 6**). La morphologie des nanofeuillets suggère qu'ils grandissent presque perpendiculairement au plan du substrat (direction hors du plan de la **Figure 6**) et sont reliés entre eux, formant un réseau de percolation avec une structure poreuse ouverte. Les nanofeuillets ont une épaisseur moyenne d'environ 10 nm et une longueur moyenne d'environ 165 nm. La morphologie de surface des films recuits à 650 °C (**Figure 6**) est différente de celle des films avant et après recuits à plus basse température. Les nanofeuillets sont transformés en nanoplaquettes, chacune d'environ 46 nm d'épaisseur et de 150 nm de longueur moyenne. Le réseau de percolation a presque disparu.

La transformation structurelle étudiée par TEM montre que le recuit à 250 °C favorise le développement de nanocristaux de spinelle avec une taille moyenne d'environ 5 nm dans les nanofeuillets. Cette croissance d'orientation aléatoire, **Figure 7**, a lieu probablement à partir de nanocristaux hydroxide dont l'axe-c est préférentiellement orienté. Les performances améliorées pseudo-capacitives correspondent à une capacité spécifique de 430 F g^{-1} à 1 A g^{-1} et avec 1 M de NaOH. Cette réponse améliorée après un recuit thermique à 250 °C est en accord avec les résultats obtenus pour les oxydes de manganèse. Un recuit à des températures élevées conduit à augmenter la taille du cristal, la **Figure 7**, tout en changeant la morphologie de la surface de percolation du réseau de nanofeuilles à un réseau de nanoplaquettes (principalement composées de cristaux maclés de forme hexagonale) qui ne présente pas une longue distance d'interconnexion, ce qui conduit à une diminution de la porosité, et par conséquent à une performance pseudo-capacitive pauvre. Bien que la transformation de films hydroxyde en spinelle a été généralement appliqué pour préparer des électrodes mixtes à base d'oxyde de supercondensateurs [31, 35], la transformation structurelle détaillée de la phase hydroxyde dans la phase de spinelle par recuit thermique et la corrélation avec la réponse électrochimique ne sont pas souvent rapportés dans la littérature [31, 35]. Ce travail va donc au-delà de la l'état de l'art en rapportant en détail ces aspects (publié dans **RSC Advances, 2015, 5, 27844-27852**).

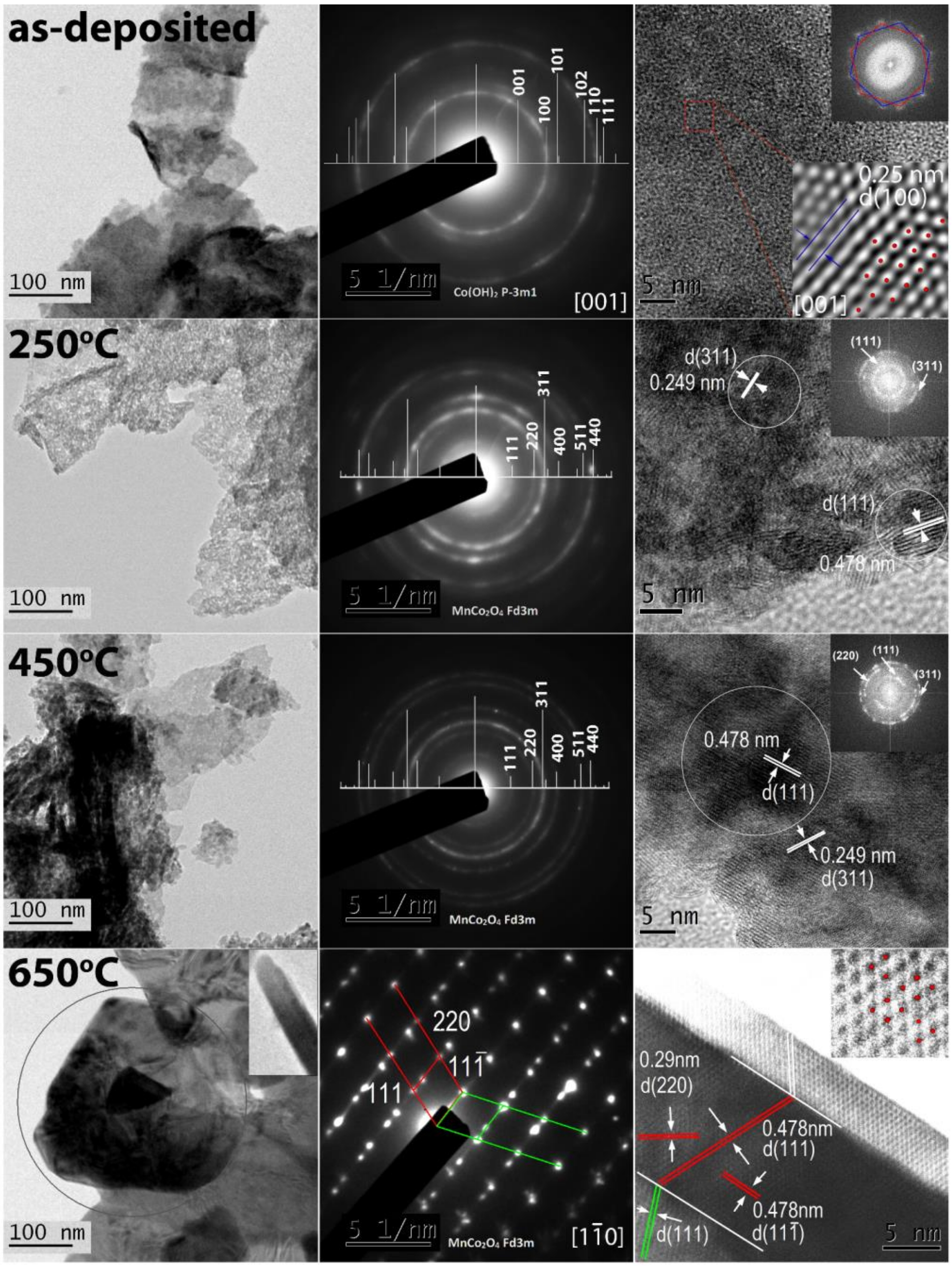

Figure 7. De haut en bas: images TEM du film tel que déposé et aprèsrecuit à 250 °C, 450 °C et 650 °C. De gauche à droite: images basse résolution (gauche), cliché de diffraction SAED (milieu) et images haute resolution HRTEM (doite). Les clichés de diffraction SAED sont indexés en superposant les lignes de diffraction du composé identifié. Encart en haut à droite: FFT de l'image HRTEM pour les films tel que déposé et recuit 250 °C and 450 °C (les hexagones bleu et rouge dans le film tel que déposé correspond à deux axes de zone [001] zone axes tournés de 25 degrés. L'encart pour le recuit à 650 °C estr un élargissemnt de l'image haute résolution avec une superposition de la structure simulée de $MnCo_2O_4$. L'encart à bas à doite pour le fim tel que déposé est la FFT inverse de la

selection marquée par un carrée rouge qui montre la symmétrie hexagonale resultant de la projection de la structure trigonale de $Co(OH)_2$ le long de l'axe de zone [001] (axes hexagonaux).

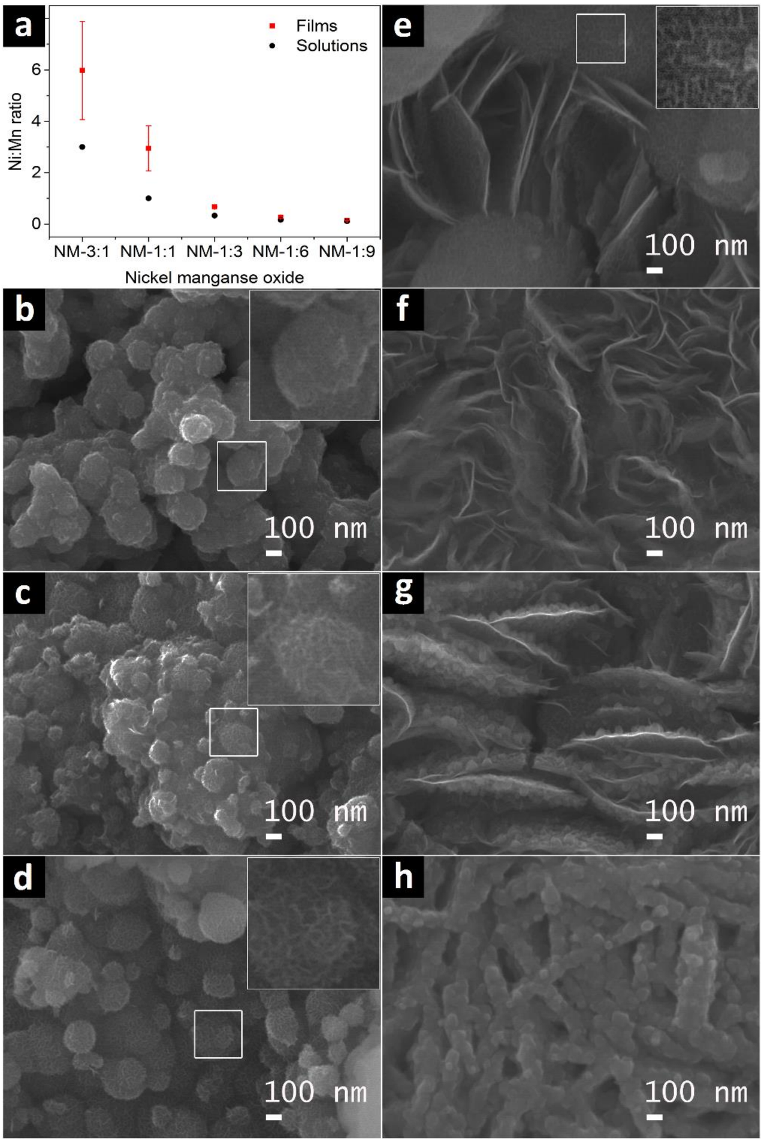

Figure 8. Composition et morpholigie des films electrodeposés. Rapport Ni:Mn dans les films (mesure EDX) *vs.* le rapport dans l'électrolyte (a). Images FEG-MEB des films NM-1:0 (b), NM-3:1 (c), NM-1:1 (d), NM-1:3 (e), NM-1:6 (f), NM-1:9 (g) et NM-0:1 (h). Encarts: agrandissement des zones marquées par des carrées blancs.

Des oxydes doubles Ni-Mn (NMO) ont été par la suite fabriqués. Ils ont été électrodéposés en mode potentiostatique, par application d'un potentiel de -1.1 V avec une charge totale de -600 mC cm^{-2}. Le rapport molaire de $Ni(NO_3)_2$ et $Mn(NO_3)_2$ varie dans l'électrolyte, tout en maintenant une concentration totale de 0,1 M. Le s rapports $Ni(NO_3)_2$:$Mn(NO_3)_2$ testés ont été les suivants: 1:0 , 3:1, 1:1, 1:3, 1:6, 1:9 et 0:1 et les films correspondants sont désignés comme NM-1:0, NM-3:1, NM-1:1, NM-1:3, NM-1: 6, NM-1:9 et NM-0: 1. Après électrodéposition, tous les échantillons ont été recuits à 250 °C pendant 3 heures. Le rapport Ni:Mn dans les films électrodéposés est supérieur au rapport correspondant dans l'électrolyte. Les rapports dans les films sont de 5.9, 2.9, 0.67, 0.27 et 0.14 pour les valeurs correspondantes dans les solutions de 3, 1, 0.33, 0.16 et 0.11 (**Figure 8a**). La variation du rapport Ni:Mn dans l'électrolyte, et par conséquent dans les films, entraîne des changements importants dans la structure (phases cristallines) et la morphologie de surface. Les morphologies de surface ont montré la présence de particules (Ni:Mn de 1:0), les particules texturées (Ni:Mn de 3:1 et 1:1), de particules texturées et de nanofeuillets (Ni:Mn de 1:3), des nanofeuillets (Ni:Mn de 1:6 et 1:9) et des nanofils (Ni: Mn de 0:1) (**Figure 8**). Un oxyde monophasé $Ni_{1-x}Mn_xO$ a été formé à basse teneur en Mn, alors que deux phases $Ni_{1-x}Mn_xO$ et $Ni_xMn_{3-x}O_4$ ont été formées à haute teneur en Mn.

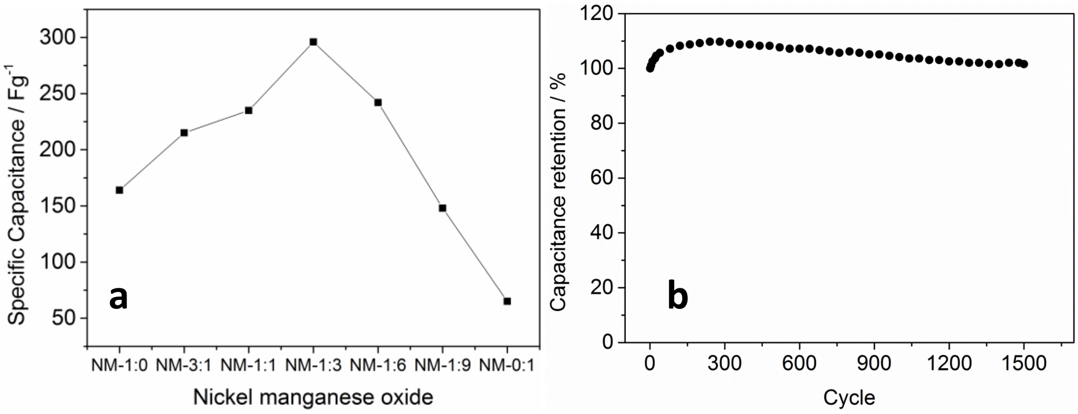

Figure 9. (a) Capacité spécifique des films pour différents rapports Ni:Mn. (b) Stabilité aux cycles du film NM-1:3 pour 1500 cycles à un courant de 3 A g^{-1}.

On obtient une capacité spécifique maximale d'environ 300 F g^{-1} (1 A g^{-1} et 1 M KOH) pour un Ni:Mn de 1:3 dans la solution (correspondant au rapport dans le film d'environ 2:3) (**Figure 9a**). Cet oxyde a montré d'excellentes performances pseudo-capacitives, affichant 103% de rétention de capacité après 1500 cycles (**Figure 9b**), ce qui atteste d’une réaction d'oxydo-réduction synergique combinant deux TMO. Ceci a révélé l'avantage de la combinaison de différents oxydes de métaux de transition, par rapport aux oxydes de Ni et Mn simples. Dans de nombreux rapports sur les oxydes mixtes, les études de comparaison avec des oxydes simples n’ont pas été abordés (par exemple $NiMoO_4$ [12]) ou montrent une pire réponse pseudo-capacitifve (par exemple les oxydes de Fe-Ni [36]). Ainsi l'avantage d'utiliser des oxydes mixtes pour le stockage de l'énergie par rapport à des oxydes métalliques simples correspondants n'a pas été suffisamment mis en évidence [12] ou même éliminé [36]. Des travaux récents (par exemple les oxydes de Ni-Zn) ont abordé la contribution d'un seul des deux oxyde dans l’oxyde mixte à la réponse redox et aucune étude de comparaison avec des oxydes simples a été publiée [37, 38]. Ce travail à base NMO mets en évidence l'utilisation prometteuse d'électrodes mixtes pour les supercondensateurs. La présence de phases coexistantes de $Ni_{1-x}Mn_xO$ et $Ni_xMn_{3-x}O_4$ avec des tailles de cristaux d'environ 2 nm et 20 nm, respectivement, et la réaction d'oxydo-réduction synergique suggérent que la réaction d'oxydo-réduction accrue est le résultat du mélange d'oxydes à l'échelle du nano plutôt que leur incorporation dans une phase unique [11, 39].

La capacité spécifique accrue de NMO pour un rapport Ni:Mn de 1:3 peut partiellement résulter d'une porosité accrue en raison de la présence de particules textures et de nanofeuillets (**Figure 8e**). Cependant, la contribution d'oxydo-réduction et la contribution de la morphologie ne peuvent pas facilement être séparés. Les changements morphologiques dépendent du rapport Ni: Mn utilisé. La littérature ne fournit pas l'origine possible (mécanisme) des modifications morphologiques observées lorsqu’on varie le métal de transition tel que rapporté pour $NiCo_2O_4$ [40] et des oxydes de Ni- Fe [36] préparé par électrodéposition et par des méthodes hydrothermales, respectivement. On peut en conclure que la morphologie de surface des oxydes double TMO peut être réglé que si une croisance différente des deux oxydes métalliques simples est obtenu dans les conditions de dépôt. De ce fait, la surface spécifique ou porosité des films peut être adaptée pour améliorer les performances électrochimiques. Ce travail a été publié dans **Journal of Material Chemistry A, 2015, 3, 10875-10882.**

Les NMO ont montré une réponse redox et une performance pseudo-capacitive très intéressantes. Cependant, les valeurs de capacité spécifiques maximales de NMO sont relativement basses par rapport à celles des oxydes $NiCo_2O_4$ [14, 32, 41]. Les valeurs de capacité spécifiques élevées de $NiCo_2O_4$ [42, 43] dans la littérature resultent de leur dépôt sur des structure ouverte (poreuse) du collecteurs de courant tels que des papiers de carbone ou de mousses de nickel. Même si, nous n’avons pas obtenu une phase spinelle unique, il est intéressant d'étudier plus en avant les oxydes obtenus. Ainsi, pour améliorer encore la capacité de stockage de NMO, les films ont été déposés sur des mousses 3D Ni-Cu (F1 et F2 dénotent des mousses de différentes épaisseurs) avec une structure poreuse ouverte (qui a également été préparée par électrodéposition). Un électrolyte contenant $Mn(NO_3)_2$ (0.075 M) et $Ni(NO_3)_2$ (0.025 M) a été utilisé pour les expériences d'électrodéposition. Les dépôts ont été réalisés en mode galvanostatique, en appliquant une densité de courant de -1 mA cm^{-2} pendant 10 minutes. Après cela les films ont été recuits à 250 °C pour 3 heures. Les films obtenus ont été désignés F1-NMO et F2-NMO. L'architecture résultante affiche une morphologie hiérarchique composée de nanofeuillets NMO plus des dendrites Ni-Cu avec une interconnectivité de longue portée (**Figure 10**) de porosité élevée.

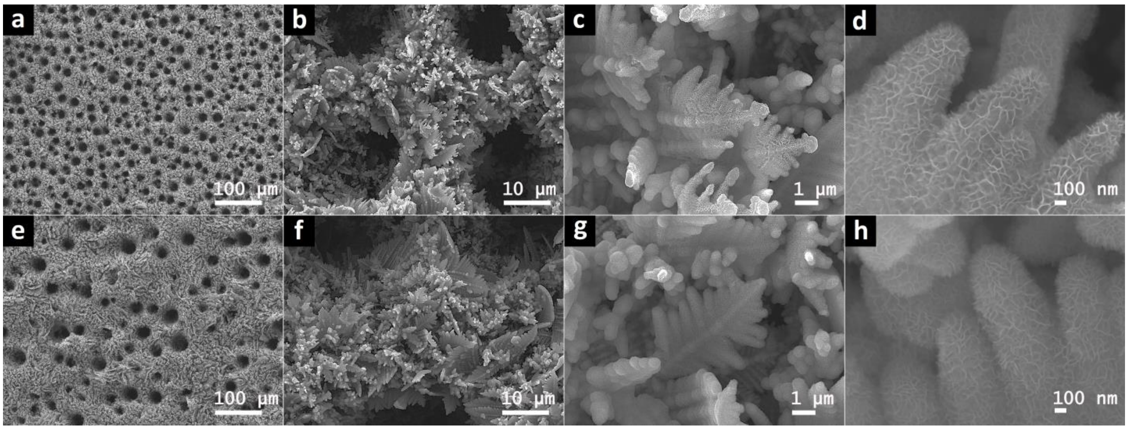

Figure 10. Images MEB-FEG des films d'oxyde de nickel-manganèse déposés sur des mousses de Ni-Cu à différents grossissements. (a-d) film F1-NMO, (e-h) film F2-NMO.

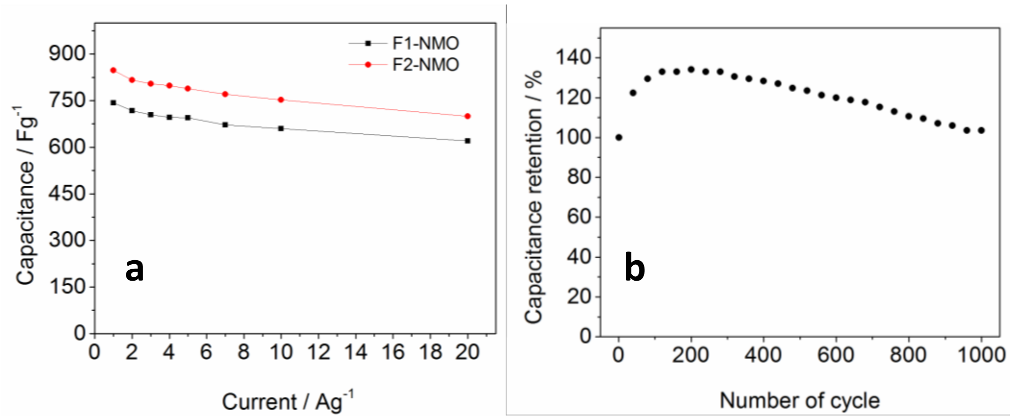

Figure 11. (a) La capacité spécifique en fonction de la densité de courant appliquée. (b) Stabilité au cyclage de la charge-décharge de F2-NMO pour 5 A g^{-1} et 1000 cycles.

Chaque nanofeuille continet la phase $Ni_{0.86}Mn_{0.14}O$. Des hautes valeurs de capacité spécifiques de 1057 F g^{-1} pour 5 A g^{-1} dans 1 M KOH après 200 cycles continus de charge-décharge ont été obtenus, qui pourrait résulter de la grande porosité de l'électrode et de la réaction d'oxydo-réduction améliorée des $Ni_{0.86}Mn_{0.14}O$ nanofeuillets. A noter des très haute capacité de debit, avec 83% de retention de pour des densités de courrant allant de 1 A g^{-1} à 20 A g^{-1} (**Figure 11**). La capacité de débit remarquable est le résultat de l'architecture hiérarchique de la nouvelle électrode composée d'un réseau de percolation de nanofeuilles d'oxyde Ni-Mn pseudo-capacitif que l'on fait croitre sur la structure 3D de la mousse Ni-Cu composé d'un réseau de percolation de dendrite (**Figure 10**). En outre, le système a présenté une très bonne stabilité aux cycles appliqués, avec 103% de retention de la capacité après 1000 cycles de charge-décharge (**Figure 11**), qui est similaire au comportement des couches d'oxyde déposé sur inox. Les résultats suggèrent que la réponse pseudo-capacitive est principalement dûe à la phase oxyde. Ce travail a été publié dans **Nanoscale, 2015, 7, 12452-12459**.

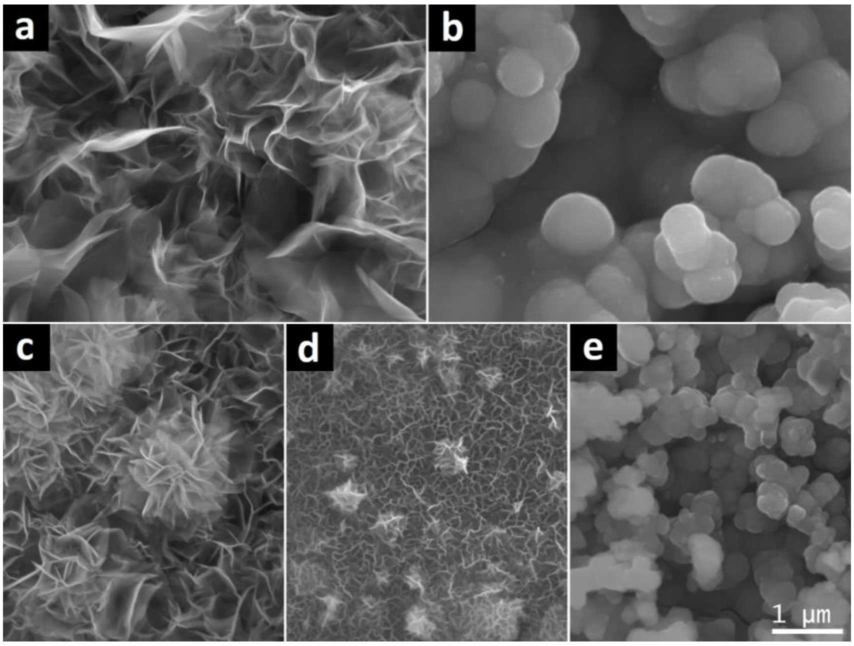

Figure 12. Images (vue d'en haut) par MEB FEG des films (a) $Co(OH)_2$, (b) $Ni(OH)_2$, (c) $Co(OH)_2$-$Ni(OH)_2$, (d) $Ni_{1/2}Co_{1/2}(OH)_2$ et (e) $Ni(OH)_2$-$Co(OH)_2$. La même barre d'échelle est appliquée pour toutes les images dans la figure.

Cette thèse traite également d'une nouvelle architecture d'électrode Ni-Co oxyde/hydroxyde, et ce au vu que les oxydes mixtes avec Ni ont montré de très bonnes performances pseudo-capacitives et en considérant que ce système est en train d'émerger comme une électrode prometteur pour les supercondensateurs, avec un nombre croissant d'articles [14, 32, 41, 44]. Ce travail a contribué au développement de ce système par la conception d'une nouvelle architecture d'électrode composée de couches d'hydroxydes de Ni et Co simples qui ont été déposés successivement sur l'acier inoxydable par l'intermédiaire de deux étapes électrodéposition. Les électrolytes utilisés pour le dépôt ont été 0.1 M $Ni(NO_3)_2$, 0.1 M $Co(NO_3)_2$ et [0.05 M $Ni(NO_3)_2$ + 0.05 M $Co(NO_3)_2$] pour l'electrodeposition de $Ni(OH)_2$, $Co(OH)_2$ et $Ni_{1/2}Co_{1/2}(OH)_2$, respectivement. Tous les films ont été électrodéposition à un potentiel constant de -1.1 V vs SCE. Des films de $Ni(OH)_2$, $Co(OH)_2$ et$Ni_{1/2}Co_{1/2}(OH)_2$ ont été déposés avec une charge totale de -1 C cm^{-2}. Des multicouches de $Ni(OH)_2$-$Co(OH)_2$ et $Co(OH)_2$-$Ni(OH)_2$ ont été préparés par dépôt de chaque couche séparément, en suivant l'ordre dans les films, avec une charge totale appliquée pour le dépôt de chaque couche de -0.5 C cm^{-2}. Les morphologies de surface des films d'hydroxides de Co, Ni et Ni-Co ont montré la présence de nanofeuillets froissés, des nanoparticules agglomérées denses et de nanofeuillets interconnectés, tandis que celle des multicouches affichent des propriétés proches de la dernière couche déposée (**Figure 12**).

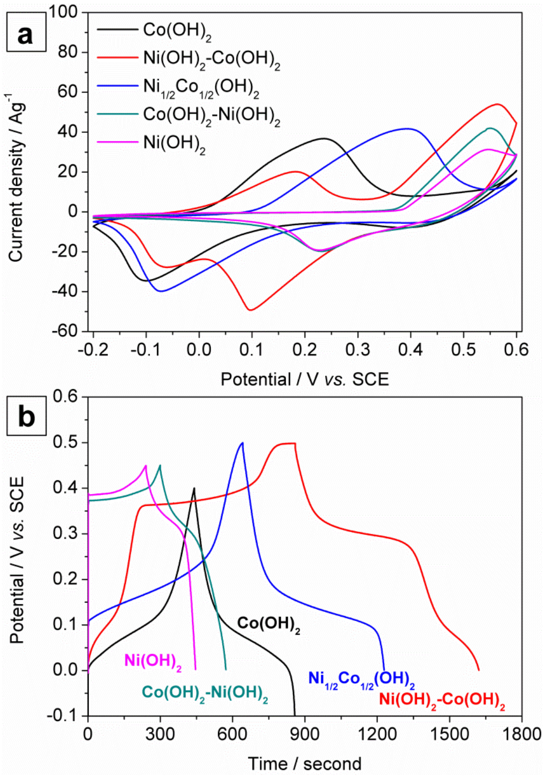

Figure 13. (a) Courbes de voltampérométrie cyclique à une vitesse de balayage de 20 mV s^{-1} et (b) courbes de charge-décharge galvanostatiques à un courant constant de 1 A g^{-1} des films $Ni(OH)_2$, $Co(OH)_2$, $Co(OH)_2$-$Ni(OH)_2$, $Ni_{1/2}Co_{1/2}(OH)_2$ and $Ni(OH)_2$-$Co(OH)_2$.

La contribution de la somme des couches d'hydroxyde individuelles dans le film $Ni(OH)_2$-Co(OH) se voit dans les voltamogrammes cycliques qui présentent deux pics redox distincts, chacun d'eux représentée pour la réaction d'oxydo-réduction de la couche d' hydroxyde correspondante (**Figure 13a**). Étant donné que $Ni(OH)_2$ a formée une couche dense au dessus de la couche de $Co(OH)_2$ composée de nanofeuilles, la contribution de la couche de $Co(OH)_2$ a été assez prononcé dans le voltamogramme cyclique, probablement en raison de la diffusion ionique élevée dans le film hydroxyde multicouches. Cette architecture en couches présente des valeurs de capacité spécifique très élevée de 1580 F g^{-1} pour une densité de courant appliquée 1 A g^{-1} in 1 M KOH (**Figure 13b**).

Cette valeur est supérieure à celle obtenue d'une part dans l'hydroxyde de Ni-Co avec des réactions d'oxydo-réduction synergiques et d'autre aart à celle des hydroxydes simple de Ni et Co 1172 F g^{-1}, 834 F g^{-1} et 457 F g^{-1} à 1 A g^{-1}, respectivement. Notez que les valeurs obtenues pour les hydroxydes de Ni-Co et $Co(OH)_2$ sont similaires aux valeurs obtenues pour les mêmes matériaux déposés sur l'acier inoxydable, qui présentaient des morphologies de surface similaires, rapportés dans la littérature [45, 46]. Aussi, il est intéressant de noter que cette valeur, obtenue par le dépôt du film directement sur le collecteur de courant no -poreux (acier inoxydable), était presque dans le même ordre de grandeur que les valeurs rapportées pour les matériaux pseudo-capacitif déposés sur des collecteurs de courant poreux [47-49]. La capacité de rétention après 1000 cycles de charge-décharge à 10 A g^{-1} est de 71%, correspondant à la valeur de la capacité spécifique de 985 F g^{-1}, indiquant une performance pseudo-capacitive remarquable sur l'acier inoxydable. La littérature indique que Ni-Co hydroxide/$NiCo_2O_4$/papier de carbone [48], $Co(OH)_2$/acier inoxidable [46] et $Ni(OH)_2$/mousse de nickel [50] preparés par electrodeposition ont une capacité de rétention de 72% après 2000 cycles, 94% après 1000 cycles et 52% a après 300 cycles, respectivement. Ainsi, la stabilité des nouvelles électrodes exposées ont une réponse similaire à celle dex hydroxides mixte Ni-Co, et semblable à des valeurs moyennes des hydroxydes simples rapporté dans des travaux antérieurs. Les valeurs de capacité spécifiques plus élevées obtenus dans les nouvelles electrodes multicouches, va au-delà de l'état de l'art pour les hydroxydes simple et mixtes, suggérant un matériau prometteur pour être utilisé comme électrodes redox de supercondensateurs.

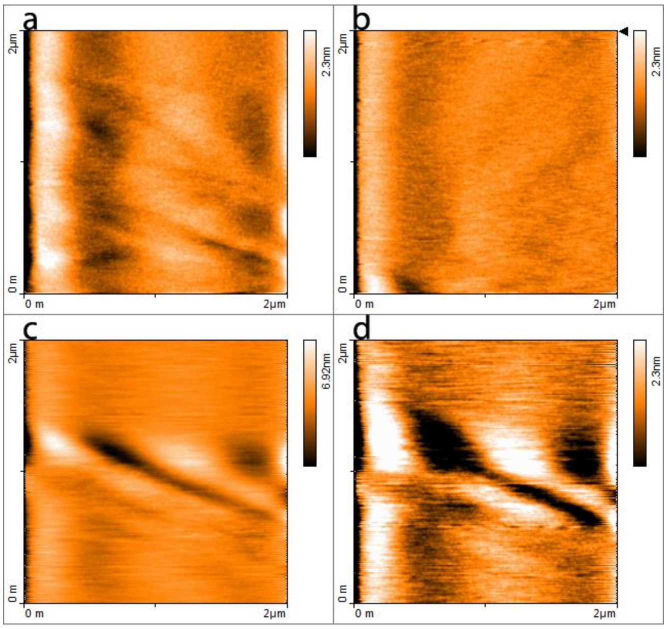

Figure 14. Résultats AFM *In situ* du film déposé à -1200 mV vs Pt. Les images AFM ont été mesurés dans une aire de 2 x 2 μm^2 (a) avant d'appliquer le potentiel et après application du potentiel pendant (b) 5 secondes, (c) 15 secondes et (d) 20 secondes.

Pour finir, le mécanisme de nucléation des films préparés par électrodéposition a été étudiée sur des films d' hydroxide Ni-Co car ils montrent la valeur de capacité spécifique la plus élevée obtenue dans cette thèse. La littérature rapporte l'électrodéposition d'hydroxide de Ni-Co soit sous forme d'électrodes pseudo-capacitives soit en tant que précurseurs pour être transformé en oxyde Ni-Co spinelle, mais le mécanisme de nucléation était encore incertain. L'analyse du courant transitoire (avec des potentiels appliqués allant de -700 mV à -1000 mV) avec différents modèles de croissance, y compris Scharifker-Hill pour les potentiels appliqués de -750 mV à -800 mV, Scharifker-Mostany et Mirkin-Nilov-Heerman-Tarallo pour les potentiels appliqués de -850 mV à -1000 mV montrent qu'un mécanisme de nucléation Iinstantannée 3D. Des experiences *in situ* de AFM ont été réalisées dans une cellule électrochimique, commandé par le potentiostat Autolab Mini, conçu pour cette mesure, en utilisant des aciers inoxydables comme électrode de travail, un anneau de platine comme contre-électrode et un fil de platine comme quasi reference électrode. Les images *in-situ* topographiques ont été enregistrées dans le microscope AFM (Easyscan microscope) à tavers Nanosurf. Les images AFM ont été obtenues juste avant d'appliquer le potential (-1200 mV *vs.* Pt (800 mV *vs.* SCE)), et après 5 secondes, 15 secondes et 25 secondes de son application. Les résultats sont présentés dans la **Figure 14**. Bien que de faible resolution, les images AFM, qui ont été prises dans un environnement liquide, montrent une augmentation du nombre de particules correspondant aux germes, après application d'un potentiel pour 5 seconds. Ceci est en accord avec les résultats de l'ajustement précédents, confirmant la nucléation instantanée. Après avoir appliqué le potentiel 15 secondes, desvallées profondes semblent se développer et semblent être davantage développée après 25 secondes, probablement à cause de la croissance de nanofeuillets interconnectées. En outre, *ex-situ* AFM et *ex-situ* FEG-MEB révèlent que les films ont tendance à se développer dans des nanoflocons interconnectés après un court temps de dépôt (20s). Ces résultats contribuent à la compréhension fondamentale de la croissance du film.

La **Table 1** et la **Figure 15** résument les morphologies, les structures et les performances pseudo-capacives y compris la capacité spécifique, la contribution de la capacité redox controlee par la diffusion, capacité de débit et la stabilité aux cycles des films dans chaque système étudiés dans ce travail.

Table 1. Morphologies et structures des électrodes pseudo-capacitives rapportés dans ce travail.

Système	Morphologie	Structure
Mn_3O_4	Nanoparticules/nanoflocons	Spinelle
MnO_2	Micro-trous distribués sur le réseau de nanofeuillets	MnO_2
$MnCo_2O_4$	Nanofeuillets	Spinelle
NMO	Nanosfeuillets – particules texturés	NiO and Mn_3O_4
NMO/Ni-Cu foam	Nanosfeuillets/dendrites	$Ni_{0.86}Mn_{0.14}O$
$Ni(OH)_2$-$Co(OH)_2$	Couche Dense layer/couche avec des Nanofeuillets	$Ni(OH)_2/Co(OH)_2$

La **Figure 15**, montre que les valeurs de capacité spécifiques des electrodes de $Ni(OH)_2$-$Co(OH)_2$ et Ni-Mn oxides/mousse de NiCu sont les plus élevées. La formation d'une couche dense de $Ni(OH)_2$ sur celle de $Co(OH)_2$ composée de nanofeuillets avec une grande capacité spécifique a révélé que la capacité de stockage de charge avec des matériaux à structure en couches est moins dépendante de la surface. Le renforcement de la capacité spécifique pour des depots de Ni-Mn oxide sur des mousses de Ni-Cu montrent que la grande aire surfacique est le parmêtre important pour améliorer la capacité spécifique d’électrodes de TMO. La formation de nanocristaux distribués dans une nanostructure améliore également la capacité de stockage de charge.

Les valeurs de capacité spécifiques obtenues pour les électrodes étudiés dans ce travail, **Figure 15**, sont encore loin des valeurs de capacité spécifiques théoriques calculées dans la partie d'introduction. Ainsi, les valeurs calculées de capacité spécifique théorique de MnO_2 et $MnCo_2O_4$ sont 1110 F g^{-1} et 1810 F g^{-1}, respectivement et celle de $Ni_{0.86}Mn_{0.14}O$ calculée vaut 2966 F g^{-1}, alors que nos valeurs expérimentales sont 305 F g^{-1}, 420 F g^{-1} et 848 F g^{-1} à 1 A g^{-1}. Les valeurs de capacité spécifiques plus petites obtenues expérimentalement indiquent que les réactions redox se produisent seulement partiellement dans les substances actives. Ceci peut être dû au fait que la partie plus grande partie des matériaux et non accessible à l'électrolyte, et que la conductivité électronique des matériaux est faible [22], conduisant à la réduction du nombre de sites de réaction actifs.

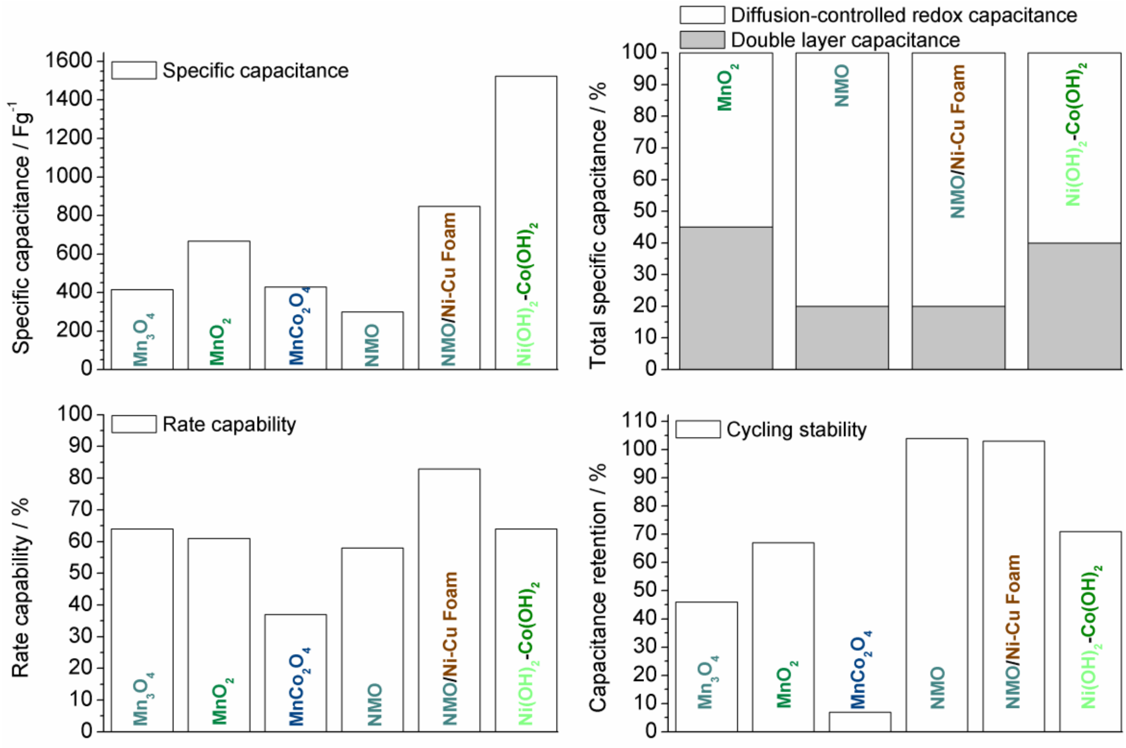

Figure 15. La performance pseudocapacitive y compris la capacité spécifique à 1 A g^{-1}, contribution des capacities redox (controllée par diffusion), capcité de débit pour des densités de courant allant de 1 à 10 A g^{-1} (tà 20 A g^{-1} pour NMO/mousse Ni-Cu) et stabilité au cyclage après 1000 cycles (200 cycles pour $MnCo_2O_4$) pour les electrodes étudiées.

Du fait de son aire surfacique grande des électrodes TMO, la contribution capacitive par formation d'une double couche est aussi présente et s'ajoutte à la contribution, donnat lieu à des capacités spécifiques accrues. La réponse pseudocapacitive des electrodes de TMO inclut une contribution importante des reactions redox controlées par diffusion avec les anions hydroxyls de l'électrolyte, donne lieu à un stockage de charge renforcée. La contribution redox à la capacité la plus élevée obtenue est de l'ordre de 80% pour des electrodes d'oxyde de Ni-Mn (**Figure 15**), ce qui suggère une réaction redox synérgique dans les oxydes mixtes. La contribution redox basse - 55% dans les électrodes MnO_2, donne une réponse pseudocapacitive avec un cycle voltampérogramme rectangulaire qui ressemble à celui des matériaux à base de carbone. Comme l'objectif principal de ce travail était de concevoir de nouveaux revêtements pour les électrodes de supercondensateurs, une compréhension plus profonde sur le processus d'oxydo-réduction (mécanisme) qui régit la performance pseudo-capacitive et qui n'a pas été effectuée dans ce travail reste un sujet intéressant à réaliser dans les travaux futurs.

La capacité de débit est exceptionelle (83%) pour les oxydes de Ni-Mn/mousse Ni-Cu comparée aux autres électrodes (**Figure 15**), ce qui traduit le potential de ces nouvelles électrodes composé de doubles réseaux de percolation pour le matériau pseudo-capacitive et d'un support comme matériau conducteur qui affiche une porosité multi-échelle, résultant en une performance redox améliorée pour des taux de réaction élevées. La stabilité aux cycles de charge-décharge des films d'oxyde de Ni-Mn (**Figure 15**) rmontre la réversibilté des réactions d'oxydo-réduction, tandis que la faible stabilité de Mn_3O_4 et $MnCo_2O_4$ est sans doute liée à un aspect irreversible de ces reactions redox. Comprendre les mécanismes qui affectent la stabilité de la réponse peut être un sujet intéressant pour des études ultérieures.

4. Conclusions et perspectives

Conclusions

Globalement, les résultats obtenus à partir de ce travail représentent un progés par rapport à l'état de l'art dans le développement de nouveaux matériaux pour les supercondensateurs redox, et contribuent au développement dans le domaine. L'influence du potentiel, de la concentration de l'électrolyte, de la charge appliqué et de la température sur la morphologie de surface et la réaction électrochimique ont été étudiés pour l'oxyde de manganèse électrodéposé (Mn_3O_4) en tant qu'électrodes à partir d'électrolytes à base de nitrate. Les modifications morphologiques dépendent des paramètres de dépôt et la réponse électrochimique a été corrélée avec les morphologies de surface des films. Parmi eux, le film avec une morphologie hiérarchique de nanoparticule/nanofeuillet montre une valeur de capacité spécifique de 416 F g^{-1} at 1 A g^{-1} dans un electrolyte 1 M NaOH. Après 1000 cycles l'électrode présente des capacités spécifiques de 196 F g^{-1}, ce qui suggère une application possible des oxydes de manganèse comme électrodes de supercondensateur avec un électrolyte alcalin de travail.

L'utilisation d'un barbotage d' hydrogène comme un matrice dynamique au cours du processus de dépôt électrolytique à partir d'électrolytes à base de sulfate, donne lieu à des électrodes d'oxyde de manganèse (MnO_2) de faible cristallinité avec des micro- trous bien répartis autour d'un réseau de nanofeuilles sur la surface de l'électrode. Les films obtenus affichent une capacité spécifique de 305 F g^{-1} at 1 A g^{-1} dans un electrolyte 1 M Na_2SO_4, une capacité de vitesse de charge 'rate capability' de 61% lorsque la densité de courant passé de 1 A g^{-1} à 10 A g^{-1}, et une rétention de capacité de 67% après 1000 cycles. Ainsi, on a proposé une application potentielle de formation de bulles d'hydrogène en tant que matrice dynamique pour fabriquer des électrodes pour des supercaondensateurs redox.

Des films d'oxydes spinelles $MnCo_2O_4$ sous forme de nanofeuilles ont été préparées par électrodéposition d'un hydroxyde Mn-Co et par transformation post-thermique dans la phase spinelle. La transformation structurelle détaillée par recuit thermique a révélé la transformation de nanocristaux d'hydroxyde Mn-Co textures (axe *c*) vers des nanocrsitaux orientées de manière aléatoire $MnCo_2O_4$ et qui germent dasn les nanofeuillets après recuit thermique à 250 °C, conduisant à une capacité spécifique accrue (de 218 F g^{-1} à 420 F g^{-1} et 1 A g^{-1}). Des recuits à des temperatures plus élevées (450 °C et 650 °C) entraînent une augmentation de la taille des nanocristaux et une porosité décroissante, conduisant à des capacité spécifique plus pauvres (271 F g^{-1} à 9 F g^{-1} à 1 A g^{-1}, respectivement).

Les oxydes Ni-Mn ont montré d'excellentes performances pseudo-capacitives, avec une capacité spécifique de 300 F g^{-1}, une capacité de vitesse de charge 'rate capability' de 58% lorsque la densité de courant passé de 1 A g^{-1} à 10 A g^{-1}, et une rétention de capacité de 101% après 1000 cycles pour les films avec un Ni:Mn de 1:3. Les films doubles TMO mettent en évidence une réaction d'oxydo-réduction synergique par rapport à un film de TMO unique. Des films avec une phase $Ni_{1-x}Mn_xO$ ou deux phases (composed of $Ni_{1-x}Mn_xO$ and $Ni_xMn_{3-x}O_4$) se forment pour des bas et haut contenus de Mn, respectivement. Les modifications morphologiques dépendent du rapport Ni:Mn ce qui suggère que la morphologie de surface peut être réglé si les deux oxydes métalliques simples peuvent croître de différentes façons. Cette route est une voie prometteuse pour adapter la morphologie de surface des double TMO.

Les oxydes Ni-Mn/3D sur des mousses métalliques affichent des valeurs de capacité spécifiques élevées (848 F g^{-1} at 1 A g^{-1}), une capacité de vitesse de charge 'rate capability' supérieure (80% lorsque la densité de courant passé de 1 A g^{-1} à 20 A g^{-1}) et une excellente stabilité de cyclage avec une rétention de capacité de 103% après 1000 cycles. La performance améliorée est le résultat de la nouvelle architecture de l'électrode, qui est constitué d'un réseau de nanofeuilles de $Ni_{86}Mn_{0.14}O$ distribute sur les dendrites 3D conductrices de la mousse Ni-Cu. Les résultats indiquent que les électrodes à base d'oxyde de Ni-Mn sont des candidats très prometteurs pour des supercondensateurs redox.

Des electrodes à base d'hydroxide $Ni(OH)_2$-$Co(OH)_2$ composé d'une couche de $Ni(OH)_2$ sur une couche $Co(OH)_2$, deposé en deux étapes d'électrodéposition, sur de l'acier inoxydable, ont montré une capacité spécifique exceptionnellement élevé - 1580 F g^{-1} à 1 A g^{-1}. Cette valeur élevée est le résultat de la contribution de chaque couche d'hydroxyde au bilan de la réaction d'oxydo-réduction totale de l'électrode. L'électrode a des valeurs de capacité spécifique élevée qui sont de 985 F g^{-1} à 10 A g^{-1} et 692 F g^{-1} (à 10 A g^{-1}) après 1000 cycles. Ces résultats révélent une nouvelle façon de concevoir des électrodes pseudo-capacitives à base d'hydroxyde pour les supercondensateurs redox.

Le mécanisme de nucléation des films hydroxyde Ni-Co préparées par électrodéposition a été étudié par l'analyse des courbes transitoires du courrant à différents potentiels appliqués et par des mesures 'in situ' d'AFM électrochimiques. Les résultats ont révélé que la formation du film est fondée sur un mécanisme de nucléation instantanée 3D, correspondant bien aux modèles de croissance 3D Scharifker-Hill, Scharifker-Mostany et Mirkin-Nilov-Heerman-Tarallo. Les films ont tendance à se développer en nanofeuillets interconnectés après un court temps de dépôt comme l'a révélé une etude *ex-situ* AFM et *ex-situ* FEG-SEM. Ainsi, les résultats ont fourni la compréhension fondamentale de la nucléation et dela croissance du film.

Perspectives

Suite aux résultats obtenus dans cette thèse de doctorat, les domaines suivants peuvent être prometteur pour de nouvelles avancés de l’état de l'art et sont des recommandations pertinentes pour des travaux futurs

- Optimisation de la formation de micro-pores dans les électrodes de MnO_2 hiérarchiques micro/nano poreuses et étension de cette approche aux dépots d'autres électrodes à base de TMO pour améliorer encore les performances et la conception de nouvelles électrodes TMO pseudo-capacitives pour les supercondensateurs.

- Adapter la morphologie de surface des autres électrodes double TMO obtenus par électrodéposition, dans lequelles les morphologies des oxydes simples correspondants seront contrôlées pour se développer dans des formes différentes sous le même paramètre de dépôt, pour régler leur porosité vers une performance améliorée pseudo-capacitive.

- Compte tenu du poids élevé de mousses de métaux de transition utilisés dans la thèse, si la masse totale de l'électrode est utilisée pour calculer la capacité spécifique, cette valeur peut être considérablement diminué. De ce fait, l'utilisation de mousses légères peut amélioré la capacité spécifique totale de l'ensemble de l’électrode. Dans cette perspective, les mousses légères tels que la mousse de graphène ou de nitrure bore peuvent être de bons candidats pour une étude plus approfondie de collecteur de courant poreux 3D pour déposer les oxydes mixtes signalés dans la thèse.

- La réalisation d'études fondamentales sur la réponse redox (mécanisme) des oxydes mixtes avec des expériences *in-situ* électrochimique telles que la spectroscopie Raman et avec des techniques plus avancées telles que EXAFS et XANES.

- Comprendre le vieillissement des électrodes en combinant différentes caractérisations électrochimiques et physico-chimiques.

References

[1] P. Simon, Y. Gogotsi, Materials for electrochemical capacitors, Nat Mater, 7 (2008) 845-854.
[2] L.L. Zhang, X.S. Zhao, Carbon-based materials as supercapacitor electrodes, Chem. Soc. Rev., 38 (2009) 2520-2531.

[3] C. Zhang, W. Lv, Y. Tao, Q.-H. Yang, Towards superior volumetric performance: design and preparation of novel carbon materials for energy storage, Energy & Environmental Science, 8 (2015) 1390-1403.

[4] M. Sevilla, R. Mokaya, Energy storage applications of activated carbons: supercapacitors and hydrogen storage, Energy & Environmental Science, 7 (2014) 1250-1280.

[5] J.P. Paraknowitsch, A. Thomas, Doping carbons beyond nitrogen: an overview of advanced heteroatom doped carbons with boron, sulphur and phosphorus for energy applications, Energy & Environmental Science, 6 (2013) 2839-2855.

[6] K. Fic, G. Lota, M. Meller, E. Frackowiak, Novel insight into neutral medium as electrolyte for high-voltage supercapacitors, Energy & Environmental Science, 5 (2012) 5842-5850.

[7] C. Largeot, C. Portet, J. Chmiola, P.-L. Taberna, Y. Gogotsi, P. Simon, Relation between the ion size and pore size for an electric double-layer capacitor, J. Am. Chem. Soc., 130 (2008) 2730-2731.

[8] M. Armand, F. Endres, D.R. MacFarlane, H. Ohno, B. Scrosati, Ionic-liquid materials for the electrochemical challenges of the future, Nat Mater, 8 (2009) 621-629.

[9] A. Ghosh, Y.H. Lee, Carbon-Based Electrochemical Capacitors, ChemSusChem, 5 (2012) 480-499.

[10] F. Yao, D.T. Pham, Y.H. Lee, Carbon-Based Materials for Lithium-Ion Batteries, Electrochemical Capacitors, and Their Hybrid Devices, ChemSusChem, 8 (2015) 2284–2311.

[11] T.-Y. Wei, C.-H. Chen, H.-C. Chien, S.-Y. Lu, C.-C. Hu, A Cost-Effective Supercapacitor Material of Ultrahigh Specific Capacitances: Spinel Nickel Cobaltite Aerogels from an Epoxide-Driven Sol–Gel Process, Advanced Materials, 22 (2010) 347-351.

[12] S. Peng, L. Li, H.B. Wu, S. Madhavi, X.W.D. Lou, Controlled growth of $NiMoO_4$ nanosheet and nanorod arrays on various conductive substrates as advanced electrodes for asymmetric supercapacitors, Advanced Energy Materials, 5 (2014) 1401172.

[13] Z.-Y. Yu, L.-F. Chen, S.-H. Yu, Growth of $NiFe_2O_4$ nanoparticles on carbon cloth for high performance flexible supercapacitors, Journal of Materials Chemistry A, 2 (2014) 10889-10894.

[14] D.P. Dubal, P. Gomez-Romero, B.R. Sankapal, R. Holze, Nickel cobaltite as an emerging material for supercapacitors: An overview, Nano Energy, 11 (2015) 377-399.

[15] L. Huang, D. Chen, Y. Ding, Z.L. Wang, Z. Zeng, M. Liu, Hybrid composite $Ni(OH)_2@NiCo_2O_4$ grown on carbon fiber paper for high-performance supercapacitors, ACS Appl. Mater. Interfaces, 5 (2013) 11159-11162.

[16] R.B. Rakhi, W. Chen, D. Cha, H.N. Alshareef, Substrate Dependent Self-Organization of Mesoporous Cobalt Oxide Nanowires with Remarkable Pseudocapacitance, Nano Lett., 12 (2012) 2559-2567.

[17] G. Zhang, X.W. Lou, Controlled Growth of $NiCo_2O_4$ Nanorods and Ultrathin Nanosheets on Carbon Nanofibers for High-performance Supercapacitors, Sci. Rep., 3 (2013) 1470.

[18] W. Wei, X. Cui, W. Chen, D.G. Ivey, Manganese Oxide-based Materials as Electrochemical Supercapacitor Electrodes, Chem. Soc. Rev., 40 (2011) 1697-1721.

[19] B. Messaoudi, S. Joiret, M. Keddam, H. Takenouti, Anodic behaviour of manganese in alkaline medium, Electrochimica Acta, 46 (2001) 2487-2498.

[20] J.P. Cheng, J. Zhang, F. Liu, Recent development of metal hydroxides as electrode material of electrochemical capacitors, RSC Adv., 4 (2014) 38893-38917.

[21] X. Xia, Y. Zhang, D. Chao, C. Guan, Y. Zhang, L. Li, X. Ge, I.M. Bacho, J. Tu, H.J. Fan, Solution synthesis of metal oxides for electrochemical energy storage applications, Nanoscale, 6 (2014) 5008-5048.

[22] G. Wang, L. Zhang, J. Zhang, A Review of Electrode Materials for Electrochemical Supercapacitors, Chem. Soc. Rev., 41 (2012) 797-828.

[23] P. Yang, Y. Li, Z. Lin, Y. Ding, S. Yue, C.P. Wong, X. Cai, S. Tan, W. Mai, Worm-like amorphous MnO_2 nanowires grown on textiles for high-performance flexible supercapacitors, Journal of Materials Chemistry A, 2 (2014) 595-599.

[24] J. Duay, S.A. Sherrill, Z. Gui, E. Gillette, S.B. Lee, Self-Limiting Electrodeposition of Hierarchical MnO_2 and $M(OH)_2/MnO_2$ Nanofibril/Nanowires: Mechanism and Supercapacitor Properties, ACS Nano, 7 (2013) 1200-1214.

[25] Q. Li, Z.-L. Wang, G.-R. Li, R. Guo, L.-X. Ding, Y.-X. Tong, Design and Synthesis of MnO_2/Mn/MnO_2 Sandwich-Structured Nanotube Arrays with High Supercapacitive Performance for Electrochemical Energy Storage, Nano Lett., 12 (2012) 3803-3807.

[26] J. Liu, J. Jiang, C. Cheng, H. Li, J. Zhang, H. Gong, H.J. Fan, Co_3O_4 Nanowire@MnO_2 Ultrathin Nanosheet Core/Shell Arrays: A New Class of High-Performance Pseudocapacitive Materials, Advanced Materials, 23 (2011) 2076-2081.

[27] L. Yu, G. Zhang, C. Yuan, X.W.D. Lou, Hierarchical $NiCo_2O_4$@MnO_2 core–shell heterostructured nanowire arrays on Ni foam as high-performance supercapacitor electrodes, Chemical Communications, 49 (2013) 137-139.

[28] A. Bard, L. Faulkner, Electrochemical Methods: Fundamentals and Applications, John Wiley & Sons, Inc2001.

[29] T. Zhou, S. Mo, S. Zhou, W. Zou, Y. Liu, D. Yuan, Mn_3O_4/Worm-like Mesoporous Carbon Synthesized via A Microwave Method for Supercapacitors, J Mater Sci, 46 (2011) 3337-3342.

[30] H. Xia, Y. Wang, J. Lin, L. Lu, Hydrothermal synthesis of MnO_2/CNT nanocomposite with a CNT core/porous MnO_2 sheath hierarchy architecture for supercapacitors, Nanoscale research letters, 7 (2012) 1-10.

[31] C. Yuan, J. Li, L. Hou, X. Zhang, L. Shen, X.W. Lou, Ultrathin Mesoporous $NiCo_2O_4$ Nanosheets Supported on Ni Foam as Advanced Electrodes for Supercapacitors, Advanced Functional Materials, 22 (2012) 4592-4597.

[32] Z. Wu, Y. Zhu, X. Ji, $NiCo_2O_4$-based materials for electrochemical supercapacitors, Journal of Materials Chemistry A, 2 (2014) 14759-14772.

[33] S.K. Meher, G.R. Rao, Ultralayered Co_3O_4 for High-Performance Supercapacitor Applications, J. Phys. Chem. C, 115 (2011) 15646-15654.

[34] S.K. Meher, G.R. Rao, Effect of Microwave on the Nanowire Morphology, Optical, Magnetic, and Pseudocapacitance Behavior of Co_3O_4, J. Phys. Chem. C, 115 (2011) 25543-25556.

[35] Q. Yang, Z. Lu, Z. Chang, W. Zhu, J. Sun, J. Liu, X. Sun, X. Duan, Hierarchical Co_3O_4 Nanosheet@Nanowire Arrays with Enhanced Pseudocapacitive Performance, RSC Adv., 2 (2012) 1663-1668.

[36] L. Zhang, H. Gong, Improvement in flexibility and volumetric performance for supercapacitor application and the effect of Ni-Fe ratio on electrode behaviour, Journal of Materials Chemistry A, 3 (2015) 7607-7615.

[37] C. Wei, H. Pang, C. Cheng, J. Zhao, P. Li, Y. Zhang, Mesoporous 3D ZnO-NiO architectures for high-performance supercapacitor electrode materials, CrystEngComm, 16 (2014) 4169-4175.

[38] H. Pang, Y. Ma, G. Li, J. Chen, J. Zhang, H. Zheng, W. Du, Facile synthesis of porous ZnO-NiO composite micropolyhedrons and their application for high power supercapacitor electrode materials, Dalton Trans., 41 (2012) 13284-13291.

[39] V. Gupta, S. Gupta, N. Miura, Electrochemically synthesized nanocrystalline spinel thin film for high performance supercapacitor, Journal of Power Sources, 195 (2010) 3757-3760.

[40] X. Lu, X. Huang, S. Xie, T. Zhai, C. Wang, P. Zhang, M. Yu, W. Li, C. Liang, Y. Tong, Controllable synthesis of porous nickel-cobalt oxide nanosheets for supercapacitors, Journal of Materials Chemistry, 22 (2012) 13357-13364.

[41] Y. Zhang, L. Li, H. Su, W. Huang, X. Dong, Binary metal oxide: advanced energy storage materials in supercapacitors, Journal of Materials Chemistry A, 3 (2015) 43-59.

[42] L. Shen, Q. Che, H. Li, X. Zhang, Mesoporous $NiCo_2O_4$ Nanowire Arrays Grown on Carbon Textiles as Binder-Free Flexible Electrodes for Energy Storage, Advanced Functional Materials, 24 (2014) 2630-2637.

[43] G. Zhang, X.W.D. Lou, General Solution Growth of Mesoporous $NiCo_2O_4$ Nanosheets on Various Conductive Substrates as High-Performance Electrodes for Supercapacitors, Advanced Materials, 25 (2013) 976-979.

[44] D. Chen, Q. Wang, R. Wang, G. Shen, Ternary oxide nanostructured materials for supercapacitors: a review, Journal of Materials Chemistry A, 3 (2015) 10158-10173.

[45] S.B. Kulkarni, A.D. Jagadale, V.S. Kumbhar, R.N. Bulakhe, S.S. Joshi, C.D. Lokhande, Potentiodynamic Deposition of Composition Influenced $Co_{1-x}Ni_x$ LDHs Thin Film Electrode for Redox Supercapacitors, International Journal of Hydrogen Energy, 38 (2013) 4046-4053.
[46] V. Gupta, T. Kusahara, H. Toyama, S. Gupta, N. Miura, Potentiostatically Deposited Nanostructured α-$Co(OH)_2$: A High Performance Electrode Material for Redox-Capacitors, Electrochemistry Communications, 9 (2007) 2315-2319.
[47] C. Shang, S. Dong, S. Wang, D. Xiao, P. Han, X. Wang, L. Gu, G. Cui, Coaxial $Ni_xCo_{2x}(OH)_{6x}$/TiN Nanotube Arrays as Supercapacitor Electrodes, ACS Nano, 7 (2013) 5430–5436.
[48] L. Huang, D. Chen, Y. Ding, S. Feng, Z.L. Wang, M. Liu, Nickel–Cobalt Hydroxide Nanosheets Coated on $NiCo_2O_4$ Nanowires Grown on Carbon Fiber Paper for High-Performance Pseudocapacitors, Nano Lett., 13 (2013) 3135-3139.
[49] Y. Bai, W. Wang, R. Wang, J. Sun, L. Gao, Controllable synthesis of 3D binary nickel-cobalt hydroxide/graphene/nickel foam as a binder-free electrode for high-performance supercapacitors, Journal of Materials Chemistry A, 3 (2015) 12530-12538.
[50] G.-W. Yang, C.-L. Xu, H.-L. Li, Electrodeposited nickel hydroxide on nickel foam with ultrahigh capacitance, Chemical Communications, (2008) 6537-6539.

Abstract

New oxide-based electrodes for advanced redox supercapacitors

Transition metal oxides (TMOs) and double TMOs are promising materials for application as electrodes in pseudo supercapacitors or redox supercapacitors because they can exhibit increased energy density resulted from redox reactions.

This PhD dissertation aims at studying and improving the electrochemical behavior of single TMOs - manganese oxides and at developing new double TMOs electrodes tailored for energy storage in redox supercapacitors, by depositing the active materials directly on stainless steel current collector *via* a flexible and costless electrodeposition route.

To study these electrodes for supercapacitors, their physic-chemical properties were characterized by scanning/transmission electron microscopy (SEM/TEM), energy-dispersive X-ray spectroscopy (EDX), X-ray diffraction (XRD), Raman & Infrared spectroscopy (FTIR), atomic force microscopy (AFM) and superconducting quantum interference device (SQUID). Their electrochemical properties were characterized by cyclic voltammetry and chronopotentiometry.

The results have detailed the growing, physic-chemical and electrochemical characterizations of Mn oxides, Mn-Co oxides, Ni-Mn oxides and Ni-Co hydroxides prepared by electrodeposition. Tailoring the morphology and architecture these electrodes and creating surfaces exhibiting high surface area are key parameters for enhanced pseudocapacitive performance. In detail, the research work contributed to the development of novel oxide (and hydroxides) materials for redox supercapacitors by: (i) providing novel electrodes with good pseudocapacitive performance for supercapacitors (Mn oxides, Ni-Mn oxides, Ni-Co hydroxides), (ii) fully understanding the effect of annealing on the transformation from electrodeposited mixed hydroxides to mixed oxide and their correlation with electrochemical properties for the Mn-Co oxide – based electrodes, (iii) detailing the growing mechanisms of Mn oxide films electrodeposited from nitrate based electrolyte, (iv) revealing a promising way of tailoring surface morphology of electrodeposited mixed oxides by controlling the growth of single oxides, (v) understanding the nucleation mechanism of hydroxides prepared by electrodeposition (Ni-Co hydroxides).

Thus, the results of this PhD dissertation go beyond the state-of-the-art and provided valuable highlights to advance the development of novel electrode materials for redox supercapacitors.

Résumé

Electrodes innovantes à base d'oxyde pour les supercondensateurs redox

Les oxydes simple ou double de métaux de transition (OMTs) sont des matériaux prometteurs pour les applications en tant qu'électrode dans des pseudo supercondensateurs ou des supercondensateur redox car ils peuvent présenter un gain de densité d'énergie résultant des réactions redox.

Ce mémoire de thèse a pour but l'étude et l'optimisation du comportement électrochimique d'électrodes d' oxydes simple de manganèse ainsi que le développement de nouvelles électrodes à base d'oxydes doubles (OMTs) conçues pour le stockage d'énergie dans les supercondensateurs redox , grâce au dépôt de ces matériaux actifs sur un collecteur de courant en acier inoxydable par électrodéposition ce qui représente une technique flexible et peu couteuse.

Afin d'étudier ces électrodes, leurs propriétés physico-chemique ont été caractérisées par microscopie électronique (SEM/TEM), spectroscopie X à dispersion d'énergie (EDX), par diffraction X (XRD), par spectroscopies Raman & Infrarrougee (FTIR), par microsopie à force atomique (AFM) et par magnétométrie SQUID (superconducting quantum interference device). Leurs propriétés electrochimique ont été caractérisées par voltamperométrie cyclique et chronopotentiométrie.

Les résultats détaillent la croissance et les caractérisations physico-chimique et électrochimique de plusieurs oxydes TMOS (TM=Mn, Mn-Co, Ni-Mn) ainsi que d'hydroxydes de Ni-Co préparés par électrodéposition. Le contrôle de la morphologie et de l'architecture des électrodes, en vue de créer des surfaces ayant des grandes surfaces actives, est le paramètre clé pour augmenter la performance du pseudo-condensateur. Dans le détail, le travail de recherche a contribué au développement de nouveau matériaux pour des électrodes à base d'oxyde (et hydroxydes) pour les supercondensateurs redox par: (i) la mise en œuvre de nouvelles électrodes avec des bonnes performances pseudocapacitive pour des supercondesateurs (Mn oxydes, Ni-Mn oxydes, Ni-Co hydroxydes), (ii) la pleine compréhension de l'effet du recuit sur la transformation de l'hydroxyde préparés par électrodéposition en oxyde et de la corrélation résultante avec les propriétés électrochimiques pour des électrodes à base d'oxyde Mn-Co, (iii) la description détaillée du mécanisme de croissance de films d' oxyde de Mn préparés par électrodéposition à partir d'électrolytes à base de nitrates, (iv) la mise en évidence d'une méthode prometteuse de mise en forme et contrôle de la morphologie de surface d'oxydes mixtes préparés par électrodéposition et ce à travers le contrôle de la croissance d'oxyde simples , (v) la compréhension du mécanisme de nucléation des hydroxydes préparés par électrodéposition (Ni-Co hydroxydes).

Les résultats de ce mémoire de thèse vont au delà de l'état de l'art et apportent des faits marquants pour l'avancée du développement de nouveaux matériaux pour électrodes dans des supercondensateurs redox.